NASA/TM—1998-112224

Boundary Layer Transition in the Leading Edge Region of a Swept Cylinder in High Speed Flow

Colin P. Coleman
Ames Research Center • Moffett Field, California

National Aeronautics and
Space Administration

Ames Research Center
Moffett Field, California 93035-1000

March 1998

Available from:

NASA Center for AeroSpace Information
800 Elkridge Landing Road
Linthicum Heights, MD 21090-2934
Price Code: A 17

National Technical Information Service
5285 Port Royal Road
Springfield, VA 22161
Price Code: A10

CONTENTS

LIST OF TABLES

LIST OF FIGURES

ABSTRACT

The flow along an attachment line with roughness may become turbulent at the lowest Reynolds number of all transition mechanisms active on a swept wing. Should the flow along the attachment line become turbulent, the flow on the rest of the wing, on both upper and lower surfaces, may also become turbulent, as evidenced during the X-21 flight program. The incomplete understanding of the attachment line and crossflow transition processes is one of the fundamental obstacles to the development of an economically viable, supersonic, laminar flow aircraft.

To date, no theoretical model for the stability of a compressible attachment-line flow has been fully validated. The main reason for this is the very limited amount of accurate experimental data currently available. Experiments were therefore conducted on a 76° swept cylinder to establish the behavior of the attachment line transition process in a low-disturbance level ("quiet"), Mach number 1.6 flow. The use of a quiet tunnel was necessary in order to duplicate the freestream disturbance level encountered at high altitude. The use of a finite length cylinder has been shown to be a useful tool for determining the flow along the leading edge of a highly swept supersonic wing and for studying the flow physics of the attachment line transition process.

The use of a pressure tapped model allowed accurate values of the appropriate viscous length scale and Reynolds number to be obtained, and these were in good agreement with those obtained with an Euler (CFL3D) and boundary layer (BL3D) computational fluid dynamics code. A hot-wire anemometer system, capable of achieving frequency responses in excess of 200 kHz, was developed for Mach 1.6 operation, since the boundary layer disturbances were anticipated to be in the 50–100 kHz range.

It was found that for a near adiabatic wall condition, the attachment-line boundary layer remained laminar up to the highest attainable Reynolds number in the Mach 1.6 Quiet Wind Tunnel at Ames Research Center ($\overline{R}$ of 760). The attachment-line boundary layer transition under the influence of trip wires was found to depend on wind tunnel disturbance level, and a transition onset condition for this flow is established. This boundary suggests that current design practice, based on previous results from conventional tunnels, may be conservative (i.e., roughnesses, twice as large as previously thought possible, could be applied to the attachment line before the onset of transition is observed).

Since the Reynolds number range of the wind tunnel was insufficient to cause transition on the model, internal heating was used to raise the surface temperature of the attachment line and alter the boundary layer mean-flow profile, so inducing boundary layer instabilities. This was demonstrated experimentally for the first time and the frequencies of the most amplified disturbances were determined over a range of temperature settings. Results were in very close agreement to those predicted by a linear stability code (2DEIG) by R. -S. Lin of High Technology Corporation, Hampton, Virginia, and provide the first experimental verification of theory and the nature of the growth of the instabilities with surface heating.

A data set was obtained for transition onset along the heated attachment line at an $\overline{R}$ of approximately 800 under quiet tunnel conditions. Transition location was found to correlate with an approximate N factor of 13.2, where transition onset is identified with a total amplification of e^N starting at the

instability point. Increasing the tunnel disturbance level through the use of trips on the walls of the wind tunnel caused the transition onset to occur at lower cylinder surface temperatures for the same freestream unit Reynolds number and Mach number. This transition location was found to correlate with an approximate N factor of 11.9, thus demonstrating that the attachment line is receptive to increases in the freestream disturbance level.

Flow visualization techniques used included Schlieren photography, oil flow, temperature sensitive paint, and naphthalene sublimation. The latter revealed the presence of stationary crossflow vortices off the attachment line, and a hot wire traversed in the chordwise direction appeared to indicate that these vortices lead to transition at an angle of about 30° around the circumference.

NOMENCLATURE

a	speed of sound, *or* hot-wire response to temperature coefficient
A_0	amplitude of instability at neutral stability point
A_{tr}	amplitude of instability at onset of transition
b	hot-wire response to velocity coefficient
c	complex phase velocity
$\overline{C}$	$\overline{C} = (\overline{R})^2$
c_p	specific heat of air at constant pressure
Cp	coefficient of pressure, $Cp = (p - p_\infty)/0.5\gamma M_\infty^2 p_\infty$
D	diameter of circular cylinder
E	d.c. voltage of hot wire
E_{rms}, E'	a.c. voltage of hot wire
f	chordwise surface static pressure distribution, $f \equiv p_e(\theta)/p_A$
k	diameter of trip wire, *or* thermal conductivity of air
L_b	balance bridge inductance
M	Mach number
N	N factor
Nu	Nusselt number
Pr	Prandtl number, $Pr = \mu c_p/k$
q	instantaneous flow quantity
r	recovery factor

R	universal gas constant
R_θ	momentum thickness Reynolds number, $R_\theta = V_e\theta/\nu_e$
$\overline{R}$	attachment-line Reynolds number, $\overline{R} = V_e\eta/\nu$
$\overline{R}_*$	modified attachment-line Reynolds number, $\overline{R}_* = V_e\eta_*/\nu_*$
$R_{\infty,D}$	Reynolds number based on cylinder diameter, $R_{\infty,D} = V_e D/\nu_e$
Re_k	trip wire Reynolds number (based on boundary layer edge conditions), $Re_k = V_e k/\nu_e$
Re_∞	freestream Reynolds number
R_a , R_c	upper bridge resistances
R_b	balance bridge resistance
R_{wire}	hot-wire resistance
R_{amb}	ambient hot-wire resistance
s	distance from trip wire (or cylinder tip if no trip wire present) to hot wire measured along attachment line
S_u	hot-wire sensitivity to velocity coefficient
S_ρ	hot-wire sensitivity to density coefficient
S_{T_0}	hot-wire sensitivity to total temperature coefficient
$S_{\rho u}$	hot-wire sensitivity to mass-flux coefficient
St	Strouhal number
t	time
T	temperature, *or* time constant
$T_{control}$	control temperature

Tu	one-dimensional turbulence intensity ratio
T_*	reference temperature, $T_* = T_e + 0.1(T_w - T_e) + 0.6(T_r - T_e)$
U, V, W	velocity components in x, y, z directions, respectively
x	chordwise direction (normal to attachment line)
y	spanwise direction (along attachment line)
z	normal direction (normal to cylinder surface)
α	wavenumber in x direction
β	wavenumber in y direction
δ	boundary layer thickness
γ	ratio of specific heats of air
η	viscous length scale, $\eta \equiv \left[\dfrac{\nu}{(dU_e/dx)_{x=0}}\right]^{1/2}$
η_*	modified viscous length scale, $\eta_* \equiv \left[\dfrac{\nu_*}{(dU_e/dx)_{x=0}}\right]^{1/2}$
μ	dynamic viscosity of air
θ	angle measured from attachment line in x direction, *or* boundary layer momentum thickness
ρ	density of air
υ	kinematic viscosity of air
τ	overheat ratio of hot wire, $\tau \equiv (R_{wire} - R_{amb})/R_{amb}$
ω	disturbance frequency
ψ	wave angle

Λ_m	sweep angle of cylinder model
Λ_s	shock wave angle

Subscripts and Superscripts

$(\,)_0$	stagnation conditions
$(\,)_{01}$	stagnation conditions upstream of a shock wave
$(\,)_{02}$	stagnation conditions downstream of a shock wave
$(\,)_1$	static conditions upstream of a shock wave
$(\,)_2$	static conditions downstream of a shock wave
$(\,)_\infty$	freestream conditions
$(\,)_*$	conditions based on the reference temperature, T_*
$(\,)_A$	conditions at the edge of the attachment-line boundary layer
$(\,)_D$	based on the diameter D
$(\,)_e$	conditions at the edge of the boundary layer
$(\,)_i$	imaginary component of complex value
$(\,)_r$	conditions based on the recovery temperature, T_r, *or* real component of complex value
$(\,)_{rms}$	root mean square value
$(\,)_{tot}$	total value
$(\,)_w$	on surface of cylinder (wall conditions)
$\overline{(\,)}$	basic state flow quantity
$(\,)'$	disturbance state flow quantity
$\hat{(\,)}$	disturbance eigenfunction

Acronyms

c.c.	complex conjugate
CFD	computational fluid mechanics
CTA	constant temperature anemometer
DNS	direct numerical simulation
FFT	fast Fourier transform
FML	Fluid Mechanics Laboratory (Ames Research Center)
HSCT	High Speed Civil Transport
LFC	laminar flow control
PSE	parabolized stability equations
PID	proportional with integral and derivative (control)
T-S	Tollmien-Schlichting
TSP	temperature sensitive paint
UV	ultraviolet

1. INTRODUCTION

1.1 Background

1.1.1 The High Speed Civil Transport

Projections made in 1988 suggested that the worldwide demand for long-range air travel would double by the year 2000 and double again by the year 2015 (ref. 1). One option to meet these demands is to consider a new generation of commercial transports that can carry approximately 300 passengers at Mach 2.4 over a 5000–6000 n. mi. range, aimed specifically at trans-Pacific routes such as Los Angeles to Tokyo (fig. 1-1). This concept, called the High Speed Civil Transport (HSCT), is projected to have a passenger seat cost per mile that is only 20% more than current economy class fares (ref. 2), and must therefore be made significantly cheaper to operate than the current Concorde. Such a feat of economics can only be achieved through the use of modern technologies such as lightweight composite structures, improved engine performance, sonic-boom alleviation and better aerodynamics. Design studies (refs. 2 and 3) have shown that actively controlling the airflow over the wings, and hence maintaining skin friction drag at its laminar value, would be a desirable technology to achieve these goals. Laminar flow control (LFC) benefits include increased range and payload, lower fuel weight and usage, lower skin temperatures, and increased altitude, and hence lower sonic-boom ground signatures (ref. 4). Particularly important to the achievement of LFC is the understanding of the boundary layer transition process in the leading edge region of such a highly swept wing.

1.1.2 Definition of the Attachment Line

Consider the flow of air approaching a wing, as sketched in figure 1-2. If the wing is unswept, then air passes over and under the wing, and the dividing streamline along the leading edge is the stagnation line. If the wing is swept back, then a component of air flows out along the leading edge toward the tip. The dividing streamline along which this component of air flows is termed an *attachment line*. This attachment line provides a mechanism for disturbances generated at the wing/fuselage juncture to travel out along the wing toward the tip. If the attachment line becomes turbulent, then disturbances from the leading edge will be transported downstream and may cause the rest of both upper and lower surfaces of the wing to become turbulent. Laminar flow control applied aft of the attachment line, designed on the assumption of a laminar attachment line, may well be insufficient to control the disturbances.

1.1.3 Supersonic Boundary Layer Transition Mechanisms

Figure 1-3 shows that there are many transition mechanisms at work on a swept wing in supersonic flow, including Tollmien-Schlichting (T-S), Taylor-Görtler, and crossflow instabilities, attachment-line contamination and attachment-line transition. T-S transition involves the amplification of initially small disturbances and is the "classical" form of transition found in two-dimensional

low-speed flows. Taylor-Görtler instability is induced by wall or streamline longitudinal curvature. Crossflow instability is caused by a point of inflection in the three-dimensional velocity profile. Consequently, by Rayleigh's theorem (ref. 5), an instability (in the form of co-rotating vortices) is formed which is unstable to a range of disturbances at infinite Reynolds number. Much work has been conducted on the formation and control of these disturbances. However, these become irrelevant should the attachment line first become turbulent.

1.1.4 Dimensional Analysis and Similarity Parameters

The steady compressible flow in the immediate vicinity of a swept-infinite attachment line depends only on the following parameters:

$$V_e, \left(\frac{dU_e}{dx}\right)_{x=0}, \nu_e, a_e, x, T_w, T_e, \gamma, Pr$$

provided surface roughness and freestream turbulence level effects are small. According to the Buckingham Pi Theorem, this flow can be completely described by six independent, nondimensional groups. The choice of groups is essentially arbitrary, but for the present purposes, it is convenient to nominate the following:

$$M_e, \left[\frac{V_e^2}{\nu_e\left(\frac{dU_e}{dx}\right)_{x=0}}\right]^{1/2}, \frac{U_e x}{\nu_e}, \frac{T_w}{T_e}, \gamma, Pr$$

In the study of the transition behavior of swept wings, several dimensionless parameters have been proposed and used as the characteristic Reynolds number for transition of the boundary layer from laminar to turbulent flow. Criteria for transition based on these parameters were generally applicable to subsonic flow conditions as they were based on incompressible flow assumptions. However, in some cases they have been extended to compressible flow.

1.1.4.1 Momentum Thickness Reynolds Number (R_θ)

This parameter was used by several authors including Gaster (ref. 6), Gregory (ref. 7), and Pfenninger (ref. 8), who applied it to swept wings in subsonic flow, and by Topham (ref. 9), who extended it to swept circular cylinders in supersonic flow. It was based on the laminar momentum thickness at the attachment line:

$$R_\theta = \frac{V_e \theta}{\nu_e}$$

where the laminar momentum thickness in incompressible flow can be expressed as:

$$\theta = 0.4044\left(\frac{V_e}{\left(\frac{dU_e}{dx}\right)_{x=0}}\right)^{1/2}$$

Since the momentum thickness is based on laminar flow conditions, the value of R_θ loses its physical significance in turbulent flow. However, it has been used indiscriminately for both laminar and turbulent flows as it is relatively easy to evaluate.

1.1.4.2 Attachment-Line Similarity Parameters ($\overline{R}, \overline{R}_*$)

$\overline{R}$ was proposed by Poll (refs. 10 and 11):

$$\overline{R} = \frac{V_e \eta}{\nu}, \text{ where } \eta \equiv \left(\frac{\nu}{\left(\frac{dU_e}{dx}\right)_{x=0}}\right)^{1/2}$$

(as formed from the above Pi Theorem analysis).

For incompressible flow conditions, $\overline{R}$ is uniquely defined as above for both laminar and turbulent conditions since the kinematic viscosity is based on T_e in both cases.

In the case of a compressible flow with strong attachment-line contamination, Poll showed that the available data could be correlated with a simple value of the similarity parameter of the attachment line $\overline{R}_*$, on the condition that the kinematic viscosity is evaluated at a reference temperature T_* (refs. 12 and 13). This temperature has been defined so as to correlate the data of heat transfer and of turbulent friction on the attachment line:

$$T_* = T_e + 0.1(T_w - T_e) + 0.6(T_r - T_e)$$

$$\overline{R}_* = \frac{V_e \eta_*}{\nu_*}, \text{ where } \eta_* \equiv \left(\frac{\nu_*}{\left(\frac{dU_e}{dx}\right)_{x=0}}\right)^{1/2}$$

1.1.5 The Transition Process, Receptivity and Bypass

The boundary layer instability and transition process is best introduced by considering the growth of two-dimensional T-S modes along a flat plate, as depicted in figure 1-4 taken from reference 14. Region 1 is the stable flow region, in which infinitesimal (small) disturbances are introduced into and received by the boundary layer (receptivity process). As the critical Reynolds number is exceeded, energy is transferred from the mean flow into selected instability waves which grow in the now unstable boundary layer, region 2. This slow growth of selected waves occurs without affecting the mean flow noticeably until a threshold amplitude of 0.5–1.0% of freestream velocity is reached. At finite perturbation amplitudes, rapid nonlinear amplification occurs through secondary and tertiary instabilities where one or more instability modes have grown sufficiently to affect the mean flow. Breakdown of the laminar boundary layer starts at disturbance amplitudes of 3–5% of the freestream velocity (region 3). Initial bursting occurs in region 4, and these bursts grow so large that they create intermittent three-dimensional "islands" of turbulence, called "spots" (region 5, also known as the intermittent region). Breakdown, or transition onset, is defined at the first occurrence of these turbulent (Emmons) spots. This leads to fully turbulent flow in region 6. It should be noted that in figure 1-4, region 2 has by far the greatest length in practical aerodynamic engineering applications.

Morkovin (ref. 15) attempted to capture the various evolutionary paths to turbulence as shown in figure 1-5. The initial external disturbances, such as freestream vorticity and sound, are believed to enter the boundary layer from the surroundings via a process known as *receptivity.* As described above, these disturbances may lead to turbulent flow through several stages. Should the initial disturbances be very large or should surface excrescences exist, then one or more of these stages may be *bypassed*, leading to premature turbulence. Bypass mechanisms are usually characterized by nonlinear three-dimensional spatial/temporal disturbances, such as roughness, noise, waviness, vibration, etc. Current boundary layer stability theory attempts to model the slow linear amplification of small disturbances for many cases.

1.1.6 Wind Tunnel Turbulence Levels

Given the fact that receptivity plays such an important part in initializing the transition process, it should not be surprising that the transition onset location is often a function of disturbances in the freestream and surroundings. Figure 1-6, from Paté's summary on the effects of wind tunnel disturbances on boundary layer transition (ref. 16), shows the three main disturbances that might influence a model in the test section: vorticity fluctuations (turbulence), entropy fluctuations (temperature spottiness), and sound waves (pressure fluctuations). Vorticity and entropy fluctuations are essentially convected along streamlines and are traceable to conditions in the settling chamber. Sound disturbances can travel across streamlines and, consequently, can originate in the settling chamber, radiate from turbulent boundary layers along the tunnel walls, and be induced by wall vibrations. These three fundamental and distinctly different types of freestream modes can exist independently in compressible flow wind tunnel facilities.

These disturbances, therefore, become a particular consideration when trying to conduct transition experiments in wind tunnels, which have historically had orders of magnitude greater disturbances when compared with flight at high altitudes (ref. 17). Therefore, great efforts are made to ensure that the tunnel environment approximates that of flight in quiescent, or quiet, altitudes. These *quiet* tunnels, as they are termed, employ techniques such as screens, boundary layer bleeds (to maintain laminar boundary layers), and structural vibration isolation in order to keep disturbances to a minimum. There are approximately only five quiet supersonic wind tunnels in the world today (1997). For more details about quiet tunnels, refer to the review of quiet tunnel technology by Wilkinson et al. (ref. 18).

1.2 Transition Prediction Schemes

1.2.1 Hierarchy of Schemes

In order of historical development and improved physical modeling (but increased computational and experimental complexity), the hierarchy of methods for transition correlation, analysis, and prediction is as follows:

(1) Methods based on integral boundary layer parameters.

(2) Methods based on linear stability theory for parallel flow (e^N method).

(3) Methods based on parabolized stability equations (PSE).

(4) Methods based on secondary, nonparallel, stability theory.

(5) Methods based on direct numerical solution (DNS) of the Navier-Stokes equations with unsteady freestream input conditions.

Method 2 is known as an amplitude-ratio method, and is currently used in most engineering design and analysis involving transition. Methods 3–5 are known as amplitude methods. For more information on PSE, see references 19 and 20.

1.2.2 Linear Stability Theory and e^N Method

The method most commonly used in industry for transition prediction is based on linear stability theory and the e^N method (refs. 21–23). These linear stability codes are used to determine the amplification of perturbation waves of given direction, frequency, and wavelength. The procedure is to establish a base flow and add disturbances of an assumed form. The system of equations is then linearized and solved. The solution can be carried out in either a temporal or spatial frame of reference. A transformation between the two frames of reference can be made with reference to the group velocity (ref. 24).

If the amplitude at the neutral stability point is called A_0 and the amplitude at the onset of transition is A_{tr}, then

$$N \equiv \ln\left(\frac{A_{tr}}{A_0}\right), \text{ or } e^N = \left(\frac{A_{tr}}{A_0}\right)$$

Empirical criteria are then used to make the predictions useful, assuming that transition occurs at a given value of N. Low values of N are associated with conventional wind tunnels (since high free-stream disturbance levels lead to high values of A_0); high values of N are presumed to be valid for flight. The value of $N = 9$ is often used, and given by the formula above this corresponds to the local amplitude being more than 8100 times the amplitude at the instability point.

The e^N method is used to analyze T-S, attachment line, crossflow, and Görtler instabilities. N-factor calculations can predict transition onset as a function of parameters which influence the mean flow, i.e., Mach number, pressure gradient, wall temperature, angle of attack, wall suction, sweep, discrete roughness, curvature, and flow chemistry. The calculations, however, cannot directly include the effects of organized vortices, combinations of nonlinear modes, and elevated disturbance fields.

Crucial to a good N-factor calculation is the fidelity of the initial three-dimensional mean flow calculation and the modeling of the receptivity mechanisms (if employed). The boundary layer flow must first be calculated for input to the linear stability code. Typically, one would first calculate the inviscid mean flow from an Euler code which then produces the edge pressures and velocities which are the input for a boundary layer calculation with a dense grid. Application of Navier-Stokes codes to generate boundary layer profiles is extremely expensive and time consuming, but may be necessary in certain flow situations, such as corner flows. All boundary layer codes must provide accurate and smooth velocity and temperature profiles and derivatives, and have adequate resolution of profiles toward the boundary layer edge for supersonic Mach numbers. (It is not uncommon to demand second derivatives of the velocity and temperature profiles of the mean flow to four decimal places).

1.2.3 Mach Number Effects

Mack (refs. 25–28) showed that for a flat plate at supersonic Mach numbers up to about four, the laminar boundary layer is unstable to what he called first-mode disturbances. These are the compressible-layer counterpart of T-S waves, except that they are most unstable when aligned at about a 50° to 60° obliqueness angle, rather than when two-dimensional. At Mach numbers above that range, a second mode of instability appears and becomes the more unstable of the two (fig. 1-7). It is unique to compressible flows, and is most unstable when aligned such as to be two-dimensional. Second-mode waves are destabilized to a moderate extent when the wall is cooled, whereas the first mode of instability is destabilized by heating. It is therefore important to realize the local Mach number of the flow of interest in order to appreciate the instability modes at work.

1.3 Literature Review

Excellent reviews of attachment-line research can be found in references 29 and 30.

1.3.1 Subsonic Flow

Early theoretical investigations in this field seemed to indicate that transition of the leading edge boundary layer would not be affected by the wing sweep. However, flight tests conducted by Gray (ref. 31) on a range of swept wing aircraft at the Royal Aircraft Establishment between 1951 and 1952 showed that the transition front moved forward very rapidly once a critical speed was exceeded. It was then generally believed that the leading edge transition was caused by the sweep induced crossflow instability. This concept of leading edge transition was further reinforced by Owen and Randall (ref. 32), who suggested that the crossflow instability arose from a secondary flow in the boundary layer directed at right angles to the external streamlines.

In 1963, projects by Handley Page Limited and Northrop Norair to produce laminar flow swept wings were not successful. These swept wings were designed with suction devices to control the crossflow instability, and hence produce extensive laminar flow. However, initial flight tests showed that the laminar flow was restricted to small regions near the wing tips, and the flow was, in general, turbulent on the attachment line. Several experiments were conducted to investigate the transition behavior of the boundary layer in the attachment line, notably by Gregory (refs. 7 and 33), Gaster (ref. 6), and Pfenninger (refs. 8 and 34).

Gregory (refs. 7 and 33) conducted experiments to investigate the transition behavior of swept leading edges in the National Physical Laboratory 13×9 ft and 9×7 ft wind tunnels. Using hot wires and hot-film gauges to detect transition, first bursts of turbulence were obtained for $\overline{R}$ between 220 and 233, while complete turbulence occurred at $\overline{R}$ between 235 and 243 in the presence of a large trip wire. When the attachment line was contaminated by a turbulent boundary layer generated by a small streamwise flat plate, it was found that transition occurred as $\overline{R}$ increased from 230 to 260.

Gaster (ref. 6) carried out flight experiments using a tapered swept wing mounted vertically above the fuselage of a Lancaster bomber. Hot-film gauges were used to detect transition. It was found that the critical value of $\overline{R}$ for the start of transition was about 220, while transition was complete at $\overline{R}$ of about 240. It was confirmed that the turbulent flow at the leading edge was caused by the turbulent contamination spreading from the wing root along the attachment line. Wind tunnel tests were also carried out in the Cranfield College of Aeronautics 8 × 6 ft subsonic tunnel at sweep angles of 40° to 60°. It was found that in the presence of large trip wires, transition occurred at $\overline{R}$ of 260, while for small disturbances, laminar flow was maintained up to the maximum obtainable value of $\overline{R}$ of 420. A device for preventing attachment-line contamination called the "Gaster bump" was tested in both wind tunnel and in flight and found to be effective up to the maximum value of $\overline{R}$ of 420. This consisted of a small fairing which was attached to the leading edge close to the wing root, and was shaped in such a way that the contaminated turbulent boundary layer was brought to rest at a stagnation point on the inboard side while a "clean" laminar boundary layer was generated on the outboard side.

Pfenninger's group carried out flight tests on the Northrop X-21A aircraft as well as model tests in the Northrop 8 × 11 ft low speed wind tunnel (refs. 8 and 34). They concluded that the turbulent flow in the inboard region was caused by the spanwise turbulent contamination along the attachment line originating from the wing fuselage junction. Using hot wires on model wings swept back at 33° and 45° and in the presence of gross disturbance sources, Pfenninger found that bursts of turbulence propagated along the attachment line when $\overline{R}$ was between 235 to 260, while transition was complete when $\overline{R}$ was between 260 and 272. With strong suction at the wing fence junction, laminar flow was obtained up to the top speed of the tunnel at $\overline{R}$ of 350, while complete laminar flow existed on both upper and lower surfaces of the wing if $\overline{R}$ was less than 250.

Cumpsty and Head (ref. 35) developed an approximate method of calculating three-dimensional turbulent boundary layers in which all terms in the momentum integral equation in the streamwise and crossflow directions were considered. This analysis was applied to the calculation of the turbulent attachment-line flow on a swept-infinite wing, and reasonable agreement was obtained with the isolated measurement by Gaster (ref. 6). They recognized that the dimensionless parameter $\overline{C}$, defined as $\overline{C} = (\overline{R})^2$, was the relevant Reynolds number for the prediction of transition on the attachment line of a low speed swept wing. The calculations were later compared to the results of wind tunnel measurements of the attachment-line boundary layer of a swept wing in low subsonic flow (ref. 36). Using a swept wing with a sweep angle of 60°, a wide range of values of $\overline{C}$ was covered in the experimental investigation. A hot-wire gauge was used to detect transition of the boundary layer. Without a trip wire, the attachment-line flow was laminar over the full range of $\overline{C}$ up to 3.7×10^5, corresponding to a value of $\overline{R}$ of about 610. With a large trip wire fitted at the leading edge, transition of the attachment-line flow was observed in the range $0.6 \times 10^5 < \overline{C} < 1.4 \times 10^5$, corresponding to $245 < \overline{R} < 374$. At higher values of $\overline{C}$, the flow was fully turbulent.

The transition behavior of the attachment-line flow was comprehensively investigated by Poll (refs. 10 and 11) in the Cranfield College of Aeronautics 8 × 6 ft subsonic wind tunnel. Using the same swept wing model as Cumpsty and Head, values of $\overline{R}$ ranging from 125 to 740 were obtained in the tests for sweep angles of 50° to 70°. A constant temperature hot-wire probe was used to detect

transition on the attachment line. Poll correlated the attachment-line transition behavior with two parameters: the attachment-line similarity parameter $\overline{R}$ and the ratio of roughness heights (e.g., trip wire height) to local length scale k/η. Results are summarized in figure 1-8.

For the smooth cylinder ($k/\eta = 0$), it was found that the subsonic attachment-line boundary layer had no unstable modes when $\overline{R} < 570$. For $\overline{R} > 570$, transition was the result of amplification of small perturbations already present in the upstream flow, leading to two-dimensional perturbation waves that were convected along the attachment line until they degenerated into turbulent spots.

For strong perturbations ($k/\eta > 2.0$) induced, for example, through attachment-line contamination or by a large diameter wire placed perpendicular to the attachment line, turbulence was triggered immediately at the wire and continued to exist downstream if $\overline{R} > 245$. For $k/\eta < 0.8$, the perturbation had no effect on the transition process. For intermediate values of k/η, the trip wire introduced disturbances into the attachment-line boundary layer that were either amplified or damped depending on the value of $\overline{R}$. Results obtained by Poll (refs. 11 and 37) confirmed that a turbulent boundary layer along an aircraft fuselage behaves as a source of strong perturbations that can trigger transition, and that this turbulence can then propagate along the leading edge if $\overline{R} > 245$.

Poll and Paisley (ref. 38) also demonstrated the phenomenon of "reverse transition" along the attachment line. On a tapered wing, $\overline{R}$ will decrease from the root to the tip (since the leading edge radius usually decreases). Near the root, $\overline{R}$ is usually larger than 250, so that the attachment-line flow is at first turbulent. However, if $\overline{R}$ becomes low enough, turbulence is no longer self-sustaining and a "reverse transition" is likely to occur.

Arnal and Juillen (refs. 39 and 40) studied attachment-line contamination along the leading edge of a 40° swept wing which was directly mounted on the wind tunnel floor in the vertical plane. They found that leading edge contamination appeared at $\overline{R} = 251 \pm 11$, and that the leading edge was fully turbulent at $\overline{R} = 318 \pm 22$. Similar results were also obtained by Hardy (ref. 41) on tapered wings, thus confirming Poll's results.

Bippes (ref. 42) also observed the "natural" transition process along the attachment line (similar to that seen by Pfenninger and Bacon (ref. 34), and Poll (ref. 10)).

In the late 1980s, a modified Jetstar was used as part of the Leading-Edge Flight Test Program (refs. 43 and 44). Gloves were manufactured by Lockheed Georgia and Douglas Aircraft Company and incorporated their own LFC system. Test conditions were Mach numbers from 0.7 to 0.8 and altitudes from 32,000 to 40,000 ft, and included operating out of Atlanta in the summer and Cleveland in the winter. The flight tests demonstrated the effectiveness and reliability of laminar flow control under simulated airline service conditions, with particular attention being given to the leading edge region. The flights also showed that, without using a turbulence-diverting device such as a Gaster bump, a significant amount of attachment-line suction was found to be necessary in order to obtain laminar flow over most of the wingspan of the test section. Other flight tests included an F-111 and an F-14, which were used to study the crossflow/T-S interaction on natural laminar flow wing surfaces (ref. 45). For a comprehensive review of flight tests, see references 46 and 47.

These results all demonstrate that maintaining a laminar attachment line is crucial in the application of laminar flow control. Therefore, the understanding of attachment-line boundary layer stability represents a practical problem of primary importance in the design of advanced laminar flow control swept wings.

The first successful theoretical investigation into the linear stability of the incompressible attachment line was made by Hall et al. (ref. 48). The base flow was modeled as a swept Hiemenz flow, and a nonparallel, linear stability theory was used in which two-dimensional Görtler-Hämmerlin (G-H) instability modes were assumed. The critical Reynolds number was found to be about $\overline{R} = 582$, which was in good agreement with the experimental data. It was also found that the attachment line was stabilized with small amounts of suction. Hall and Malik (ref. 49) later explained the absence of upper branch neutral stability modes as being due to a subcritical bifurcation along most of the upper branch.

Spalart (ref. 50) used a full nonlinear approach by solving the three-dimensional, time-dependent Navier-Stokes equations. White noise was introduced and its growth checked for decreasing values of $\overline{R}$. He found that, indeed, the G-H disturbances were the most unstable. Starting from a large value of $\overline{R}$ for which the attachment line was turbulent, he found that the turbulent structures disappeared for $\overline{R}$ between 250 and 300. He also investigated the effects of suction, and compared the results to linear theory and found that suction has a much weaker effect on the nonlinear phenomena than on the linear stability of the laminar boundary layer. Two independent wind tunnel studies by Poll and Danks (ref. 51) and Juillen and Arnal (ref. 52) showed that turbulence propagating along the attachment line can be relaminarized by applying surface suction. Their results agreed well with the direct numerical simulations of Spalart.

Joslin (ref. 53) also conducted a direct numerical simulation by introducing two- and three-dimensional disturbances into the three-dimensional attachment-line boundary layer. His results agreed with Hall and Malik (ref. 49) in that he too found that a two-dimensional nonlinear disturbance growth occurs near branch II of the neutral curve. In general he found that three-dimensional instabilities were more stable than two-dimensional, and that suction stabilized the flow.

More recently, Lin and Malik (refs. 54–56) developed a two-dimensional partial-differential stability approach for the stability of the attachment-line boundary layer. Results obtained by this generalized method confirm the critical Reynolds number reported by Hall et al. (ref. 48). Effects of surface curvature and nonuniform suction on the stability were also addressed by Lin and Malik (ref. 54).

1.3.2 Supersonic Flow

Dunning and Ulmann (ref. 57) conducted wind tunnel tests at Mach 4.0 to determine the effects of leading edge sweep and angle of attack on crossflow boundary layer transition on flat plate wings with blunt leading edges. The results showed that transition always occurred along a front parallel to the leading edge. An increase in sweep angle caused the transition front to move closer to the leading edge and decreased the transition Reynolds number.

One of the first supersonic flight tests to use flow visualization as a means of transition detection was carried out by McTigue et al. (ref. 58) on an F-104. The aircraft had sharp leading edges with low sweep and supersonic leading edges. The left wing was cleaned up by smoothing the leading edge slat joint and residual roughness; the right wing had a fiberglass fairing with imbedded temperature gauges. Tests at Mach 2.0 and an altitude of 55,000 ft produced crossflow striations and turbulent wedges in the sublimating chemicals.

Topham (ref. 9) carried out a survey of experimental data of heat transfer rates on swept cylinders and leading edges in supersonic flow up to Mach 10. He found good correlation between the transition characteristics at the attachment line and Reynolds number based on the laminar momentum thickness. It was deduced that transition of the attachment-line boundary layer in supersonic flow began when R_θ was 130, corresponding to a value of $\overline{R}_*$ about 310. Based on the experimental and theoretical results of Beckwith and Gallagher (ref. 59), he further proposed that the flow would be completely turbulent when R_θ was 450 ($\overline{R}_*$ of 1070).

Measurements of heat transfer rate at the attachment line of a swept circular cylinder at Mach 2.4 and $R_{\infty,D}$ of 10^5 were carried out by Brun et al. in 1965 (ref. 60). Transition of the attachment-line flow was observed at a value of $\overline{R}_*$ of about 220 when the flow was contaminated by turbulence from a streamwise end plate. Similar measurements were conducted by Bushnell (ref. 61) on a swept circular cylinder with a wedge attached to the base of the model at Mach 8. He found that the attachment-line flow changed from laminar to fully turbulent over the test Reynolds number $R_{\infty,D}$ of 0.77×10^5 to 8.7×10^5. The onset of transition in the presence of the wedge occurred at $R_{\infty,D}$ of about 1.4×10^5 ($\overline{R}_*$ of about 210). Based on a survey of heat transfer data for swept leading edges at M_∞ between 2.5 and 8, he deduced that transition generally occurred at $R_{\infty,D}$ of about 2×10^5 for sweep angles greater than 40°. Without the turbulent contamination of an adjoining surface, laminar flow at the leading edge was maintained up to $R_{\infty,D}$ of 8×10^5.

Bushnell and Huffman (ref. 62) surveyed a large amount of heat transfer data for swept leading edges with sweep angles from 10° to 80° at supersonic and hypersonic speeds. They developed a criterion which stated that attachment-line transition occurred at $R_{\infty,D} = 0.2 \times 10^6$ for large upstream disturbances, but when there were no disturbances, there were no occurrences up to the upper limit for the available data at that time ($R_{\infty,D} = 0.8 \times 10^6$).

Poll developed a prediction criterion for transition induced by a gross disturbance at the attachment line in supersonic flow by introducing the compressible similarity parameter $\overline{R}_*$ evaluated at a reference temperature (refs. 12 and 13). He correlated all the available data at that time with this parameter and showed that transition of the attachment-line flow would begin at $\overline{R}_*$ of 250 and would be complete when $\overline{R}_*$ reached a value of 384.

Yeoh (ref. 63) conducted supersonic attachment-line transition experiments in the Cranfield College of Aeronautics supersonic tunnel at Mach 1.7 to 2.4 using a swept cylinder. Four basic configurations were tested using a circular trip wire and two end plates of different size and shape

as gross disturbances in the Reynolds number range $R_{\infty,D} = 1.2–3.2 \times 10^5$. Using a hot-film gauge, it was deduced that transition along the "clean" attachment line was influenced by the wind tunnel boundary layer which was deemed to be acting as an effective disturbance source (and hence the tunnel was considered noisy). The values of $\overline{R}_*$ for the onset of transition of the attachment-line flow in the presence of a gross disturbance were in the range 240 to 278, which bracketed the value suggested by Poll (ref. 10) of 250. Fully developed turbulent flow was not seen, however, and was attributed to the slight favorable pressure gradient and a reduction in the value of $\overline{R}_*$ along the attachment line.

In 1985, an F-15 and an F-106 were used for supersonic natural laminar flow research flight testing (ref. 64). In both cases, the use of a Gaster bump was found to be critical in maintaining a laminar attachment line.

For a comprehensive review of flight tests, see references 46 and 47.

In the 1980s, experiments were conducted to investigate the effects of wind tunnel noise levels on compressible attachment-line transition using swept cylinder models in the NASA Langley Mach 3.5 Quiet Tunnel (refs. 65–67). Four swept cylinder models, of 45° and 60° sweep, were tested. Transition location was determined by a sharp increase in the recovery factor as measured by thermocouples. The cylinders were tested with and without trip wires placed perpendicularly across the attachment line. Freestream turbulence levels, in terms of the root mean square fluctuating pressure normalized by the mean static pressure, were varied from 0.05 to 0.5% by the opening and closing of the boundary layer bleeds near the throat of the tunnel. It was found that without trip wires, attachment-line transition occurred at $R_{\infty,D} = 0.7–0.8 \times 10^6$ ($\overline{R}_* = 650–700$) independent of tunnel noise levels, but with a small trip on the attachment line, transition Reynolds numbers were reduced by high tunnel noise. The trips were therefore deemed to be a mechanism for the freestream turbulence to enter into the attachment-line boundary layer and accelerate the transition process. Crossflow vortices were observed downstream of the attachment line for laminar boundary layer flows using oil flow visualization at $R_{\infty,D} = 4.6 \times 10^5$.

Malik and Beckwith subsequently analyzed Creel's experiments at 60° sweep using the one-dimensional quasi-parallel linear stability computer code COSAL (ref. 68), first based on a swept-infinite cylinder (ref. 67) and then incorporating the finite length (ref. 69). Good comparison was obtained between the computed wavelength of the most amplified stationary crossflow disturbances and the oil flow measurements. Along the attachment line, spatial growth rates were calculated to be the greatest for oblique waves with angles of 50°–60°, with frequencies of 100–175 kHz, and a critical $\overline{R}$ of 640 was obtained. It was also found that moderate amounts of wall cooling significantly stabilized the attachment-line boundary layer. However, it was noted that the boundary layer thickness decreases with cooling, and may become more sensitive to surface roughness resulting in subcritical transition, which the attachment-line boundary layer is known to exhibit as shown by previous theoretical calculations for incompressible flow and experiments in subsonic flow.

Wie and Collier (ref. 70) followed with their own stability calculations for a swept-infinite cylinder for Mach numbers from 0 to 3.5 using the BLSTA boundary layer code (ref. 71) and e^{Malik} (ref. 72). For the experiment of Creel, they calculated a critical $\overline{R}$ of 613 for a wave angle of 60°, close to the $\overline{R}$ of 640 calculated by Malik and Beckwith. They found that a wave angle closer to 50° gave the minimum critical $\overline{R}$ of 573 and noted that this value may decrease with the inclusion of nonparallel effects, as was the case for incompressible flow (ref. 48). Small amounts of suction on the attachment-line boundary layer was shown to be stabilizing by increasing the critical Reynolds number.

Creel (ref. 73) later conducted tests on cylinders with sweep angles of 60° and 76° in the NASA Langley Mach 3.5 Quiet Tunnel. A saw-toothed leading edge, a square device, and a fence were tested to assess their effectiveness in relaminarizing the attachment-line boundary layer. Several of the devices were successful at a sweep angle of 76° (subsonic leading edge), but none were successful at 60° (supersonic leading edge).

Da Costa et al. (refs. 74 and 75) tested a swept cylinder at Mach 7.1 with 74° sweep and various streamwise end plates attached to the apex to act as a gross disturbance source. Pressure and heat fluxes were measured along the attachment line, and transition was detected by thermocouples welded to the inside of the thin-walled model. It was found that transition appeared around $\overline{R}_* = 250$ if the boundary layer on the end plate was turbulent. Wall cooling (with liquid nitrogen) was found to have a small stabilizing effect on transition. A detailed examination of the spanwise evolution of disturbances found that when the boundary layer on the end plate was laminar, attachment-line transition was triggered by the increased turbulence level of the tunnel.

Arnal et al. (refs. 76 and 77) studied boundary layer tripping due to three-dimensional roughness elements placed on and near an attachment line at Mach 10 in the R3Ch wind tunnel. Two steel cylinders were equipped with hemispherical noses and tested at sweep angles from 20° to 70°. The boundary layer state was determined from temperature sensitive paint, thermocouples and an infra-red camera. Their results showed that for a large roughness element placed on the attachment line, a turbulent wedge could develop right behind it with a fully developed turbulent boundary layer downstream. Poll's criterion was validated and they confirmed that Poll's criterion could be applied for several types of gross disturbances, e.g., end plates and tripping devices. They also investigated the effects of placing a roughness element off the attachment line. Turbulence was generated directly behind a roughness element place at 10° off the attachment line, but the amplitude in the spanwise direction quickly decreased with the far downstream part of the cylinder still being laminar. They concluded that for a roughness placed off the attachment line, the strong negative pressure gradient damps out the generated disturbances, and turbulent structures cannot develop. By contrast, there is no streamwise pressure gradient along the attachment line, and transition occurs; hence the attachment line is the location where the boundary layer is the most sensitive to roughness elements. Temperature sensitive paint visualization revealed stationary vortices at around 40°, and one-dimensional linear stability theory was used to predict the frequency of these streaks for three increasing wall temperatures (refs. 77 and 78). The value of the most unstable wavelength was not very sensitive to wall temperature, and roughly agreed with experiment flow visualization. For large three-dimensional trips placed on the attachment line, tripping became effective as soon as $\overline{R}_*$ exceeded 250, in agreement with Poll's criterion. A similar result was obtained by da Costa using

trip wires normal to the attachment line (ref. 75). Placing trips off the attachment line required larger trip heights to trip the attachment-line flow, and this height increased with distance in the chordwise direction.

Skuratov and Federov (ref. 79) studied the effect of a variable height two-dimensional disturbance and isolated three-dimensional roughness on the attachment line of 45° and 60° swept cylinders with hemispherical caps at Mach 6.0. The two-dimensional disturbance consisted of a small "wall" across the attachment line that could be raised and lowered by means of a micrometer screw gauge. However, it is suspected that this introduced end effects and was not a true two-dimensional disturbance such as a trip wire. The nature of the boundary layer was determined by comparing the measured value of heat flux to calculations. For the case of two-dimensional roughness they found that self-sustaining turbulence occurs above $\overline{R}_* = 240$ and is almost independent of the roughness height, consistent with Poll's criterion range. For distributed roughness, four rows of emery grains were bonded onto the smooth cylinders perpendicular to the attachment line. Self-sustaining turbulence was observed for $\overline{R}_* = 250$, again confirming Poll's criterion.

Cattafesta performed crossflow transition experiments on a 77.1° symmetric delta wing in the NASA Langley Mach 3.5 Quiet Tunnel. Surface temperature distributions were obtained with temperature sensitive paint, and transition results were compared with the e^N code COSAL (ref. 80). It was found that an N factor of 14 best correlated the results, and that traveling crossflow disturbances in the 40–60 kHz range were the most amplified. Experiments with suction were later conducted (ref. 81), with Lin et al. (ref. 82) simultaneously performing stability calculations using the compressible linear code $e^{Malik3D}$ (ref. 83). In both cases it was found that distributed suction had a stabilizing effect, and that Reynolds number had a first-order effect on transition location. The modes with the highest N factors were found to be traveling crossflow disturbances with frequencies in the 20–90 kHz range, and the transition N values ranged from 10.5 to 14.

Holden and Kolly (ref. 84) studied the attachment-line transition on a swept cylinder for $M_\infty = 10$ to 12 with sweep angles between 60° and 80°. The effects of attachment-line contamination were investigated by testing several configurations and with surface roughnesses. Thin-film heat transfer gauges were used to identify transition onset. For smooth, highly swept configurations, transition was observed on the attachment line for Reynolds numbers greater than $R_{\infty,D} = 8 \times 10^5$. For flows with attachment-line contamination, attachment-line transition was observed for $\overline{R}_*$ between 300 and 500, depending upon the magnitude of the upstream disturbance. However, it is believed that their trip wires were placed too close to the tip of the model and so were in the developing flowfield, which is known to yield results that do not truly represent a fully developed attachment-line boundary layer.

Murakami et al. (ref. 85) performed experiments in the DLR hypersonic Ludweig tube wind tunnel at $M_\infty = 5.0$ and 6.9. Experiments were conducted on cylinders with 30°, 45°, and 60° sweep, with and without large end disturbances. Attachment-line transition was determined using the liquid crystal technique. Their results showed that attachment-line transition occurred at about $R_{\infty,D} = 1.5\text{–}3.3 \times 10^5$ and $9\text{–}12 \times 10^5$ with and without end plates, respectively. The gross disturbance results agree with both Poll's criterion and the Bushnell and Huffman transition criteria

discussed above. Transition aft of the attachment line was also observed as evidenced by a fine streak pattern in the liquid crystals, typical of that induced by crossflow instability.

Recently, Bernard et al. (ref. 86) investigated the attachment-line boundary layer at Mach 7.1 at 60° and 70° sweep angles. Transition Reynolds numbers were obtained from heat transfer measurements. They validated Poll's criterion at 60° sweep and found that three-dimensional roughness elements seemed much more efficient in promoting transition than two-dimensional ones.

Lin and Malik (ref. 87) extended their two-dimensional incompressible theory (refs. 54–56) to supersonic speeds and studied the linear stability characteristics of the attachment-line boundary layer on a 60° sweep infinite span cylinder in a Mach 3.5 freestream using an eigenvalue approach. They found that the most unstable disturbances in this flow were oblique traveling waves with frequencies on the order of 100 kHz. Due to the strong destabilizing effect of nonparallel terms, the critical Reynolds number decreased from $\overline{R} = 573$ ("1-D" parallel theory) to $\overline{R} = 349$ ("2-D" eigenvalue approach).

Lin (ref. 88) has incorporated nonparallel effects into a compressible attachment-line stability computation. Modeling the finite length cylinder of Creel et al. (refs. 65–67), Lin found the frequencies of unstable oblique traveling modes to be of the order of 100 kHz. Calculations found that the most unstable mode led to an N factor of 11.7 at $y/D = 5$ (position of measured transition onset for clean model). Details of this code are given in Chapter 5.

Two F-16XL aircraft were modified by NASA Dryden for supersonic laminar flow control research up to Mach 2 (refs. 89 and 90). The F-16XL wings had inboard sweep of 70° and outboard sweep of 50°, similar to the proposed HSCT wing configuration. Ship 1 was modified to accommodate an LFC suction glove on the left wing and a passive glove on the right wing. Attachment-line contamination was to be controlled by a wing root cutout and maintaining a sharp leading edge, and crossflow was to be controlled by suction. Instrumentation included static pressure, skin temperature gauges and hot-film sensors. It was found that small regions of laminar flow were obtainable near the leading edge for the case of no suction, and that this area increased with suction applied. However, no laminar flow was obtained at the design flight condition of Mach 1.6 and 44,000 ft.

Earlier, Iyer (ref. 91) had conducted linear stability analyses of fully three-dimensional boundary layers formed on the laminar flow control glove fitted on the F-16XL using the linear stability code COSAL. It was found that in each case the most amplified modes were traveling crossflow waves. In addition, suction was found to have a stabilizing influence, significantly extending the possible extent of laminar flow. COSAL was also applied to the suction glove of the F-16XL (ref. 92), and a study of the attachment-line location and crossflow profiles to angle of attack for the F-16XL were conducted by Flores et al. (ref. 93).

The F-16XL ship 2 aircraft was similar to ship 1 in planform and was configured with a passive glove on the right wing, and an active suction glove on the left wing from the leading edge to approximately 50% chord. Hot films and pressure taps determined the state of the boundary layers and mean flow. Smith (ref. 94) noted that the supersonic laminar flow control experiment achieved about 70–80% of the initial goals (which included achieving 50–60% chord laminar flow). Because

of the potential benefits to the HSCT, specific results of the flight experiment are sensitive information and are not available.

1.4 Purpose of This Investigation

In surveying the foregoing literature review, several points become clear. First, natural transition along supersonic attachment lines has rarely been observed in wind tunnel tests. This is attributed to noisy wind tunnels, available run lengths of experiments and operating conditions. Subsequently, the majority of the surveyed literature covers the case of gross contamination of the attachment-line boundary layer. It is also apparent that code validation is needed if progress is to be made regarding understanding the transition physics. Only by first understanding the underlying boundary layer transition physics can one hope to control the transition process and hence reduce drag. This has been hampered, however, by the fact that instability waves have never been directly measured in a supersonic attachment line. In order to advance the understanding of the supersonic attachment-line boundary layer, the following objectives for this research are presented:

(1) Conduct experiments in a "quiet" supersonic wind tunnel.

(2) Place two-dimensional trip wires across the attachment line to represent the steps and gaps in a wing's joined surface.

(3) Obtain measurements in an unstable viscous layer at and near an attachment line for "natural" forcing conditions.

(4) Employ hot-wire anemometry to discern the nature of the boundary layer and the frequencies of the most amplified disturbances.

(5) Compare results from a compressible attachment-line stability code to the experiment to analyze computational transition modeling.

These unique data will be directly applicable to the HSCT, and important design information will be obtained.

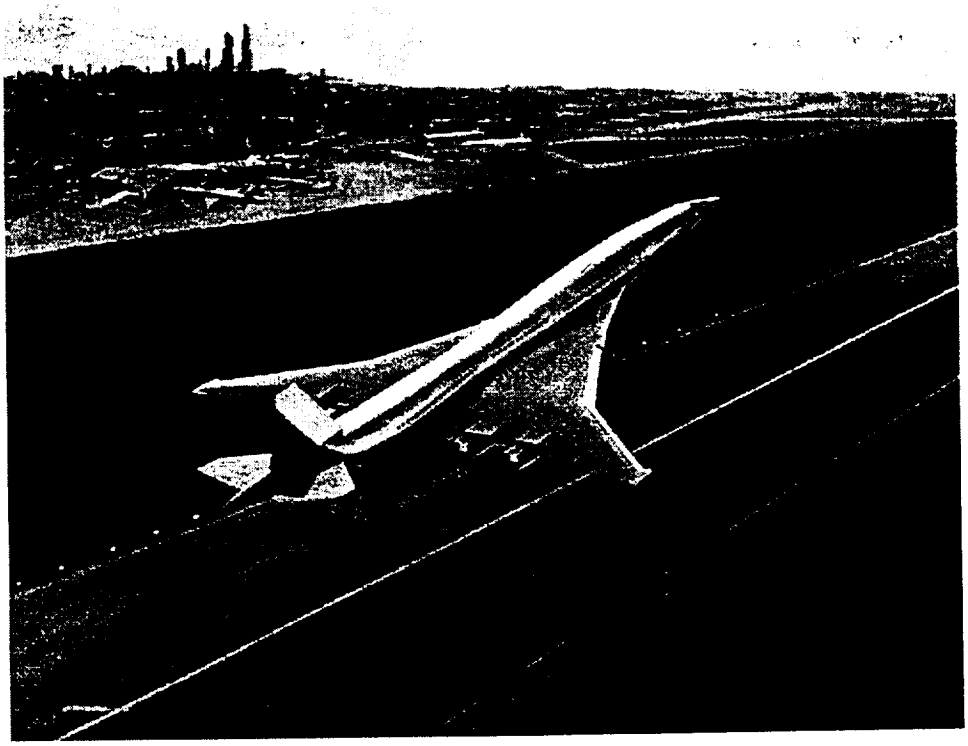

Figure 1-1. Artist's impression of the High Speed Civil Transport.

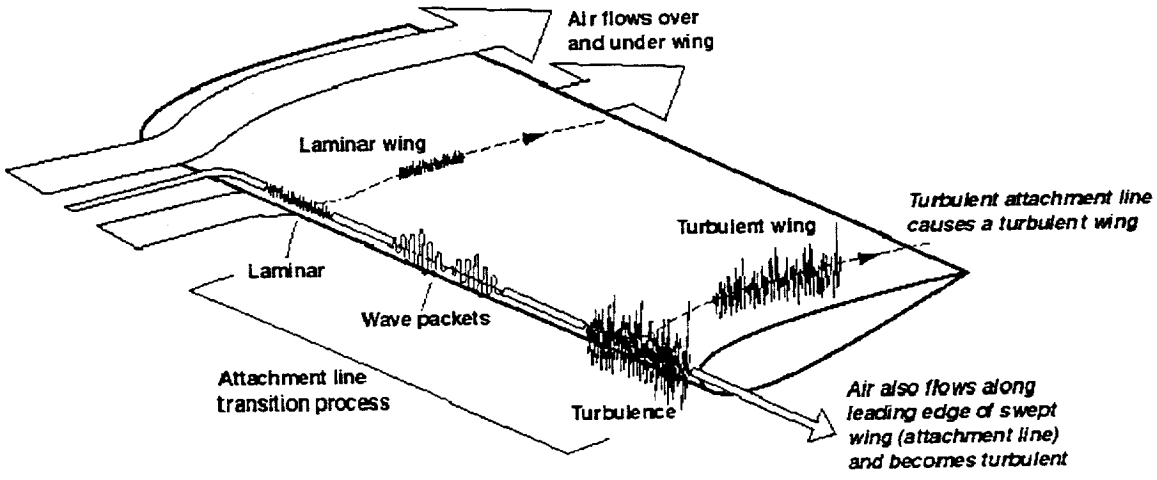

Figure 1-2. Attachment-line transition process.

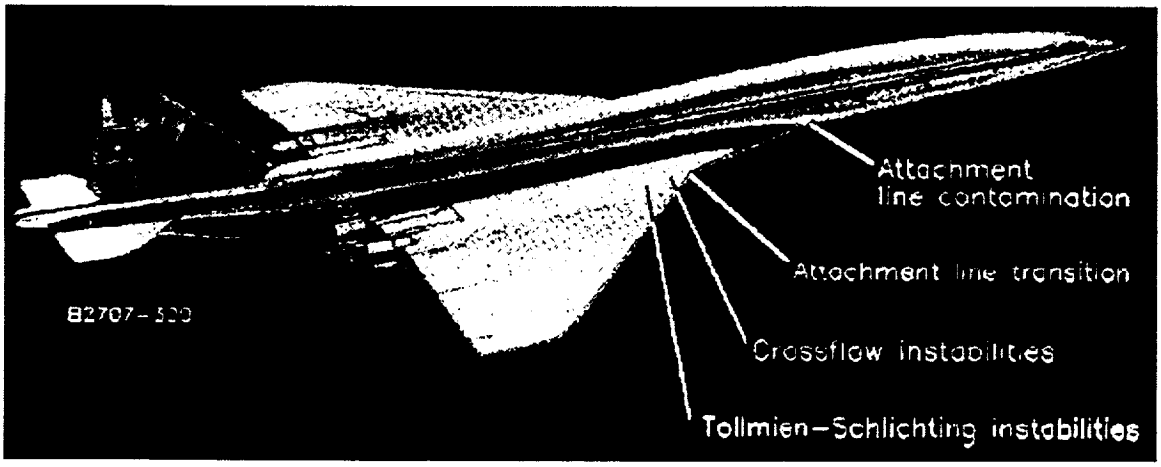

Figure 1-3. Boundary layer transition on a highly swept HSCT wing.

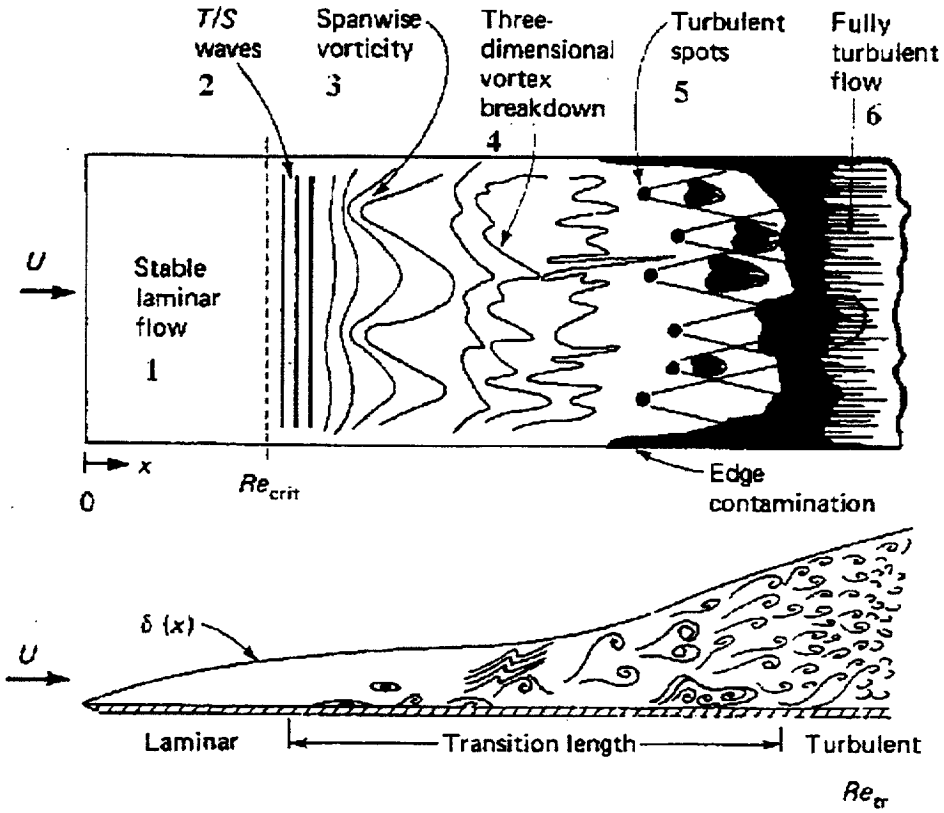

Figure 1-4. Boundary layer transition process along a flat plate (ref. 14).

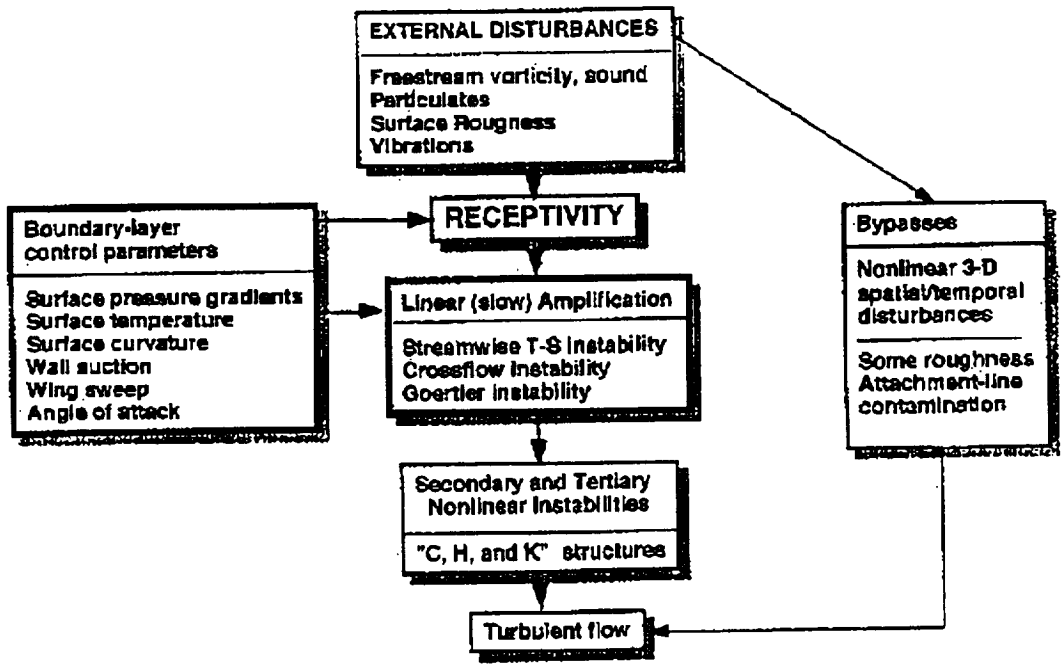

Figure 1-5. Various paths to turbulence, including bypass (ref. 15).

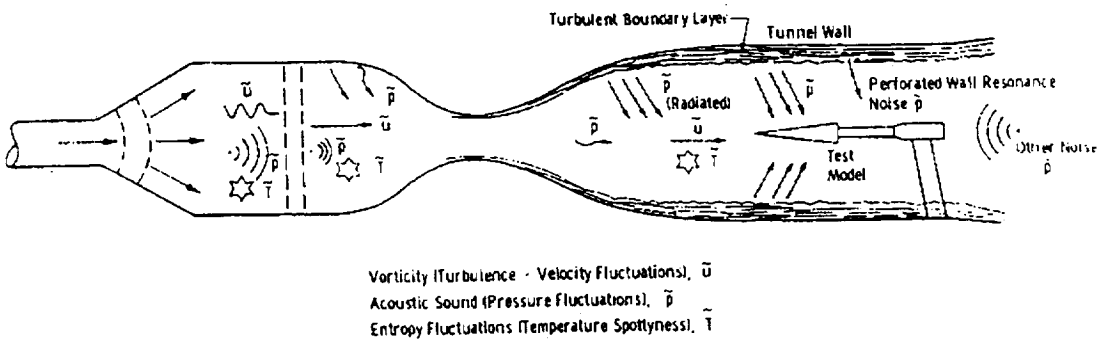

Figure 1-6. Flow disturbances in wind tunnels (ref. 16).

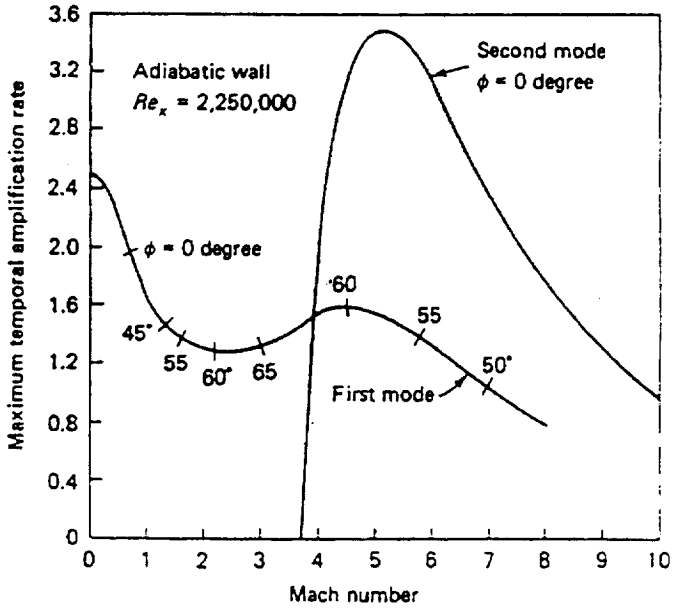

Figure 1-7. Effect of Mach number on instability mode (ref. 26).

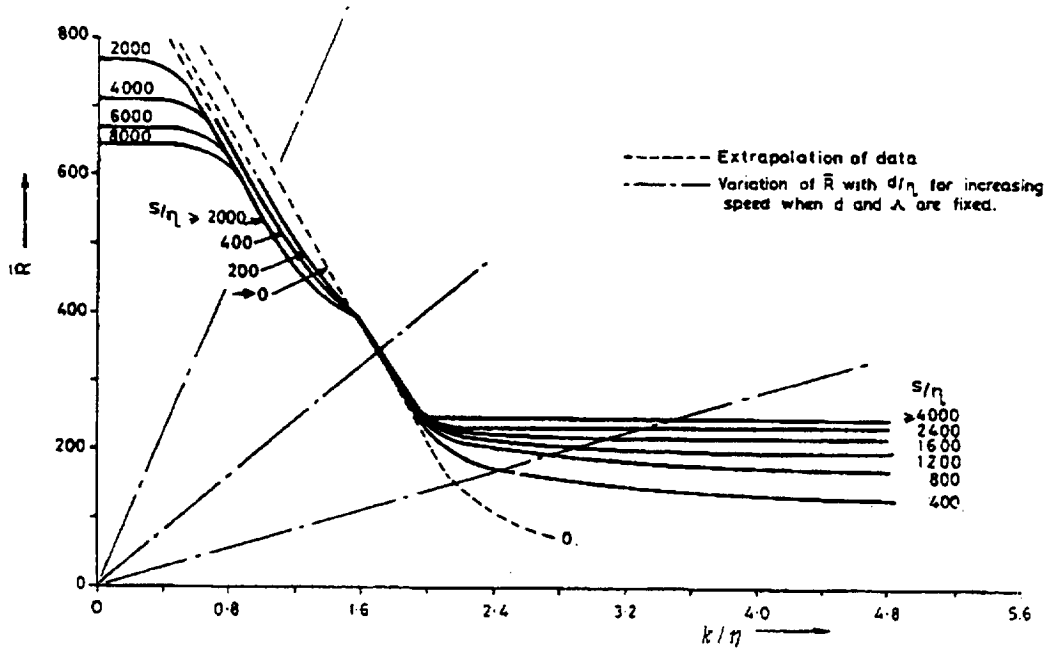

Figure 1-8. The variation of $\bar{R}$ with k/η and s/η for the appearance of first bursts of turbulence (ref. 10).

2. EXPERIMENTAL CONFIGURATION AND TEST CONDITIONS

2.1 Idealization of the Leading Edge Region of a Swept Wing

The leading edge of a high speed aircraft's swept wing has a complex geometry, often incorporating a varying nose curvature, variable sweep angle, surface excrescences, and control surfaces. In order to explore the aerodynamics of a suitably generic configuration (with a reduced number of parameters) that could be applied to a swept wing, it was decided to model the leading edge region as a swept circular cylinder (fig. 2-1). This configuration allowed for the replication of in-flight boundary layer Reynolds numbers due to Mach number and $\overline{R}$ scaling, while retaining simplicity in design and manufacture. Boundary layer stability results obtained with the swept cylinder would therefore be directly applicable to real applications, such as the HSCT.

Further factors influenced the choice of testing parameters and model dimensions. The chosen wind tunnel defined the operating conditions (Mach number, Reynolds number) and constrained the diameter of the cylinder. Computational fluid dynamics (CFD) codes were then used to predict mean flow parameters for various sweep angles and Reynolds numbers to finalize the parameter space.

2.2 Configuration and Geometry Selection

2.2.1 Parameters Set by Wind Tunnel Constraints

Since experiments were to be conducted in the Mach 1.6 Quiet Wind Tunnel at Ames Research Center (Section 3.4), the freestream Mach number and Reynolds number range were predetermined. The diameter of the cylinder was chosen to maximize the achievable $\overline{R}$ while not exceeding 10% frontal area blockage to avoid tunnel starting problems. The test section of the wind tunnel measures 8×16 inches in cross section. Therefore, a cylinder could either be 16 inches long (in frontal projection) and 0.8 inch in diameter mounted normal to a side wall, or 8 inches long and 1.6 inches in diameter mounted normal to the upper or lower wall. Since it can be shown that the value of $\overline{R}$ varies as $\sqrt{D}$ (ref. 11), the larger diameter of 1.6 inches was chosen in order to maximize $\overline{R}$; hence the model had to be mounted to either the upper or lower wall of the test section.

In order not to convect the boundary layer off the tunnel walls and along the attachment line, the tip of the model was chosen to be in free space. This resulted in a forward swept cylinder that did not extend all the way across the tunnel. In this way, a clean attachment-line boundary layer could be initialized from the most forward point of the cylinder. Another consideration was the shape of the most forward part of the cylinder. Creel (refs. 65–67) had selected an apex aligned with the streamwise flow (fig. 2-2), i.e., one that was cut so as to be parallel to the freestream. This gave a bow shock wave that was attached at the apex which took several diameters of length in the spanwise direction to become approximately parallel to the cylinder surface. Consequently, swept-infinite flow conditions were not established immediately but were approached at some distance down the attachment line. Arnal (ref. 40) and Skuratov (ref. 79), however, selected a hemispherical end for their cylinders.

This produced a standoff bow shock wave and allowed the shock wave to become substantially parallel to the cylinder surface in only a few diameters distance in the spanwise direction. (For this work, spanwise is defined as along the attachment line.) This feature also had the added benefit of allowing the cylinder to be turned about its centerline axis without affecting the external flow, and so allowed for just one spanwise line of instrumentation to map out the whole surface of the cylinder. However, the hemispherical end introduces complex entropy swallowing effects. The streamwise cut shape was selected for the present work since, for the data to be compared with computation, it was necessary to define initial conditions for the attachment-line boundary layer at some convenient spanwise position. This was easier to accomplish with the streamwise cut shape than the hemispherical cap since the freestream streamline of interest would cross the bow shock near the apex, and hence the bow shock angle at the crossing point would be better known.

2.2.2 Coordinate System

Figure 2-2 shows the coordinate system used for this work. A right-handed coordinate system was chosen for the model surface, with its origin at the apex of the cylinder. The x-axis was aligned normal to the attachment line in the chordwise direction, the y-axis was aligned along the attachment line in the spanwise direction, and the z-axis was aligned normal to the surface (positive away from the surface).

2.2.3 Parameters Suggested by CFD Analysis

In order to set the sweep angle of the cylinder, two CFD codes were run at three sweep angles to calculate the spanwise distribution of $\overline{R}$ and other parameters of interest. At each sweep angle, the code CFL3D (ref. 95) was run in inviscid (Euler) mode to calculate the mean flow around the swept cylinder configurations. This code provided the boundary layer edge conditions which were then used for the boundary layer computation using a simplified version of BL3D (ref. 96).

2.2.3.1 Description of CFD Codes CFL3D and BL3D

The CFL3D code solves the time-dependent conservation-law form of the compressible Navier-Stokes equations using a thin-layer approximation in all three coordinate directions. The code solves the discretized flow equations implicitly using an upwind-biased spatial-differencing scheme with either flux difference splitting or flux vector splitting for the pressure terms, and central differencing for the shear stress and heat transfer terms, resulting in a global second-order accuracy.

Several turbulence models are available to the user of CFL3D. The zero-equation (algebraic) Baldwin-Lomax model is implemented with the option of using the Degani-Schiff modification. The Johnson-King, one-half-equation model is implemented for single zone cases only. The Baldwin-Barth and Spalart-Allmaras one-equation models and the two-equation k-ω models of Wilcox, Menter, and Anderson are available for multizone grid applications.

The input options for CFL3D allow the user to have flexibility in spatial differencing, time advancement, and turbulence model. From one case to another, most parameters remain unchanged. The physical input parameters include freestream Mach number, sweep angle, Reynolds number per unit length, and static temperature. The computational input data includes CFL number (or time step if time accurate), choice of multigrid cycle, flux vector or flux difference splitting, diagonal or 5×5 block inversions, choice of flux limiter, and choice of spatial accuracy.

Several quantities are output from CFL3D that provide useful information. A residual (L_2norm of density) is output as one measure of convergence. Flow properties including skin friction, pressure and temperature can be output on selected surfaces. PLOT3D files (ref. 97) are also output for more detailed postprocessing. Further details concerning CFL3D as well as some applications can be found in references 98–102.

The BL3D code solves the compressible, three-dimensional laminar boundary layer equations to generate smooth boundary layer mean flow profiles, such as may be required as input to a boundary layer stability analysis. The solution procedure is based on the specification of the boundary layer edge quantities U_e, V_e, and T_e. In addition, the computation of the edge density requires the specification of the inviscid pressure p or the pressure coefficient Cp (for flows that involve a shock wave between the freestream and the attachment line). These values are all interpolated from the CFL3D solution. The linearized system of the boundary layer equations are solved using a fourth-order accurate Padé formula scheme in the wall normal direction. Further details concerning BL3D can be found in Iyer (refs. 91 and 96).

2.2.3.2 Application of CFL3D and BL3D to the Swept Cylinder Case

CFL3D computational grids were constructed by first generating a two-dimensional volume grid from GRIDGEN (ref. 103). The three-dimensional grid was then formed by stacking these two-dimensional "slices" in the spanwise direction at the appropriate leading edge sweep angle. Note that this results in a coordinate system that is not aligned with the coordinate system defined in figure 2-2. This process had already been carried out by Iyer in support of the experiments by Creel (refs. 65–67) and computational grids existed for 45°, 60°, and 76° swept cylinders. A grid convergence study was undertaken at that time (undocumented) which resulted in the following dimensions. The CFL3D grid was composed of two blocks to form a C-H topology and is shown in figures 2-3 and 2-4. Block 1 (fig. 2-3) was a grid that wrapped around the cylinder surface and extended out into the mean flow in all three directions. Block 2 was an inner grid that was superimposed on block 1 in order to allow flow through the space just upstream of the cylinder tip (fig. 2-4). This was required to fully capture the tip flowfield correctly. Block 1 consisted of 65 points in the i direction, 129 points in the j direction, and 65 points in the k direction. Block 2 consisted of 9 points in the i direction, 93 points in the j direction, and 37 points in the k direction. A point of note here is that the experiments conducted by Creel were with cylinders that had an elliptical afterbody in order to reduce the possibility of wake interference effects. This elliptical shape is reproduced in these grids. However,

flow parameters of interest are along the attachment line, and the effect of the afterbody shape was deemed negligible on these results as a first approximation.

The CFL3D code was operated in Euler mode; i.e., viscous and turbulent stresses were ignored. Flux difference splitting was used for the 60° and 76° swept cylinders (subsonic leading edges) while flux vector splitting was used for the 45° case (supersonic leading edge).

The BL3D grid did not cover the entire surface of the cylinder, but was modified in order to calculate just the attachment-line parameters of interest; i.e., it did not extend in the chordwise direction. The BL3D grid consisted of 81 points in the wall normal direction and 52 points in the spanwise direction along the attachment line. The mean flow solution generated by CFL3D for the first five spanwise stations near the tip were ignored since the flow there was considered complex. Subsequently, the boundary layer calculations were initiated just downstream of the tip.

Both of these codes were run on the Numerical Aerodynamic Simulation (NAS) Cray C-90 computer at Ames Research center in batch mode. CFL3D runs never exceeded the 30 Mw memory and 10,000 CPU second time limits set for batch job submissions. PLOT3D output of the CFL3D mean flow solution was sent to an SGI Personal Iris workstation for visualization of the bow shock wave using FAST software (ref. 104).

2.2.3.3 Swept Cylinder Mean Flow Conditions at Three Sweep Angles

CFL3D and BL3D were used to calculate the mean flow, achievable $\overline{R}$, and boundary layer parameters for 45°, 60°, and 76° swept cylinders. Figure 2-5 shows the $\overline{R}$ distribution for these three sweep angles at $Re_\infty = 3.4 \times 10^6$/ft. As can be seen, the 76° sweep angle produces the largest value of $\overline{R}$ of just over 700, which was estimated to approach that of an HSCT aircraft. BL3D was then applied to these three sweep angles for an adiabatic wall condition. Figure 2-6 shows that the boundary layer thickness increases with sweep angle. This is an important consideration since any experimental stability analysis would undoubtedly rely upon a physical probing of the boundary layer which would be made easier if the layer was as thick as possible. However, at only 8.5 to 9 thousands of an inch, the 76° boundary layer is still only two and a half times the thickness of a human hair.

Based on this preliminary design process, the 76° sweep angle was chosen. This last piece of information completed the design of the experimental configuration and parameters. The selected geometry consisted of a forward swept circular cylinder of 1.6 inch diameter, mounted from the top of the wind tunnel test section in the centerline vertical plane, swept at 76° to a Mach 1.6 freestream, with the apex aligned with the streamwise flow. Note that this final configuration closely resembles that of the Tu-144 inboard wing leading edge region in supersonic cruise, as shown in figure 2-1. Therefore, the information gained from this investigation will be typical of existing and future supersonic flight vehicles.

2.3 CFD Calculations for 76° Swept Cylinder

The CFL3D generated $\overline{R}$ and $\overline{R}_*$ distributions along the 76° swept attachment line at two freestream conditions are shown in figure 2-7. These freestream conditions correspond to typical operating limits of the Mach 1.6 wind tunnel. Therefore, the values of $\overline{R}$ and $\overline{R}_*$ represent the maximum and minimum experimentally obtainable values. Note that the model can attain an $\overline{R}$ in excess of 700 at large Re_∞. This is a very large value since most aircraft in service can attain an $\overline{R}$ around 300, and a Boeing 747 can attain values of $\overline{R}$ up to 600. Also note that even at 76° a distance of at least two diameters in length is required before the attachment-line boundary layer is near swept-infinite conditions.

The CFL3D *Cp* distribution along the attachment line for a Mach 1.6 freestream flow is shown in figure 2-8. As can be seen, the finite length model produces a favorable pressure gradient over the first four diameters length from the tip, and tends to asymptote to the swept-infinite value of 0.061. Entropy swallowing effects can be addressed by examining the attachment-line boundary layer edge Mach number (M_e). Figure 2-9 shows that the local Mach number asymptotes within three diameters distance from the tip, thus suggesting that the effect of the tip configuration is such as to minimize the entropy swallowing to this region. Visualization of the bow shock wave was undertaken using FAST software. Figure 2-10 shows the density plotted in the center plane. The bow shock wave is clearly seen and appears to be attached to the cylinder's apex.

BL3D was run with an adiabatic wall condition to predict the boundary layer parameters. Figure 2-11 shows one such plot of the viscous length scale η and boundary layer thickness δ along the attachment line, again at the two ends of the operating spectrum. Within two diameters' distance from the tip, the boundary layer thickness is seen to approximate a near-constant value. In order to probe these thin layers and measure high frequencies, very small instruments would be required, such as hot-wire anemometers. Based on this preliminary CFD analysis, work began in designing a suitable hot wire probe (see Chapter 3). Figure 2-12 shows the wall temperature distribution along the attachment line at $Re_\infty = 2.4 \times 10^6$/ft ($T_0$ = 20° F).

Every parameter studied suggested that a spanwise-varying flowfield existed in the apex region of the cylinder. It was decided that no trip wires or hot wires should be placed in this area during the experiment.

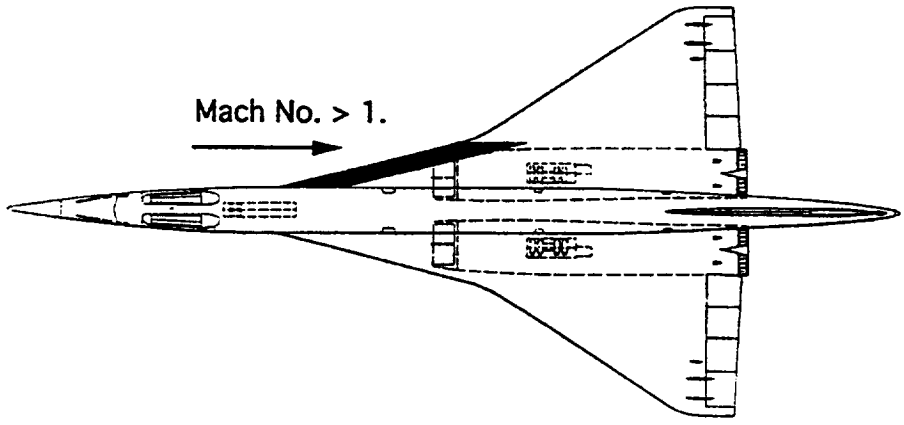

Figure 2-1. Leading edge of a supersonic aircraft may be modeled as a swept cylinder.

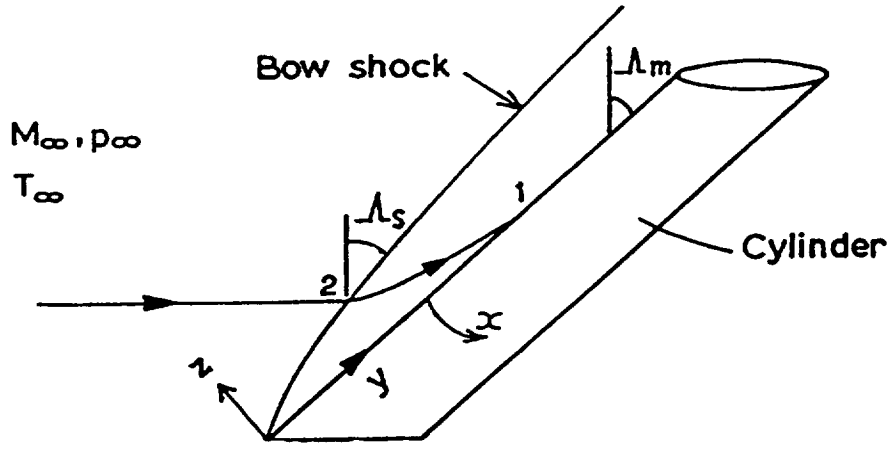

Figure 2-2. Semi-infinite circular cylinder in supersonic flow.

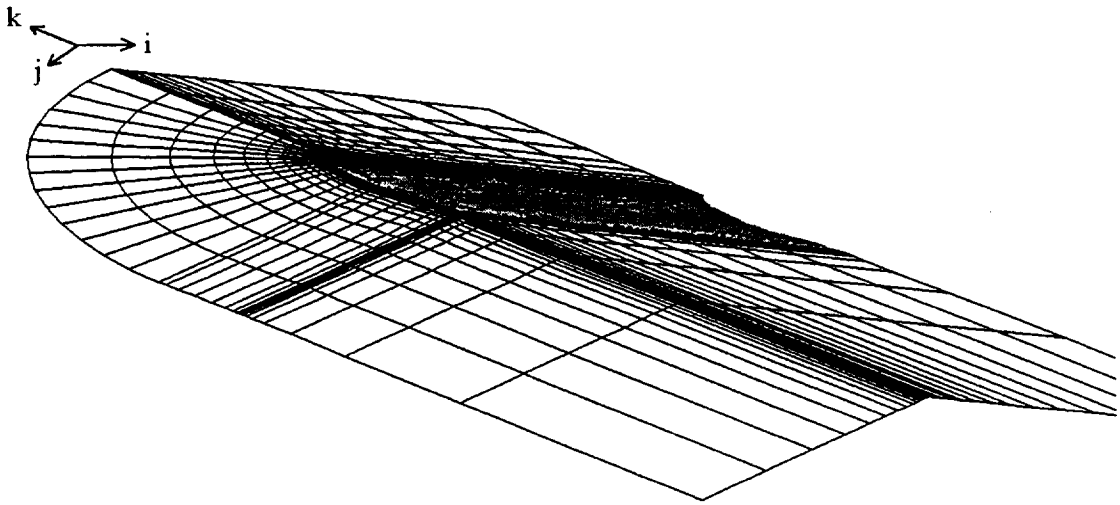

k index is in stream direction.

Every fourth point in i,j,k shown.

I = 9 and k = 1 planes shown.

Note: i,j,k not aligned with physical coordinate system defined in figure 2-2.

Figure 2-3. CFL3D block 1 grid fitted to swept cylinder with elliptical afterbody.

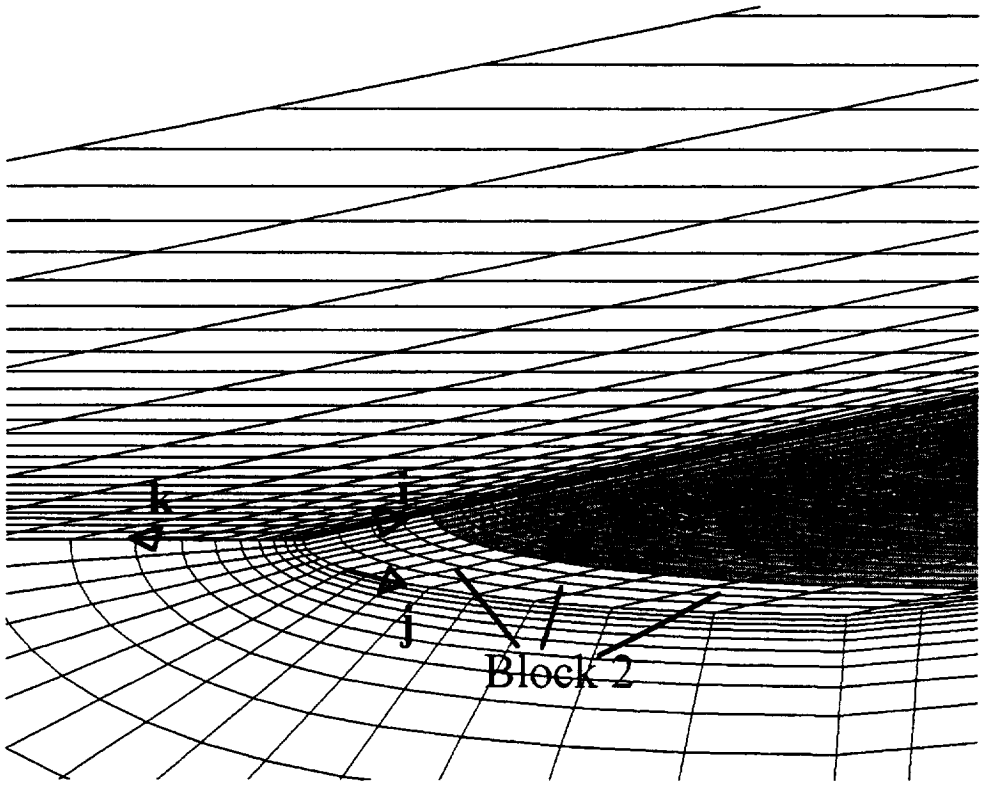

Every second point in i and every fourth point in j,k shown.

I = 1 and k = 1 planes shown.

Figure 2-4. Enlarged view of CFL3D grid in cylinder apex area to show block 2.

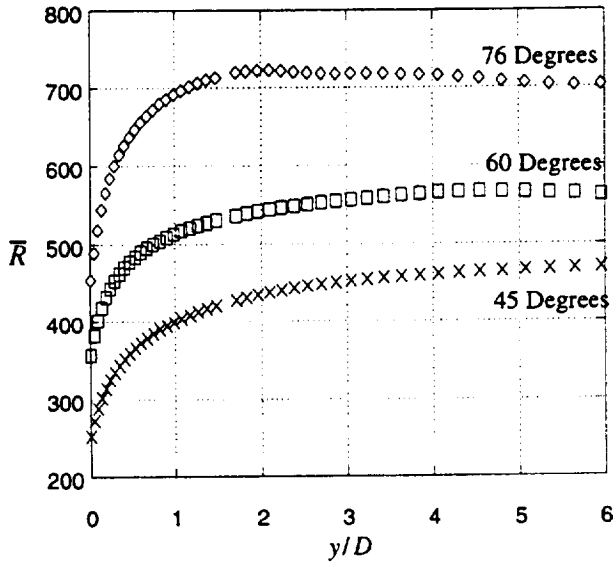

Figure 2-5. $\overline{R}$ along the 45°, 60°, and 76° attachment lines at $Re_\infty = 3.4 \times 10^6$/ft as predicted by CFL3D.

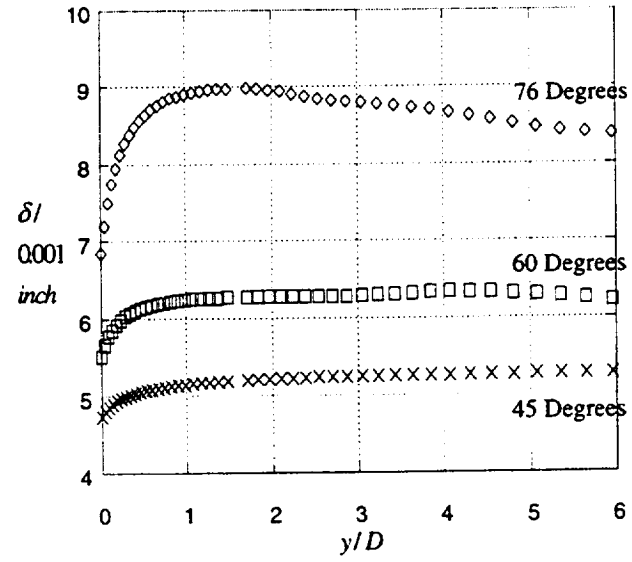

Figure 2-6. δ along the 45°, 60°, and 76° attachment lines at $Re_\infty = 3.4 \times 10^6$/ft as predicted by BL3D.

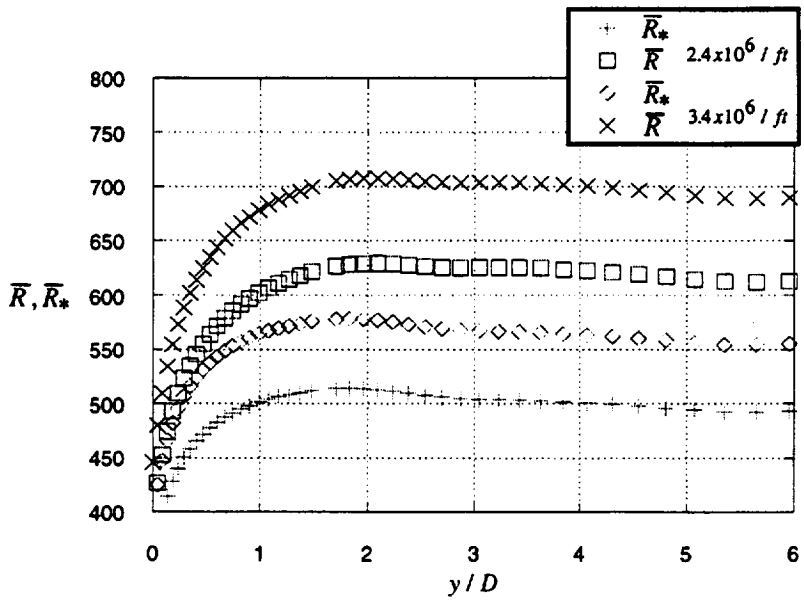

Figure 2-7. $\overline{R}$ and $\overline{R}_*$ along the 76° attachment line as predicted by CFD codes. Re_∞ = 2. 4 × 10^6/ft and 3.4 × 10^6/ft.

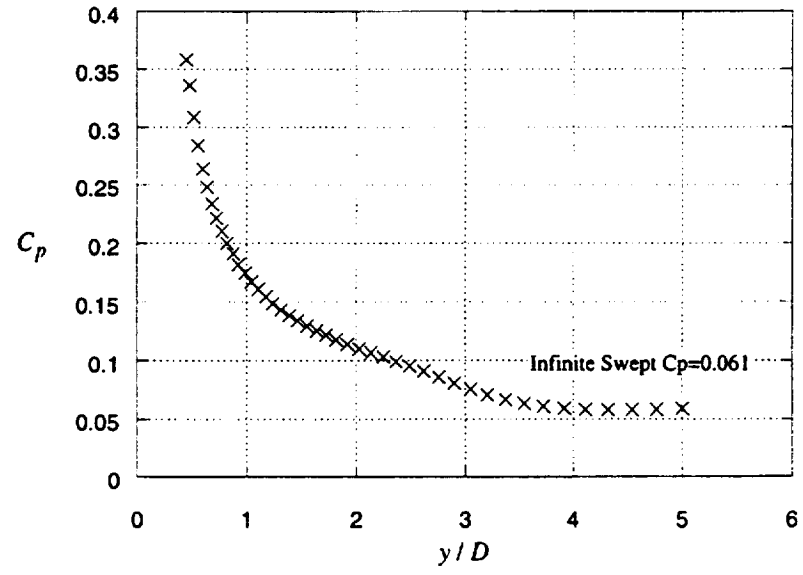

Figure 2-8. CFL3D *Cp* distribution along the 76° attachment line.

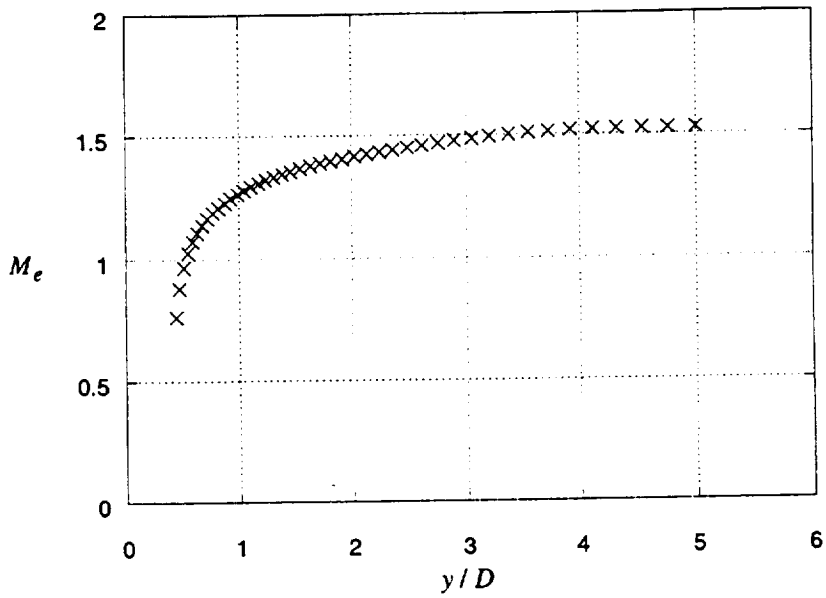

Figure 2-9. CFL3D M_e distribution along the 76° attachment line.

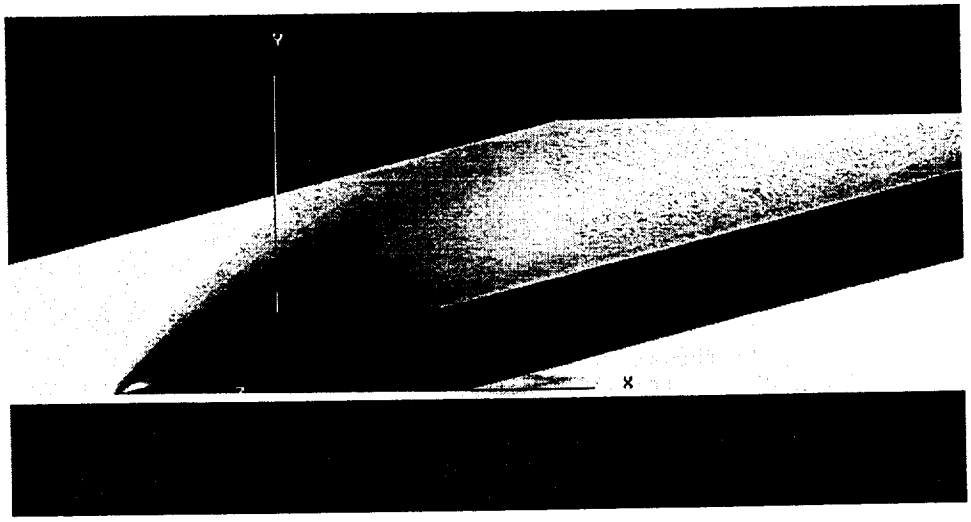

Figure 2-10. FAST visualization of bow shock wave.

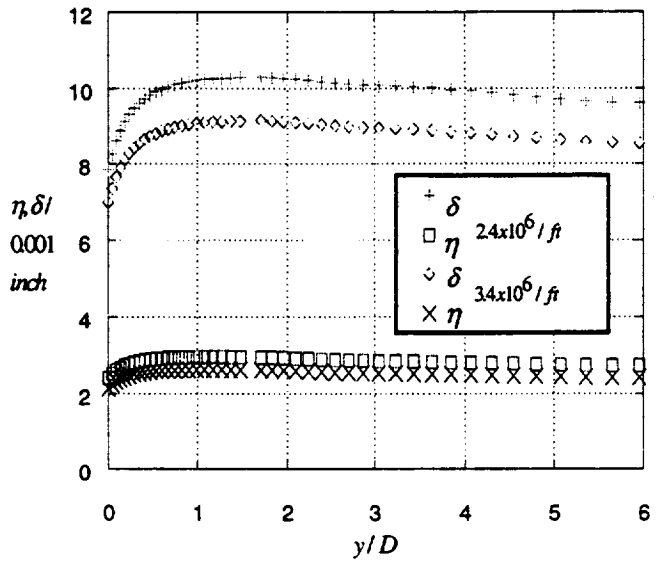

Figure 2-11. η and δ along the 76° attachment line as predicted by CFD codes. $Re_\infty = 2.4 \times 10^6$/ft and 3.4×10^6/ft.

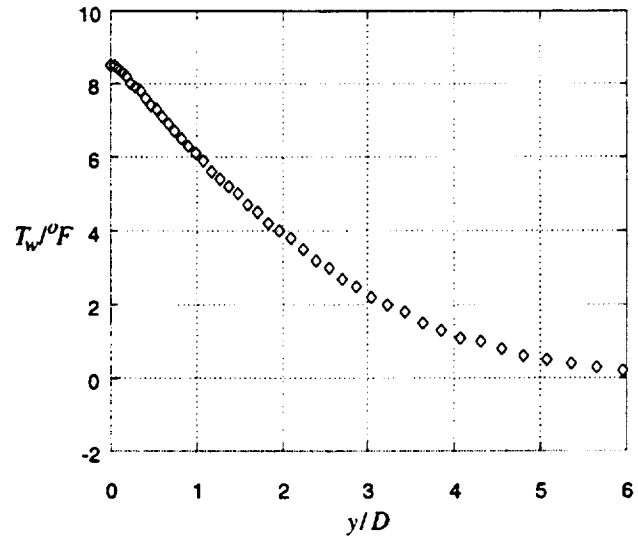

Figure 2-12. BL3D wall temperature distribution at $Re_\infty = 2.4 \times 10^6$/ft ($T_0 = 20°$ F).

3. EXPERIMENTAL APPARATUS AND PRELIMINARY TESTS

3.1 Fourier Analyzer

Dynamic signal analyses for the hot-wire, pressure transducer, and accelerometer signals were performed using a Tektronix 2642A Fourier analyzer system. The Tektronix 2642A can sample four input channels at up to 512 kHz with 16-bit resolution, and it provided averaged 4096-point real time fast Fourier transforms (FFTs), data capture, and display. Most of the signals were captured using a Hanning window and anti-alias filtering, with 20 FFTs averaged for each power spectrum. High and low pass filters were usually set at 250 Hz and 100 kHz, respectively. All data were then collected onto a PC computer for data archiving, postprocessing, and data presentation.

3.2 Constant Temperature Anemometer Hot-Wire Systems

The constant temperature anemometer (CTA) hot-wire system was the primary diagnostic tool for detection of disturbances in the swept cylinder boundary layer. The hot-wire system was also used to detect disturbances in the test section freestream flow. The underlying principle of operation was the same for both cases, although the probe design and method of operation were different.

The hot-wire anemometer has been used extensively as a flow diagnostic tool, primarily for subsonic speeds. Any instrument that physically probes a flow has to be comparatively small so as not to induce any artificial disturbances into the flow. The hot wire is ideally suited for this purpose since it combines smallness of size with potentially high frequency response. Probe design, therefore, is a key issue in the successful application of this technique. Also of importance is the attainment of high frequency response, especially in supersonic flow. This is an important consideration since the frequencies of the boundary layer disturbances tend to be in the 50–100 kHz range at low supersonic Mach number (ref. 26).

A hot-wire anemometer is an electric device which passes an electric current through a fine filament which is exposed to the flow. The filament consists of a material which possesses a temperature coefficient of resistivity; i.e., as the temperature changes, so also does the resistance and Joule heating. The variation of resistance is used to generate signals which are related to the flow velocity or temperature. The instrument is therefore a thermal transducer which is capable of measuring instantaneous velocities and/or temperatures. In supersonic flow, however, the introduction of compressibility causes the wire to respond to fluctuations in mass flux and total temperature.

3.2.1 Theory of Operation

In the CTA mode of operation, the filament is placed in a Wheatstone bridge and a feedback amplifier is used to maintain the wire at very nearly constant resistance (and hence temperature). Fluctuations in the cooling of the filament cause fluctuations in the wire current which lead to voltage fluctuations which are measured at the top of the bridge. For CTA units, the wire current increases for increases in velocity (mass flux) and decreases in (total) temperature.

The main components of a Wheatstone bridge are shown in figure 3-1. The resistors forming the upper half of the Wheatstone bridge define the cross-bridge ratio, i.e., $R_c / R_a = 10$, which is typical. R_b is used to set the resistance of the hot-wire filament, and hence its overheat ratio (τ). τ is defined as $\tau \equiv (T_{wire} - T_r)/T_0$, where T_{wire} is the wire temperature and T_r is the recovery temperature (ref. 105). The overheat ratio was also interpreted as $\tau \equiv (R_{wire} - R_{amb})/R_{amb}$, where R_{wire} and R_{amb} are the hot and ambient wire resistances, respectively.

If the bridge is in 10:1 configuration, R_b is usually a dial resistor, and a variable inductor, L_b, is also used to compensate for the inductance in the hot-wire probe and cable. If the bridge is in 1:1 (symmetric bridge) mode, then R_b is replaced with a length of cable that is identical to that used for the hot-wire probe, and a suitable metal film resistor.

Care was also taken to measure the resistances of probes and cables with a bridge circuit, since a voltmeter would pass a small current through the device and hence raise its resistance reading.

3.2.2 Probe Designs

Two boundary layer hot-wire probes and a single freestream hot-wire probe were used in this investigation.

3.2.2.1 Freestream

The freestream probe consisted of a bare 5.0 μm tungsten hot wire spot-welded to two stainless steel needles. The needles were attached to the end of a rod that had been bent so as to point upstream. The rod was then fed through a side window of the wind tunnel test section and clamped into a manual traverse mechanism. The traverse had a 5 inch range, and so traverses were usually made from both wind tunnel side walls in order to measure the freestream disturbance field. A 5 m length of RG-58 coaxial cable connected the probe to a Disa 55M10 (10:1) constant temperature anemometer.

3.2.2.2 Model Boundary Layer

Two probe designs were used to detect disturbances in the swept cylinder boundary layer. The most successful was a probe based on a subsonic design (known as the Mark 1). A probe based on a design by Laufer and developed by Kendall was also used, although with less success (Mark 2 design). Both wires had a number of common features, including hot-wire element, method of attachment of the probe body to the model, and CTA units used. From the outset, it was decided that the hot-wire probes should be attached to the cylinder surface to reduce the possibility of vibration that could possibly lead to wire breakages.

Initial tests conducted in the freestream using a 5 μm tungsten wire and the Ames Fluid Mechanics Laboratory (FML) CTA unit yielded a top frequency of only 20–25 kHz. Since the anticipated frequencies of the boundary layer disturbances were expected to be much higher, it was decided to use 2.5 μm tungsten wire. The wires were copper plated, and an active length of 0.5 mm

(aspect ratio of 200) was produced by acid-etching the copper. Copper plating was preferred over bare tungsten since the copper acted as extra structural support. Direct spot welding of bare tungsten wire to the hot-wire probe needles was discarded since the presence of the needles would influence the cooling rate of the hot wire through end conduction effects. Since the boundary layer was predicted to be 0.009 inch thick, it was initially desired to place the hot wire at approximately 0.005 inch off of the cylinder surface. Wire breakages at this height, however, later forced the wire to always be set at 0.010 inch. The wire height above the cylinder surface in a wind-off condition was set by placing the probe body on a dummy cylinder of 1.6 inch diameter and measuring the distance with an inspection microscope in the Ames Calibration Laboratory. After positioning, the probe assembly was then carefully transferred to the cylinder in the wind tunnel test section. An attempt was made to use a telescope to measure the height of the hot wire above the cylinder surface. This was made impossible, however, by a high level of vibration in the observed image. It was found that the vibration persisted even with the tunnel and compressor tunnel off. When the compressor came on line, the vibration level increased. It was therefore believed that this unsteadiness entered the telescope via floor vibration and the tripod holding the telescope, and was not originating at the model. (The test section is structurally insulated from the downstream portion of the tunnel to prevent structural vibration problems such as this.) Further work is required to accurately determine the hot-wire height.

Both probe designs were positioned from y = 6 to 8 inches (y/D = 3.75 to 5.00) from the apex along the cylinder utilizing wedge-shaped support blocks. A compromise had to made in the angle of this support; a thin wedge was desired to accommodate an attached shock wave, but this decreased the chordwise dimension that the support block could have on the cylinder. The bottom of the support blocks were covered by a Teflon sheet to protect the polished cylinder surface. The hot-wire support blocks were attached to the cylinder with plastic tie wraps. This arrangement provided a stable fixture only if the ties went around a circular cross section of the cylinder. Placing the support block forward of y/D = 3.75 resulted in a noncircular cross section and hence a loose fixture. A level was used to position the wires to within 0.1° in the chordwise direction. Initial testing used tape to secure the hot-wire leads to the model surface, but these bubbled and lost their adhesiveness with increasing surface temperature. Plastic ties were then used and found to be much better.

The most successful probe, the Mark 1, was based on a subsonic design that was characterized by long (5.0 mm) tapered needles. The probe was held at a 10° angle to the attachment line by a support block with a set screw (figs. 3-2 and 3-3).

The Mark 2 design used a horizontal razor blade with short-length, thin needles made from jewelers' broaches. This was joined to a center support piece which was slotted into the middle of the support block, and the complete assembly was held together by two set screws (figs. 3-4 and 3-5). This design suffered from numerous wire breakages, the cause of which was never realized. The design also had an unfortunate characteristic in that the harmonics of the fundamental frequency of the needles occurred at exactly the frequencies of the boundary layer disturbances, whereas the subsonic design had harmonics at very low frequencies.

2.5 and 3.8 μm diameter wires made from platinum-rhodium (10%) were also tried using the Mark 2 design. However, the tungsten wires were preferred due to their strength and higher coefficient of resistivity.

All hot-wire filaments were made with a slight (0.001 inch) bow in them. Postmortems, using a microscope, were always carried out after wire breakages. Wires broken in the middle were usually representative of too much overheat. A particle impact would remove the whole segment of etched wire. Stresses in the wire and prongs would pull one end of the etched-wire filament away from the unetched part.

A concern was raised that the hot-wire leads and aluminum probe support bodies were directly mounted on the heated cylinder surface and would therefore be heated. This would increase the bridge resistance and hence lead to breakages through too much overheat. Tests were subsequently performed on probes with the hot-wire needles shorted out. The bridge resistance initially fell as the tunnel cooled down, but did not increase with surface heating. This proved that the surface temperature was not as important as air temperature.

Another initial concern was that electromagnetic interference (e.m.i.) would be generated by the electrical supply cables passing closely to the hot-wire lead through the same instrument access hole into the cylinder. This effect was measured to be appreciable, and a separate access hole through the wind tunnel wall was made specifically for the hot-wire lead. This reduced the e.m.i. effect to an immeasurable amount.

In order to move the hot-wire probe back along the model so as to capture a transition front, a simple traverse system was devised. Teflon-coated electrical wires were feed through to the test section from the outside of the tunnel and wrapped around the plastic ties securing the hot-wire support block to the cylinder. The electrical wires were then secured to the surface of the cylinder with plastic ties, so as to allow free movement of the wires along the model. Alternate pulling of the top and bottom wires resulted in the support block "inching" backward along the model. Extra holes were drilled into the test section window blank for the electrical wires to pass through, and these holes had their edges rounded so as not to cut the wires. Marks were made on the cylinder at 1/4 inch intervals from $y = 6$ to $y = 9$ inch, and spanwise position was indicated by the trailing edge of the most rearward plastic tie aligning with one of these marks. Tension had to be maintained in these electrical wires at all times so that they did not get sucked into the tunnel. Screw down clamps held the loose ends of the wires on the outside of the tunnel.

Two hot wires were used simultaneously to investigate the nature of the boundary layers in the chordwise direction as well as the attachment line. However, with the chordwise hot wire at $\theta = 40°$ it was found that both wires exhibited an apparent turbulent signal. Schlieren photography confirmed that the reflected bow shock wave was well behind the position of the probes. This was immediately suspect, since previous tests with the attachment-line hot wire alone had shown that the attachment-line signal should have been laminar. Removing the chordwise hot wire from the cylinder surface immediately returned the attachment-line signal to laminar. It was therefore concluded that the hot-wire support blocks created enough disturbances to be "felt" by the other wire. One possibility was that the 40° wire was yawed enough to produce a shock wave strong enough to separate the boundary layer on the attachment-line probe and produce a subsonic region with some upstream influence. It was decided not to use both wires together. This also meant that the wave angle of the assumed oblique disturbances in the attachment-line boundary layer could not be explored using the wedge-shaped hot-wire support blocks. Further work is required to develop a two hot-wire support mount with minimal interference effects.

3.2.3 Frequency Response Issues

The frequency response of the hot-wire system was indicated by the wire's response to a square wave signal input as measured on an oscilloscope trace (fig. 3-6). This method was a quick technique of estimating the response of the wire system, and was in close agreement with the standard 3 dB system roll-off definition.

The frequency response of the hot-wire system depends on a number of parameters, including the probe design, the CTA unit employed, and operating conditions. Several bench tests were made in an effort to obtain a high wind-off frequency response of a CTA system.

Initial investigations utilized the FML CTA unit which incorporates a 10:1 bridge and gives a frequency response of approximately 25 kHz in low speed flow. After tuning both the feedback and output amplifier circuits to give a flat response out past 200 kHz, it was found that the maximum response in a wind-off condition remained at 25 kHz with 0.7 overheat ratio. This anemometer was then converted to a symmetric bridge, and a selection of variable inductors were used in order to match the inductance of the 5 m length of cable and hot-wire probe. This produced no improvement, however, possibly due to the value of the resistors in the bridge. Attempts to further increase the response of the FML CTA were not pursued.

The Dantec 55M12 unit was then tested. The symmetric bridge design required an identical length of RG-58 cable in the resistance setting circuit, and a range of metal film resistors to set overheat (metal film to keep inductance to a minimum). Multiple resistance settings were achieved by placing up to three metal film resistors in parallel. This immediately obtained wind-off responses in excess of 60 kHz with a 0.8 overheat, and exceeded 200 kHz when placed in the supersonic freestream of the tunnel.

Retuning of the wire was always necessary after the air flow was turned on, and was always done with the boundary layer laminar. Frequency response increased with the Reynolds number and overheat ratio. In order to obtain maximum response at each Reynolds number, the wire would need to be retuned. In practice, however, the wire was tuned at just one Reynolds number and overheat ratio due to the small Reynolds number range of these tests.

Other frequency-maximizing techniques included using low inductance cables that were as short as possible with minimal connections. In fact, a continuous cable was used from the outside of the test section to the CTA unit.

3.2.4 Data Gathering

The output from the hot wires was directed to the Tektronix 2642A Fourier analyzer system. Data were recorded for a time span that was large compared to the time span associated with the boundary layer (due to capturing bursts propagating down the attachment line), i.e.,

$$T >> \frac{\delta}{U}$$

As $\delta = 0.01$ inch and $U = 1500$ ft/sec (approximately), then $T > 4.4 \times 10^{-6}$ seconds. The data recording time base was set to 0.199814×10^{-3} seconds, i.e., 450 times larger.

3.2.5 Calibration

3.2.5.1 Test Section Freestream

The following argument follows the arguments of Izsak (ref. 106) and Rose (ref. 107). Voltage fluctuations in the output signal can be related to property variations by the following relation:

$$\frac{E'}{E} = S_u\left(\frac{u'}{u}\right) + S_\rho\left(\frac{\rho'}{\rho}\right) + S_{T_0}\left(\frac{T_0'}{T_0}\right) \tag{3-1}$$

The problem of determining the behavior of hot wires can thus be reduced to determining the behavior of the sensitivity coefficients S_u, S_ρ, and S_{T_0}. It can be shown that when operating at a high overheat ratio, $S_u \approx S_\rho$ and $S_{T_0} << S_u$. Therefore, equation (3-1) reduces to:

$$\frac{E'}{E} = S_{\rho u}\frac{(\rho u)'}{\overline{\rho u}} \tag{3-2}$$

where $S_{\rho u}$ replaces S_ρ and S_u. Differentiating equation (3-2):

$$S_{\rho u} = \frac{\partial[\ln(E)]}{\partial[\ln(\overline{\rho u})]} \tag{3-3}$$

Thus, the slope of a plot of $\ln(E)$ versus $\ln(\overline{\rho u})$ would yield $S_{\rho u}$, where the mass flux is obtained from the isentropic relations:

$$\rho_\infty U_\infty = p_0 M_\infty\left[1 + \left(\frac{\gamma - 1}{2}\right)M_\infty^2\right]^{\left(\frac{\gamma-2}{\gamma-1}\right)}\sqrt{\frac{\gamma}{RT_0}}$$

Rearranging equation (3-2):

$$\frac{(\rho u)'}{\overline{\rho u}} = \frac{E'}{ES_{\rho u}} \tag{3-4}$$

Since the objective is to determine the turbulence level, $u'_{rms}/\overline{u}$, simplifying assumptions are required. Consider the definition of stagnation temperature (ref. 108):

$$CpT_0 = \frac{U^2}{2} + \left(\frac{\gamma}{\gamma - 1}\right)\left(\frac{p}{\rho}\right)$$

Log differentiating, introducing Mach number and gas law:

$$\left(1 + \left(\frac{\gamma - 1}{2}\right)M^2\right)\frac{T_0'}{\overline{T}_0} = (\gamma - 1)M^2\frac{u'}{\overline{u}} + \frac{p'}{\overline{p}} - \frac{\rho'}{\overline{\rho}} \tag{3-5}$$

We then assume that there are two types of disturbances, sound waves (irrotational) and incompressible, rotational turbulence. If sound were the only disturbance, we could reasonably use the isentropic assumption. If $\overline{T} \leq 0.01$, velocity fluctuations will have a Mach number of approximately 0.01 to 0.02, even for moderate supersonic mean flow Mach numbers. Therefore, this assumption ($\overline{T} \leq 0.01$) would give low Mach number turbulence carried along by supersonic flow, and would itself be close to an incompressible, turbulent pattern.

Therefore,

$$p' \approx \left(\frac{1}{2}\right)\rho(u')^2$$

We can reasonably assume that $p'/\overline{p} << u'/\overline{u}$ and so we can neglect $p'/\overline{p}$ in equation (3-5). This now allows us to obtain density and velocity fluctuations separately. Note that T_0 may still fluctuate, because the turbulent pattern carries along a temperature "spottiness" because of its past history of dissipation.

Therefore, applying:

$$\frac{m'}{\overline{m}} = \frac{(\rho u)'}{\overline{\rho}\overline{u}} = \frac{\rho'}{\overline{\rho}} + \frac{u'}{\overline{u}}$$

to equation (3-5) gives:

$$\frac{u'}{\overline{u}} = \frac{1}{1 + (\gamma - 1)M^2}\left(\frac{m'}{\overline{m}}\right) + \frac{\left[1 + \left(\frac{\gamma - 1}{2}\right)M^2\right]}{\left[1 + (\gamma - 1)M^2\right]}\left(\frac{T_0'}{\overline{T}_o}\right)$$

If total temperature fluctuations are now ignored:

$$\frac{u'}{\overline{u}} = \frac{1}{1 + (\gamma - 1)M^2}\frac{(\rho u)'}{\overline{\rho}\overline{u}}$$

Therefore equation (3-4) becomes:

$$\frac{(\rho u)'}{\overline{\rho}\,\overline{u}} = \frac{E'}{ES_{\rho u}} = \frac{u'}{u}\left[1+(\gamma-1)M^2\right]$$

implying:

$$\frac{u'}{\overline{u}} = \frac{E'}{ES_{\rho u}} \frac{1}{\left[1+(\gamma-1)M^2\right]}$$

Hence, noting the change to root mean square (rms) fluctuation values:

$$Tu \equiv \frac{\sqrt{\overline{u'^2}}}{\overline{U}} = \frac{E_{rms}}{E\left[\frac{\partial \ln E}{\partial \ln(\rho u)}\right]\left[1+(\gamma-1)M_\infty{}^2\right]} \tag{3-6}$$

This neglects both pressure and total temperature fluctuations.

The wire was operated at the highest practical overheat ratio of 0.7 in order to reduce the sensitivity of the wire to temperature fluctuations. The logarithmic derivative was found by recording the mass flux and d.c. hot-wire signal as the stagnation pressure of the tunnel was varied. This method yielded a value of *Tu* which was in very close agreement to that obtained following the method of Smits et al. (ref. 109).

3.2.5.2 Swept Cylinder Boundary Layer

No calibration of the swept cylinder boundary layer hot wire was attempted for several reasons. First, the $Nu = Nu(Re)$ relationship that governs hot-wires becomes $Nu = Nu(Re, M)$ for Mach numbers below 1.2. This would be reached at $y/\delta = 0.6$ in the attachment-line boundary layer, as predicted by BL3D. Second, the Reynolds range of the tunnel is relatively small, and calibration of the wire with minimum freestream Reynolds number would be equivalent to $y/\delta = 0.6$ in the boundary layer with maximum freestream Reynolds number. Third, the total temperature distribution through the boundary layer was unknown. And fourth, a calibration of a hot wire normally requires a pitot tube, commonly made from a hypodermic needle. The smallest commercially available hypodermic needle had an outer diameter of 0.004 inch, and so would not be able to provide the required resolution through the 0.009 inch boundary layer.

Since the wires could not be calibrated, disturbance amplitudes were not obtainable. Quantitative frequency spectra, however, could still be extracted from the recorded analog signals, and qualitative information on the state of the boundary layer could be inferred from the nature of the time history, the shape of the frequency spectra, and the rms value of the hot-wire signal.

3.3 Pressure Transducer System

The Kulite pressure transducers were powered by high frequency response signal conditioners (Dynamic 8000s with a 3 dB drop-off at 500 kHz). Freestream measurements of the pressure disturbances were made with a Kulite pressure transducer model XCS-062-15A (number 3643-5-708) mounted in the linear traverse mechanism. No temperature compensation was used for this transducer since the factory supplied calibration curve was outside of operational temperatures.

Disturbances (such as shock waves) were primarily evidenced by a change in the d.c. signal.

3.4 Mach 1.6 Quiet Wind Tunnel

3.4.1 General Description

Experiments were conducted in the Mach 1.6 Quiet Wind Tunnel in the FML. This unique facility, described in references 110 and 111, provides low freestream turbulence and noise level, essential for transition research, over a range of unit Reynolds numbers from 2.4×10^6/ft to 3.6×10^6/ft. The distinctive features of the wind tunnel are a low-disturbance settling chamber, steady supersonic diffuser flow and low structural vibration of the nozzle and test section walls. Furthermore, the tunnel is designed to run continuously at unusually low stagnation pressures. The tunnel achieves this by utilizing the FML compressor and a two-stage injector drive system, which results in a very unusual layout, as shown in figure 3-7.

The test section is fed with regulated, unheated, dried air from the Ames 3000 psia supply. This supply merely provides a source of air with a low dew point of about –50°F and does not drive the tunnel. For Mach 1.6 operations, the stagnation pressure in the settling chamber (p_0) is variable up to 10.3 psia, which corresponds to a maximum flow rate of approximately 26 lb/sec with $T_0 = 0$°F. The inlet air cools due to expansion, and causes the stagnation temperature in the settling chamber to drop about 60°F below ambient. This large temperature drop stabilizes in the settling chamber after about 20 minutes of tunnel operation.

The settling chamber is equipped with pressure reduction elements, a series of flow straighteners and flow conditioners, and vibration isolation from the support structure, as shown in figure 3-8. The nozzle and contraction are fabricated as one component out of 6061-T6 aluminum, and were hand polished to give a surface finish better than a 10L standard (roughness height 10 microinches). Since the settling chamber is square, the contraction ratio based on the throat dimensions is 6.2:1 vertically and 2.45:1 horizontally, which combine to give an overall high contraction ratio of 15.25:1. (The overall contraction ratio based on the test section dimensions is 12:1.) No boundary layer bleed valves are fitted to the tunnel—quiet flow in the test section is achieved purely through the use of screens and proper contouring of the three-dimensional nozzle. The dew point of the air supply was continuously monitored with a Nyad Model 140 Hygrometer positioned in the settling chamber.

The test section is 8 inches high, 16 inches wide at its entrance, and 32 inches long. All round optical access is made possible by 2.0 inch thick windows made of optical quality Schlieren glass. The stabilization of test section stagnation temperature causes the upstream window to move with respect

to the window frame, and great care is exercised to ensure that the appropriate loading is applied to the window so the flow surface is smooth and does not trip the tunnel boundary layer. The test section floor and ceiling diverge at a total angle of 0.5 degree to allow for boundary layer growth on all four walls. The side walls are parallel. The test section is cantilevered from the nozzle contraction, with the downstream end attached to the supersonic diffuser by a rubber isolator to prevent conduction of injector vibration into the test section and nozzle structure. Models and instrumentation can be mounted in the test section from window blanks fitted in any one of four window frames. Since the tunnel operates at subatmospheric pressures, leaks were a major concern and great care was always exercised to ensure that warm, moist air did not penetrate into the tunnel.

The wind tunnel is operated using an industrial type control system with PC Windows running on an ordinary 486/33 MHz computer (fig. 3-9). A real-time display shows inlet air parameters and the status of control valves. The tunnel start and shutdown are handled automatically to prevent compressor surge. Only p_0 is available to set tunnel operating conditions, and can generally be held to within 0.1 psia using a proportional with integral and derivative (PID) controller. Since a heater is not installed to control stagnation temperature, T_0 varies with climatic variations and also during a run, due to compressor pumps charging the high pressure air reservoir and hence doing work on the air.

The three compressor pumps with 3000 psia supply could deliver more than the 30 lb/sec that the tunnel drew at high Reynolds number. However, most runs were made during periods in which only two pumps were working, so the supply was only 18 lb/sec. Therefore, runs were started with a maximum head of pressure in the relatively large reservoir and generally lasted about 1 to 2 hours, before the supply pressure reached 2500 psia, at which point the tunnel was turned off so as not to risk unstarting the tunnel with the model in the test section.

Two configuration changes were made to the wind tunnel over the time period during which these tests were conducted: (1) The first stage of the pressure reduction system had 17 holes drilled in it so as to increase the flow-through area by 5%. (2) Following a leak of water into the high pressure air system, the tunnel was completely disassembled and cleaned; the opportunity was taken to replace the Rigimesh linings in both the second and third stages of the pressure reduction system (fig. 3-8), and this was found to lower the test section disturbance level.

3.4.2 Data Acquisition Systems for Pressures and Temperatures

Temperatures were measured with type-T (copper-constantan) thermocouples connected to a THERM-ACQ unit by DIANACHART, Inc. The THERM-ACQ unit was controlled by a PC computer and could simultaneously measure 48 channels with 16-bit accuracy. An isothermal cold junction assembly ensured that all thermocouples were referenced to a common temperature. Data were continuously displayed, and were recorded every 10 seconds.

Pressures that were specific to the control of the tunnel were measured by self-contained industrial-type pressure transducers, and their signal was sent directly to the tunnel control computer. Measured pressures from the test section and models were fed to a four-barrel Scanivalve unit. Each barrel of the Scanivalve unit contained a 0–15 psia pressure transducer. All pressures measured with this unit were referenced to atmospheric pressure. Each Scanivalve pressure transducer was powered

by a high frequency response signal conditioner (Dynamics 8000 with a 3 dB drop-off at 500 kHz). The signal conditioners allowed for suitable "buck-and-gain" of the analog signal before being sent to a 12-bit A/D board in the data acquisition computer (CIO-AD16 A/D board by Computer Boards, Inc.). The port positioning of the Scanivalve barrels was controlled by a Scanivalve Solenoid Controller CTLR2/S2-S6 which received step input signals from the data acquisition computer. The pressure transducers were calibrated before every test using a manual vacuum pump and a vertical mercury manometer board. A straight line curve was fitted to the results. Absolute pressures were obtained after noting the atmospheric (reference) pressure.

3.4.3 Low Disturbance Level Environment

The low disturbance, or "quiet," test section environment was first measured. This configuration had smooth walls with no trips fitted to the walls. All window blank joins were fitted to be as smooth as possible. Note that both total pressure and hot-wire signals include signal noise.

3.4.3.1 Total Pressure Fluctuations

For these traverses, the Kulite was positioned in the forward streamwise location such that the head of the transducer was 1 inch aft of the nozzle/test section join. A flange on the rear of the Kulite probe prevented data from being taken closer than 3.5 inches from the side walls. Mounting the traverse from both side walls enabled most of the test section to be probed. Data were taken at both low and high freestream Reynolds numbers. The signal noise was calculated by dividing the wind-off rms pressure by the wind-on total pressure, and the maximum occurred at $Re_\infty = 2.7 \times 10^6$/ft (0.009%).

Figure 3-10 shows the test section pressure fluctuations (p_{rms}/p_{total}) at this location. The low disturbance level environment of the tunnel improved following the replacement of the Rigimesh pressure reduction screens in stages two and three of the pressure reduction unit. In fact, the Rigimesh screens had never been replaced since the tunnel first became operational in 1994. Currently, the consensus is that flow is "quiet" if the freestream is spatially and temporally uniform with acoustic and convected disturbances (ratio of total pressure rms to total pressure, p_{rms}/p_{total}) less than 0.1% (refs. 110–112). Since the data are all well under this level and approaching that of the signal noise level, the tunnel is indeed quiet in an acoustic sense.

The data shown in figure 3-10 for "after Rigimesh replacement" were taken both before and after the transition tests were conducted, and represent over 66 data points. The repeatability of the data is remarkable, and shows that the disturbance level did not change substantially with Re_∞. Also, as far as pressure fluctuations go, no degradation of the tunnel occurred during the transition testing.

3.4.3.2 Mass Flux Fluctuations

A 5 μm tungsten hot wire operating at an overheat ratio of 0.7 was used to obtain the freestream fluctuation data shown in figure 3-11 (shown without noise signal removed). The turbulence intensity was obtained following the method described in Section 3.2, and produced a value of 0.035% at the

The hot wire was also traversed into a side wall boundary layer. It detected a 1.0–1.5 inch thick layer that was defined by an increased observation of "spots" (mass flux or temperature)—as the probe went in, it saw spots for longer percentages of the time. The thickness and state of the wall boundary layers are currently under investigation.

3.4.4 Raised Disturbance Level Environment

In order to raise the disturbance level of the test section, 1/2 inch wide strips of size 80 grit sandpaper (0.025 inch height) were stuck to upper and side walls of the tunnel using double-sided tape. The upper wall trip was located such that its leading edge was 1.25 inches forward of the test section/nozzle join, while the side trips were placed with their leading edges 6.25 inches forward of the join. The shock waves generated by the trips passed in front of the model and did not interfere with the attachment-line boundary layer. These trips were sufficient to cause turbulent boundary layers to form on the tunnel walls, and in so doing, irradiate the test section with increased levels of primarily acoustic noise.

3.4.4.1 Total Pressure Fluctuations

Figure 3-12 shows that tripping the tunnel walls significantly increased the rms pressure disturbance level of the freestream by approximately eight times. Figure 3-13 shows that this increase in noise is broadband, with no particular frequency being selectively amplified. Therefore, the turbulent boundary layer walls are effectively raising the overall "white noise" of the freestream.

3.4.4.2 Mass Flux Fluctuations

Because of time constraints, only half of the test section was traversed with the hot wire. Figure 3-14 shows that the hot-wire fluctuations also increased as a result of the trips, but only by a factor of two. This suggests that the trips primarily increase the pressure disturbance level of the freestream.

3.5 Swept Cylinder Models

The design process described in Chapter 2 led to a forward swept circular cylinder of 1.6 inch diameter, mounted from the top of the tunnel in a vertical plane, swept at 76° to the Mach 1.6 freestream with the apex aligned with the streamwise flow. The next task was to design a model that would fit into the wind tunnel test section with these parameters.

3.5.1 Positioning of the Models in the Test Section

The usable test length of any cylinder model would be ended by a bow shock wave reflecting off the upper tunnel wall and striking the model. A slight shock was also anticipated to come off the cylinder apex downward, reflecting off the lower wall and later striking the model. As a result, there would an optimum vertical height at which the two reflected shocks would intersect the cylinder at one spanwise location. The cylinder design would therefore have to incorporate a mechanism for altering the vertical height of the model to obtain this optimum position, provide access for installing the instrumentation, provide a means for attachment to the tunnel wall, and, of course, be simple and cheap to manufacture.

An initial idea for vertical movement employed a circular cylinder. This idea was discarded, however, since the vertical cylinder would have a detached bow shock wave. The standoff distance would increase rapidly as the Mach number decreased toward unity, thus influencing more of the precious spanwise test length of the cylinder. Instead, wedge-shaped blocks were chosen to provide the vertical spacing. The wedge spacer was designed with a 11.3° half angle so as to have an attached shock wave up to a Mach number of 1.47, according to two-dimensional theory. The wedge spacer was made from a fully cured polyurethane polymer in an effort to thermally insulate the model from the warmer wind tunnel walls. The bow shock angle obtained from the CFL3D solution was used to calculate the optimum vertical position and hence the thickness of the wedge spacer. For the chosen 76° swept cylinder, the apex was to be 2.5 inches from the bottom tunnel wall, thus giving a maximum usable spanwise test length of approximately 8 inches and a wedge height of 1.5 inches. The test section height is 8 inches, implying a cylinder model 16 inches in length. The model was mounted from a specially constructed upper window blank, as shown in figure 3-15. A 1/2 inch and a 3/8 inch bolt secured the cylinder and the wedge spacer to the window blank, and a third 11/16 inch hole just upstream of the bolts was provided for instrumentation leads to pass from the model interior to the laboratory.

The test section of the Mach 1.6 wind tunnel does contain slight disturbances. Earlier tunnel tests using Schlieren photography revealed a slight shock/expansion wave emanating from the joint between the upper window blank and the window frame. This disturbance moves across the working section at the Mach angle. Pressure tap measurements taken along the leading edge of an F-16XL model confirmed that this did not result in a noticeable pressure jump. In order to assure quiet flow, it was decided to conduct the experiments in a forward streamwise position. This placed the apex of the cylinder in the nozzle, but downstream of the last expansion wave so as to be in a truly Mach 1.6 flow (fig. 3-16). The disadvantage of this position was that only the rear of the cylinder was viewable through the side windows. In order to discern the nature of the bow shock wave at the apex, it was decided to also have an aft streamwise testing position, 6 inches downstream of the forward position, which would enable photography of the apex area. These criteria positioned the bolt-hole pattern necessary in the test section roof for attachment of the model (fig. 3-17).

3.5.2 Swept Cylinder Load Analysis

Load calculations were carried out as part of the FML's Test Readiness Review policy. These design calculations are shown in Appendix A. Aluminum 6061-T6 was chosen as the material for its strength and its ability to aid in quick thermal stabilization of the model wall temperatures.

3.5.3 The Need for Three Swept Cylinder Models

As this investigation progressed, it became apparent that three swept cylinder models, identical in external geometry and dimensions, would be required in order to meet all the experimental requirements.

First, a model with a smooth (less than 10 microinches) surface was required for the transition experiments. This led to a hollow model that would generate near-adiabatic wall temperatures. This model could also be used for gross contamination studies, in which trip wires are affixed to the surface. The model became known as the "adiabatic cylinder."

In order to obtain the chordwise velocity gradient, which is a necessary component of $\overline{R}$, the chordwise pressure gradient would need to be acquired. In previous swept cylinder experiments (with the exception those in ref. 63) the relevant $\overline{R}$ values were obtained from CFD calculations or empirical calculations. This was deemed unacceptable, and a truly experimentally derived value for $\overline{R}$ was required. Since pressure tap orifices would cast off disturbances into the boundary layer flow, taps could not be installed in the adiabatic cylinder. A "cylinder with pressure taps" was therefore required to obtain the cylinder's pressure distribution.

Finally, if boundary layer disturbances could not be observed with the adiabatic cylinder, surface heating would be introduced. Requiring a solid interior, this model would be different again from the adiabatic cylinder, while still retaining the identical external geometry. This model became known as the "internally heated cylinder."

3.5.4 Adiabatic Cylinder

The adiabatic cylinder was machined from a solid piece of aluminum 6061-T6, and had a wall thickness of nominally 1/8 inch. The surface of the cylinder was highly polished and finished to below 10 microinches rms. Five copper-constantan (type-T) thermocouples (24 gage) were placed at equal intervals along the attachment line from 3.7 inches to 11.7 inches from the apex. These were placed in the wall at 0.012 inch from the external flow surface. Great care was exercised so that no part of the exterior surface was broken while machining. It would have useful to have an access panel on the back face of the model running the length of the cylinder, to aid in thermocouple installation. Cost limitations and the possibility of warpage due to machining, however, limited the access to 1/2 inch diameter holes which were later plugged. The apex region of the cylinder was welded to seal the model and machined to dimensions. Two 3/8 inch diameter holes were placed on the back face of the model to allow for quick depressurization during the wind tunnel startup. After all machining was

completed, an x-ray of the model was taken to ensure that the placement of the thermocouples was correct. The design drawing of the adiabatic cylinder model is shown in figure 3-18.

Thermocouple response to changes in freestream total temperature was rapid, and thermal equilibrium of the model was established in a matter of a few minutes after tunnel start. The wall temperature along the attachment line was almost uniform, with the maximum difference between any two thermocouples being of the order 1°F. These results are in close agreement with the predicted values (fig. 3-19). Based on a wall temperature of 0°F and a stagnation temperature of 20°F, the recovery factor was 0.844 (near-laminar).

After 20 minutes of running the tunnel, it was found that the wall temperatures began to rise slightly, which was attributed to rising total temperature. It was realized that the high pressure air compressor pumps were continually operating and were thus doing work on the relatively large high pressure air reservoir which in turn slowly raised the stagnation temperature. A point of note here is that the total temperature measurement was made near the settling chamber wall and was therefore influenced by the temperature of the tunnel wall. A slight (less than 1°F) temperature difference was known to exist across the cross section of the tunnel, implying that the total temperature being measured was not exactly the same as the total temperature at the apex of the model. Ideally, a removable, independent measurement of the freestream total temperature behind the screens in front of the contraction was desired. A total temperature probe was placed in the Mach 1.6 test section, but this test was inclusive since the probe's own recovery factor could not be determined.

3.5.5 Cylinder with Pressure Taps

In order to obtain accurate values of $\overline{R}$ and the viscous length scale η at each spanwise location for comparison with CFD, it was decided not to rely upon an empirical estimate of $(dU_e/dx)_{x=0}$, such as given by the modified Newtonian pressure distribution, but to determine it directly from measured pressures. Because of budget constraints, a cylinder equipped with pressure taps (fig. 3-20) was machined in the FML workshop by the author over a four week period. Details of the model machining can be found in Appendix B. Upon completion of machining, the model was taken to the Ames Research Center Calibration Laboratory for accurate determination of pressure tap hole placement, the results of which are listed in table 3-1. Measurements from an initial test of the pressure model produced unacceptable results, and led to modifications of the acquisition system. Having obtained satisfactory surface pressures from a second test, the task was then to obtain chordwise velocities and hence $\overline{R}$ and η. This required the boundary layer edge temperature, and an analysis was undertaken to assure that a correct value was used. Curve fitting analyses were also undertaken to assure that the velocity distribution obtained was as accurate as possible.

3.5.5.1 Design of the Pressure-Tapped Cylinder

The spanwise locations of the pressure taps were chosen to match the spanwise locations of the thermocouples in the adiabatic cylinder model. The taps were arranged in chordwise rows so as to be perpendicular to the cylinder's attachment line, as shown in figure 3-21. At each spanwise station, 0.020 inch internal diameter taps were placed at 10° intervals from –50° to +50° in the chordwise

direction, with a reduced concentration of taps being placed downstream of the predicted impact location of the reflected bow shock wave, giving a total of 62 taps. At 3.7, 5.7, and 7.7 inches from the apex, a full chord array of 11 taps was used to define the chordwise velocity profile, but at 2.7, 4.7, and 6.7 inches, only six taps were used in a half chord array. This was done so as to minimize the number of taps required, as it was thought that the half chord array would be sufficient to define the velocity profile. After initial testing, it was decided to place the taps in full chord arrays, as shown in figure 3-22. Essentially, those taps positioned aft of the reflected bow shock wave impact position were moved forward to complete the full array pattern, with four additional taps being made to bring the total to 66 taps.

3.5.5.2 Surface Pressure Measuring Apparatus—First Test

During initial testing, the plastic Tygon tubing from the pressure taps was connected directly to the tunnel pressure measuring Scanivalve unit described in Section 3.4.2. Since the pressure transducers were housed directly within each barrel, only a small amount of time was required after port selection for the pressures to stabilize and measurements to be taken. A constraining factor, however, was that these transducers were referenced to atmospheric pressure and had non-optimal gain settings. One count of the 12-bit A/D system was found to be equivalent to 0.006 psia which, although sufficient for the majority of tunnel pressure measurements, was unsatisfactory for the resolution of differential surface pressures.

3.5.5.3 Surface Pressures Obtained from First Test

The first entry of the pressure model produced results which were deemed unacceptable for several reasons. First, the differential surface pressure between two ports was obtained by measuring each surface pressure relative to atmospheric and then obtaining the difference. This difference of two large numbers was inherently inaccurate and led to the acquisition of a differential pressure transducer. The second issue concerned the resolution of the pressure transducers. It was found that curve fits applied to the calculated chordwise velocity distribution exhibited repeatability errors that were traced to insufficient resolution of pressure (pressures were required to 0.001 psia, but available resolution was only 0.006 psia). Another issue concerned the use of four separate pressure transducers, each with its own slightly different calibration. And last, it was recognized that the half chord array of pressure ports were simply insufficient to properly define the chordwise distribution of pressure. These reasons led to the modification of the pressure port hole pattern and the pressure data acquisition system.

3.5.5.4 Surface Pressure Measuring Apparatus—Second Test

A number of changes to the pressure measuring system were made before the second test of the pressure model. In order to ensure that the model was isolated from the outside of the tunnel, a pressure-sealed box was placed over the mounting and instrumentation holes on top of the test section (fig. 3-23). When the tunnel started, this box could be visibly seen to be "sucked down" over the holes, forming an airtight seal. Plastic Tygon tubing from the pressure taps was then connected to ports on the inside face of the box, and tubing connected to the outside face of the box transmitted the

pressures to a second Scanivalve system placed under the test section of the tunnel. This Scanivalve system was separate from the one used for tunnel pressure measurements; the Scanivalve barrels in this system did not contain pressure transducers and were used solely as pressure port selectors.

The model surface pressures were sequentially applied to one side of a ±0.5 psia MKS Baratron type 223B differential pressure transducer via the new Scanivalve mechanism, with freestream pressure applied to the other side. This transducer had an accuracy of ±0.0015 psia with a resolution of ±0.00005 psia. Using a single common transducer instead of four separate ones reduced errors caused by slightly different calibrations. Freestream pressure, however, was required to be referenced back to atmospheric pressure. It was hoped to obtain a new transducer for this purpose coupled with a 16-bit A/D system to increase resolution, but this was never realized, and one of the 0–15 psia transducers from the tunnel pressure measuring Scanivalve system had to be used for this purpose. However, the gain for this transducer was changed from the first test such that one count of the 12-bit A/D system was equivalent to 0.0033 psia.

Since the 66 surface pressures were to be sequentially applied to a single transducer, and one Scanivalve barrel had only 48 ports, two barrels were required to measure all pressures. Thus, a need arose to switch between the two barrels. An initial piping and switching system was found to suffer from a severe time lag. Closer examination of the switching valves and piping revealed that they had a large internal volume in comparison to the volume in the pressure lines. After replacing the valves and piping with smaller diameters, the time required for pressure stabilization before recording data was reduced to 3 seconds. This could have been reduced even more by suitable reduction of piping volume.

The tunnel was then found to exhibit a periodic oscillation in p_0 of approximately 0.05 Hz, which produced the same periodic oscillation in p_∞ and the model surface pressures, p_e. This was attributed to non-optimal settings in the PID control system for the tunnel valve. Tests were conducted to check for time lag between p_e and p_0, but this was found to be negligible. The Baratron MKS transducer could quite easily resolve this oscillation, but the Scanivalve transducers, being referenced to atmospheric pressure, did not have sufficient resolution. Consequently, attempts to form a *Cp*, which would normally have taken the unsteadiness into account, failed since p_e was measured as oscillating and p_∞ was not. The only course of action left, therefore, was to record the pressures over long time periods and average the results. The three pressures of interest, p_0, p_∞, and $p_e - p_\infty$, were therefore recorded by the A/D at 50 Hz (i.e., 16.7 Hz per channel) for 80 seconds, giving a total of 4000 samples over three channels (computer direct memory access buffer size limited the total time period). These were then averaged to produce mean pressures and a mean value of *Cp* for each port.

3.5.5.5 Procedure to Obtain Accurate dU_e/dx

The values of $\overline{R}$ and η are based on the chordwise velocity gradient, $(dU_e/dx)_{x=0}$. Therefore, at each spanwise location, the chordwise distribution of velocity was required, which is based on knowing the values of the boundary layer edge temperature and pressure at the attachment line (p_A and T_A, respectively). Since pressure is assumed constant through the boundary layer, the value of

p_A would be equal to the experimentally measured pressure on the attachment line. However, since the pressure taps were not exactly aligned with the attachment line, p_A was obtained by fitting even polynomial functions to the chordwise distribution of p_e and noting the pressure at $\theta = 0°$. T_A was obtained by considering the streamline that crosses the bow shock wave and arrives at the point of consideration. An analysis was undertaken of the correct bow shock wave angle to use. Throughout all stages of these calculations, it was realized that $\overline{R}$ is very sensitive to $(dU_e/dx)_{x=0}$ and one must go to great lengths to ensure its accuracy. Parts of the following analysis are taken from references 113 and 114 and are reproduced here for completeness.

3.5.5.6 Boundary Layer Edge Temperature Determination

At present, it is not possible to obtain direct measurements of the static temperature at the edge of the attachment-line boundary layer (T_A). It therefore follows that it is necessary to relate T_A to the attachment-line static pressure (p_A) and shock shape (Λ_s). Consider the situation sketched in figure 2-2. The streamline which first enters the boundary layer at point 1 has passed through the bow shock at point 2. We may write:

$$\frac{p_A}{p_\infty} = \frac{p_A}{p_{0_1}} \frac{p_{0_1}}{p_{0_\infty}} \frac{p_{0_\infty}}{p_\infty}$$

Since the flow upstream of the shock is isentropic:

$$\frac{p_{0_\infty}}{p_\infty} = \left[\frac{T_0}{T_\infty}\right]^{\frac{\gamma}{\gamma-1}}$$

Moreover, the flow between the bow shock and the cylinder is also isentropic and so:

$$\frac{p_A}{p_{0_1}} = \left[\frac{T_A}{T_0}\right]^{\frac{\gamma}{\gamma-1}}$$

Therefore:

$$\frac{T_A}{T_\infty} = \left[\frac{p_A}{p_\infty} \frac{p_{0_\infty}}{p_{0_1}}\right]^{\frac{\gamma-1}{\gamma}}$$

Finally, if the bow shock is swept an angle Λ_s relative to the freestream direction, then the change of total pressure across the shock can be obtained from the oblique shock relations:

$$\frac{p_{0_\infty}}{p_{0_1}} = \left[\frac{(\gamma-1)M_\infty{}^2\cos^2\Lambda_s + 2}{(\gamma+1)M_\infty{}^2\cos^2\Lambda_s}\right]^{\frac{\gamma}{\gamma-1}} \left[\frac{2\gamma M_\infty{}^2\cos^2\Lambda_s - (\gamma-1)}{(\gamma+1)}\right]^{\frac{1}{\gamma-1}}$$

and so:

$$\frac{T_A}{T_\infty} = \left[\frac{p_A}{p_\infty}\right]^{\frac{\gamma-1}{\gamma}} \left[\frac{(\gamma-1)M_\infty{}^2\cos^2\Lambda_s + 2}{(\gamma+1)M_\infty{}^2\cos^2\Lambda_s}\right]\left[\frac{2\gamma M_\infty{}^2\cos^2\Lambda_s - (\gamma-1)}{(\gamma+1)}\right]^{\frac{1}{\gamma}} \tag{3-7}$$

The above equation allows the unknown temperature T_A to be obtained from the measured surface static pressure and the known shock sweep angle, as measured from the Schlieren photography. It follows immediately that:

$$\frac{\rho_A}{\rho_\infty} = \frac{(p_A / p_\infty)}{(T_A / T_\infty)}$$

$$\frac{M_A}{M_\infty} = \frac{1}{M_\infty}\left[\frac{2}{(\gamma-1)}\left(\frac{T_0 / T_\infty}{T_A / T_\infty} - 1\right)\right]^{\frac{1}{2}}$$

$$\frac{V_A}{Q_\infty} = \frac{M_A}{M_\infty}\left[\frac{T_A}{T_\infty}\right]^{\frac{1}{2}}$$

$$\frac{T_0}{T_\infty} = 1 + \left(\frac{\gamma-1}{2}\right)M_\infty{}^2$$

During examination of the Schlieren photographs, one question that arises is what is the exact value of Λ_s to take; i.e., where does the streamline that impacts the attachment line at a given y location, first cross the bow shock wave? And is this value really critical? In order to answer the latter question, an analysis was undertaken of p_{0_∞} / p_{0_1} as a function of Mach number and shock angle (fig. 3-24). For a freestream Mach number of 1.6, p_{0_∞} / p_{0_1} is approximately constant up to a Λ_s of 65°. Since the Schlieren photographs show that the bow shock is still highly curved near the apex of the cylinder (where the streamline of interest must pass through), Λ_s will be below this value, and so the value of Λ_s becomes virtually inconsequential for the purpose of this calculation. Now:

$$\left(\frac{p_{0_\infty}}{p_{0_1}}\right)^{\frac{\gamma-1}{\gamma}} = \frac{\left(\frac{T_A}{T_\infty}\right)}{\left(\frac{p_A}{p_\infty}\right)^{\frac{\gamma-1}{\gamma}}}$$

Therefore, for fixed freestream conditions ($M_\infty, T_\infty, p_\infty$) and obtaining p_A from the experiment, T_A will also be invariant with Λ_s.

If the freestream Mach number was higher, then the choice of the correct Λ_s would become critical, and some form of flow visualization would be required to establish the exact point at which the streamline of interest crossed the bow shock (such as in an experiment, or from a CFD solution). As can be seen, this is an especially significant consideration for hypersonic flows.

3.5.5.7 Obtaining Experimental Velocities

Consider figure 3-25, a schematic diagram of the flow over the windward face of an swept-*infinite* cylinder. Since the cylinder is swept-infinite, all flow variables are independent of spanwise position. At the edge of the attachment-line boundary layer, the total temperature, T_0, and the local total pressure, p_0, are linked to the local static values by the isentropic relation, which for a perfect gas with constant specific heats is:

$$\frac{p_0}{p_A} = \left(\frac{T_0}{T_A}\right)^{\frac{\gamma}{\gamma-1}}$$

Moreover, since the total temperature and local total pressure are constant along the streamline which is coincident with the body surface, at any given point the local static pressure and local Mach number are such that:

$$\frac{p_0}{p_e} = \left(1+\left(\frac{\gamma-1}{2}\right)M_e{}^2\right)^{\frac{\gamma}{\gamma-1}} = \frac{p_0}{p_A}\frac{p_A}{p_e} = \left(\frac{T_0}{T_A}\right)^{\frac{\gamma}{\gamma-1}}\frac{p_A}{p_e}$$

or:

$$M_e{}^2 = \frac{2}{(\gamma-1)}\left\{\frac{T_0}{T_A}\left(\frac{p_e}{p_A}\right)^{\left(\frac{1-\gamma}{\gamma}\right)} - 1\right\}$$

Noting that the speed of sound a_e is given by:

$$a_e{}^2 = \gamma R T_e = \gamma R T_A\left(\frac{p_e}{p_A}\right)^{\left(\frac{\gamma-1}{\gamma}\right)}$$

it follows that:

$$Q_e^2 = \frac{2\gamma RT_0}{(\gamma-1)}\left\{1-\frac{T_A}{T_0}\left(\frac{p_e}{p_A}\right)^{\left(\frac{\gamma-1}{\gamma}\right)}\right\}$$

For a swept-infinite flow:

$$Q_e^2 = U_e^2 + V_\infty^2$$

and, at the attachment line:

$$\frac{2\gamma RT_0}{(\gamma-1)} = \frac{2\gamma RT_A}{(\gamma-1)} + V_\infty^2$$

Hence:

$$U_e = a_A\left\{\frac{2}{\gamma-1}\left[1-\left(\frac{p_e}{p_A}\right)^{\frac{\gamma-1}{\gamma}}\right]\right\}^{\frac{1}{2}} \tag{3-8}$$

Note that V_∞ is the spanwise velocity along the cylinder, and provided that to a first approximation this does not vary with θ, then this analysis holds even for a finite length model, when the shock is not parallel to the cylinder. Also note that U_e has no freestream dependence.

3.5.5.8 Velocity Curve Fit Routines

It was found that fitting a curve to the chordwise velocity distribution produced a much more accurate result for the velocity gradient than extracting the velocity distribution from the curve fit to the chordwise pressure distribution.

Recall the incompressible potential flow solution for the crossflow velocity around a cylinder is an antisymmetric function:

$$\frac{U_e}{U_\infty} = 2\sin\theta = 2\left(\theta - \frac{\theta^3}{3!} + \frac{\theta^5}{5!} - \ldots\right)$$

Appropriate curve fits would therefore be:

$$\frac{U_e}{U_\infty} = a\theta + b\theta^3 \text{ , and } \frac{U_e}{U_\infty} = a\theta + b\theta^3 + c\theta^5$$

As can be seen in figure 3-26, the third order polynomial does well in representing the behavior of $2\sin\theta$ up to at least $\theta = \pm 50°$. The fifth-order polynomial is particularly successful since it takes advantage of all inflections in the velocity distribution to as far as $\theta = \pm 90°$. Fifth-order polynomials were therefore fitted to the velocity distributions obtained at each spanwise location using a least squares technique.

3.5.6 Internally Heated Cylinder

A cylinder capable of generating internal heat and raising its own surface temperature was also designed and produced. In order to raise the surface temperature, cartridge heaters placed inside a solid model were utilized. Surface temperature was set by inputs to a temperature control system.

3.5.6.1 Heating Requirements

A steady state heat flux calculation was carried out in order to calculate the power necessary to raise the wall temperatures 150°F above stagnation temperature (about 171°F). Experimental results for a cylinder in crossflow as a function of Nu, Pr, and Re_∞ are found in references 115 and 116. These data yielded a 2.0 to 2.4 kW power requirement, assuming a 15% power loss via conduction through the end support into the wall with no radiative losses accounted for. The accuracy of these results was deemed to be no better than 25%. The details of these calculations are given in Appendix C.

3.5.6.2 Selection of Heaters

Because of the internal size constraint of the cylinder, a large watt density (power per unit volume) would be required. This ruled out applying hot films to the interior surface, since the maximum commercially available hot-film watt density was one-tenth of that required. A radiative heating element, such as used in furnaces, and heater elements for hot water tanks were also considered, but these too were discounted since they had end fittings that were too large for the 1.5 inch internal diameter. Hot oil from an external pump was also considered. This had the advantage of approximating a uniform heat flux distribution inside the cylinder, but this too was ruled out since the heat loss from the oil en route to the cylinder would have necessitated an even larger power input. Cartridge heaters were found to fulfill all the requirements, being small with a high watt density and cheap. A single heater, however, would not be able to fit far up inside the highly swept nose. Three 3/8 inch diameter, 8 inch long, Omega cartridge heaters (CIR-2089/240) were selected, giving a maximum power output of 3 kW when connected to a 240V a.c. supply. This overdesign was to allow for the inaccuracy of the heat flux calculation and leave a reserve margin. The use of three heaters allowed for an even distribution of power from the three-phase electrical power supply.

3.5.6.3 Design of the Internally Heated Cylinder

The need to accommodate the cartridge heaters inside the model resulted in a three-piece configuration, as shown in figure 3-27. All components were made of aluminum 6061 T6 so as to conduct the heating quickly and as uniformly as possible.

The model's highly polished outer shell formed the exterior flow surface and was finished to below 10 microinches rms. Ten T-type thermocouples (24 gage) were evenly placed along the attachment line of the cylinder, from 2.7 to 11.7 inches from the apex (y/D from 1.7 to 7.3). These were placed in the 1/8 inch thick wall at 0.020 inch from the external flow surface line, and were set in place from the rear of the cylinder using access holes (fig. 3-28).

The cartridge heaters were symmetrically positioned inside a heater block which slid inside the outer shell (fig. 3-29). Special conductive paste (aluminum particulate-based OmegaLux heat transfer and release coating) facilitated better thermal contact between all components. The two heaters closest to the attachment line started at 3 inches ($y/D = 1.9$) from the tip of the model, and the third heater started at 4.8 inches ($y/D = 3.0$). The leads from the attachment-line thermocouples were laid down in a groove cut into the heater block so as to be just behind the attachment line. This design compromise meant that the attachment line was shielded from direct heating by the thermocouple leads, but heat easily passed through the highly conductive cylinder walls to uniformly raise the attachment-line temperature. Using a sliding insert prohibited thermocouples from being placed off the attachment line in the chordwise direction. Because of the expected high internal temperature of the heater block, care was taken to ensure that the protective sheathing around the thermocouples did not exceed the manufacturer's recommended maximum temperature of 500°F. This was achieved by surrounding the thermocouple bundle with a layer of fiberglass, and positioning an additional two thermocouples to measure the temperature of the bundle itself. One thermocouple was placed at the lowest point of the cut groove, while the other measured the external temperature of a thermocouple sheath in the bundle.

A solid end piece was fitted to provide end support and accommodate the two attachment bolts.

3.5.6.4 Design of the Heating Control System

The three heaters were controlled by a single Omega 8501-TC-DC-1 temperature control unit employing PID control. The thermocouple at the 8.7 inch ($y/D = 5.4$) location was selected as the sensing unit for the control temperature. 208V a.c. power, located in the test cell, was ducted off from a junction box and brought to a quick disconnect box and the temperature control unit located on the south secondary injector. The principle behind the control unit was that a single temperature would be used to control all three heaters together; i.e., they would all come on and go off at the same time. A system was designed using three solid state relays, as shown in the electrical drawing (fig. 3-30) and photograph (fig. 3-31). The heaters were connected in a delta load configuration. Using a 208V a.c. versus a 240V a.c. supply meant that the heaters would only supply 0.75 kW each with a line current of 6.30 amps and a line voltage of 120.1. Line currents were therefore protected by 10 amp fuses.

No forced internal cooling was provided with this design, since the model would normally be operated in the cool convective freestream of the tunnel. However, a bench test was made in the ambient still air of the laboratory in order to test the control system and compare the attachment-line

temperatures as recorded by the internal thermocouples with an external thermocouple. The temperature controller had an automated tuning process in which step inputs of heat were applied and the thermal response times of the cylinder measured. The controller then calculated the appropriate rate settings for the PID algorithm. Once this was done, the cylinder achieved typical set points of 50°F or 100°F above ambient in under a minute with no overshoot. Attachment-line temperatures as measured by the external thermocouple were slightly below that recorded inside, which was to be expected given the finite thickness of the cylinder wall. The rate settings were calculated again when the model was placed in the tunnel freestream. The model again achieved target temperatures in approximately one minute with little overshoot, and held the set temperature to within 1°F by appropriate on/off switching (rate setting) of the solid state relays connected to the heaters. With use of the available three-phase, 208V electrical supply, the heaters could raise the wall temperature of the cylinder well in excess of 250°F above the adiabatic wall temperature.

3.5.6.5 Electrical Power Supplied to Model

The three electrical heaters each received one phase of the three-phase supply, and this supply was either fully on or off. The average electrical power supplied to the model was therefore calculated by measuring the percentage of time the heaters were on:

$$[(\text{percentage on}) \times 3 \times 0.75 \times 1000] \text{ watts}$$

An Aero-Med Model Dash IV strip chart was connected to the input side of one of the solid state relays that received the control signal from the temperature control unit, and was used to measure the time the heaters were on. The strip chart was marked with a pen at the beginning and end of each power setting. The time base was set at 5 mm/sec. A Fluke Model 87 multimeter was used to measure one of the single-phase line voltages.

Measurements were made with the model in the forward position at $Re_\infty = 2.7 \times 10^6$/ft and 3.6×10^6/ft with varying $T_{control}$. At least four cycles of on/off heating were recorded at each set $T_{control}$. At every $T_{control}$, the $Re_\infty = 3.6 \times 10^6$/ft setting took more power than the $Re_\infty = 2.7 \times 10^6$/ft setting. At $T_{control} = 0$°F and $Re_\infty = 2.7 \times 10^6$/ft, the heaters were hardly on (3.4%), but at $T_{control} = 240$°F and $Re_\infty = 3.6 \times 10^6$/ft, the heaters were on for well over half the time (55.1%). Figure 3-32 and table 3-2 show the average electrical power supplied to the swept cylinder for various control temperatures at the two Re_∞ values. Average Nusselt numbers for $T_{wall} = 170$°F are calculated in Appendix C to be in the 639–766 range for these two Re_∞. Following the same assumptions as used there, the measured power results gives Nusselt numbers in the 361–495 range.

3.5.6.6 Attachment-line Temperature Gradient with Internal Heating

Figures 3-33 and 3-34 show the temperature distributions along the attachment line for different control temperatures at $Re_\infty = 3.65 \times 10^6$/ft and $Re_\infty = 2.72 \times 10^6$/ft, respectively. The spanwise gradient was unavoidable due to the finite-sized cartridge heaters being unable to reach all the way to the tip inside the model. Consequently, the thin apex region of the model was colder than the main section of the model, and this temperature difference increased with control temperature. At 120°F,

one sees that there is about a 45°F difference in temperature over a 4 inch distance. It can also be seen that the solid cylinder also has a near adiabatic temperature distribution (assuming the model is allowed fully quench thermally).

In order to see if this temperature gradient could be lessened, one of the three heaters was disconnected and the PID autotune was reset. This had no effect on the temperature gradient along the attachment line from $y = 0$ to 6.7 inches, and simply increased the percentage of the time that the heaters were on. Downstream of $y = 6.7$ inches, the temperatures increased more steeply, which corresponds to the physical location of the third cartridge heater. Three heaters were therefore used for the remainder of the experiments.

3.5.7 Attachment-Line Boundary Layer Sensitivity to Tip Roughness Effects

Initial testing of the heated swept cylinder model with a hot wire on the attachment line repeatedly gave an apparent turbulent signal, regardless of Reynolds number or any other parameter. Pushing the wire to the tip of the model, with the hot wire protruding out into the freestream flow ahead of the bow shock wave, gave a laminar signal. Close examination of the tip region revealed a 0.001 inch ($Re = 300$) upturned burr on the nose (fig. 3-35). This problem was removed after polishing, but served to illustrate the sensitivity of the transition process to surface roughness at the nose at these Reynolds numbers.

3.5.8 Splitter Plate Concerns

A cylinder placed normal to a flow will, under certain conditions, generate a Karman vortex street behind it, with its subsequent shedding of oscillatory vortices. This produces an upstream influence whereby the downstream periodic motion transmits pressure signals upstream through the subsonic boundary layer. This phenomenon was also considered a possibility for a swept cylinder, and might therefore alter the attachment-line transition mechanisms. The controlling parameters in this case would be the crossflow component of velocity. Murthy and Rose (ref. 117) showed that this shedding of vortices was bounded by both Mach number and Reynolds number limitations, and was generally found to occur for Strouhal numbers in the range $0.17 < St < 0.23$, for $Re_D = <0.5 \times 10^6$ and $M_\infty < 0.9$. The 76 degree swept cylinder had a subsonic normal Mach number of 0.39 and $Re_D = 0.46 \times 10^6$ which placed the flow in this category. Based on the component of the freestream velocity normal to the cylinder, a potential for shedding vortices with frequencies in the range $431 < f < 582$ Hz existed.

Degani and Zilliac (ref. 118) showed the effect of a splitter plate in alleviating such disturbances by breaking up the oscillatory motion of the shed vortices and establishing a symmetrical shedding pattern. This dramatically reduces the lateral forces on the cylinder, which is also an important consideration when considering the stresses induced in a cantilever cylinder. A cylinder in incompressible flow was estimated to perturb its surrounding flow for roughly five diameters in all directions; hence it was decided to design a splitter plate that would extend from the rear of the swept cylinder to at least five diameters downstream. It was also hoped to double-check the influence of the splitter plate

by installing Kulite pressure transducers at ±90° to see if there was any boundary layer pumping with the plate off.

Figure 3-17 shows the splitter plate in side view connected to the cylinder and window blank. Note that the splitter plate could only be fitted to the window when the cylinder was in the forward position. Figures 3-36 and 3-37 show the vertical spacer and support blocks that were designed to hold the splitter plate.

3.6 Accelerometer System

In order to unobtrusively measure the dynamic characteristics of the swept cylinder model, small and light accelerometers that could be mounted to the surface of the cylinder were required. The easiest way to do this was to mount the accelerometers to the rear of a hot-wire probe body. A small 1/2 inch cube was attached to the rear of a Mark 2 hot-wire support block, and the two accelerometers (Endevco Model 2222C), weighing 0.5 g each were recessed mounted into this block such that their axes were at right angles, and parallel to the vertical center plane, to an accuracy of 1° (fig. 3-38). The accelerometers were attached to the block using cyanoacrylate adhesive (SuperGlue). The accelerometers had a charge sensitivity of 1.4 pC/g, and a frequency range of 20 to 10,000 Hz. The system was completed by an Endevco power supply (Model 109) and a two-channel charge signal conditioner (Model 104).

The complete assembly was secured on the attachment line with plastic ties such that the accelerometers were at $y = 8.0$ inches. The sensitivity of each accelerometer was dialed in on the signal conditioner, and the output gain was set to 1.0. The signals were then passed to the Tektronix Fourier analyzer.

3.6.1 Cylinder Wake/Body Interaction Investigation

Previous swept cylinder tests have sometimes been performed with a faired after-body to reduce the possibility of unsteadiness in the wake that might buffet the body or propagate disturbances upstream through the cylinder boundary layer. A series of tests were therefore performed to investigate whether there was any interaction of the wake on the cylinder body. Two accelerometers were mounted on the cylinder, as described above, and a 5.0 μm freestream hot-wire probe was traversed into the wake one cylinder diameter downstream of the model to investigate the frequencies of the wake.

3.6.1.1 Wind-Off Structural Response of Cylinder

A static vibration analysis was first undertaken to assess the resonant frequencies of the model. The model and test section were hit with a rubber mallet at various locations, and the transient responses of the model were recorded by an HP Dynamic Signal Analyzer Model 35665A, set to pretrigger. By striking the underside and side of the model, the resonant vertical frequency was found to be 104 Hz, and the resonant yaw frequency 92 Hz. Higher frequencies were induced by striking the top and side of the test section (i.e., setting the support mount into vibration).

Cylinder vertical mode	104 Hz
Cylinder horizontal mode	92 Hz
Test section vertical modes	1.0, 1.9, and 3.8 kHz
Test section horizontal modes	1.1 and 2.1 kHz

Figure 3-39 shows the vertical response of the model to a vertical hit, showing a classic decaying sinusoid in the time domain. Figure 3-40 shows the characteristic spike of this resonant mode at a frequency of 104 Hz.

3.6.1.2 Traverses of the Cylinder Wake and Accelerometer Response

During the tunnel runs, the signals from the accelerometers were recorded at various frequency ranges to get a clearer resolution of the processes at work (0–0.5, 0–2, 0–5, and 0–10 kHz). The dominant vertical frequencies were measured to be 4.8, 3.8, and 2.8 kHz and 930 Hz. Dominant yawing frequencies were 4, 2.3, 1.5, and 1 kHz. Fundamental frequencies were measured at 92 Hz (yaw) and 104 Hz (vertical). All of these frequencies were invariant with changes in freestream Reynolds number. Therefore, for the range of frequencies that these accelerometers are rated (0–10 kHz) the detected vibrations were structural and not related to aerodynamics.

The horizontal acceleration was always measured to be greater than the vertical, and these accelerations were greater at $Re_\infty = 3.4 \times 10^6$/ft than at $Re_\infty = 2.4 \times 10^6$/ft (vertical/yaw accelerations = 0.82 and 0.76, respectively). These results make sense since the model was bolted in the vertical plane and was therefore stiffer in the vertical plane. The maximum yaw displacement was 0.1 mm.

A 5.0 μm freestream hot-wire probe was traversed into the wake one cylinder diameter downstream of the model. The wake was clearly defined and had a typical peak in the hot-wire a.c. output at the wake edge (fig. 3-41). The nature of the hot-wire response is in agreement with that observed by Uberoi and Freymouth (ref. 119). It was also found that the wake definition was virtually unchanged with Re_∞.

As the wake was probed, frequency spectra were recorded with varying ranges (0–100, 0–20, and 0–1 kHz). Comparing the freestream points to points "on the edge of the wake," no changes in the frequency spectra were found except for an overall rise in rms level, i.e. no new peaks appeared. The rise in rms level was accompanied by an increasing number of spikes in the time signal, but since no well-defined frequency band was associated with this in the FFT, this was attributed to bursts of broad-band turbulence; i.e., no periodic shedding was occurring behind the cylinder.

3.6.1.3 Comment on Effect of Wake on Transition Results

The only discernible frequencies in the accelerometer signals were those due to cylinder and tunnel vibration. It was concluded that the wake consisted of near-uniform turbulence with no periodic shedding, and that the wake caused no adverse interactions for this configuration under these conditions; i.e., the effect of the wake on the attachment-line transition was too small to measure.

3.7 Schlieren Photographic System

3.7.1 Theory

Figure 3-42 shows a practical Schlieren system employing concave mirrors. Light from a uniform illuminated line source of small but finite width is collimated by the first mirror and then passes through the test section. It is then brought to a focus by the second mirror and projected on the screen. At the focal point, where there exists an image of the source, there is introduced a knife-edge which cuts off part of the light. With no flow in the test section, the knife-edge is usually adjusted so as to intercept about half the light, and the screen is uniformly illuminated by the portion of the light escaping the knife-edge. When the flow is established in the test section, any light ray passing through a region in which there is a density gradient normal to the light direction will be deflected as though it had passed through a prism. Therefore, depending on the orientation of the knife-edge with respect to the density gradient, and on the sign of the density gradient, more or less of the light passing through each part of the test section will escape the knife-edge and illuminate the screen. Thus the Schlieren system makes density gradients visible in terms of intensity of illumination. A photographic plate at the viewing screen records density gradients in the test section as different shades of gray. For practical reasons the source and its image must usually be off-axis, and this produces some astigmatism. For instance, the position of the source image is different for horizontal and vertical knife-edge arrangements, and the knife-edge must accordingly be moved from one position to the other.

When viewing three-dimensional flows, special consideration must be given to the fact that the image on the screen is an integration along the light path through the test section, and no depth perception information is available for interpreting the results.

3.7.2 Equipment

The high intensity, short duration light source was provided by a Palflash 500 manufactured by Photonics Analysis Ltd. This unit produces a spark between two electrodes that have a 10,000 volt differential voltage applied across them. Argon gas from a nearby tank was available for purging the air from between the electrodes so as to produce brighter and more predictable sparks than in air alone; the argon gas also reduced electrode wear. Flashing of the unit was controlled by a Palseq 400, also by Photonics Analysis Ltd. The Palflash was usually configured to give a continuous beam of light, until triggered by the Palseq 400, which in turn was triggered by the opening of the lens. The Palflash was positioned on the north side of the tunnel on an adjustable tripod, and was aimed at the first of two 17 1/2 inch diameter concave mirrors (fig. 3-43). Parallel light from the mirror then passed

through the optical quality windows of the test section and reflected off of the second concave mirror on the south side of the tunnel. The reflected, converging light was brought to a focus at a vertical razor blade which acted as the knife-edge (fig. 3-44). A Sinar optics bench was used to adjust the positioning of the knife-edge, lens aperture, and image plane. Images were formed on a flat-ground glass plane at the rear of the optics bench. Photographs were taken using Polaroid Polapan ASA 400 film housed in a film carriage. A 30 second developing time was usually required. A video camera was also focused on this plane and its image displayed on a television monitor to provide real-time images and data recording.

Air from the high pressure air supply was directed through pipes over each of the test section windows so as to form a sheet of dry, purging air. This helped in maintaining the outside of the windows free from condensation for about 40 minutes after tunnel start.

3.7.3 Procedures

The Schlieren image was extremely sensitive to the position of the knife-edge. Before every run, the system was retuned and checked. A good test of whether the knife-edge was in the correct position was to slowly screw the knife-edge into the focal point and check that the image became darker uniformly across the field of view. If the image darkened from one side or the other, the knife-edge was not at the true focal point. The final setting was sensitive enough to detect body heat in still air conditions.

These alterations were made with the continuous light source on. However, the spark produced by the Palflash, especially in air, sometimes had a light path that was different from the continuous light path, thus resulting in poor quality photographs. Ultimately, trial and error were the best ways to tune the system.

In order to take a photograph, the film was loaded into the film carriage and mounted onto the rear of the optics bench. The test section windows were wiped clean and dry. The lens aperture was primed in the closed position, and the film cover removed. The room lights were then turned off, and a remote trigger was pushed which opened the aperture and also sparked the Palflash. The room lights were turned back on, the film cover replaced, and the carriage removed from the optics bench. The film was removed from the carriage and developed.

3.7.4 Photographs

Before each test, a wind-off photograph was taken for reference purposes. Masking tape was stuck on the outside of the test section windows to define a 1 inch distance.

After placing the swept cylinder model into the test section for the first time, Schlieren photography was used to determine the nature of the bow shock wave, specifically to see where the reflected bow shock wave hit the cylinder and to check for other disturbances in the flow.

The bow shock wave was studied with the swept cylinder model in the aft position. Figure 3-45 shows that the bow shock wave is attached at the tip and is slightly curved, which is in qualitative agreement with the CFL3D solution. The initial shock wave angle at the tip was measured to be 50° bending back to 43° downstream. The CFL3D solution gave 45° bending back to 40°, the difference being possibly due to viscous effects.

With the cylinder in the forward testing position, the location of where the reflected bow shock wave impacted the attachment line was found. Figure 3-46 shows the reflected shock wave hitting the rear of a hot-wire probe at a spanwise distance of 9 inches, which agrees with the predicted value arrived at in the design of the wedge spacer using the CFL3D solution. The cylinder was thus in the correct vertical position to achieve an optimum test run length along the attachment line, and no further adjustments had to be made to the wedge spacer.

Figures 3-45 and 3-46 also show other disturbances in the test section, which were traced back and found to be emanating from various joints of the wind tunnel walls. These waves were found to have an angle of 39°, which is exactly the Mach angle for a Mach 1.59 flow. Therefore, these waves are Mach waves and are of very low strength. Attempts were made to reduce these as much as possible. The tunnel was always allowed to thermally stabilize after startup. This process lasted approximately 20 minutes, which aided in the correct fitting of the joins. Shims placed under the upper window blank were very successful in reducing the wave emanating from the upper window blank/test section join. Hand polishing of all the joins also helped considerably but never removed the waves totally. However, none of these waves impinged on the transition test surface of the model, as seen by the lack of a wave reflecting off of the surface of the model, and the path of the disturbance before the cylinder being exactly in line with the path after the cylinder. (The bow shock wave's path before the cylinder forms two parallel paths after the cylinder that are not in line, thus showing that the bow shock wave has wrapped around the cylinder.) Since the Schlieren system integrates the optical image along its light path through the test section, waves believed to be confined near the walls of the tunnel give the appearance of spanning the tunnel. (This was based on the fact that hand polishing was very difficult to accomplish near the right-angled corners of the tunnel and subsequently small steps were left there.)

Figure 3-46 also shows a 1/2 inch thick layer along the tunnel wall which at first appears to be a turbulent boundary layer. However, due to the integration of the final image along the optical path, this could possibly be caused by corner vortex flows in the rectangular test section. This hypothesis is further supported by the observation that shock waves in test section appear to pass right through this apparent turbulent layer and reflect off the tunnel walls. Further investigation is required to determine the exact nature of the boundary layers on the test section walls. As far as the experiment is concerned, however, only the freestream disturbance level where the model is located needs to be determined. So long as this disturbance level is suitably low and quantified, then investigation of the boundary layer is not required at this time.

Other points of interest can also be seen. Figure 3-45 shows that the disturbance generated off of the lower surface of the apex is also a Mach wave, as evidenced by its angle. The boundary layer on the lower (flat) section of the apex can be seen to be clearly growing in thickness with downstream location. Figure 3-46 shows the wakes generated behind the swept cylinder and the hot-wire probe. Notice, however, that the boundary layer along the attachment line that is upstream of the hot wire

cannot be seen with this "global" Schlieren system. This should not be surprising since the hot-wire signal indicated a laminar boundary layer, which the BL3D calculations predict to be 0.009 inch thick. However, this optical method only detects density gradients, and the density gradient in the outer part of the boundary layer is probably too small to be detected. Therefore, the true boundary layer thickness is probably much thicker than can be optically detected.

3.7.5 Surface Flow Visualization

3.7.5.1 Oil

The oil flow visualization technique was used in order to gain an understanding of the overall flow pattern over the model. The heated cylinder was fixed to a clear (Perspex) window blank so that all-round optical access could be obtained. Several mixtures of oil, lamp black, and oleic acid were tried, but the most successful consisted of an oil of 750 centipoises viscosity mixed with lamp black and two of drops of dispersing oleic acid. The most satisfactory results were obtained when the mixture was applied liberally over a 3/4 inch strip along the attachment line. The flow was allowed to carry the mixture back over the complete surface of the model, which took about 5 minutes after startup. Photographs were taken while the tunnel was running, since the shock wave passing through the test section at shutdown altered the pattern. Due to the cold freestream temperatures, it was found that maintaining the internal heaters at $T_{control}$ = 60°F aided in the oil dispersion. All results were obtained at $Re_\infty = 2.4 \times 10^6$/ft.

Several distinguishing features were evident in the overall pattern (fig. 3-47). First, the reflected bow shock wave is clearly seen at y = 9.3 inches, and this caused a slight buildup of oil at the incident location. The line of separated flow is also clearly visible at around 90° before the incident shock wave, moving up to 70° after the shock. Crossflow vortices are evident from about 20° around to the separated flow region. Measurements from the photographs revealed a crossflow vortex spacing of approximately 0.04 inch.

Figure 3-48 shows the diverging flow pattern around the attachment line, and provided a sound double-check that the cylinder was truly aligned in the tunnel with no induced yaw angle. A turbulent wedge, caused by particulate in the oil mixture near the tip, is clearly seen.

3.7.5.2 Naphthalene Sublimation

The naphthalene sublimation technique (ref. 58) was applied to see if crossflow vortices could be observed in the chordwise direction.

The naphthalene was dissolved in freon (until the freon became fully saturated), filtered, and applied to the model with an airbrush. Great care was exercised to ensure that the mixture was applied evenly and consistently over the surface. Applying the mixture with the model in situ was awkward and did not provide the most uniform coating possible with this technique. Best results were obtained when several coats were applied and the rough surface was smoothed over using the tips of one's fingers (while wearing latex gloves). At all times, the application of naphthalene was undertaken while

wearing protective gloves and a respirator, with good room ventilation. After spraying, the surface was marked with a black pen to indicate 30° angle increments from the attachment line, at about 6 inches from the apex. Photographs were always taken in a wind-off condition. Black felt mounted on cardboard was used to completely line the working section to provide a backdrop. The internal heaters were kept on to reduce condensation effects while the test section windows were open to the moist atmospheric air.

It was found that with two coats of mixture the naphthalene sublimated off the relatively warm surface before the model had cooled to its equilibrium (adiabatic) state. Applying three coats resulted in the naphthalene staying on the surface, but then it would not sublimate at all at equilibrium temperatures. A compromise was found by slowly increasing the heat supplied to the model. Although this is not truly the same as increasing the freestream temperature, it did bring out some of the flow characteristics. Figure 3-49 shows the cylinder coated in naphthalene just before the run, as well as a 0.025 inch diameter trip wire which was known to create fully turbulent flow. Figure 3-50 was taken immediately after startup. Note that the trip wire caused an immediate sublimation of napthalene right behind the trip. Also note that the napthalene sublimated away to around 100–110°, but this might have been due to a thinner application of paint in this area. Figure 3-51 is a global view after shutdown, and figure 3-52 is a close-up. Here, transition due to stationary crossflow vortices is clearly seen in the white mixture, as evidenced by the classic feathered trailing edge. Across a 1 inch arc length, there were approximately 30 striations in the mixture, giving a wavelength of 0.033 inch ($\lambda/\delta = 3.3$) at $Re_D = 4.5 \times 10^5$, which is comparable to the oil measurement. These results are also of the same order as measured in references 66 and 67 at Mach 3.5 using oil (wavelengths from 0.03 to 0.04 inch ($\lambda/\delta = 5-7$) at $Re_D = 4.6 \times 10^5$). The sublimation solution revealed the high shear and increased temperatures associated with the attachment line, since no mixture remained there. A pattern was also seen in which the trailing edge was seen to be asymptoting toward a line parallel to the attachment line at $\theta \approx 30°$ as one would expect to occur in swept-infinite flows. This suggested that a hot wire traversed in the chordwise direction (normal to the attachment line) should be able to detect a rise in signal due to turbulent flow created by crossflow vortices near this angle.

These results were obtained with the internal heaters set to $T_{control}$ = 30°F. Therefore, could the internal heaters have caused this feathered pattern? The heaters are positioned at ±40° and one at 180°. Therefore, maximum surface heating would occur around 40°, but this was close to where the napthalene remained. Therefore the sublimated shape was not a result of the heaters but of the air flow.

3.8 Temperature Sensitive Paint System

The temperature sensitive paint (TSP) technique was applied to quantify the global surface temperature distribution and possibly locate a boundary layer transition front along the attachment line.

3.8.1 Theory

In the TSP technique, a special paint is applied to the surface of interest. The surface is then illuminated with ultraviolet (UV) light which excites a fluorescence in the paint that is temperature dependent. The molecules in the paint are then excited to an upper singlet state by the absorption of

light. The decay back to the ground state occurs through fluorescence, phosphorescence, or vibrational relaxation. The rates of these competing processes are temperature dependent and quantifiable. The surface temperature is then directly related to the intensity of light emitted from the paint.

For this study, a rare earth complex, Europium Thenoyltrifluoroacetonate (EuTTA), was used as the fluorescent paint. More details concerning the governing equations for this technique can be found in reference 120.

3.8.2 Equipment

The model was first uniformly sprayed with a white undercoating. Three ink dots were then applied along the attachment line as locator marks at approximately $y = 1$, 5, and 9 inches. The cylinder was then coated with a solution of EuTTA paint mixed in dope, as used by Liu (ref. 120). The paint mixture consisted of 75 ml dope and dope thinner with 1 gm of EuTTA. The dope to dope thinner ratio was 3:1.

A charged coupled device (CCD) camera and one or two UV lamps were mounted vertically above the cylinder outside of the tunnel. The CCD camera was mounted in a specially built trussed cantilever frame (fig. 3-53). The cross bracing of the frame aided in reducing lateral movements of the camera to a minimum. Liquid cooling of the camera was required in order to maintain operation temperatures. The upper wall of the test section was made from optical quality Plexiglas and so allowed visual access. The lamps had an excitation wavelength of 365 nm, and the CCD camera filter was set to the paint emitting wavelength of 620 ± 10 nm. Images were taken and averaged for each condition using a computer with imaging software.

Initially, only one UV lamp was used to illuminate the model, and it was positioned in the same vertical plane as the camera. What was at first thought to be blemishes in the paint finish were in fact reflections of the UV lamp filaments off of the upper and lower window blanks. Indeed, moving the lamp made the "blemishes" disappear. A problem in positioning the single light source was that the lamp always had to be in the vertical center plane to provide symmetrical illumination but as such the filaments always reflected into the camera. The solution was to mount two lamps equidistant from the vertical center plane on their own cantilevered mounts, as shown in figure 3-53. One precaution was to ensure the lamps were not so close to a window as to melt it.

3.8.3 Data Acquisition and Reduction Procedures

The UV lamps were switched on and allowed to warm up for 15 minutes prior to taking images. When not taking images, the top of the test section was covered by a black cloth in order to prevent unnecessary paint degradation. UV protective glasses were always worn by researchers in the immediate vicinity while the lamps were on. The lamps were angled so as to uniformly illuminate the model surface as much as possible, although this was not crucial since variations in surface intensity due to illumination would be accounted for in the final processing of images.

The camera first took a "dark image" of the model, which was essentially an image as if a lens cap was on the camera. This gave the noise level. Ten images were taken for each condition. No problem was encountered with pixel to pixel mapping due to the rigid support of the camera with respect to the model. As each image was read in, the "dark image" was subtracted, so that the running total was minus the noise level. Ten images were taken for the wind-off condition, and ten images at each temperature setting. This "summed image" was then spatially filtered, in which the intensity at the pixel of interest was averaged over itself and its eight neighboring pixels. The ratio of wind off/wind on was then taken element by element. This resultant matrix (of ratios) was then spatially filtered as well, and the data were then written to file and saved. The thermocouple locations along the attachment line were located in pixel space. At each thermocouple location, the intensity ratio was averaged over a 5×5 pixel area, centered on the thermocouple. This produced a listing of temperature versus intensity ratio (from all temperature settings). The intensity ratios were then multiplied by the exposure ratio at that setting. As the surface temperature increased, the paint was seen to become duller. In order to achieve best results, the exposure time was varied at each temperature setting. At the highest temperature settings, parts of the image were cropped to prevent overexposure of the CCD camera. When the data were plotted as (intensity ratio $\times$ exposure ratio) versus temperature, a single curved line was produced (fig. 3-54). Various orders of polynomial fits were applied, and it was found that a fourth-order fit gave the most reasonable approximation. Fitting all the data points onto a single line was legitimate since the images were all acquired during the same run, and so had the same stagnation temperature (i.e., the conditions were the same for all images except for the surface temperature distribution). Therefore, for any intensity ratio and exposure ratio setting, the surface temperature could be found. Since the maximum temperature measured by a thermocouple along the attachment line was 158°F, the calibration was only truly valid up to this temperature. If an intensity ratio indicated a higher temperature than this, it was capped at 158°F. Therefore, it was expected that areas of constant 158°F would be seen, especially off the attachment line and at high temperature settings. This limit was placed for a number of reasons. Firstly, to truly interpolate intensity readings using the calibration curve. Secondly, at high temperatures, the intensity ratios were very low. Multiplying these by very high calibration slope coefficients would have produced numerical errors.

Previously, in Coleman et al. (ref. 121), temperatures were obtained by applying a linear calibration fit to the thermocouple data along the attachment line for each particular temperature setting. This produced a number of different linear calibration curves equal to the number of temperature settings. High temperatures were obtained by extrapolating these linear calibration curves, although the paint was known to exhibit nonlinear behavior at higher temperatures. This approach was dropped when it became apparent that all data collapsed onto a common curve.

3.8.4 Transition Front Location Test

Trial runs, without any paint, were made with a 0.025 inch trip wire placed across the attachment line. Previously conducted tests (ref. 122) had shown that this size of trip wire caused the boundary layer to become turbulent immediately behind the wire, resulting in a local increase of surface temperature around 2–3°F (fig. 3-55). However, applying this trip to the solid cylinder used in this series of tests did not produce a local rise in temperature, but instead raised all wall temperatures by 2–3°F. It is believed that this was because the model, being made from solid aluminum, was a good conductor of heat, diffusing any local heating effects through the metal. It was therefore suspected

beforehand that TSP would not be able to find a transition location on the solid heated model, and that an insulated model would be required to detect transition.

3.8.5 Surface Temperatures

Figures 3-56 through 3-67 show false color TSP images of the surface temperature distribution and plots of the attachment-line temperature distribution for six heating levels at $Re_\infty = 3.65 \times 10^6$/ft. The apparent hole in the tip of the model was due to a preexisting drilled hole in the Plexiglas window. Figures 3-56 and 3-57 show the no heating (adiabatic) condition. Most noticeable is the increased heating along the attachment line, which is characteristic of stagnation line flows. As the heating level was increased to $T_{control} = 30°F$ (fig. 3-58), the nature of the temperature distribution changed to a predominately spanwise variation from the tip rearward, with no significant variation in the chordwise direction. As the heating was increased to $T_{control} = 60°F$, the chordwise distribution changed due to the positioning of the internal heaters. The heaters extend from $y = 2.75$ inches to $y = 11.75$ inches, and this becomes more apparent in the images with increasing $T_{control}$. At $T_{control} = 90°F$, the temperatures at the edge of the image begin to exceed 158°F. At $T_{control} = 120°F$, up to half the surface is hotter than 158°F. As can be seen in figure 3-64, the temperature gradient at this setting is now predominantly in the chordwise direction. As the heating was increased still further to $T_{control} = 150°F$, the intensity of the paint showed that most of the model was above 158°F.

Table 3–1. Location of pressure taps

	y/inches									
	2.7	3.7	4.7	5.7	6.7	7.7	8.7	9.7	10.7	11.7
+50	2.7186/ +49.1220	3.7138/ +49.1044	4.7146/ +49.2107	5.7144/ +49.1528	6.7150/ +49.0932	7.7145/ +49.1150		9.7168/ +49.1203		11.7190/ +49.1738
+40	2.7180/ +39.2582	3.7208/ +39.1283	4.7187/ +39.0182	5.7201/ +39.0320	6.7191/ +38.8775	7.7150/ +38.8480				
+30	2.7043/ +29.4570	3.7023/ +29.4332	4.7024/ +29.5676	5.7050/ +29.3179	6.7047/ +29.1523	7.7060/ +29.2127		9.7081/ +29.1234		
+20	2.7049/ +19.9001	3.7023/ +20.4165	4.7057/ +19.8069	5.7053/ +19.8445	6.7072/ +19.7612	7.7078/ +19.6609		9.7106/ +20.2571		11.7120/ +19.6254
+10	2.6980/ +9.8519	3.6971/ +9.8657	4.6982/ +9.8980	5.6995/ +9.7657	6.6979/ +9.8755	7.6982/ +9.8286		9.7003/ +9.6558		11.6940/ +9.5381
0	2.6910/ −1.2770	3.6908/ −1.4004	4.6882/ −1.2756	5.6904/ −1.3297	6.6907/ −1.4640	7.6934/ −1.4506	8.6967/ −1.5089	9.7014/ −1.5948	10.7010/ −1.6351	11.7000/ −1.6122
−10	(2.7058) −11.9522	3.6992/ −11.3503	(4.7046) −11.5301	5.6969/ −11.4267	(6.7058 −11.6226	7.6951/ −11.5351				
−20	(2.7058) −22.2495	3.7045/ −21.6269	(4.7046) −21.7977	5.6988/ −21.7853	(6.7058) −21.5684	7.6988/ −21.8041				
−30	(2.7058) −31.4321	3.7048/ −30.9592	(4.7046) −31.5302	5.6970/ −30.8447	(6.7058) −31.9476	7.6993/ −31.0215				
−40	(2.7058) −42.1785	3.7048/ −41.3157	(4.7046) −42.2006	5.7009/ −41.3146	(6.7058) −42.4106	7.7003/ −41.4769				
−50	(2.7058) −51.8158	3.7049/ −50.8376	(4.7046) −51.4067	5.7055/ −50.6797	(6.7058) −52.2064	7.6992/ −51.0768				

θ/ degrees

Table 3-2. Average electrical power supplied to swept cylinder for various control temperatures

$T_{control}$ /°F	Percentage of time heaters on	Average power/watts
0	3.4	76
40	7.8	175
80	15.4	347
120	20.7	466
160	28.4	639
200	34.6	780
240	41.8	942

Results for $Re_\infty = 2.7 \times 10^6$/ft.

$T_{control}$ /°F	Percentage of time heaters on	Average power/watts
0	3.6	81
40	11.8	265
80	21.3	479
120	30.7	693
160	41.6	937
200	50.0	1127
240	55.1	1241

Results for $Re_\infty = 3.6 \times 10^6$/ft

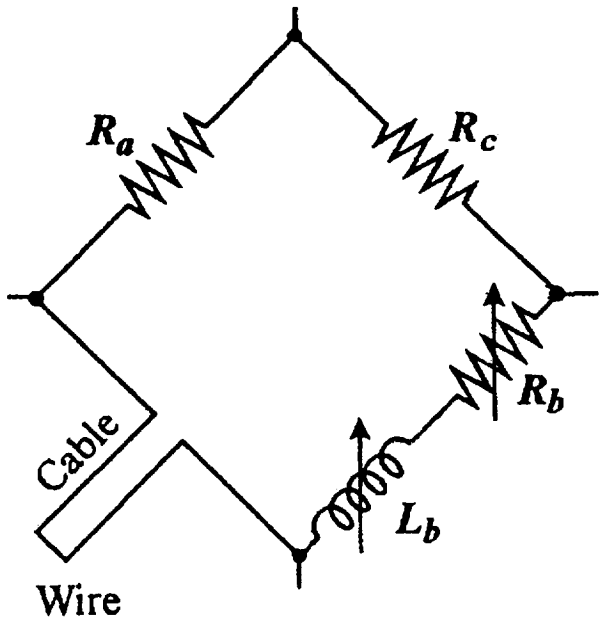

Figure 3-1. Wheatstone bridge components (feedback amplifier circuit not shown).

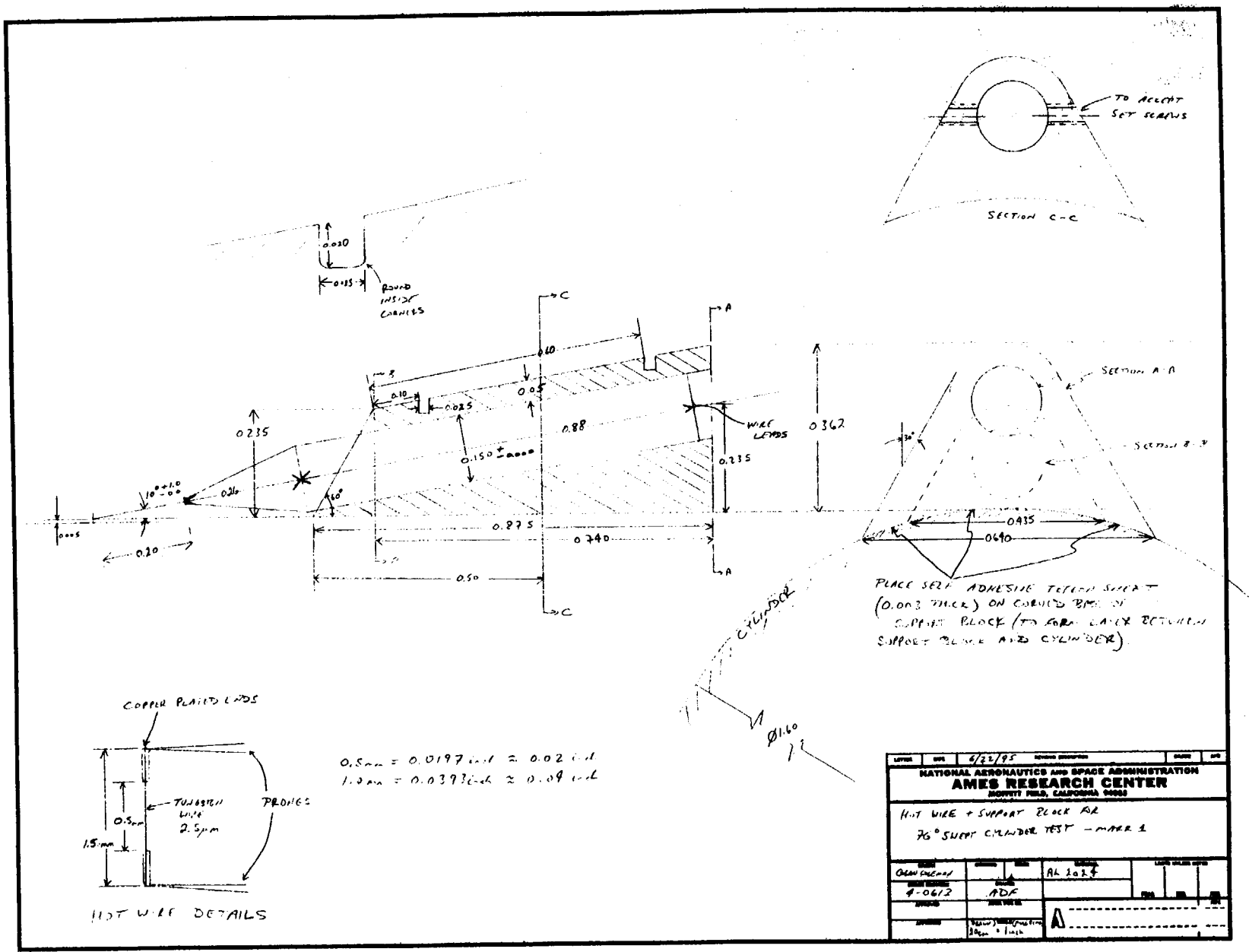

Figure 3-2. Design drawing of Mark 1 hot-wire probe.

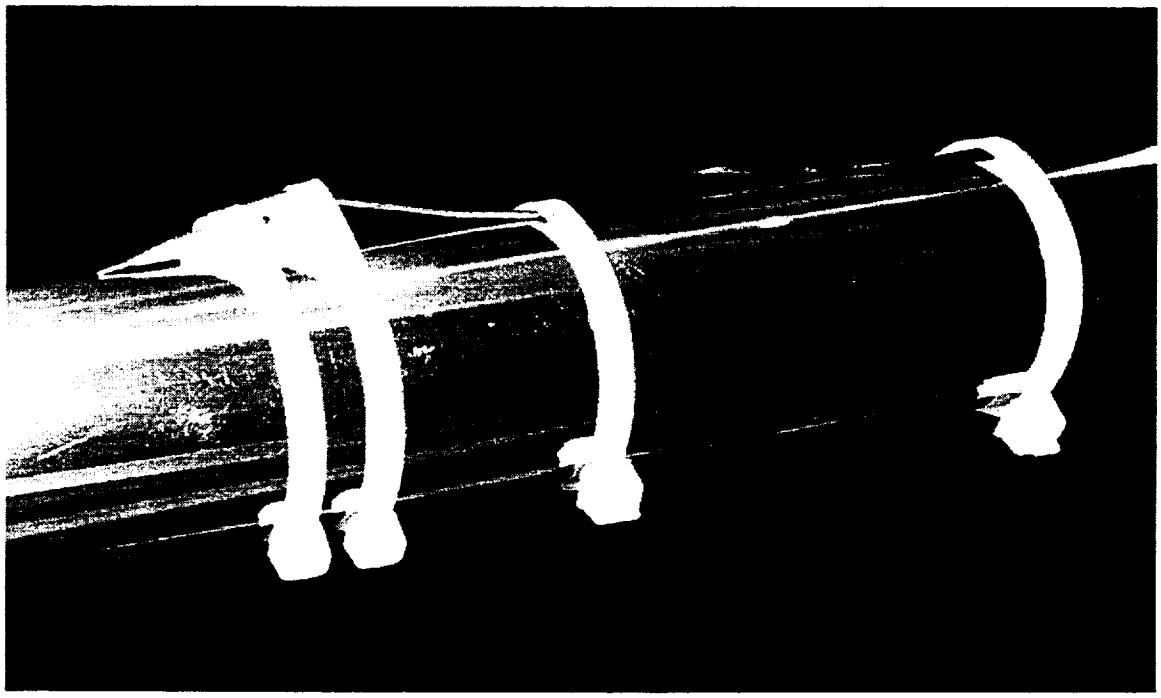

Figure 3-3. Mark 1 hot-wire probe attached to swept cylinder surface.

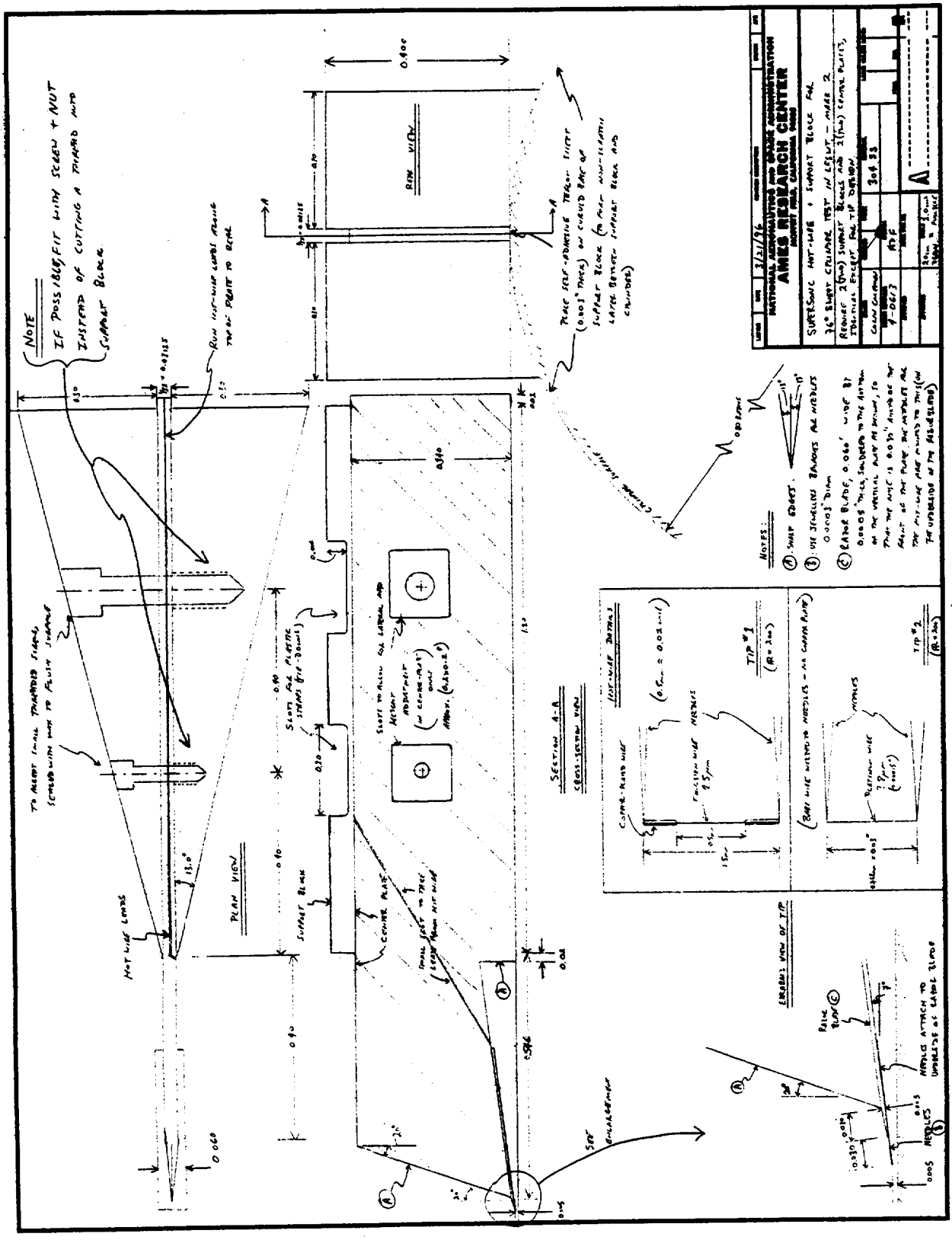

Figure 3-4. Design drawing of Mark 2 hot-wire probe.

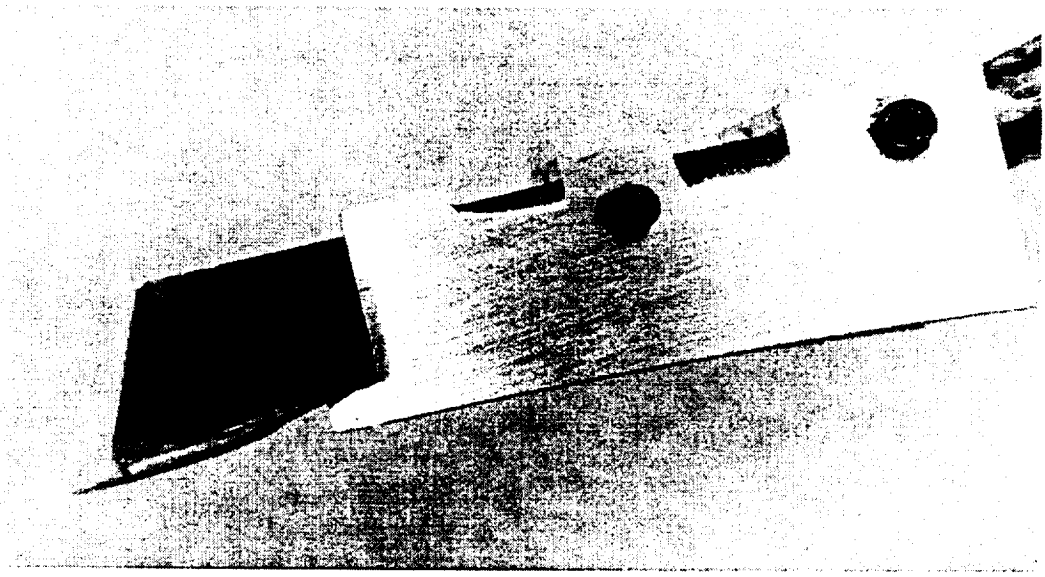

Figure 3-5. Close-up of Mark 2 hot-wire probe.

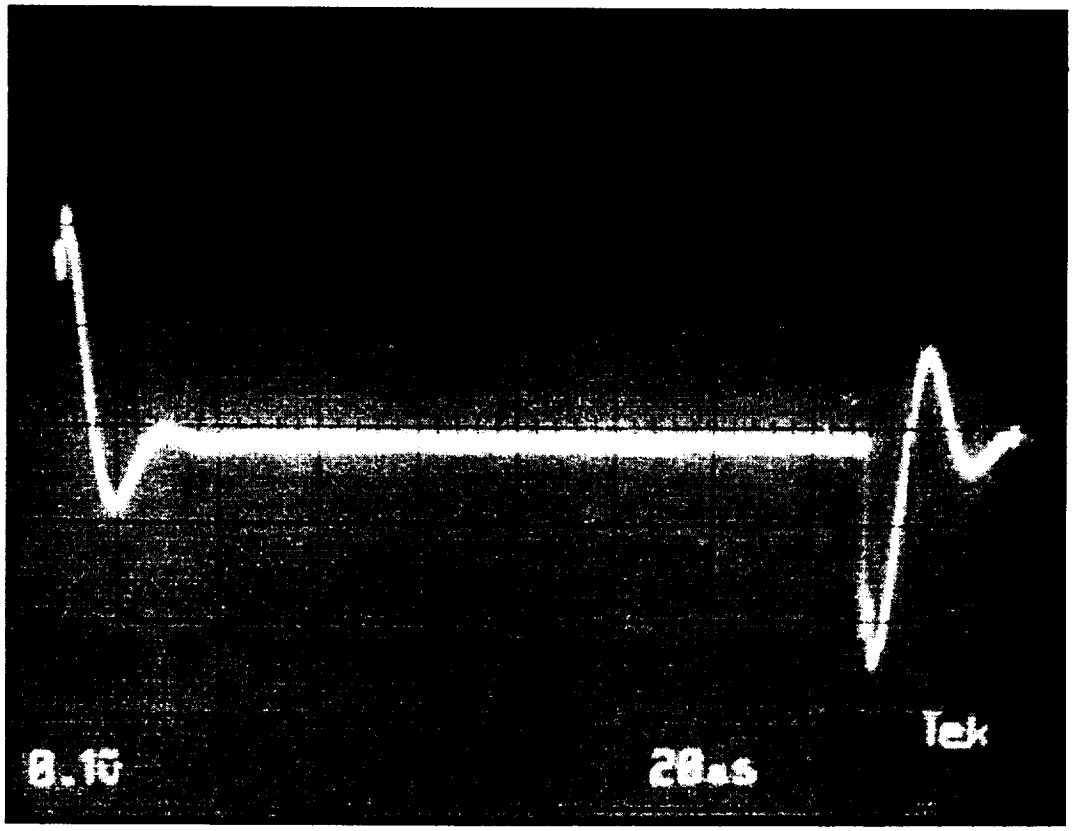

Figure 3-6. Hot-wire response to a square wave input.

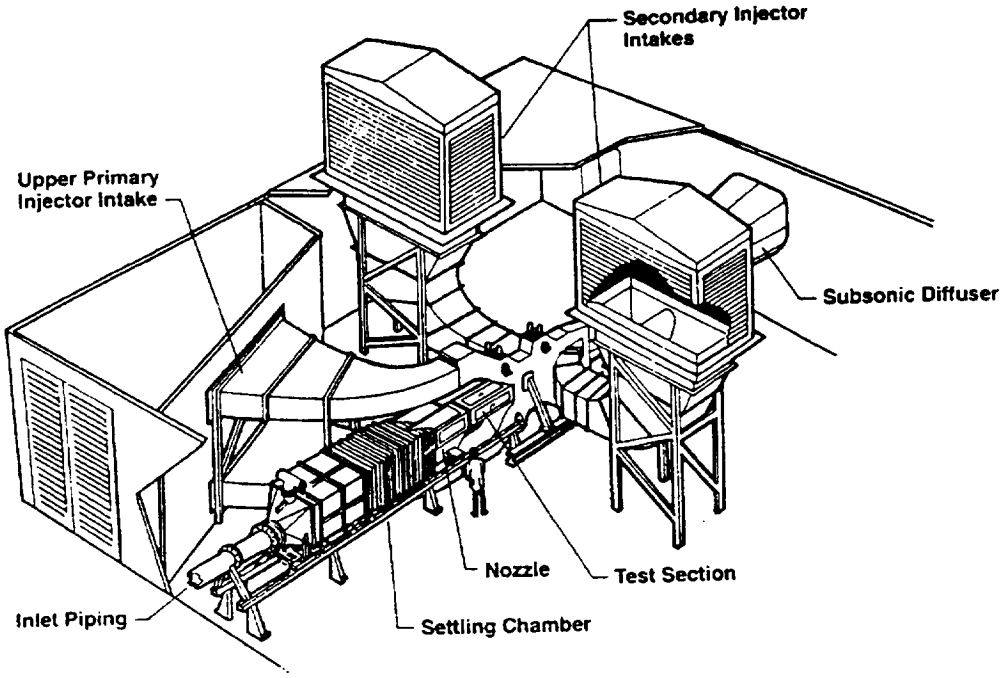

Figure 3-7. Schematic diagram of the Mach 1.6 Quiet Wind Tunnel.

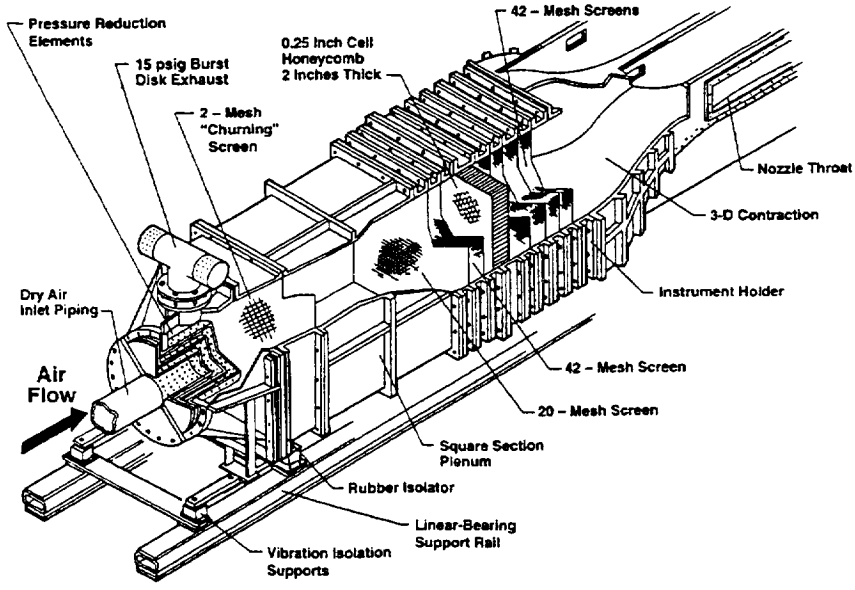

Figure 3-8. Mach 1.6 Quiet Wind Tunnel settling chamber components.

Figure 3-9. Wind tunnel control and data acquisition computers.

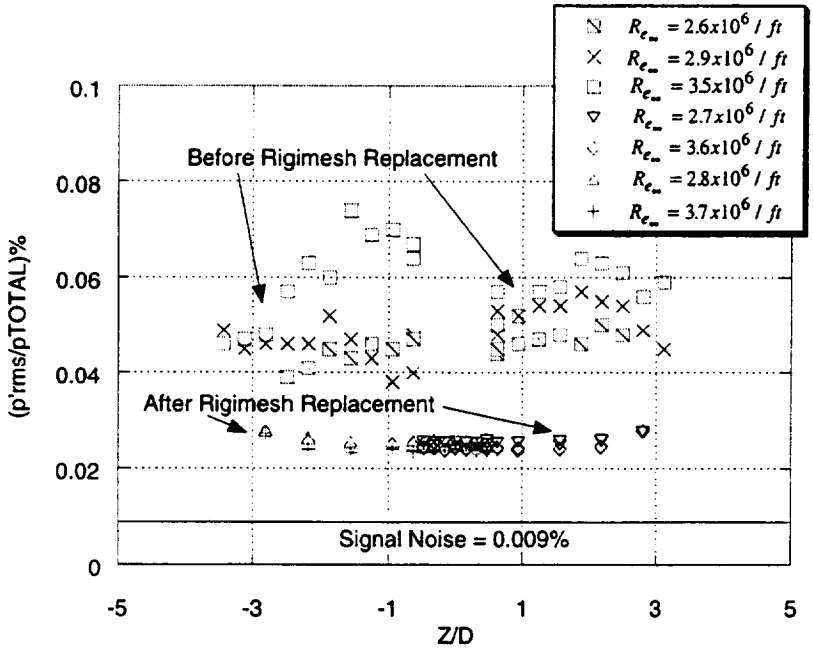

Figure 3-10. Pressure fluctuation data across the center of the test section 1.0 inch downstream of the nozzle exit. 250 Hz–100 kHz range.

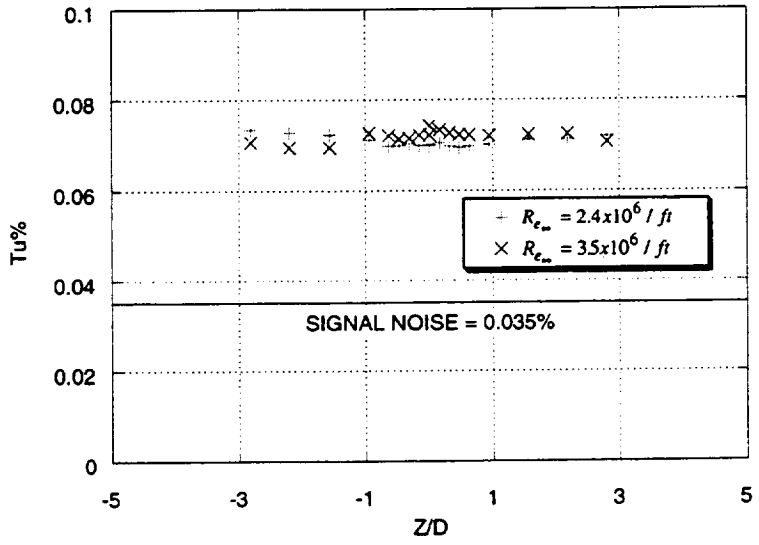

Figure 3-11. Hot-wire fluctuation data across the center of the test section 1.9 inches downstream of the nozzle exit. 250 Hz–100 kHz range, overheat ratio = 0.7.

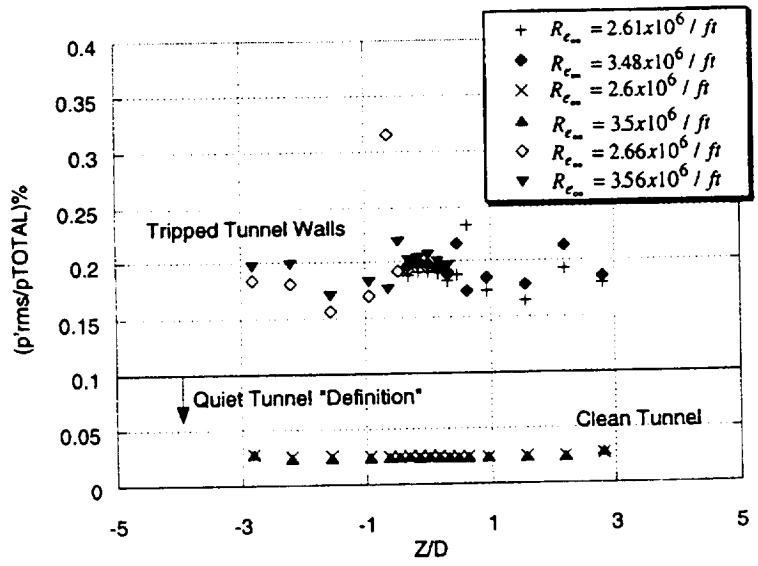

Figure 3-12. Pressure fluctuation data across the center of the test section 1.0 inch downstream of the nozzle exit with tripped tunnel walls. 250 Hz–100 kHz range.

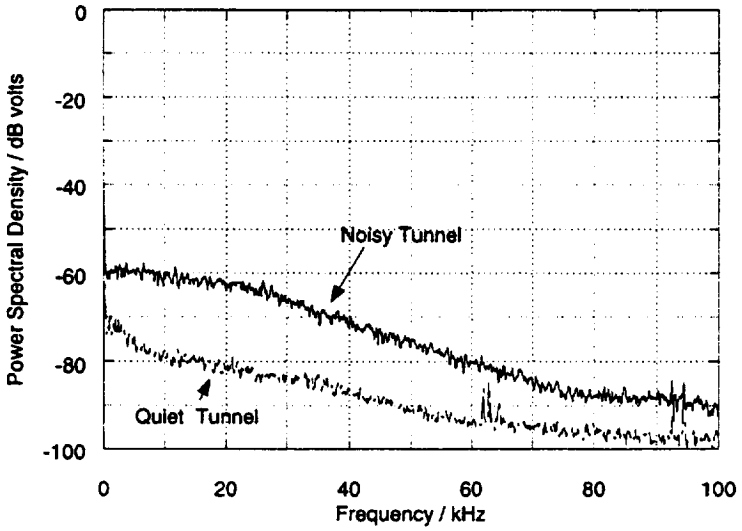

Figure 3-13. Effect of tripping wind tunnel walls on freestream frequency spectra, tunnel centerline 1.0 inch downstream of the nozzle exit. $Re_\infty = 3.65 \times 10^6$/ft.

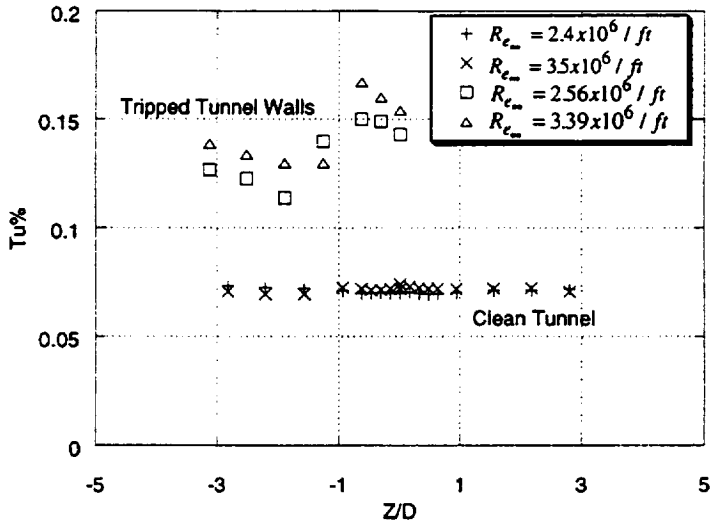

Figure 3-14. Hot-wire fluctuation data across the center of the test section 1.9 inches downstream of the nozzle exit with tripped tunnel walls. 250 Hz–100 kHz range, overheat ratio = 0.7.

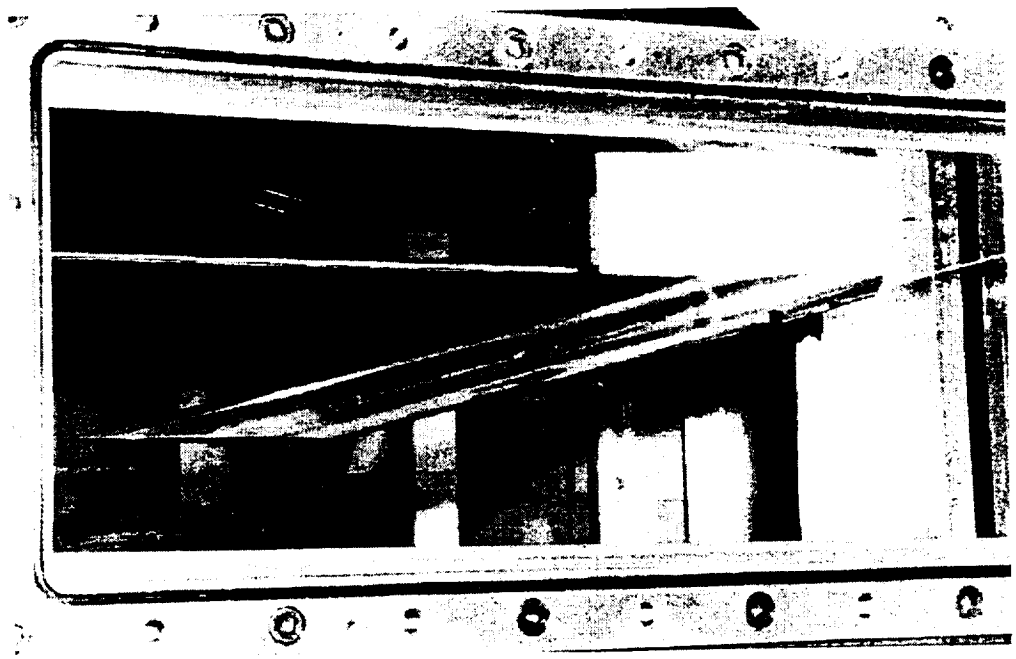

Figure 3-15. Final swept cylinder configuration (shown in aft testing position).

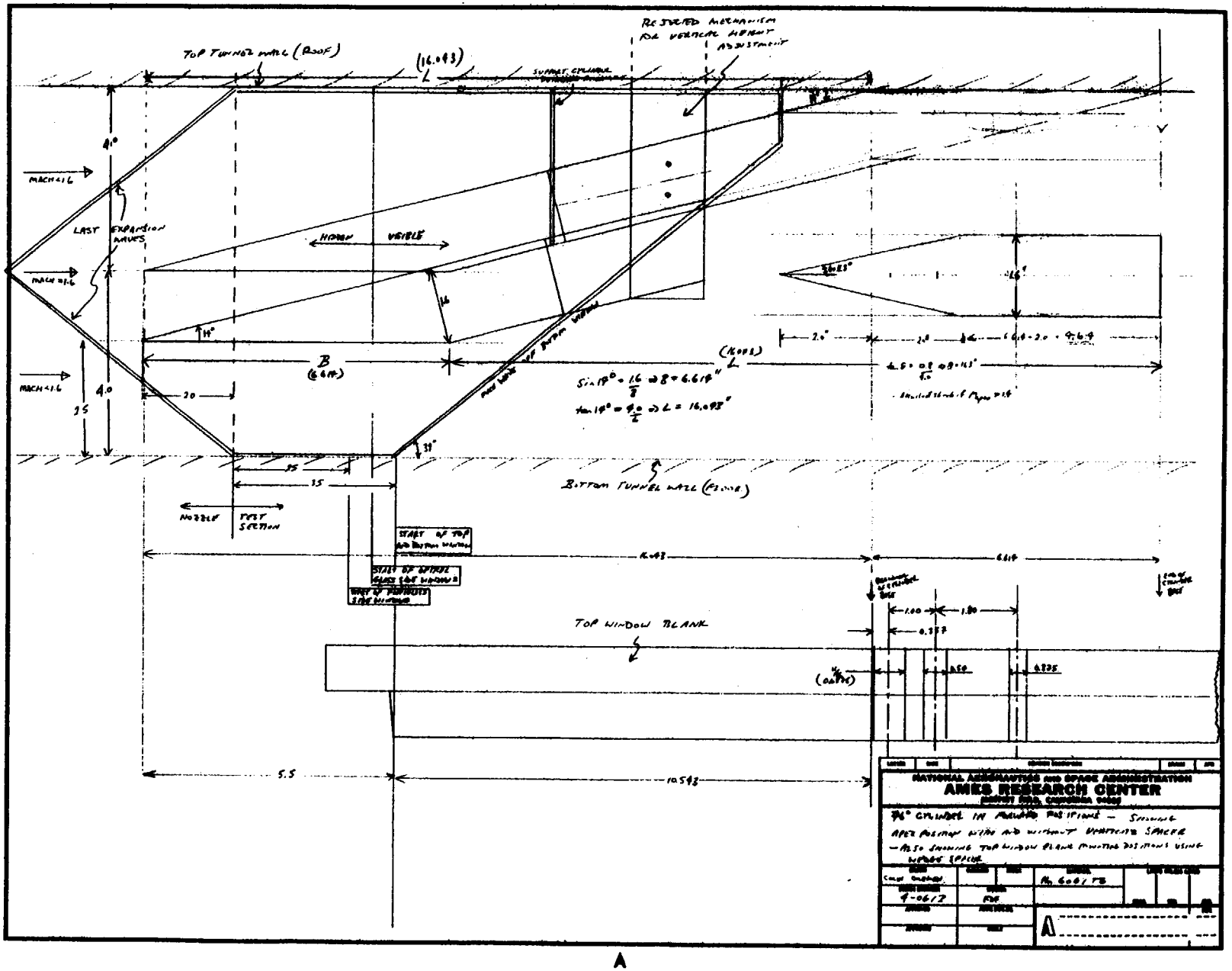

Figure 3-16. Forward testing position places swept cylinder tip into nozzle.

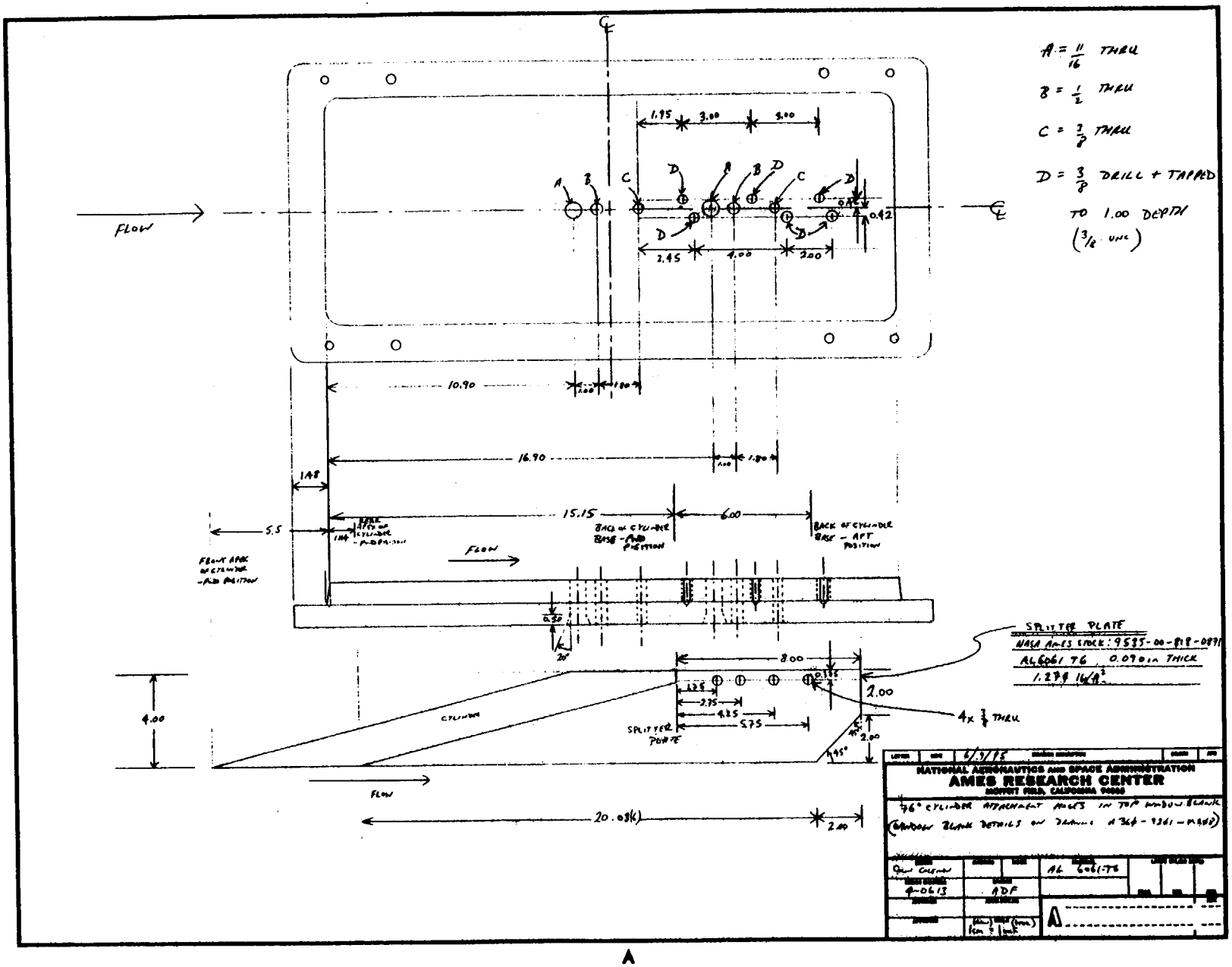

A

Figure 3-17. Upper window blank and splitter plate details.

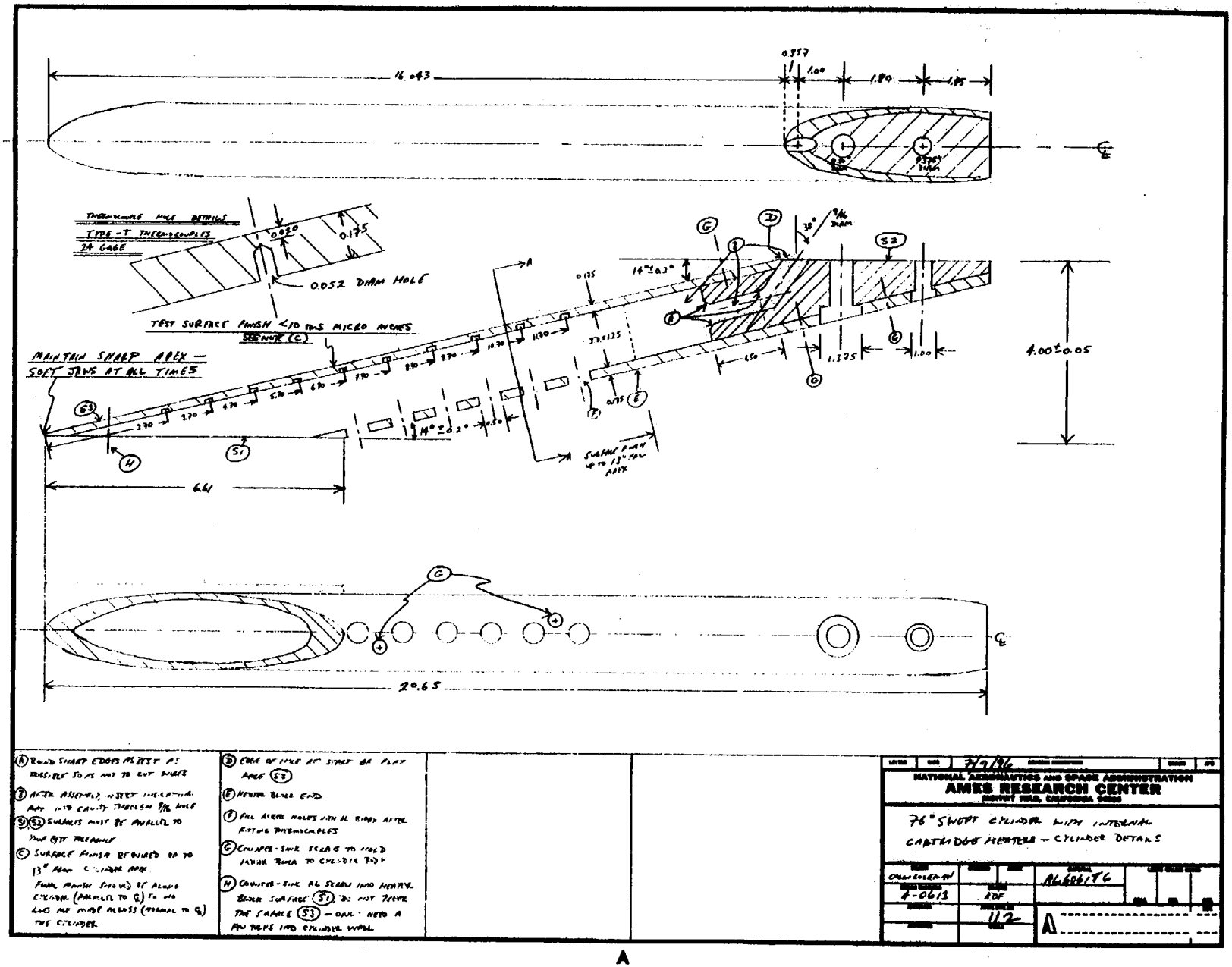

Figure 3-18. Design drawing of the adiabatic cylinder.

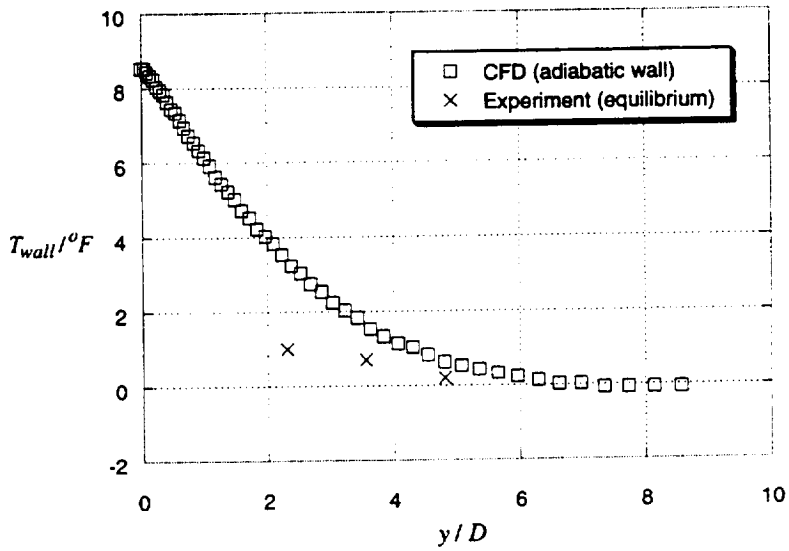

Figure 3-19. Comparison of wall temperatures along the attachment line. $T_0 = 20°F$, $Re_\infty = 2.4 \times 10^6$/ft.

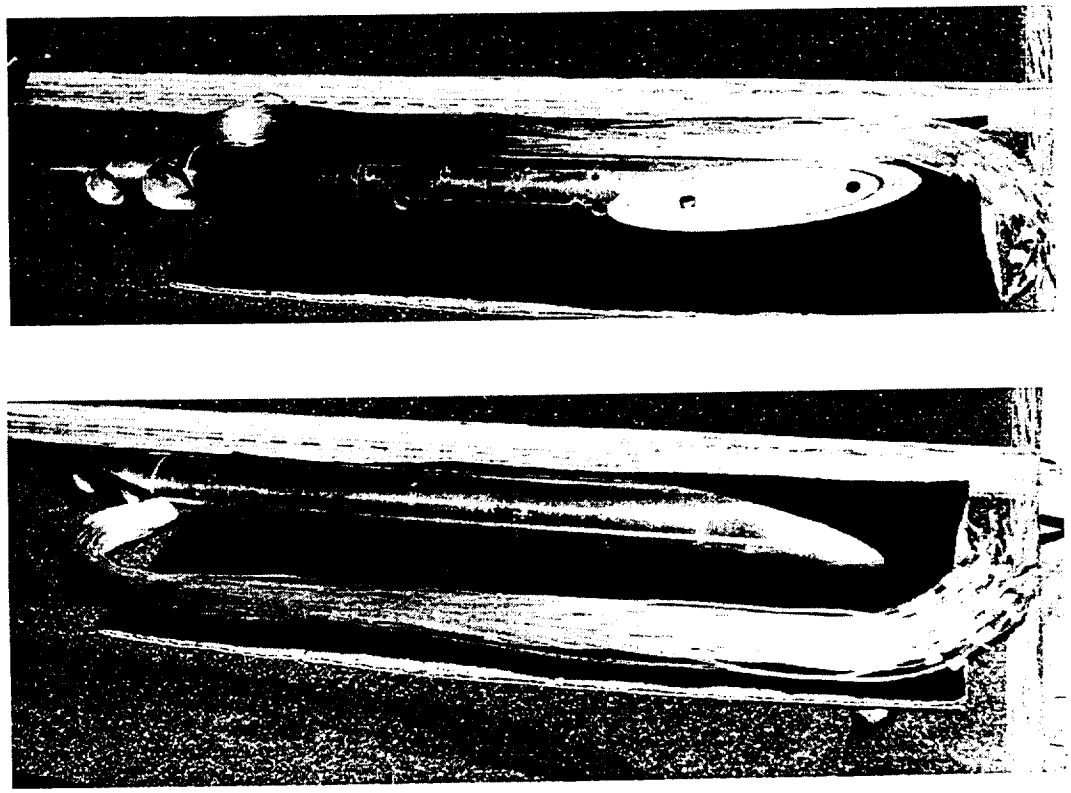

Figure 3-20. Views of the pressure tap model.

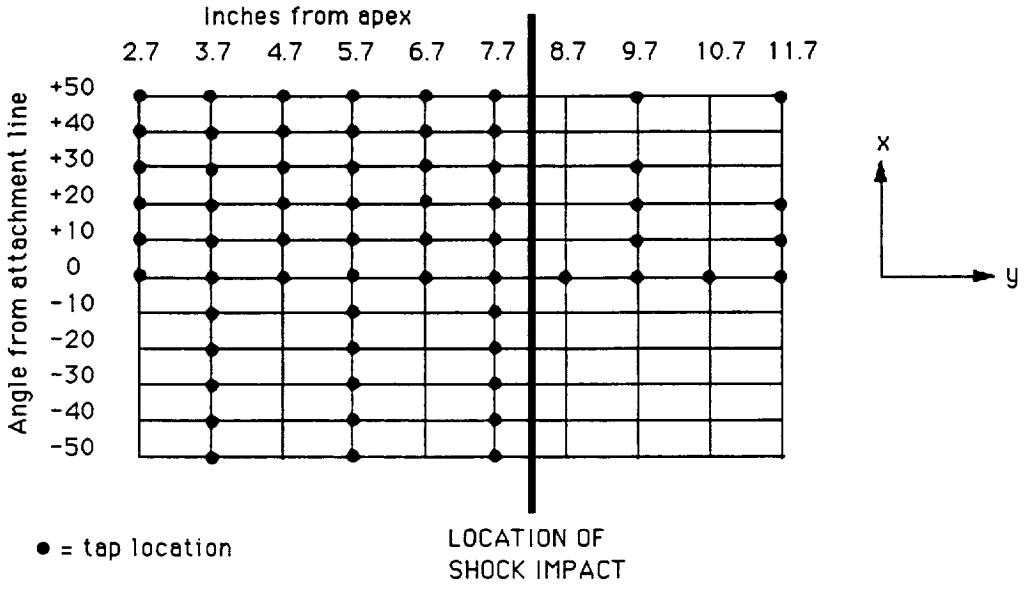

Figure 3-21. Initial arrangement of pressure taps on model surface.

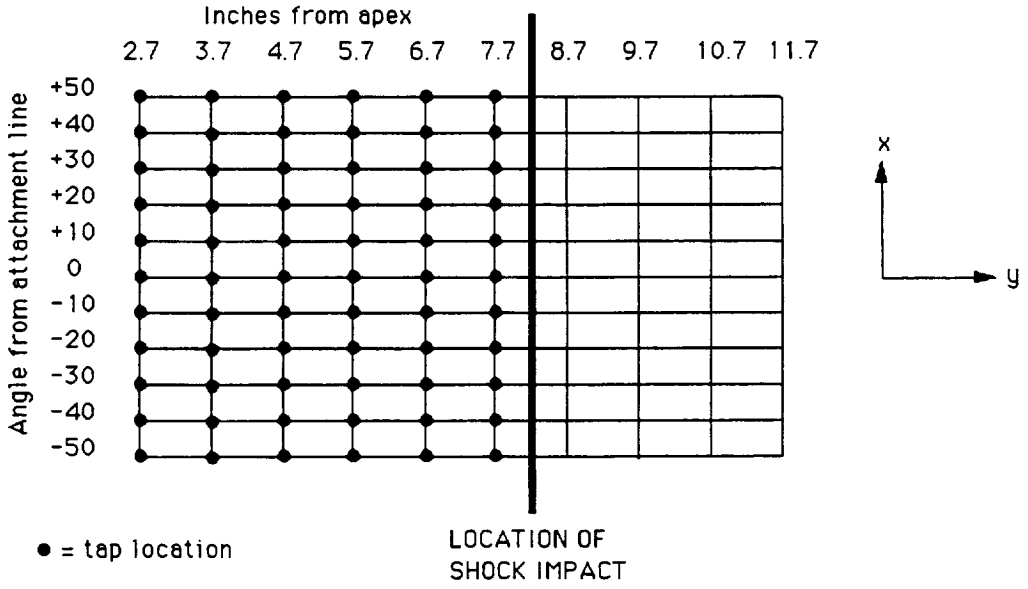

Figure 3-22. Final arrangement of pressure taps on model surface.

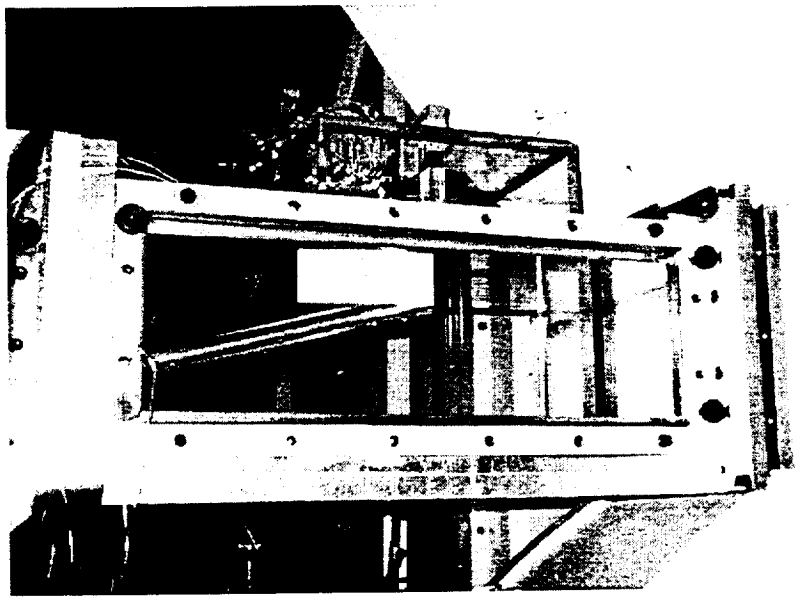

Figure 3-23. Pressure tap model with pressure sealing box.

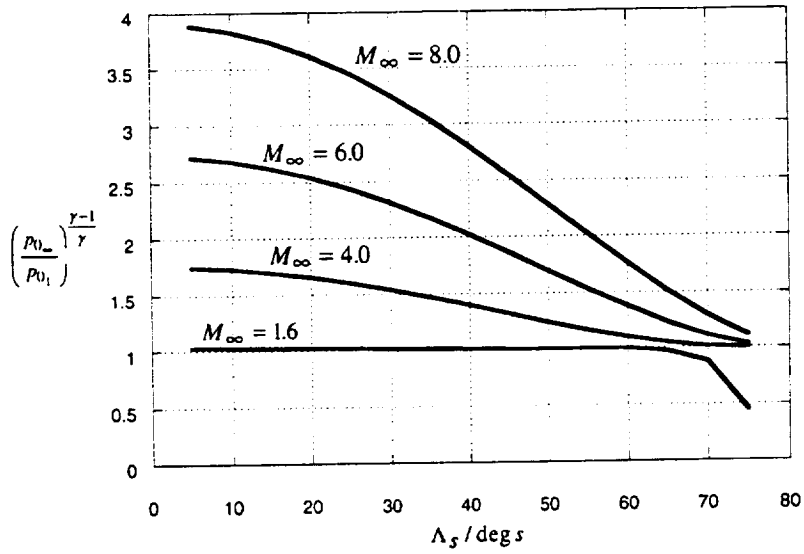

Figure 3-24. Effect of M_∞ on choosing the correct Λ_s for the streamline of interest that enters the attachment line from the freestream.

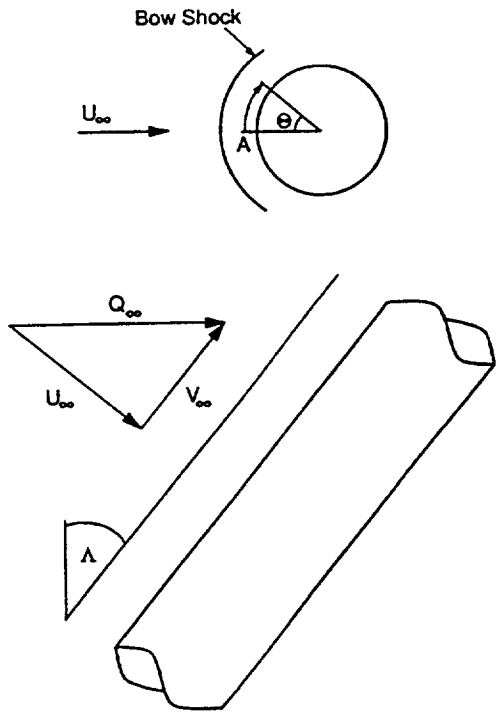

Figure 3-25. Schematic diagram of the flow over the windward face of a swept-*infinite* cylinder.

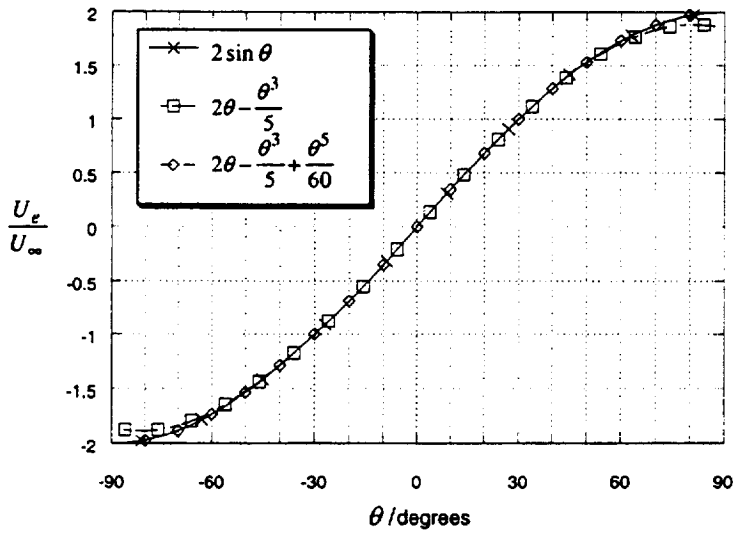

Figure 3-26. Approximating the potential flow solution for the crossflow velocity around a cylinder.

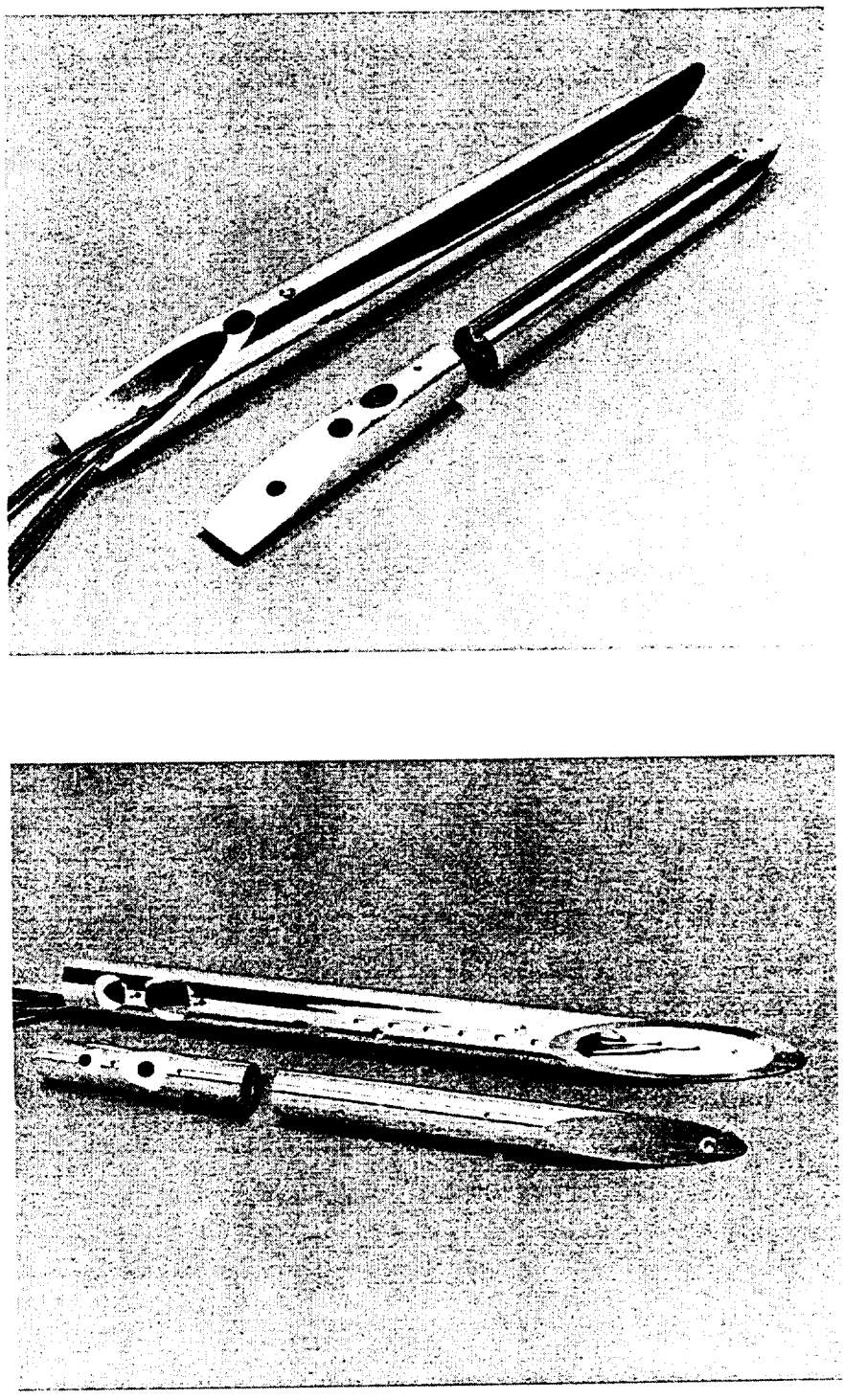

Figure 3-27. Heated swept cylinder model prior to assembly, showing outer shell, conformally fitting heater block, and support plug.

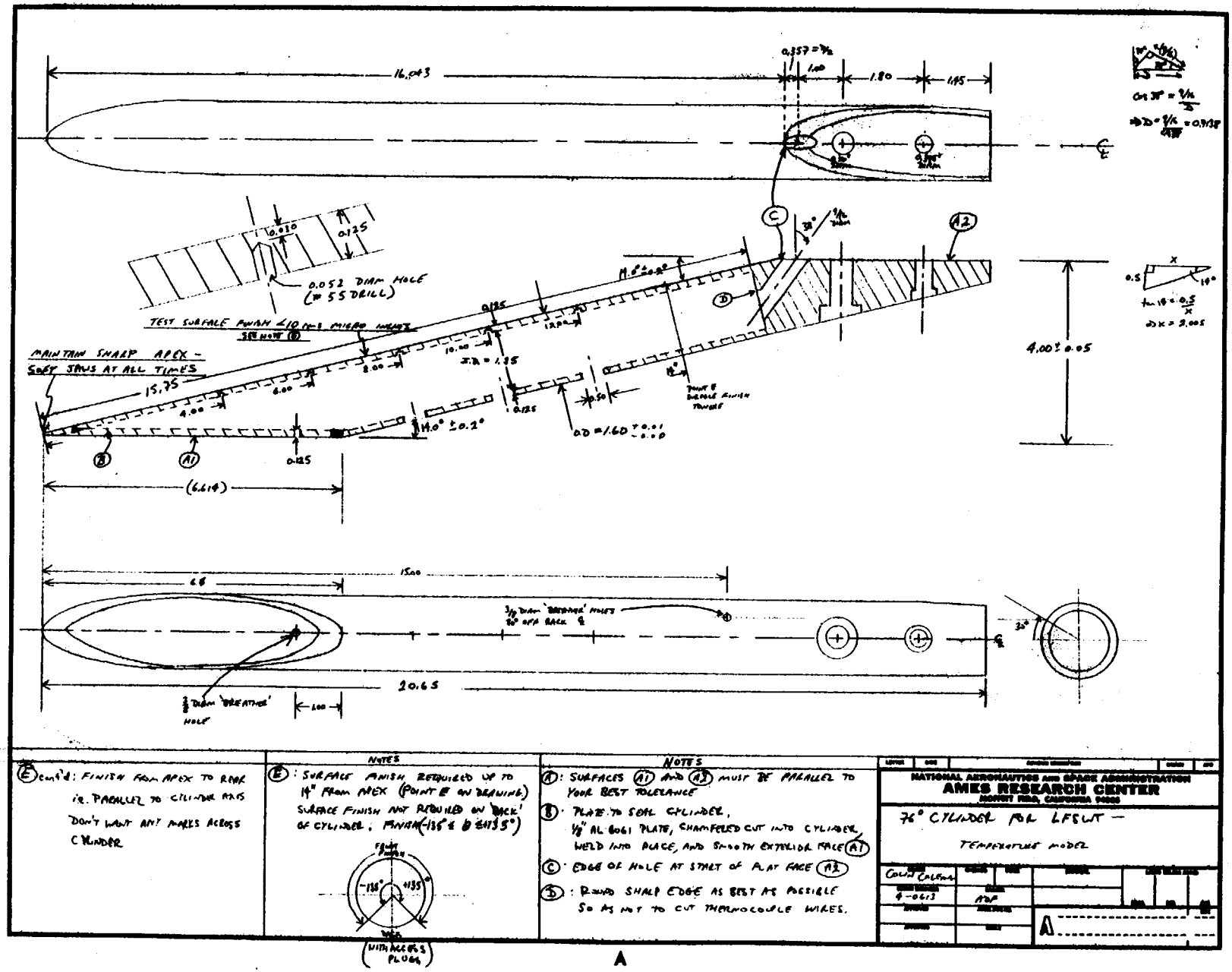

Figure 3-28. Design drawing of the outer shell of the heated swept cylinder model.

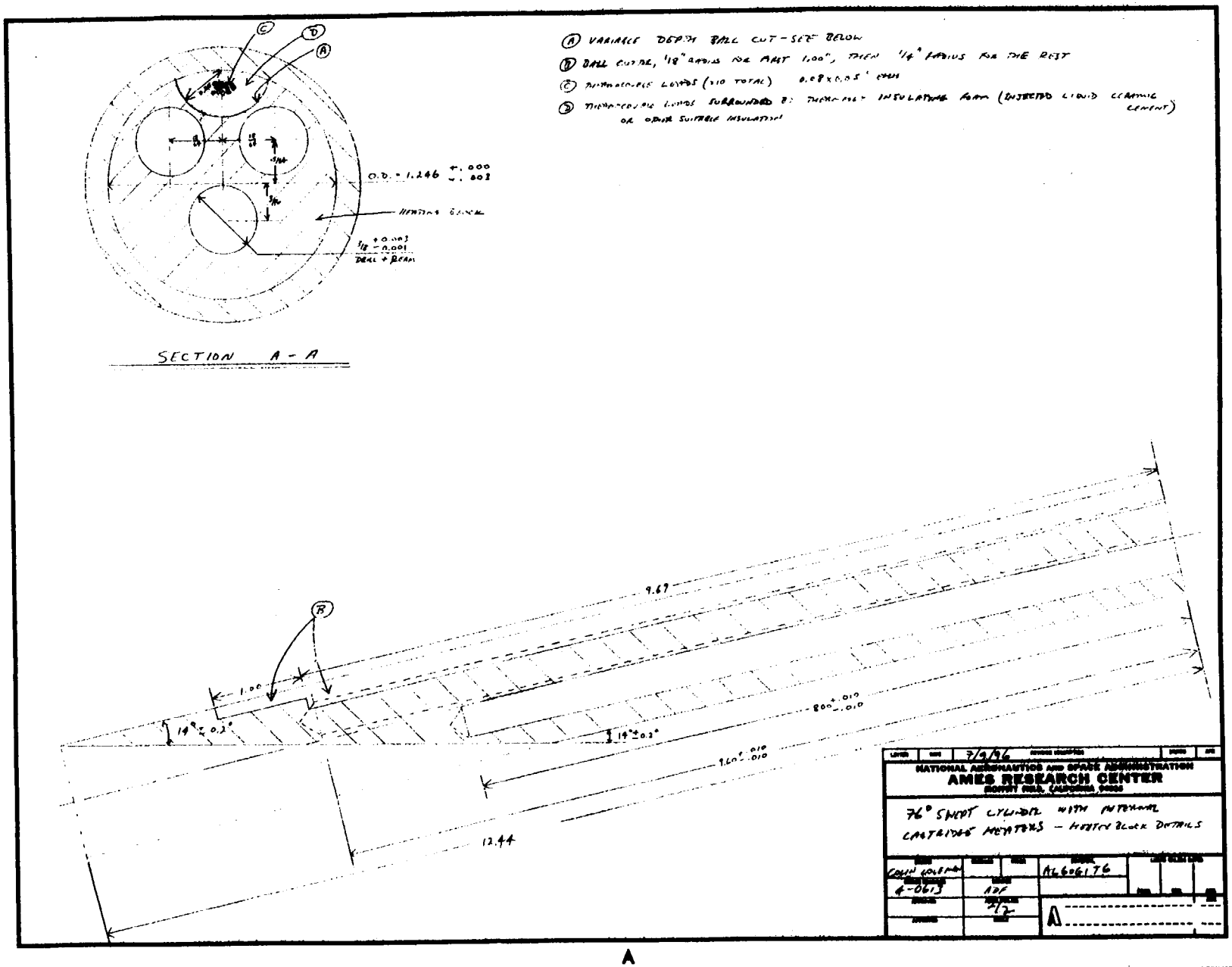

Figure 3-29. Design drawing of the heater block insert of the heated swept cylinder model.

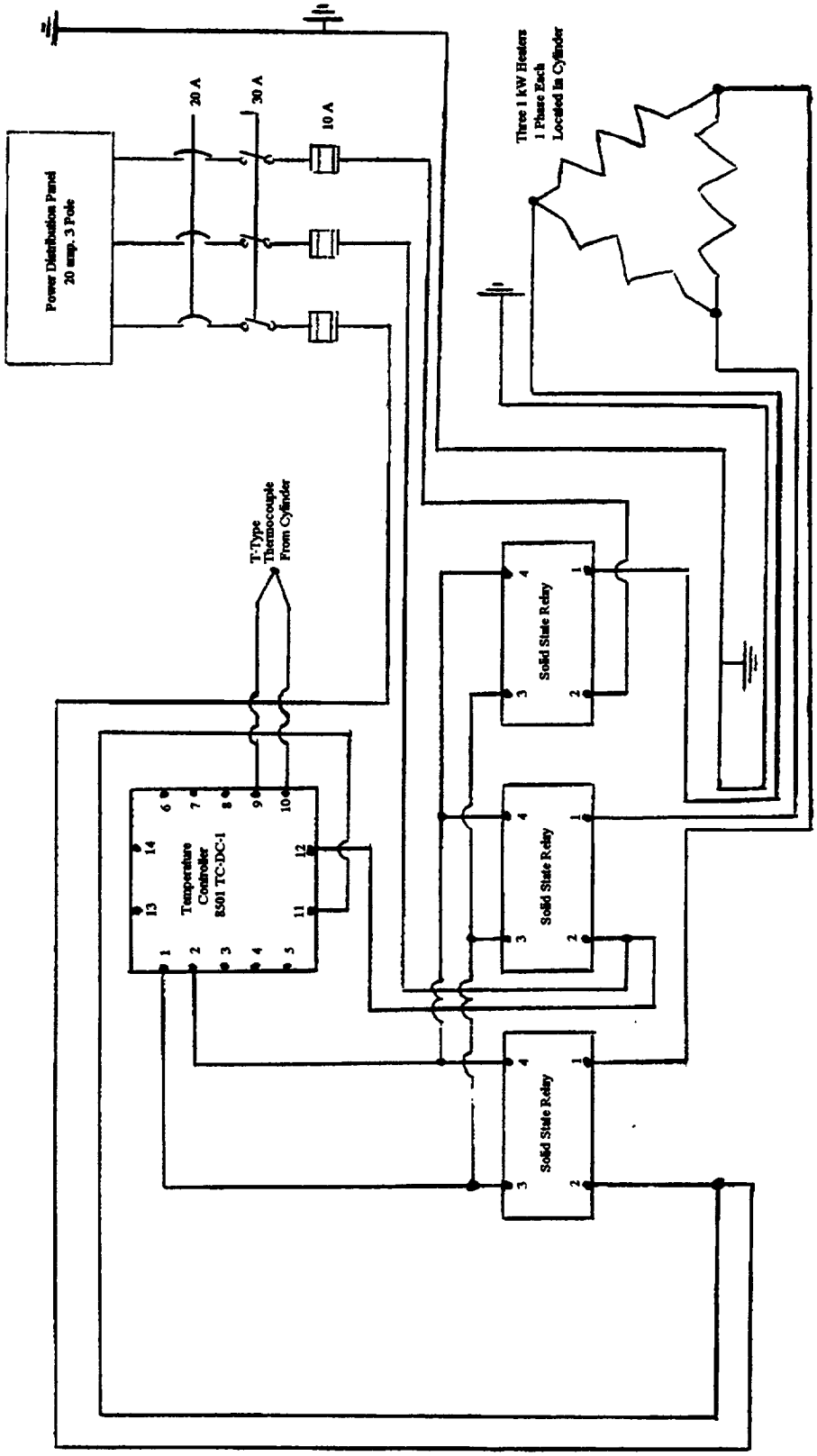

Figure 3-30. Electrical drawing of the heating control system.

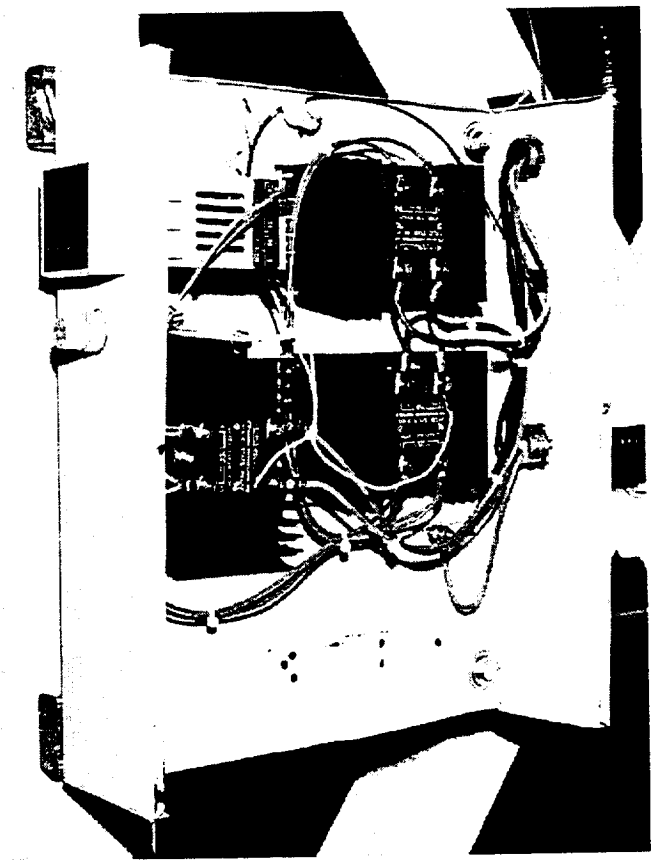

Figure 3-31. Photograph of heating control system.

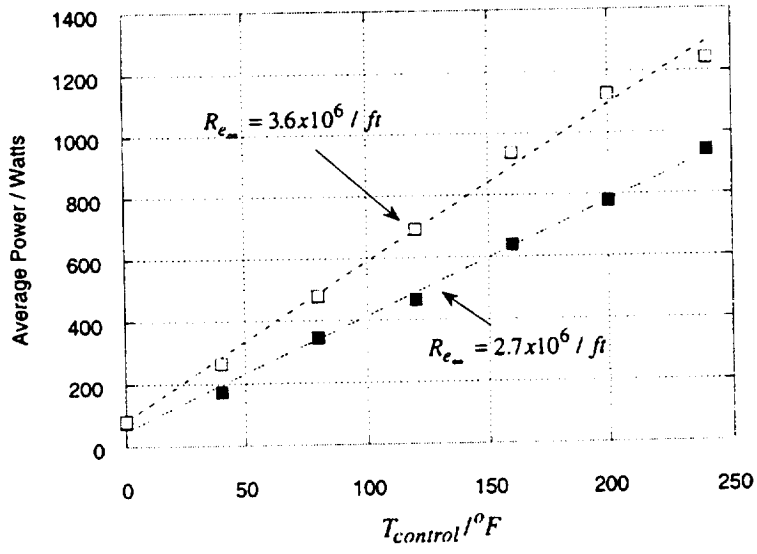

Figure 3-32. Average electrical power supplied to swept cylinder for various control temperatures.

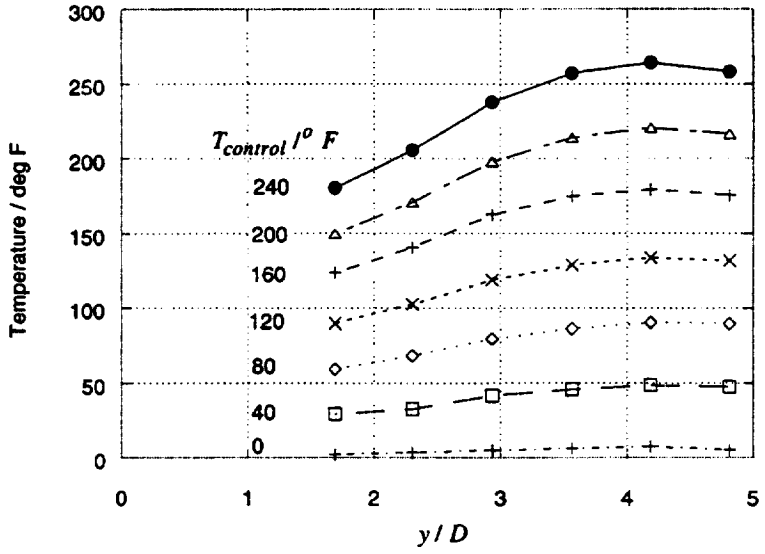

Figure 3-33. Attachment-line temperature distribution with increasing control temperature, $Re_{\infty} = 3.65 \times 10^6$/ft.

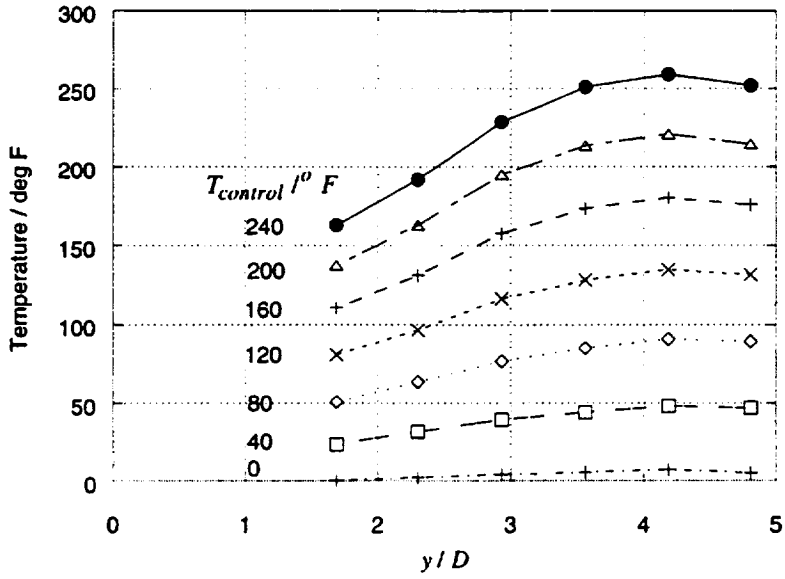

Figure 3-34. Attachment-line temperature distribution with increasing control temperature, $Re_{\infty} = 2.72 \times 10^6$/ft.

Figure 3-35. Enlarged view of upturned burr on cylinder tip.

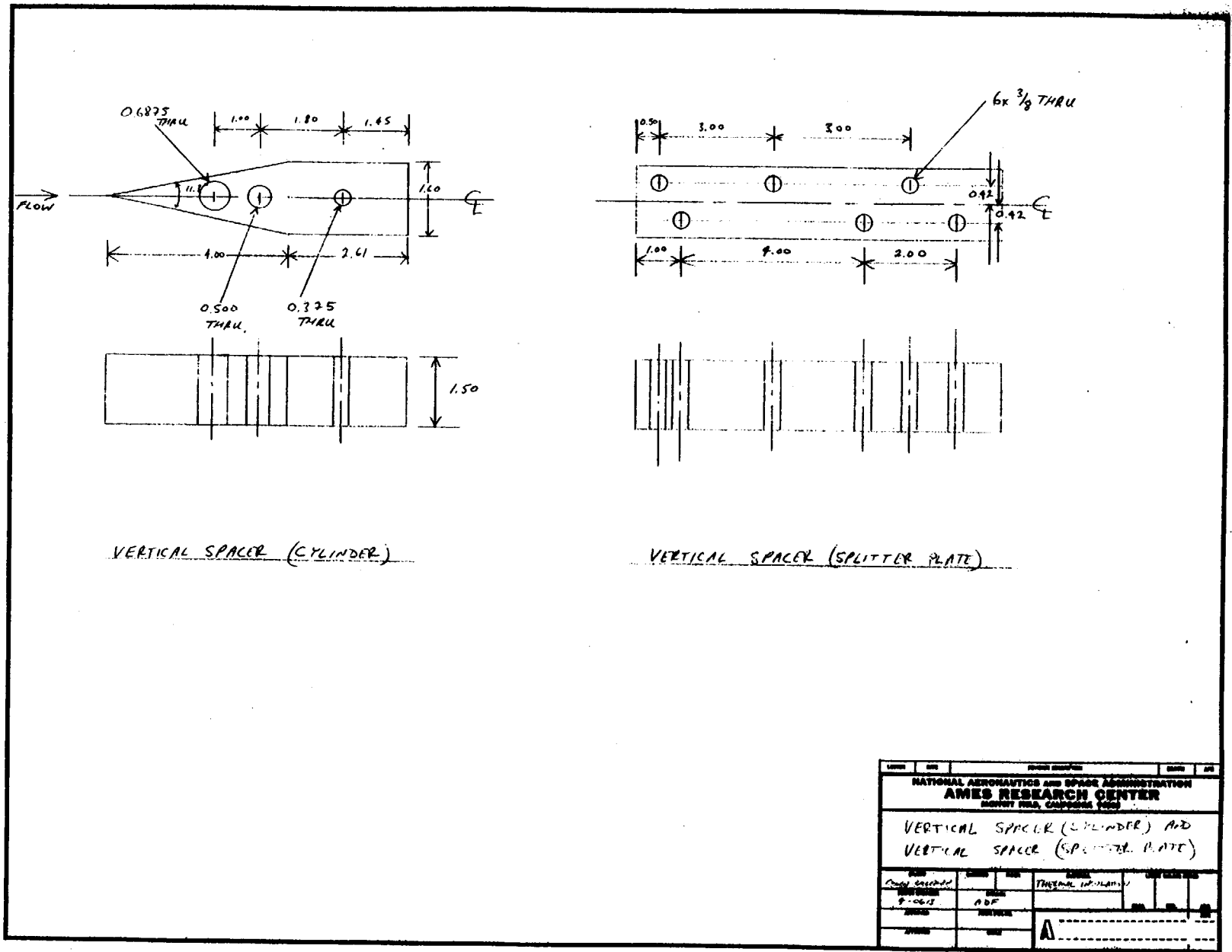

Figure 3-36. Design drawing of vertical spacers.

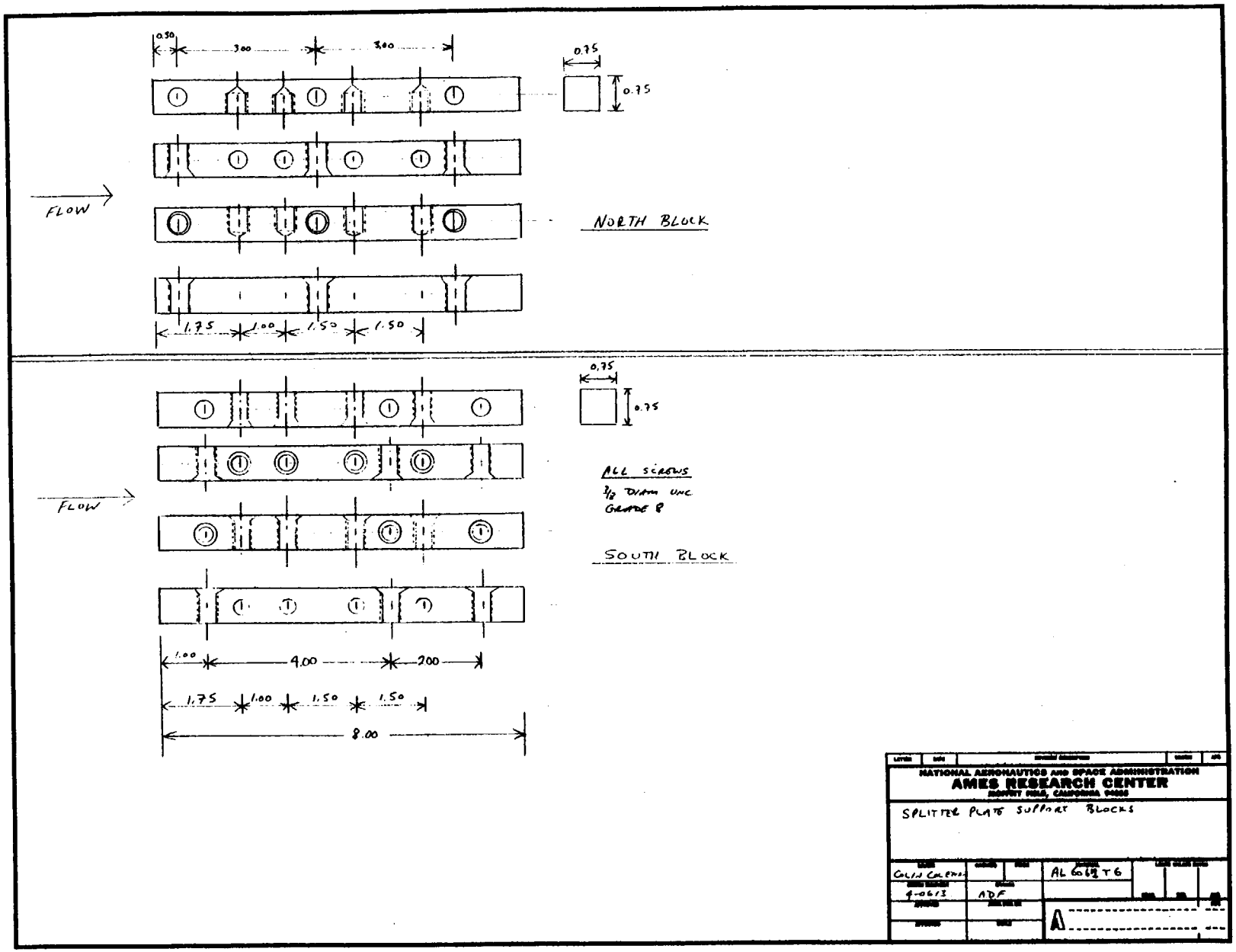

Figure 3-37. Design drawing of splitter plate support blocks.

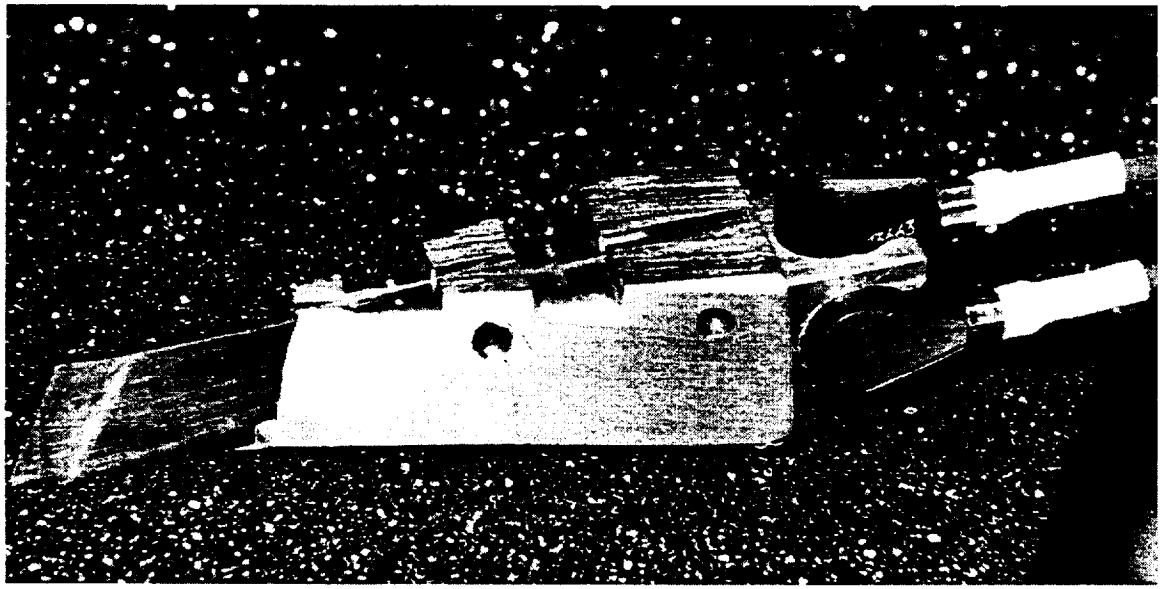

Figure 3-38. Accelerometers mounted on a hot-wire support block.

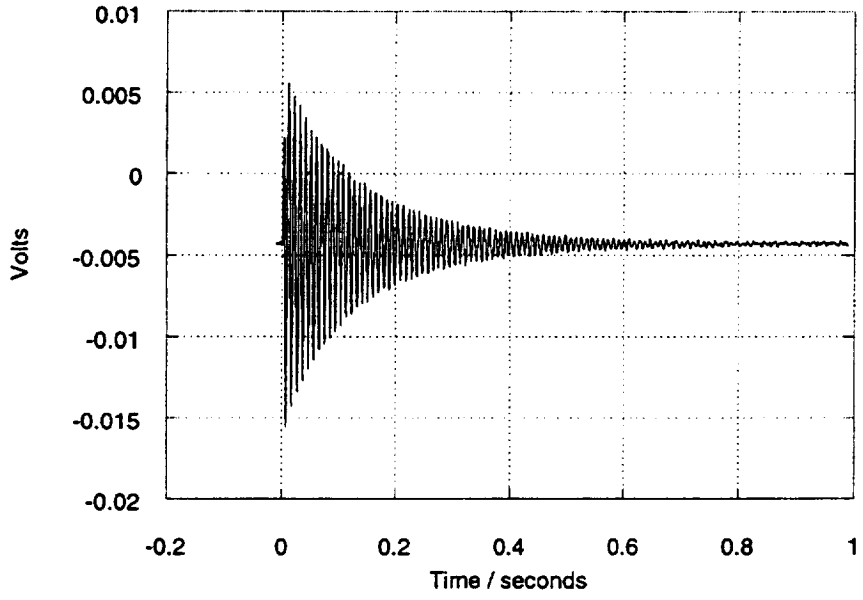

Figure 3-39. Response of vertical accelerometer to vertical blow on model.

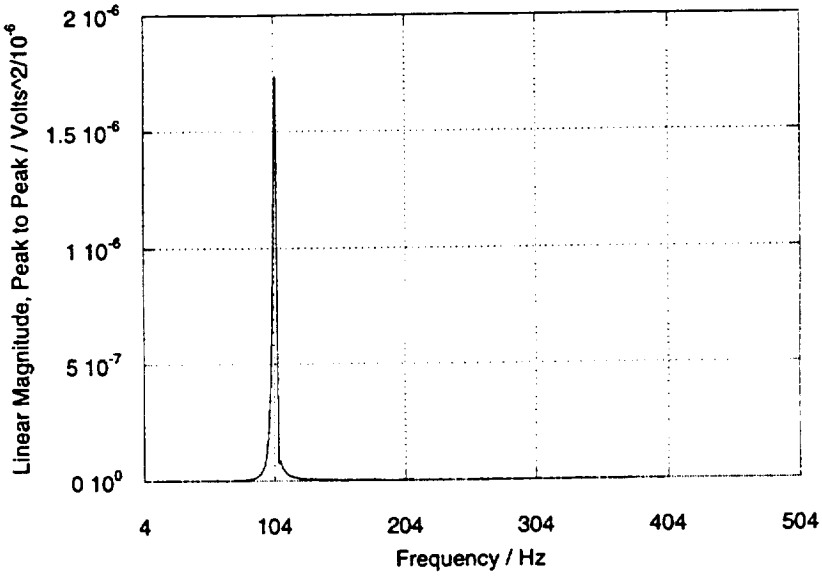

Figure 3-40. Power spectrum of vertical accelerometer due to vertical blow on model.

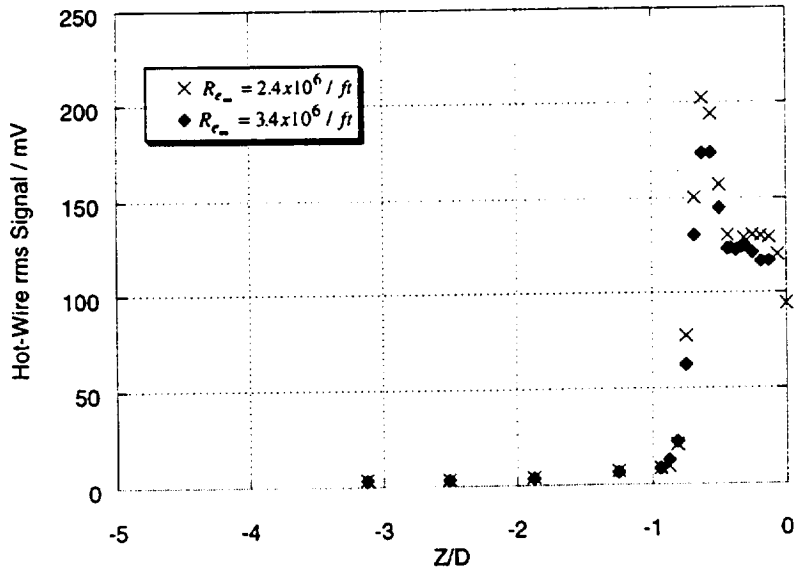

Figure 3-41. Hot-wire traverse of cylinder wake (5.0 microns, 18 inches downstream of apex).

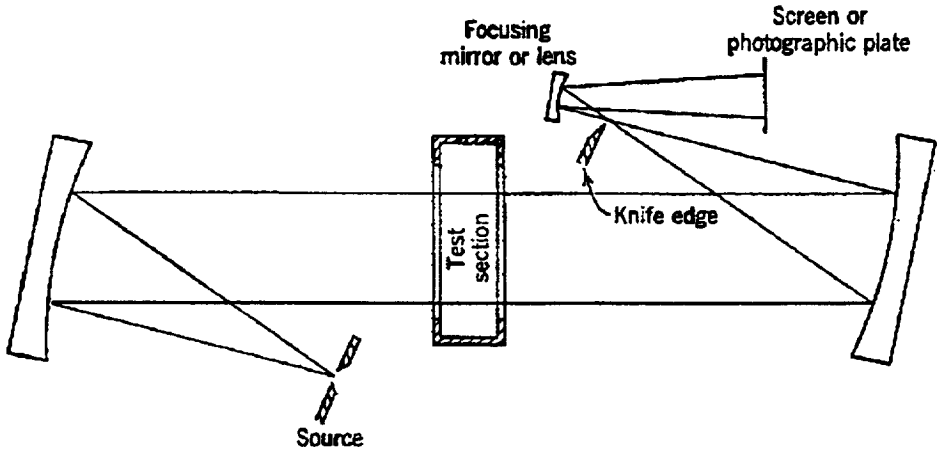

Figure 3-42. Schlieren system with concave mirrors.

Figure 3-43. Schlieren spark source and mirror.

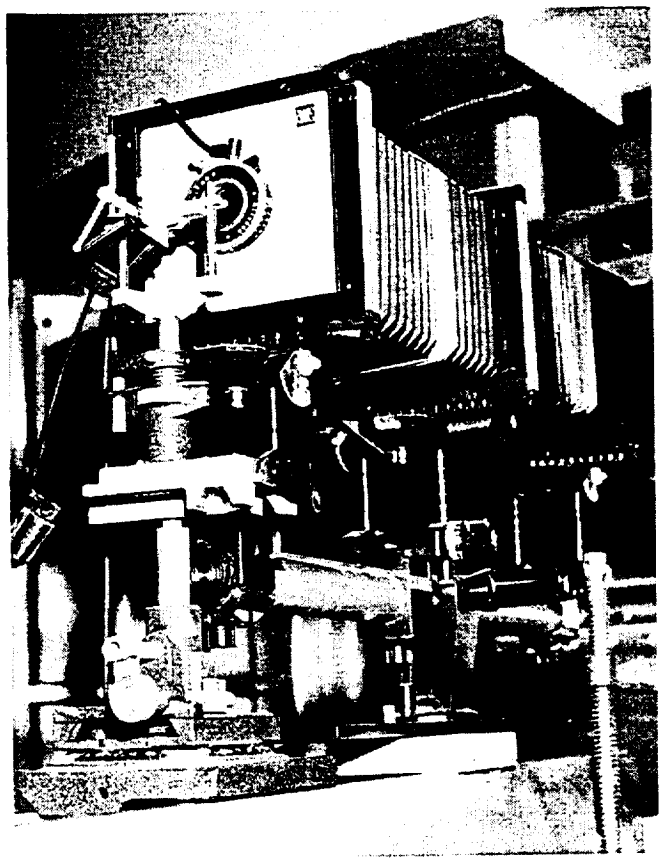

Figure 3-44. Schlieren system knife-edge and optics bench.

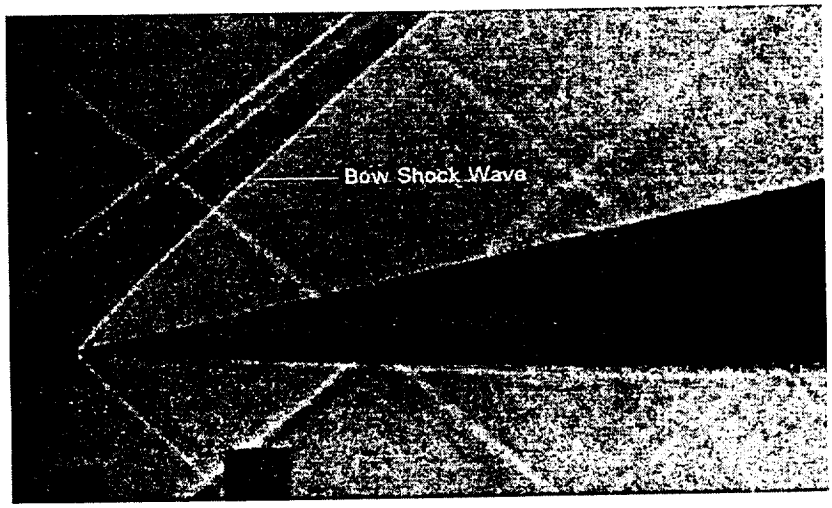

Distance between tapes is approximately 1 inch.

Figure 3-45. Schlieren photography to determine the nature of the bow shock wave. $Re_{\infty} = 2.4 \times 10^6$/ft.

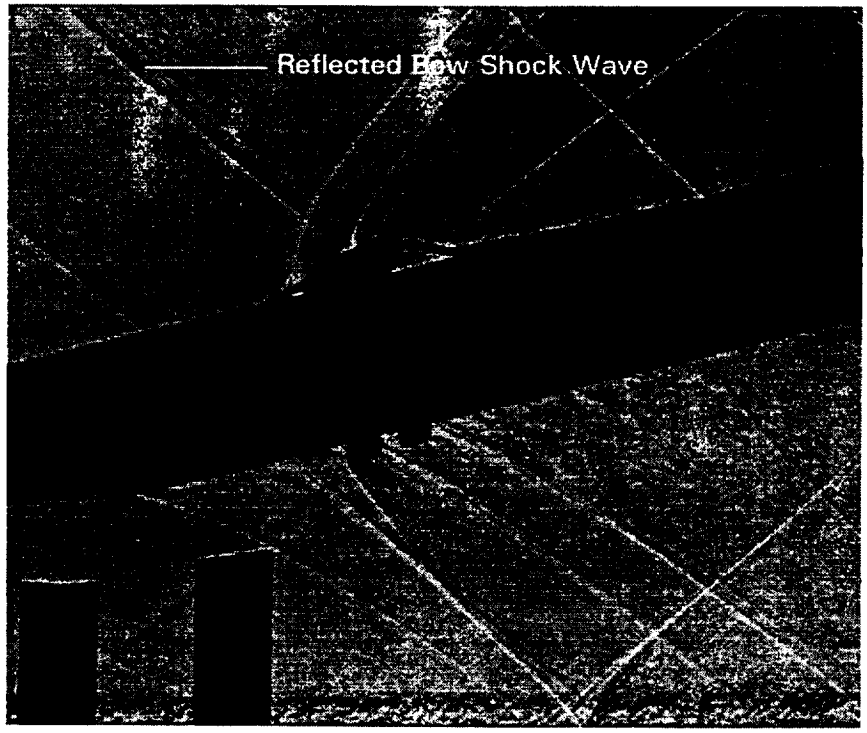

Figure 3-46. The reflected bow shock wave hits the rear of the hot-wire probe body at $y/D = 5.6$. $Re_\infty = 2.4 \times 10^6$/ft. Distance between tapes is approximately 1 inch.

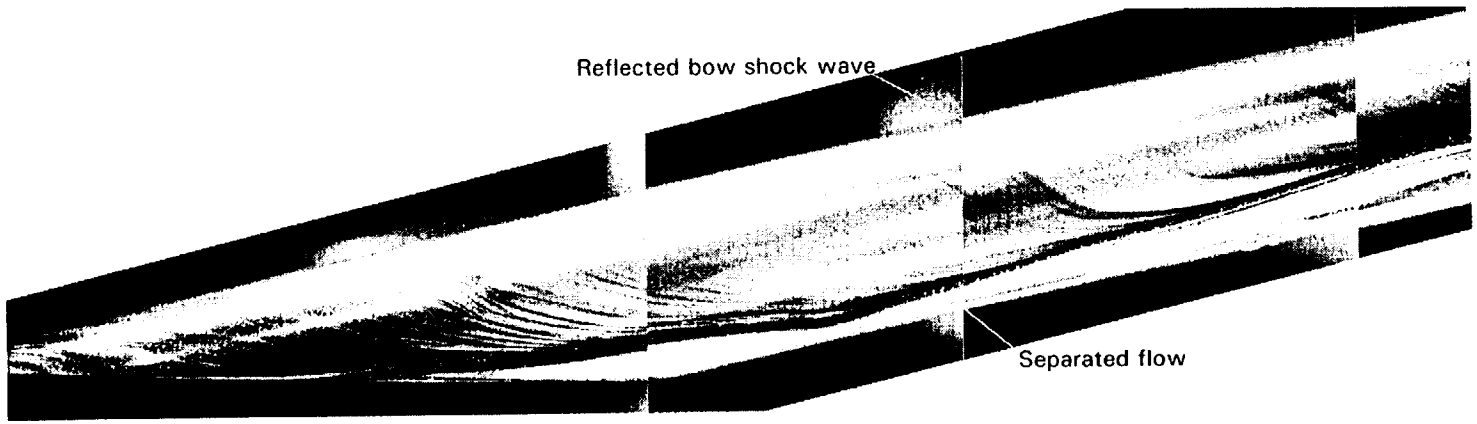

Figure 3-47. Overall flow pattern, showing reflected bow shock wave and stationary crossflow vortices.

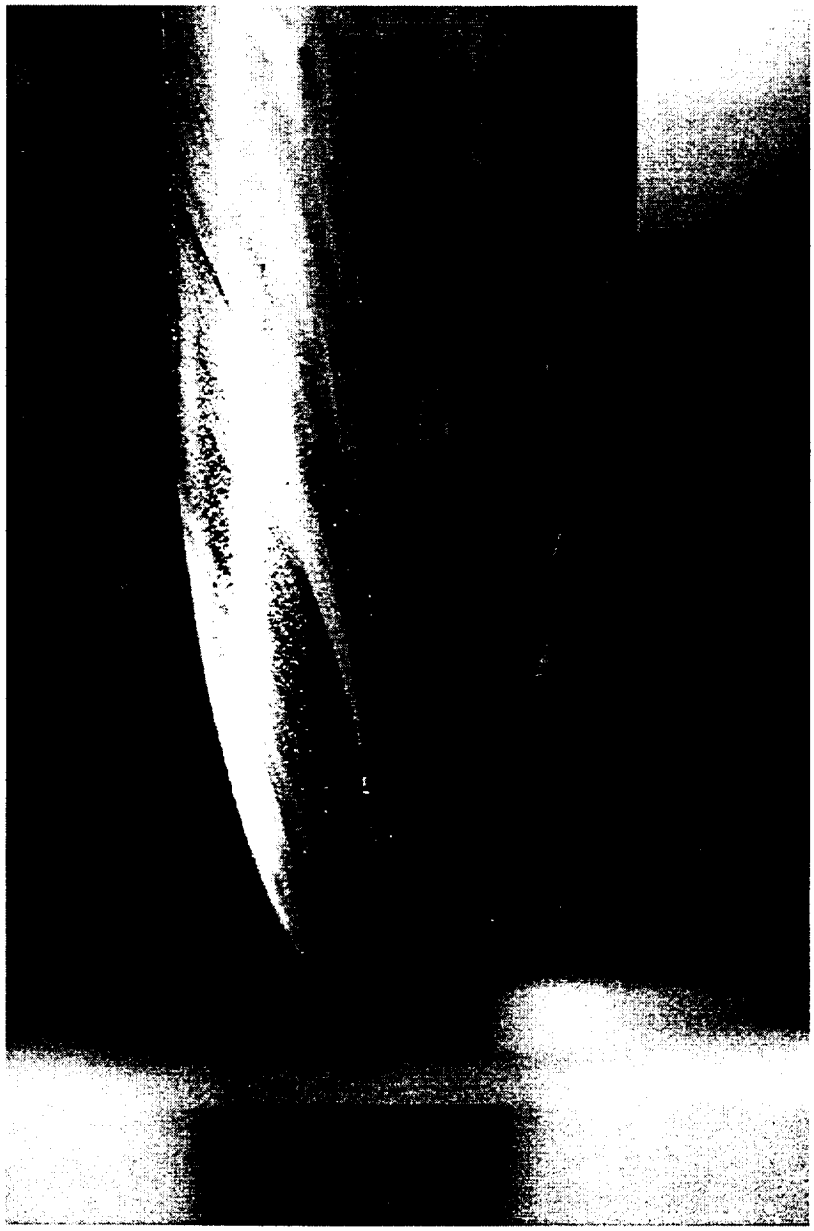

Figure 3-48. Enlarged view of the attachment-line oil flow pattern.

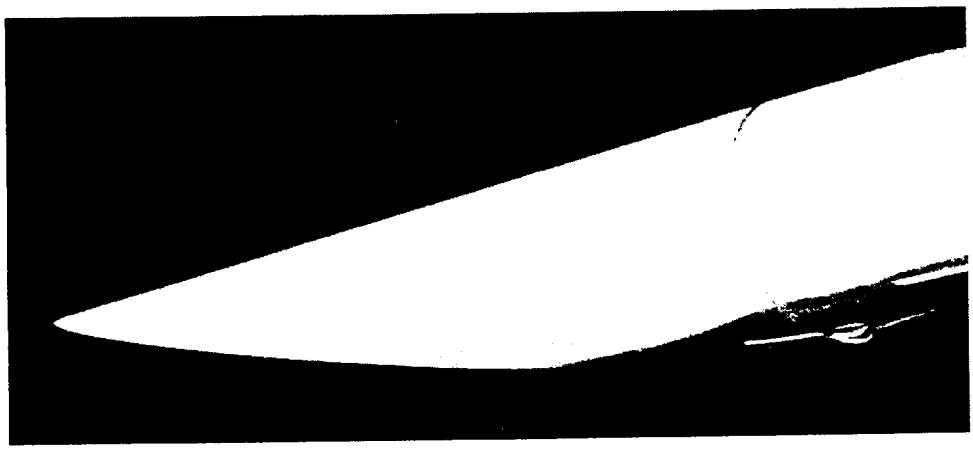

Figure 3-49. Naphthalene before testing with 0.025 inch trip wire.

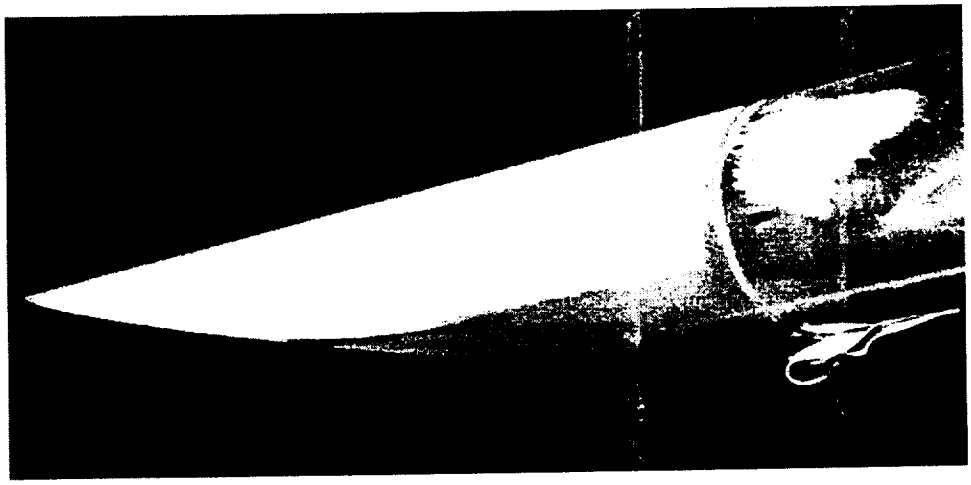

Figure 3-50. Naphthalene immediately after wind tunnel start.

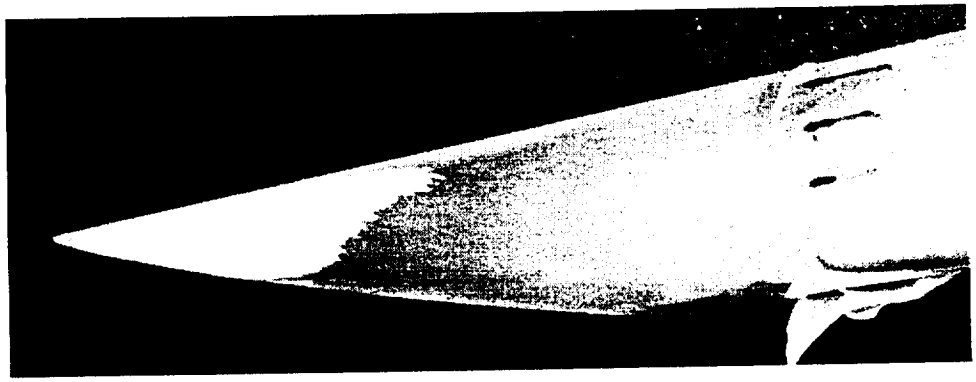

Figure 3-51. Global view of naphthalene after shutdown.

Figure 3-52. Observation of stationary crossflow vortices using the naphthalene sublimation technique.

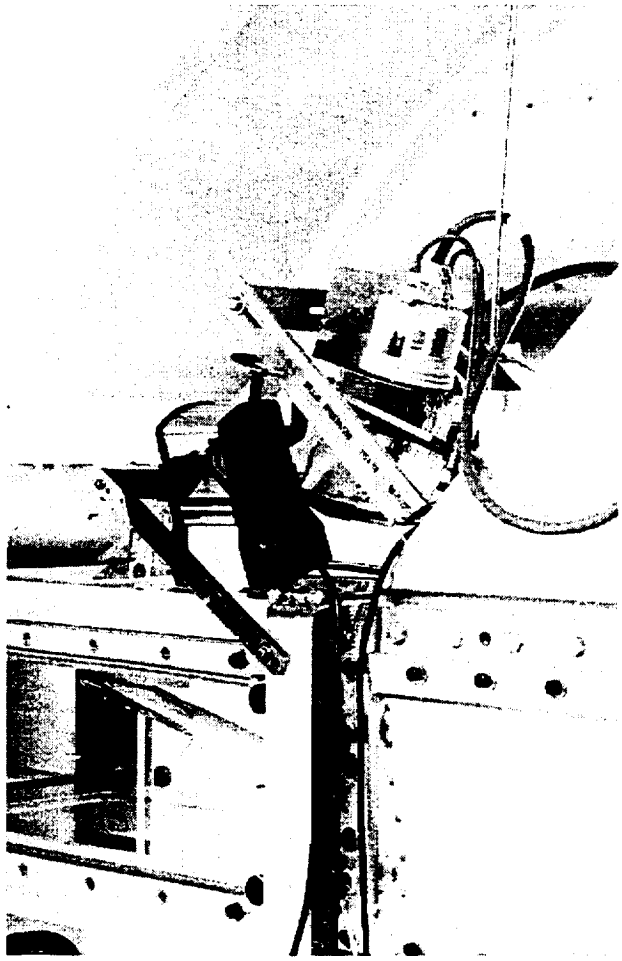

Figure 3-53. Temperature sensitive paint system.

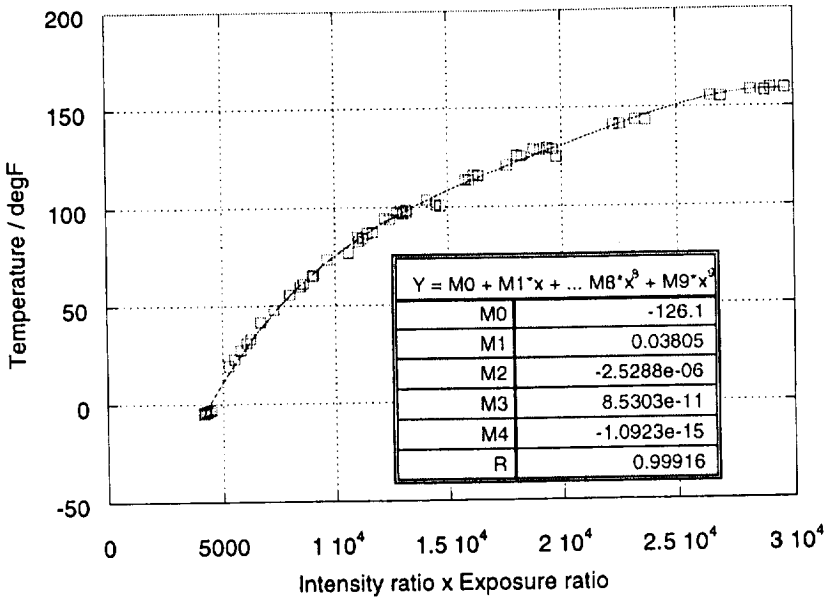

Figure 3-54. All TSP data fall onto a common calibration curve.

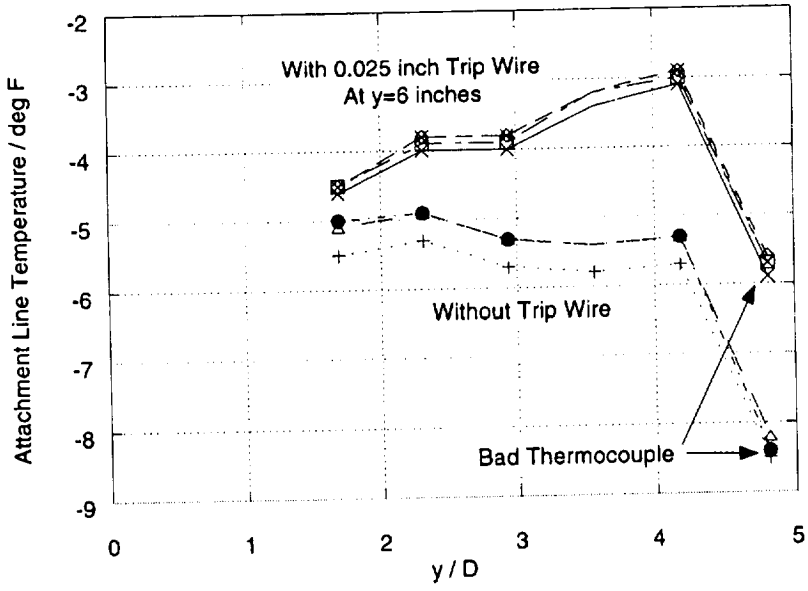

Figure 3-55. TSP feasibility test.

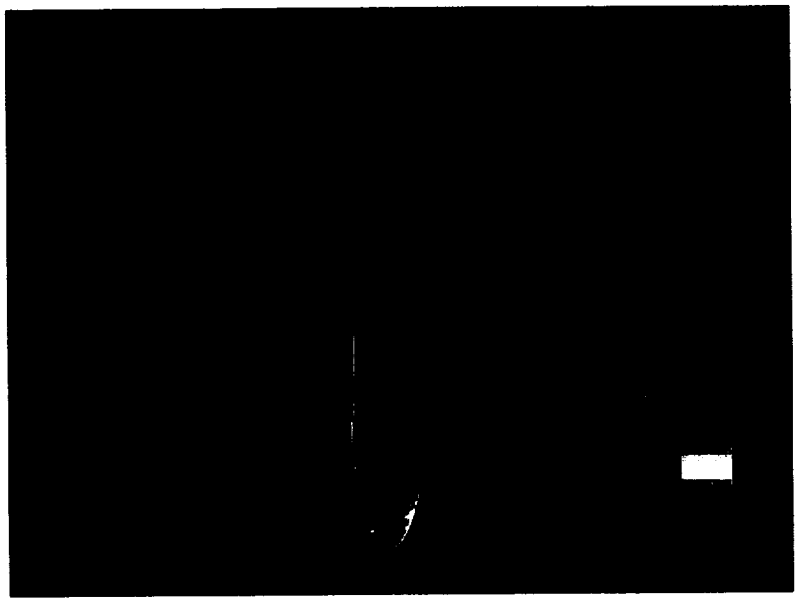

Figure 3-56. Surface temperature distribution for the adiabatic condition (no heating). $Re_\infty = 3.65 \times 10^6$/ft.

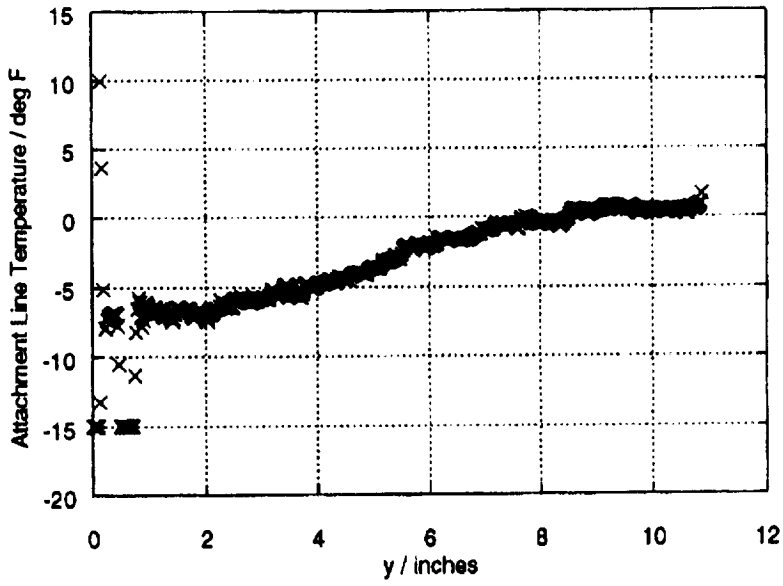

Figure 3-57. Attachment-line temperature distribution for the adiabatic condition (no heating). $Re_\infty = 3.65 \times 10^6$/ft.

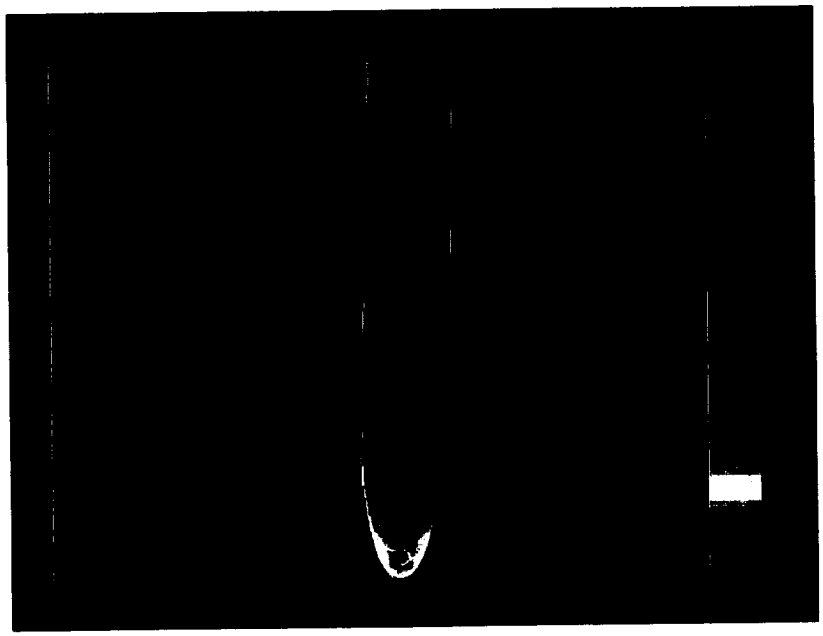

Figure 3-58. Surface temperature distribution for $T_{control}$ = 30°F. Re_{∞} = 3.65 × 10^6/ft.

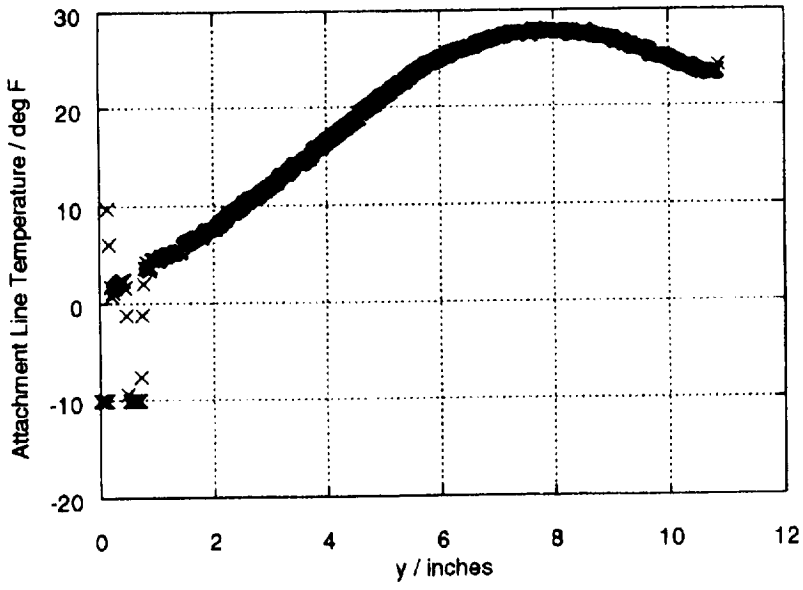

Figure 3-59. Attachment-line temperature distribution for $T_{control}$ = 30°F. Re_{∞} = 3.65 × 10^6/ft.

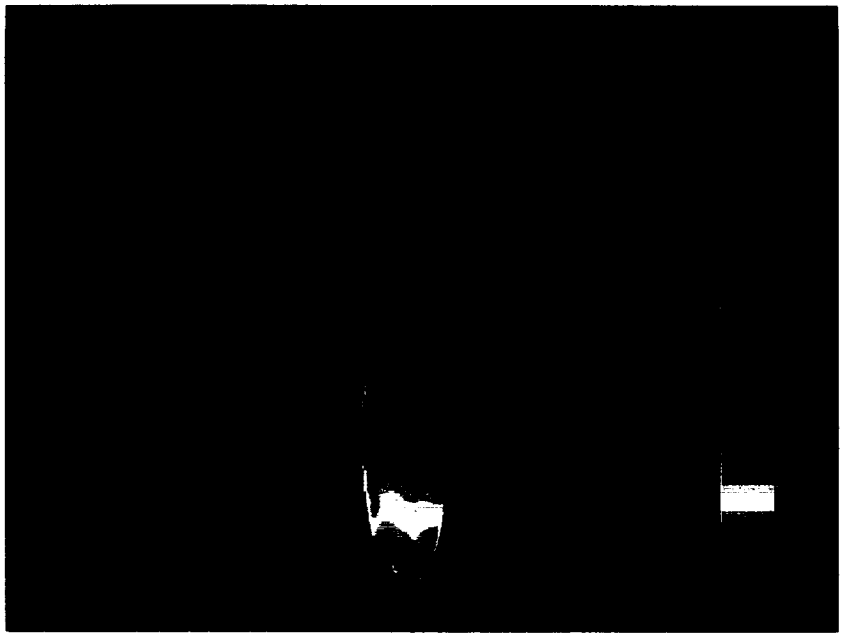

Figure 3-60. Surface temperature distribution for $T_{control}$ = 60°F. Re_{∞} = 3.65 × 10^6/ft.

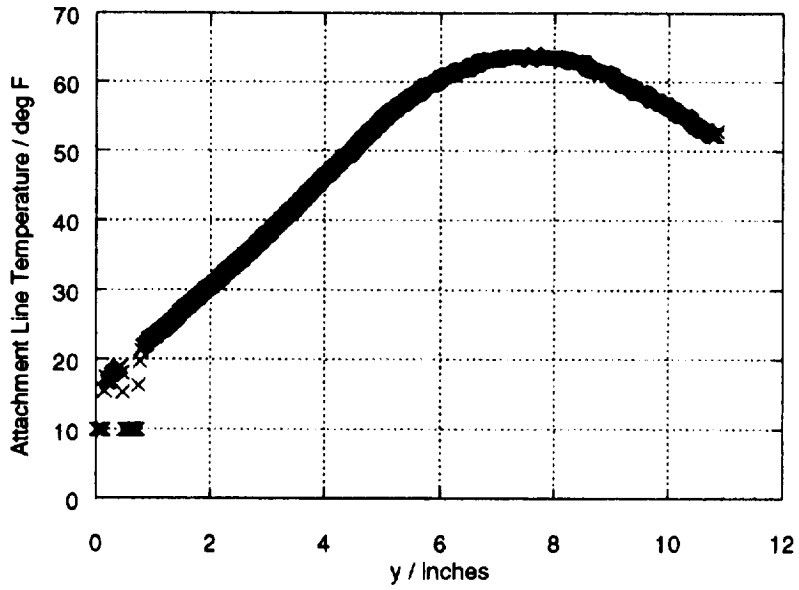

Figure 3-61. Attachment-line temperature distribution for $T_{control}$ = 60°F. Re_{∞} = 3.65 × 10^6/ft.

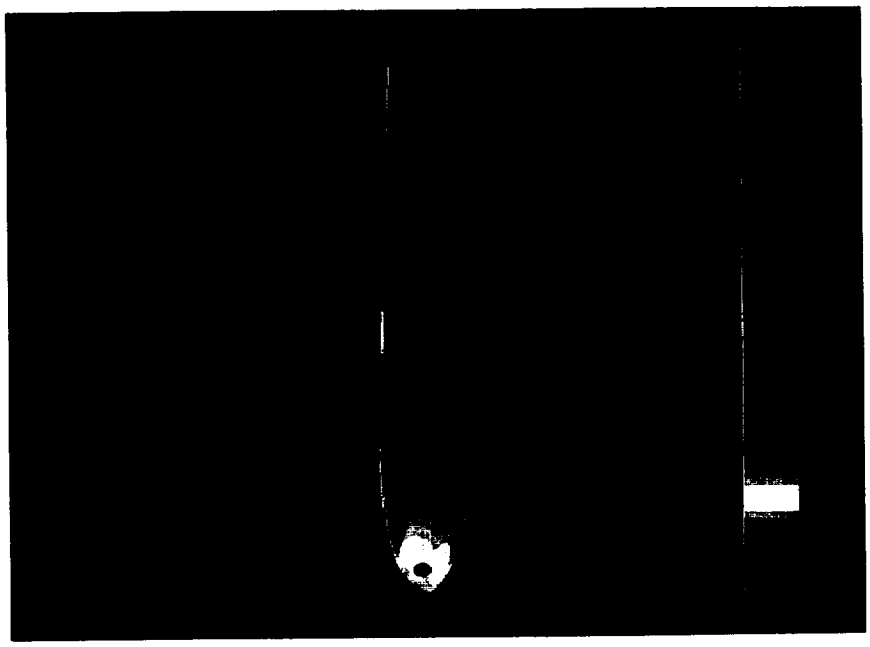

Figure 3-62. Surface temperature distribution for $T_{control}$ = 90°F. Re_{∞} = 3.65 × 10^6/ft.

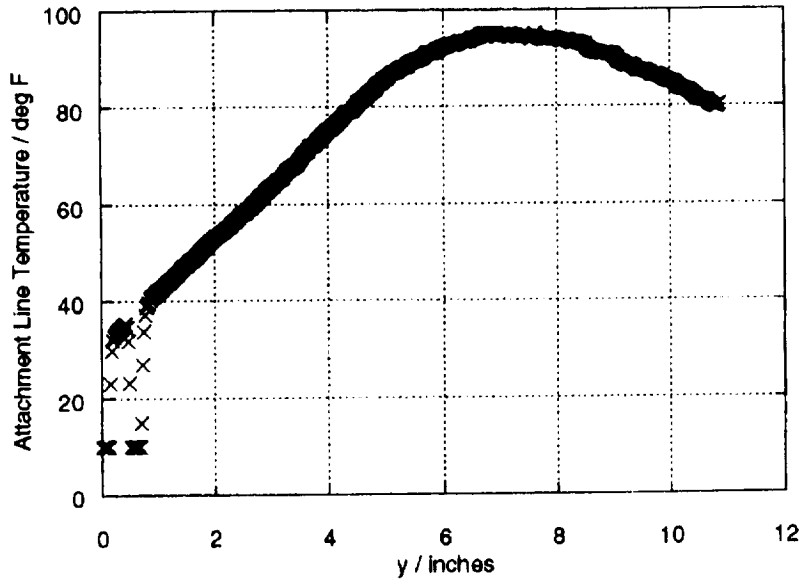

Figure 3-63. Attachment-line temperature distribution for $T_{control}$ = 90°F. Re_{∞} = 3.65 × 10^6/ft.

Figure 3-64. Surface temperature distribution at $T_{control}$ = 120°F. Re_{∞} = 3.65 × 10^6/ft.

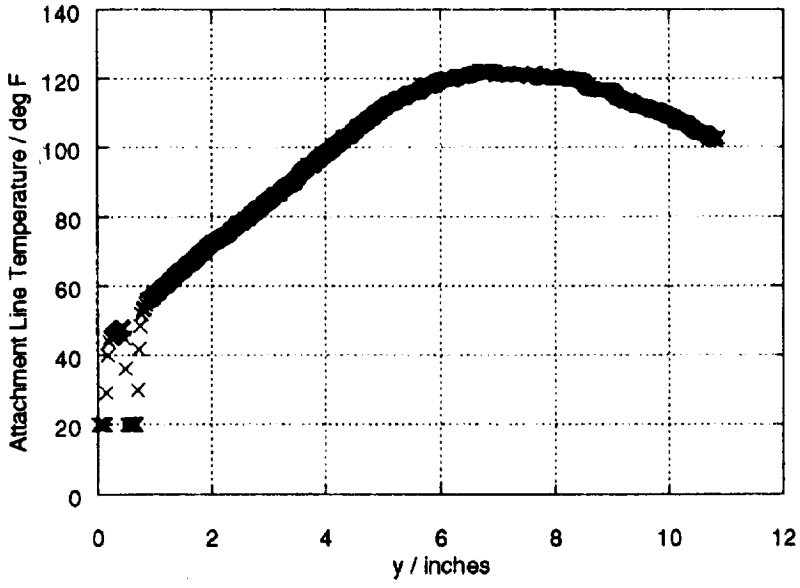

Figure 3-65. Attachment-line temperature distribution for $T_{control}$ = 120°F. Re_{∞} = 3.65 × 10^6/ft.

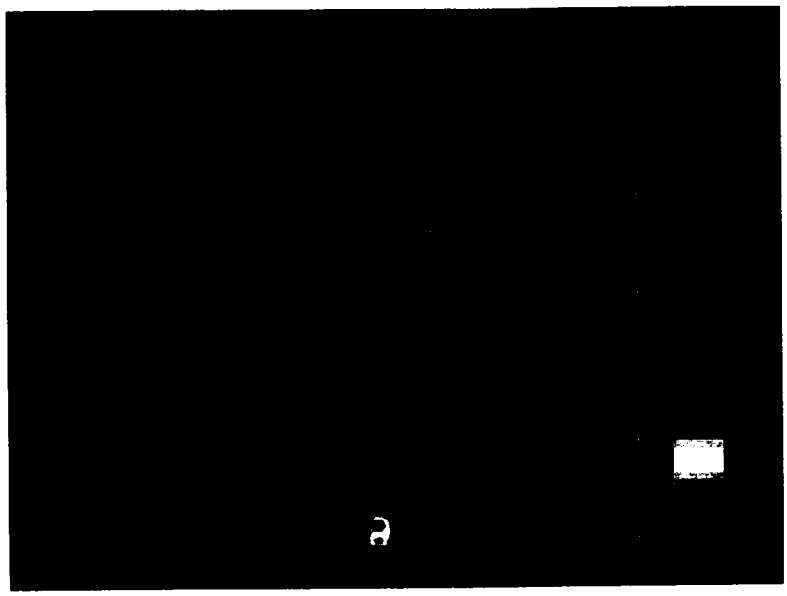

Figure 3-66. Surface temperature distribution for $T_{control}$ = 150°F. Re_{∞} = 3.65 × 10^6/ft.

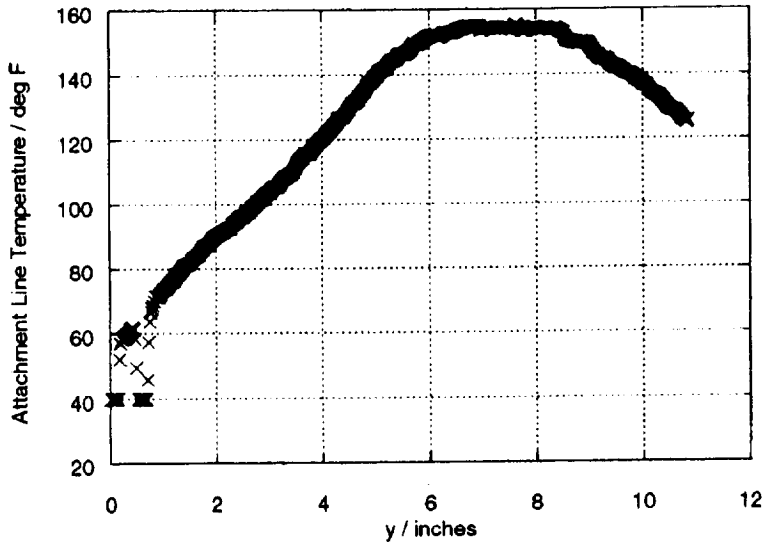

Figure 3-67. Attachment-line temperature distribution for $T_{control}$ = 150°F. Re_{∞} = 3.65 × 10^6/ft.

4. EXPERIMENTAL RESULTS

4.1 Thin-Walled Cylinder

The hot-wire probe was attached to the model and the clean attachment line was studied over the Reynolds number range of the wind tunnel. Two-dimensional disturbances in the form of trip wires were then placed across the attachment line. Laminar, intermittent, and fully turbulent flow were observed over a range of conditions. Based on the CFD-generated values of $\overline{R}$ and η, the tripping criteria were then mapped out on a so-called Poll chart for the quiet tunnel operational conditions. The effect of increased tunnel disturbance level was then considered, and the results were compared with the quiet flow conditions.

4.1.1 Smooth Cylinder Surface

With the hot-wire probe positioned just in front of the reflected bow shock wave, it was found that the "clean" (no trip) cylinder had a laminar attachment-line flow up to the highest Reynolds number available ($\overline{R} \approx 760$ at a distance of $s/\eta = 3300$ from the apex, based on the CFD results in Chapter 2). No turbulence or bursting was seen at equilibrium temperatures.

Bursts were often seen, however, immediately after tunnel start, while the model was still relatively warm. As the model cooled, the amount of bursting (intermittency) decreased until, when the model was fully quenched, no bursting or disturbances were seen. This indicated the destabilizing effect of a warm wall on the boundary layer condition. Since ambient room temperatures were commonly only 70°F above the fully quenched wall temperatures, it was expected that an increase of the wall temperature by 100°F would produce continuous bursting, i.e., transition onset.

4.1.2 Trip Wires Placed on the Model

For these tests, the hot wire was always positioned 8 inches from the apex so as to maximize spanwise test length, and trip wires (from 0.001 to 0.025 inch diameter) were placed at various locations from the tip (from 3.88 to 7.5 inches). The trip wires were attached to the cylinder surface with duct tape in such a way that the tape did not interfere with the attachment-line flow. Figure 4-1 shows a close-up of the hot-wire probe and trip wire attached to the model. On one occasion, the trip wire (0.005 inch) came unstuck from the model. The hot-wire signal immediately went from turbulent to laminar, thus proving that the trip wire was inducing a *convective*, rather than an *absolute*, instability along the attachment line.

4.1.2.1 Testing in a Low Disturbance Level Environment

The placement of variable sizes of trip wire at various distances from the cylinder tip over the Reynolds number range allowed for the observation of laminar, intermittent, and fully turbulent flows. Turbulent hot-wire signals with a characteristic flat power spectrum were obtained with large trip

wires and these differed considerably from the laminar (untripped) signals. Focused Schlieren flow visualization of the attachment-line boundary layer was attempted to corroborate this information (fig. 4-2). This provided an estimate of the boundary layer thickness (laminar 0.007 inch and turbulent 0.025 inch) and also showed the shock wave structure that formed on the hot-wire probe. (Note that the BL3D solution gave a laminar boundary layer thickness of 0.009 inch.) Clearly seen are the shock waves emanating from the hot-wire element, a crossbar that joins the two needles, and the main body of the probe.

During one test, in which a 0.009 inch trip was placed at 6.5 inches from the tip with the hot wire at 8.0 inches, laminar, intermittent, and fully turbulent flows were observed with increasing Reynolds number (fig. 4-3). (Note the factor of 10 difference in scale for the laminar spectrum.) The observation of turbulent flow was accompanied by a rise in measured recovery factor from 0.864 to 0.880. The high voltage level of the intermittent signal is due to the wide range of disturbance frequencies and their associated energies that are contained within the bursts. A 5% intermittency (first appearance of bursts) was used as a threshold for the definition of transition onset.

Figure 4-3 also shows that the hot-wire system used in these tests had a frequency response of approximately 50 kHz, as seen by the roll-off of the frequency spectrum. This low response was due to the fact that the FML CTA unit was used for these tests. This was sufficient in order to define the gross nature of the boundary layer, i.e., laminar or turbulent, but would not be sufficient for the resolution of boundary layer disturbances.

Results were plotted against several nondimensional parameters which were extracted from the CFD solution at the appropriate spanwise location along the attachment line. Note that Re_k is based on boundary layer edge conditions.

The tripped flow results are shown in figures 4-4 through 4-6. Figures 4-4 and 4-5 show that the trip Reynolds number for this Mach 1.6 flow appears to be just below 1900. This can be compared with the critical trip Reynolds number for a flat plate with an adiabatic wall in supersonic flow, as summarized by Gibbings (ref. 123):

Flat plate Mach number	Re_k
0.0	850
2.0	2,000
4.0	10,000

Figure 4-6 displays the results as $\overline{R}$ versus k/η as proposed by Poll (ref. 10). A transition onset boundary, offset from previous results, is evident. In an attempt to collapse the data to an incompressible form, Poll proposed that a modified Reynolds number ($\overline{R}_*$) be used which evaluates the boundary layer parameters at the reference temperature condition, and this is shown in figure 4-7 (refs. and 125).

The first thing that strikes the observer is the apparent shift to higher k/η of the transition onset boundary. At the time these measurements were made, it was not known whether the CFD-generated values of $\overline{R}$ and η were correct. However, later tests conducted with the pressure model (Section 4.2) confirmed the values of $\overline{R}$ and η used in these plots, thus proving that the location of the data with respect to the chart axes was accurate. Therefore, the apparent shift of the transition onset boundary could be attributed to the low disturbance testing environment. Increased wind tunnel disturbance levels have been shown to have a marked effect on the location of the onset of transition, as observed by Creel (ref. 65).

Disturbances in the boundary layer were detected when the hot wire was placed 0.5 inch behind a 0.009 inch trip ($\overline{R}$ = 760, s/η = 204, and k/η = 3.67). When the Reynolds number was increased from $\overline{R}$ = 660 to $\overline{R}$ = 760, a broad-peak curve appeared in the frequency spectrum. As can seen in figure 4-8, the central frequency of this curve is located at 41 kHz, with the edges of the curve at roughly 37 and 44 kHz. At first it was thought that this curve might be due to the natural disturbances of boundary layer. However, later investigation with the heated cylinder model (Section 4.3) seemed to suggest that this curve was a characteristic of the flowfield of the trip wire and a consequence of the way in which the trip wire inserts disturbances into the flow.

4.1.2.2 Testing in a Raised Disturbance Level Environment

Increased wind tunnel disturbance levels have been shown to have a marked effect on the location of the onset of transition, due to the receptivity mechanism which makes the attachment line more sensitive to freestream disturbance levels. To test this hypothesis, an attempt was made to increase the noise level in the Mach 1.6 Quiet Tunnel to a critical level. When the tunnel was "clean" and a 0.005 inch diameter trip wire was placed on the cylinder at 4 inches from the apex, the recorded signal at y = 8 inches was laminar ($\overline{R}$=760, k/η=2.04). Size 80 grit sandpaper of 0.025 inch height was then placed on the upper and lower walls near the nozzle exit such that the shock waves produced by these trips passed in front of the apex, reflected off the opposite tunnel walls, and impinged on the model aft of the hot-wire probe location (trailing edge of 1/2 inch wide upper wall trip tape 2 inches forward of test section/nozzle join; trailing edge of lower wall trip tape 1/2 inch behind test section/ nozzle join). Intermittent bursts were then observed under these conditions, thus proving that the increased levels of tunnel disturbances hasten the transition to turbulence in the presence of a trip wire. These results are consistent with the observations of Creel (refs. 65–67). Further investigations are required to correlate the relationship between the tunnel disturbance level and the height of wall trips in this location.

4.2 Cylinder with Pressure Taps

4.2.1 Surface Pressures

Surface pressures obtained during the second test of the pressure model were acquired from $Re_\infty = 2.4 \times 10^6$/ft to $Re_\infty = 3.4 \times 10^6$/ft in 0.2×10^6/ft intervals. Chordwise pressure plots revealed that the true attachment line was offset 1.4° from the geometric coordinate system. (A later inspection

found that the two attachment bolt holes were misaligned by the same amount.) Corrections were made so that chordwise plots were consistent with the true aerodynamic attachment line. Plots such as figure 4-9 revealed no variation in the *Cp* distribution due to Re_∞.

Figure 4-10 shows the complete *Cp* distribution over the swept cylinder at Mach 1.6. The experimentally obtained *Cp* distribution along the attachment line is compared with the CFD solution in figure 4-11. The two distributions have the same qualitative form, and seem to be asymptoting toward the swept-infinite *Cp* value of 0.061 at large y/D. A weak pressure gradient along the cylinder is evident.

4.2.2 Comparison of dU_e/dx with Other Swept Cylinders in Supersonic Flow

Poll (ref. 114) surveyed a large quantity of pressure data for two dimensions and long, swept circular cylinders with normal to leading edge Mach numbers in the range 1.3 to 13 and derived expressions which described the variation of velocity gradient with the normal to leading edge Mach number. He defined the chordwise surface static pressure distribution as:

$$f \equiv \frac{p_e(\theta)}{p_A}$$

where $\theta = 0$ corresponds to the attachment-line conditions (subscript A). Differentiating twice with respect to θ:

$$\frac{1}{a_A}\left(\frac{dU_e}{d\theta}\right)_{\theta=0} = \left\{-\frac{1}{\gamma}\left(\frac{d^2 f}{d\theta^2}\right)_{\theta=0}\right\}^{1/2} = \left\{-\frac{1}{\gamma} f''(0)\right\}^{1/2}$$

This was cast as:

$$\left(\frac{d(U_e/U_\infty)}{d\theta}\right)_{\theta=0} = \left\{-\frac{p_A}{\rho_A U_\infty^2} f''(0)\right\}^{1/2}$$

Hence, for swept-infinite cylinders, plots of $f''(0)$ versus normal to leading edge Mach number would demonstrate any Mach number dependency of the chordwise velocity gradient. The fifth-order velocity curve fit for $Re_\infty = 2.4 \times 10^6$/ft at $y = 5.7$ inches was used as a typical example. It was found for this case that $f''(0)) = -0.576$, which is plotted in figure 4-12 along with the incompressible result ($f''(0) = 0$). As can be seen, these data show that the chordwise velocity gradient for swept cylinders is not independent of the Mach number normal to the leading edge for values below 2.0. This therefore demonstrates that attachment-line transition is sensitive to the Mach number normal to the leading edge through the chordwise velocity gradient term.

4.2.3 Experimentally Obtained Values of $\overline{R}$

Following the procedure outlined in Chapter 3, velocity curve fits were obtained from the pressure data. Figure 4-13 shows the experimentally obtained $\overline{R}$ distribution at $Re_\infty = 2.4 \times 10^6$/ft and 3.4×10^6/ft compared to the CFD results. It can be seen that these values are higher, but are still within 10% of the CFD solution. For the purposes of plotting results, the experimental values were used.

4.3 Internally Heated Cylinder

4.3.1 Testing in a Low Disturbance Level Environment

For this series of tests, the heated cylinder model was mounted in the forward position. Both the interior walls of the wind tunnel and the surface of the model were kept as clean as possible in order to avoid contamination of the results.

An attempt was first made to capture a turbulent attachment-line boundary layer with heating, using just the global Schlieren system. Unfortunately, a clearly defined turbulent boundary layer was not apparent upstream of $y = 8$ inches (fig. 4-14). However, the region where the reflected bow shock wave impacted the cylinder offered some interesting images. As the surface temperature of the model was increased, small amounts of turbulence could just be seen (fig. 4-14).

4.3.1.1 Observation of Instability Waves with Increasing Surface Temperature

Most of the heated cylinder runs were made with a fixed-position hot wire, and the transition front was moved upstream toward the tip by increasing the control temperature.

Figures 4-15 through 4-17 show a typical output signal for a hot wire positioned at $y/D = 4.4$ at three different control temperature settings. As heating was applied, perturbations in a nominally laminar flow (fig. 4-15) were seen to increase in amplitude, with well defined modulated wave packets being observed at a control temperature setting of 110°F (fig. 4-16). As the heating was increased further, the amplitude of the waves was seen to increase until large amplitude turbulent fluctuations were observed with no discernible wave packets (fig. 4-17). A point of note here is that, as heating was increased, no bursts were seen at this wire location but, rather, a direct move from "laminar" flow (with very high amplitude waves) straight into turbulent flow.

The power spectra of these signals are seen in figures 4-18 and 4-19. As heating was applied, a "bulge" appeared in the spectrum centered at 70 kHz with limits of 100 and 40 kHz (fig. 4-18). Just as this bulge appeared, the oscilloscope displayed the modulated sinusoidal waveform associated with the most amplified wave and thus provided an independent verification of the frequency of the most amplified disturbance (set to trigger at packet onset). This bulge is indicative of wave packets, such as seen with T-S waves along flat plates, and is the envelope of all detectable amplified disturbances.

Further heating caused the bulge to grow and the overall rms level to rise (fig. 4-19), until a point was reached when the amplitude associated with the most amplified disturbance began to fall. This occurred for a control temperature in excess of 210°F, at which point no further heating was applied. Operating at a lower Reynolds number caused this amplification effect to occur at a higher wall temperature.

An attempt was made to use two hot wires simultaneously, but this arrangement generated mutual interference effects and the wave angles were not determinable.

4.3.1.2 Capture of Transition Front Along Attachment Line

Rather than drive the transition front over a fixed hot wire with increasing surface temperature, it was desired to obtain a transition location for a fixed surface temperature distribution (as seen by a rise in the hot-wire rms signal). This would provide unique transition data for future stability calculations. Due to the narrow y/D range over which the hot wire could be attached to the cylinder, it was necessary to find the appropriate conditions which would cause the transition front to be positioned at approximately $y = 7$ inches. A simple traverse was devised which pulled the probe support block back along the model using wires attached to the plastic ties that held the hot wire to the model. For these runs, the temperature ratio T_w / T_0 would have to remain approximately constant.

Figure 4-20 shows the results of one such run at $Re_\infty = 3.56 \times 10^6$/ft with a control temperature of 125°F. The onset of transition is seen to occur around $y/D \approx 4.3$. The surface temperature distribution, with $T_0 = 13$°F, was as follows:

y/D	T_w/°F
1.69	104
2.31	120
2.93	140
3.56	148
4.19	145

The power spectra of these signals are seen in figure 4-21. As the hot wire was pulled back along the attachment line, the amplitude of the boundary layer disturbances increased and a bulge in the frequency spectrum appeared. The sharp, well-defined peak at 65 kHz was presumed to be caused by a structural vibration mode of the hot wire.

4.3.1.3 Crossflow Investigation

To investigate the chordwise boundary layer under adiabatic wall conditions, a hot wire was traversed away from the attachment line at $y/D = 3.98$ and $\overline{R} = 680$ (fig. 4-22). Since no traverse mechanism was available, this was accomplished in several start-and-stop operations. As can be seen, the rms voltage rises quickly around 25° and peaks around 40° before falling back to a near-constant level at 50° or above, which is very characteristic of a laminar-transitional-turbulent process (ref. 126). This also agrees with the napthalene sublimation results. Figure 4-23 shows the power spectrum for this traverse, and indicates a laminar boundary layer up to $\theta = 20°$, with a marked transition to a turbulent boundary layer around $\theta = 30°$ to 40°. To further investigate this, the hot wire was traversed in the chordwise direction at $y/D = 3.59$, 4.30, and 4.92. At all three stations, it was found that the $\theta = 30°$ signal was always at least intermittent, while the $\theta = 20°$ signal was always laminar. Hence, for an adiabatic wall, there was always a laminar attachment line with a transition occurring by $\theta = 30°$, presumably due to crossflow instability. Traverses on both sides of the model produced the same results, thus proving that the cylinder was aligned correctly in the flow, with no off-centerline surface irregularities that would cause asymmetry of the results.

Several runs were made with surface heating while the hot wire was traversed in the chordwise direction at $y/D = 3.59$, 4.30, and 4.92. All three locations exhibited the same behavior. Figure 4-24 shows one such result at $\theta = 20°$, which looks very similar to the attachment-line behavior, with the familiar bulge appearing out of a background signal typical of a laminar boundary layer. At $\theta = 30°$, however, the boundary layer was nominally intermittent-turbulent, and high levels of surface heating were required before the bulge could be made to appear (fig. 4-25). One can therefore conclude that heating had no detectable effect on the crossflow instability, and only when the attachment line exhibited large amplitude disturbances did the crossflow instability signal change.

4.3.2 Testing in a Raised Disturbance Level Environment

In order to see whether the transition mechanism along the attachment-line boundary layer was sensitive to acoustic noise, trips were fitted to the wind tunnel walls (as described in Chapter 3). The model was mounted in the rear testing position. Schlieren photography (fig. 4-26) revealed that the weak shock wave emanating from the upper wall trip passed just ahead of the tip of the model, thus ensuring that the attachment line was irradiated with noise from turbulent boundary layers on both the upper and side walls. (Note that since the wave emanating from the upper wall trip is not parallel to the Mach wave emanating from the tunnel wall joins, we know that the trip is casting off a shock wave of finite strength.)

4.3.2.1 Observation of Instability Waves with Increasing Surface Temperature

The hot wire was positioned at $y/D = 4.02$ and heating was applied in a similar manner as for the quiet tunnel tests. Figure 4-27 shows the power spectra results for $\overline{R} \approx 780$. The overall trend is very similar to that under quiet conditions (fig. 4-18) with a wider range of frequencies being amplified for the same heating levels.

4.3.2.2 Capture of Transition Front Along Attachment Line

The hot wire was then traversed along the model in the y-direction in order to locate a transition onset front. With $T_{control}$ = 90°F and $Re_{\infty} = 3.36 \times 10^6$/ft, a front was located at $y / D \approx 4.3$ as shown in figure 4-28. Its shape and location coincided with the transition front found for the quiet tunnel case. Therefore, the lower wall temperatures effectively pushed the transition front away from the tip, but was counteracted by the increased noise level in the tunnel which pushed it back toward the tip. (In the this case, the wall temperature distribution was lower than for the quiet tunnel results, 80–110°F versus 100–150°F, respectively. Moreover, the adiabatic T_{wall} was –10°F for the quiet case and 10°F for the noisy case. Therefore, the ratio of $T_{wall} / T_{wall(adiabatic)}$ in absolute terms was much lower for the noisy case compared to the quiet case, 1.15 to 1.21 versus 1.24 to 1.36, respectively.)

Figure 4-29 shows the frequency spectra for this traverse, which also seem to follow that of the quiet tunnel results, except that a given spectrum shape occurred at lower wall temperatures, as mentioned above.

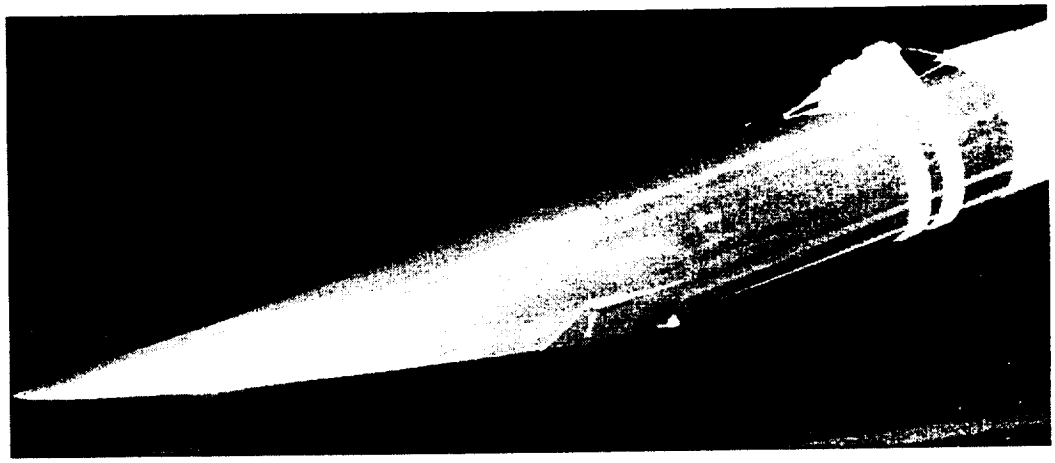

Figure 4-1. Enlarged view of the hot-wire probe and trip wire attached to the model.

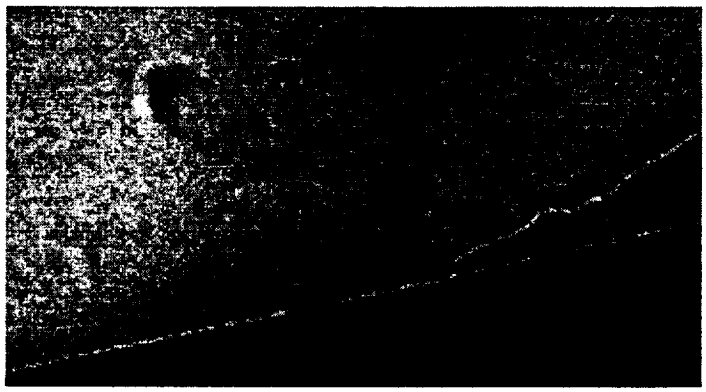

Wind off.

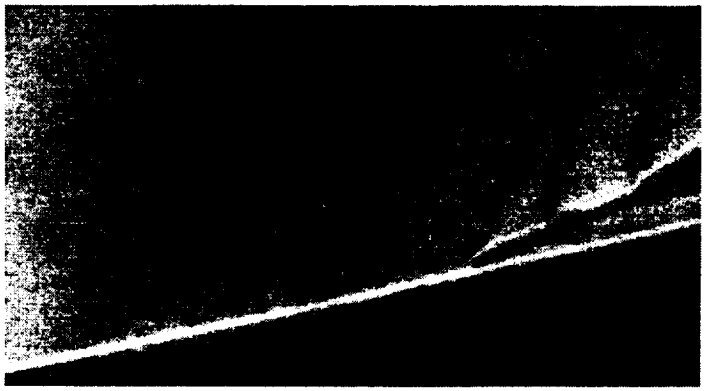

Laminar flow. No trip, $\overline{R} = 760$.

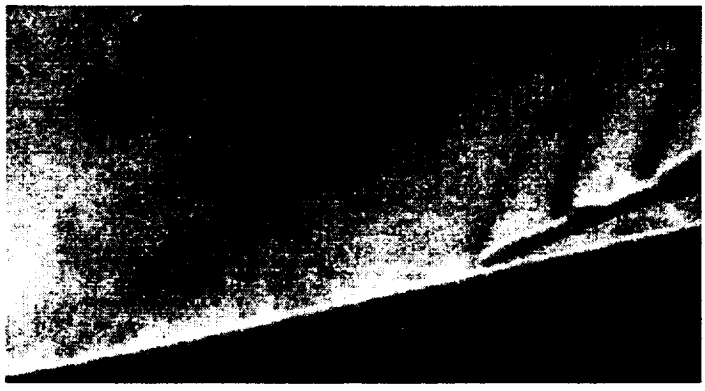

Turbulent flow. 0.025 inch trip wire at $y/D = 4.22$, $\overline{R} = 760$.

Figure 4-2. Attempted focused Schlieren photography of the attachment-line boundary layer, showing the difference between laminar and turbulent cases. Hot wire at $y/D = 5.00$.

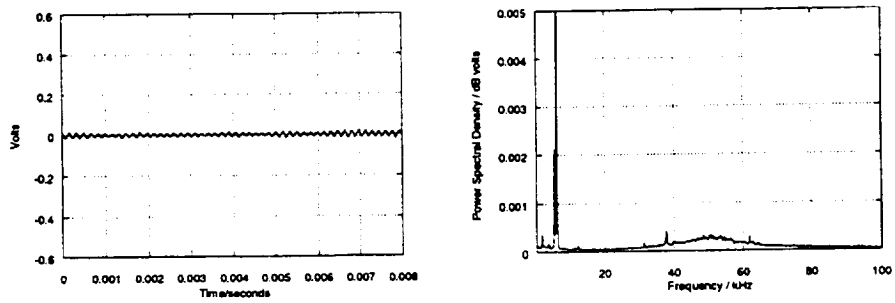

Laminar flow.

$\overline{R}$ = 596 ($\overline{R}_*$ = 480), Re_k = 1896, k/η = 3.10, s/η = 517, r = 0.864. rms = 7 mV.

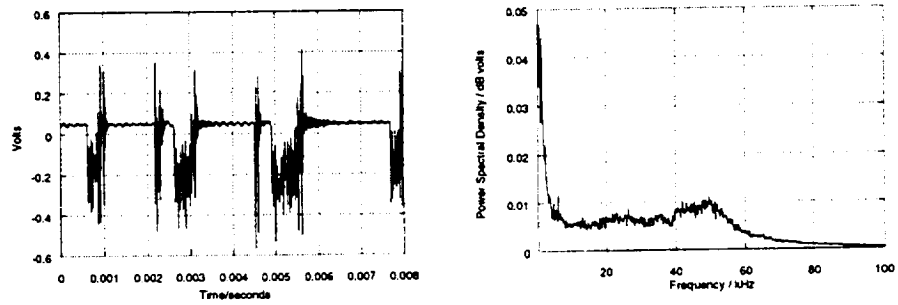

Intermittent flow (intermittency ≈ 40%).

$\overline{R}$ = 657 ($\overline{R}_*$ = 529), Re_k = 2292, k/η = 3.42, s/η = 570, r = 0.868. rms = 121 mV.

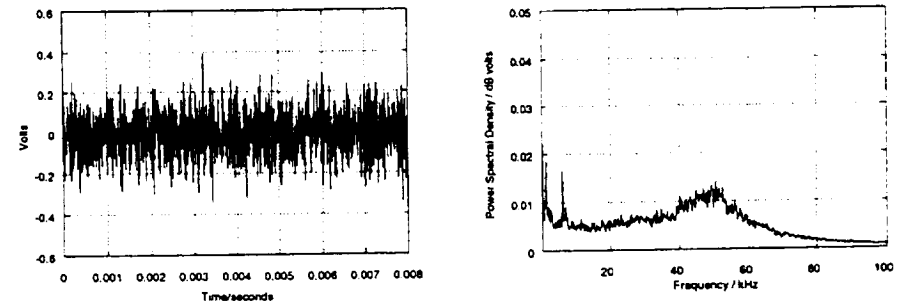

Turbulent flow (intermittency ≈ 100%).

$\overline{R}$ = 700 ($\overline{R}_*$ = 560), Re_k = 2636, k/η = 3.63, s/η = 605, r = 0.880. rms = 98 mV.

Figure 4-3. Observation of laminar, intermittent and turbulent flow with a 0.009 inch trip wire at y = 6.5 inches.

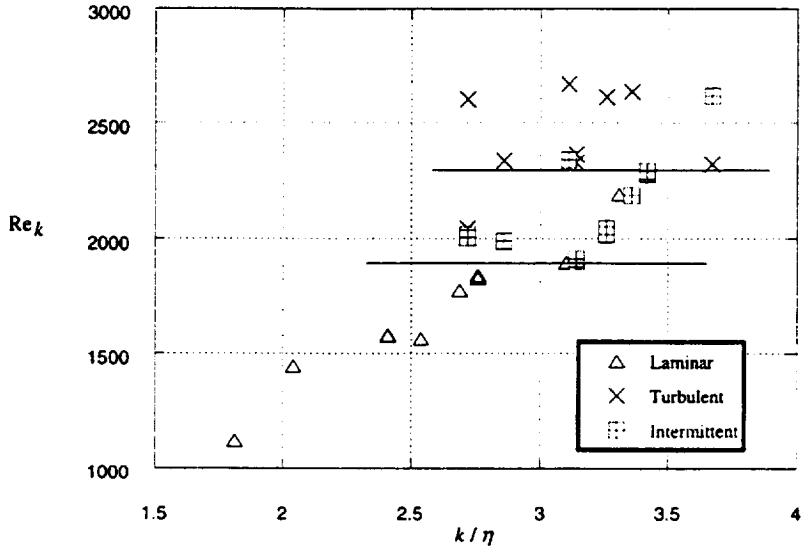

Figure 4-4. Trip wire Reynolds number as a function of nondimensional trip height.

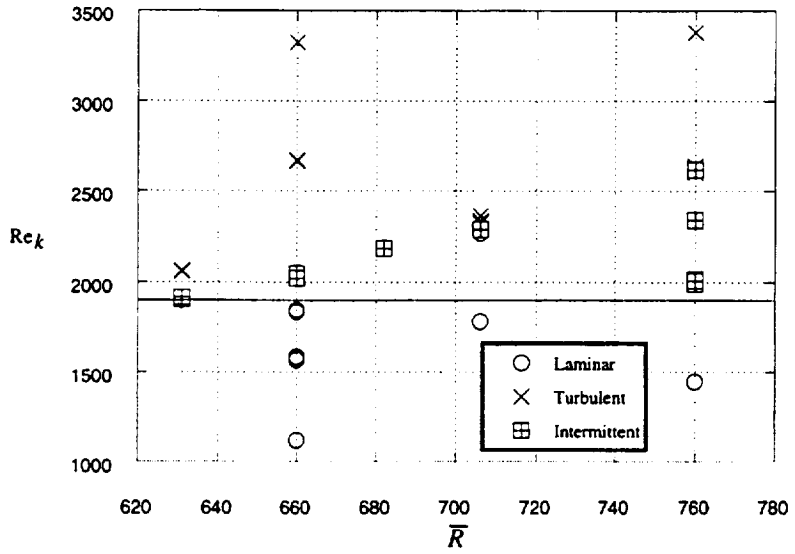

Figure 4-5. Trip wire Reynolds number as a function of $\overline{R}$.

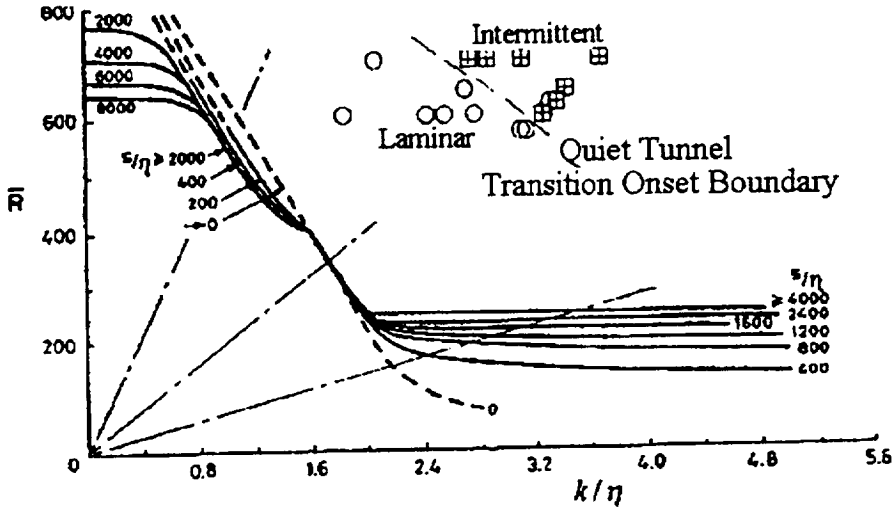

Figure 4-6. Low disturbance wind tunnel results compared to correlation of attachment-line transition onset with surface roughness height as proposed by Poll (ref. 10).

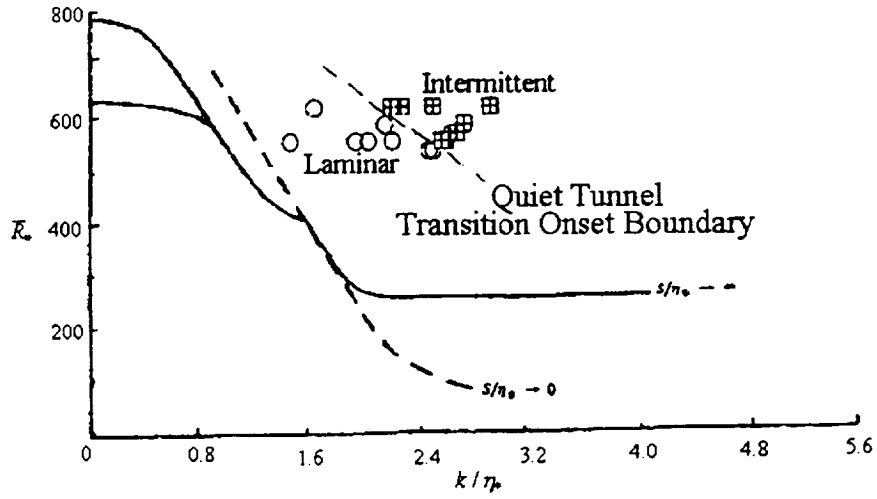

Figure 4-7. Comparison of present results with Poll's correlation based on the reference temperature.

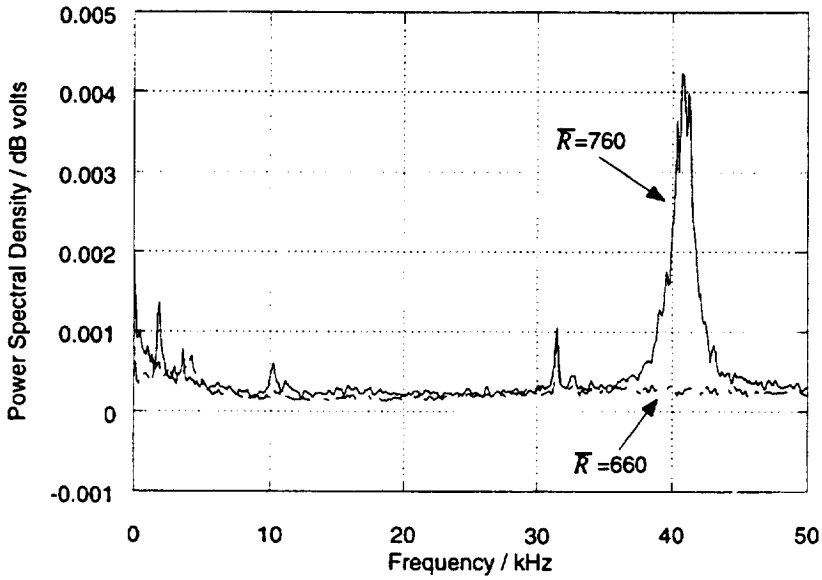

Figure 4-8. Appearance of broad-peak curve in frequency spectrum at $\overline{R} = 760$ ($s/\eta = 204$, $k/\eta = 3.67$).

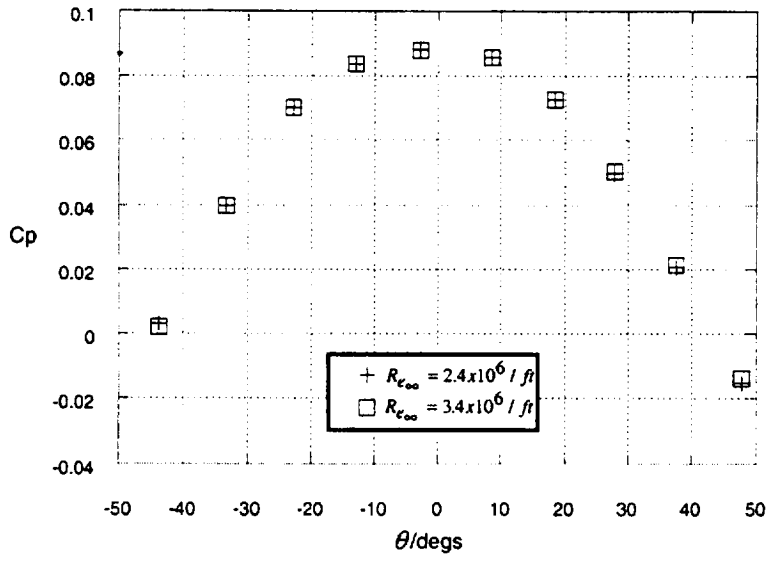

Figure 4-9. Comparison of experimental Cp distribution at $y/D = 4.2$, $Re_\infty = 2.4 \times 10^6$/ft and 3.4×10^6/ft.

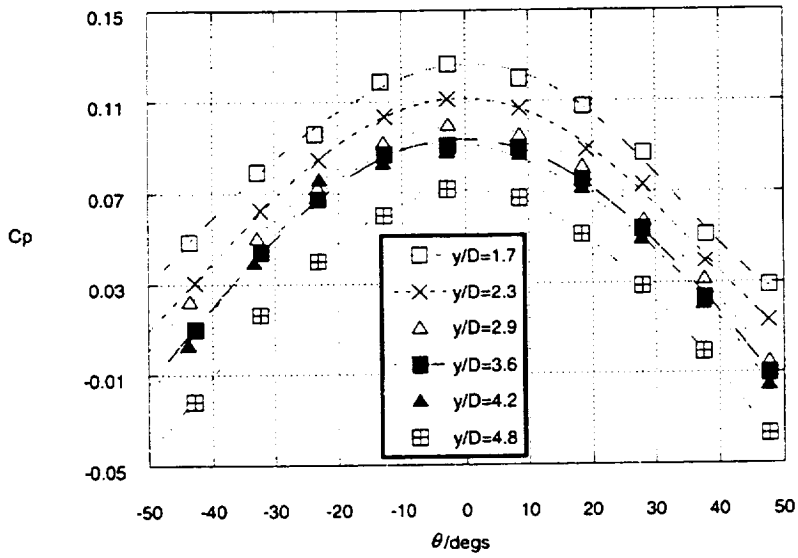

Figure 4-10. Complete experimental surface *Cp* distribution on the swept cylinder.

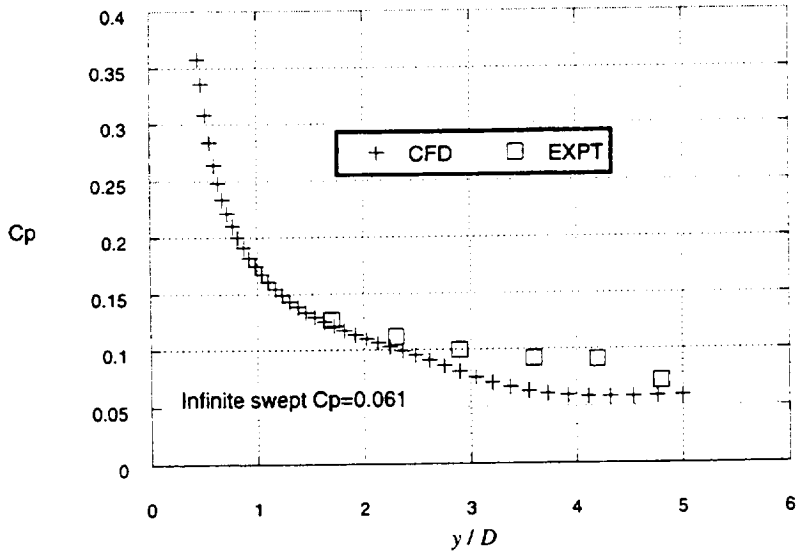

Figure 4-11. Comparison of experimental and CFD *Cp* distributions along the attachment line.

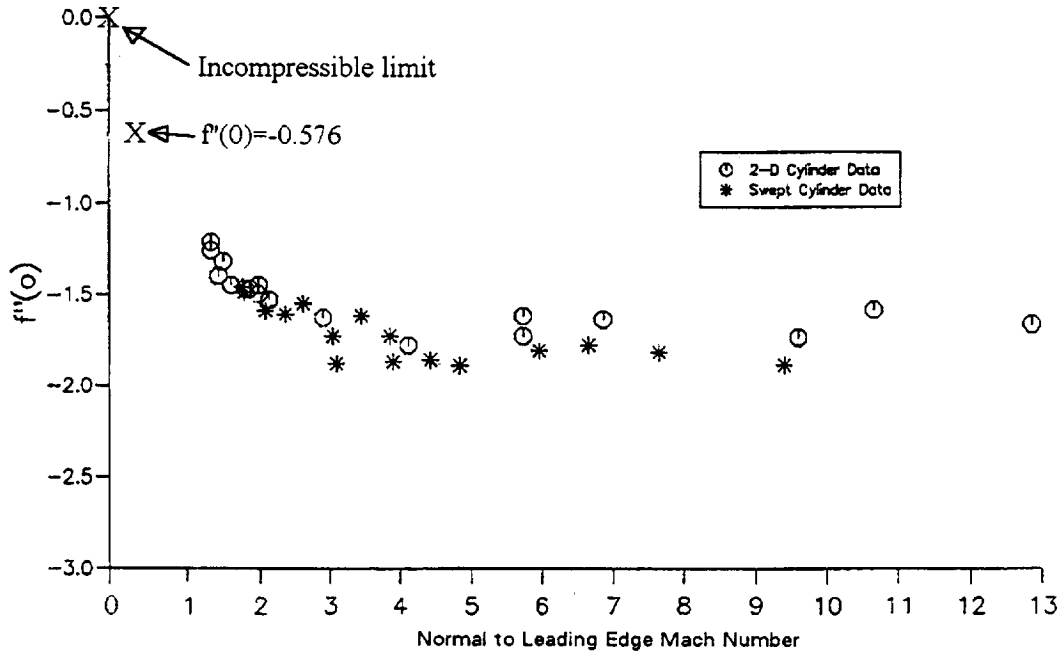

Figure 4-12. Variation of chordwise velocity gradient with normal to leading edge Mach number.

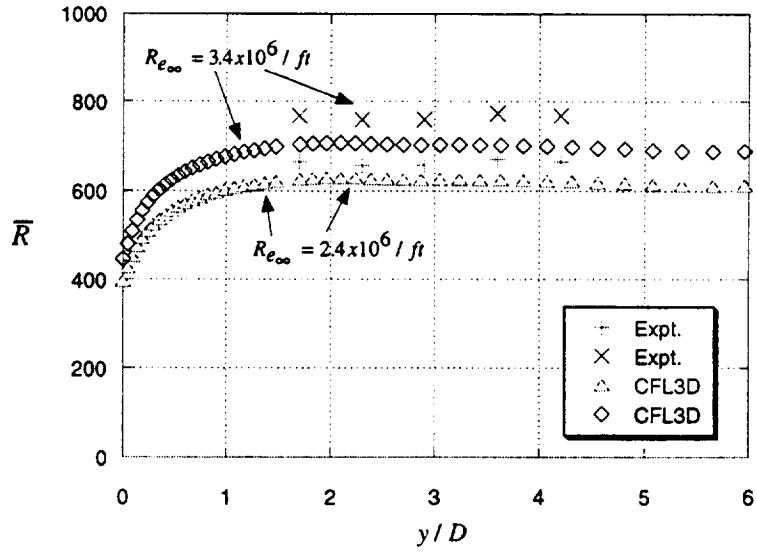

Figure 4-13. Experimentally obtained $\overline{R}$ distribution along the attachment line at $Re_\infty = 2.4 \times 10^6$/ft and 3.4×10^6/ft.

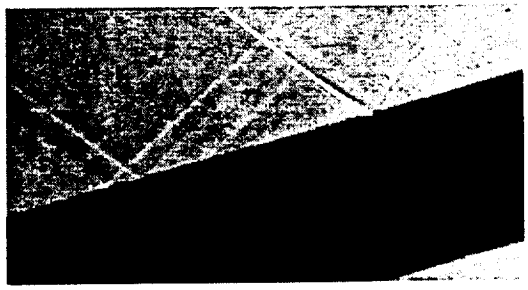

$Re_\infty = 2.76 \times 10^6$/ft, $T_{control} = 75°F$

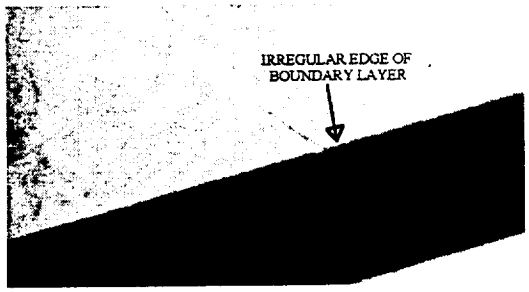

$Re_\infty = 2.75 \times 10^6$/ft, $T_{control} = 150°F$

Figure 4-14. Apparent appearance of turbulence with surface heating.

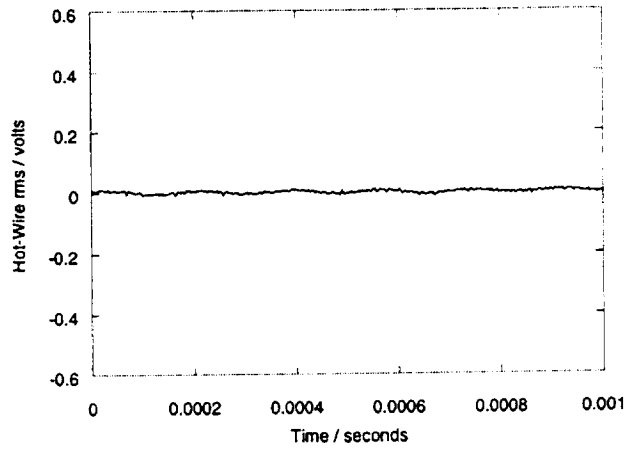

Figure 4-15. $T_{control} = 40°F$, $y/D = 4.4$, $\overline{R} \approx 800$. No disturbances detected by hot wire.

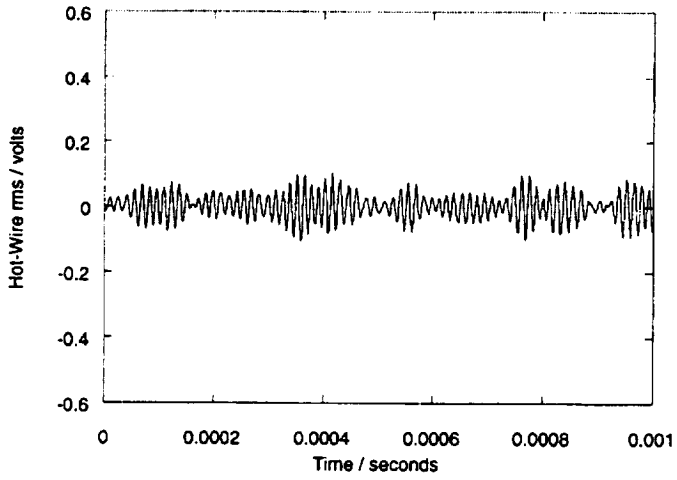

Figure 4-16. $T_{control}$ = 110°F, y/D = 4.4, $\overline{R} \approx 800$. Modulated wave packets detected by hot wire.

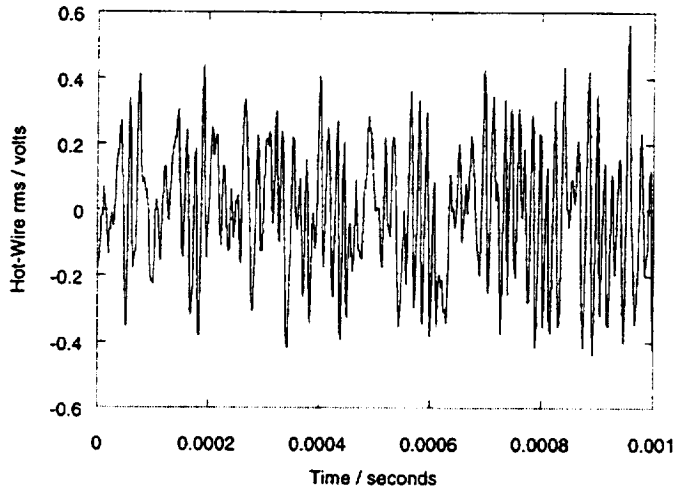

Figure 4-17. $T_{control}$ = 210°F, y/D = 4.4, $\overline{R} \approx 800$. Large amplitude, fully turbulent signal detected by hot wire. Wave packets no longer seen.

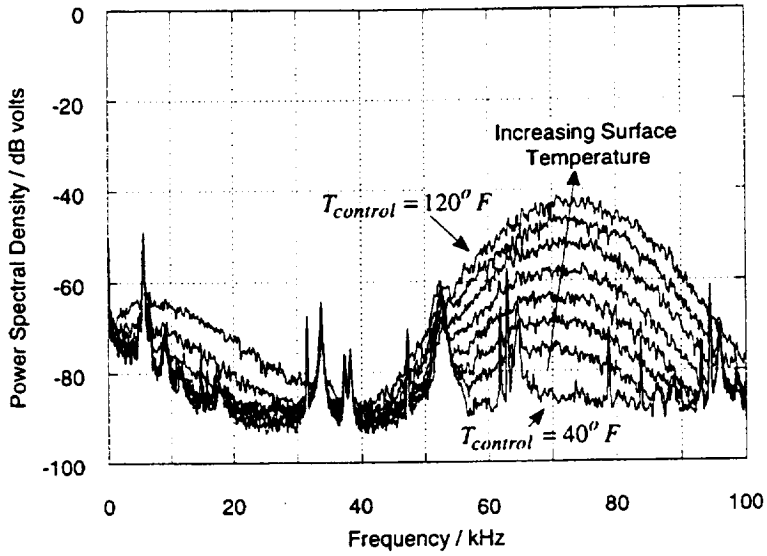

Figure 4-18. Power spectra of hot-wire response with increasing surface temperature. $40°F \leq T_{control} \leq 120°F$, $y/D = 4.4$, $\overline{R} \approx 800$.

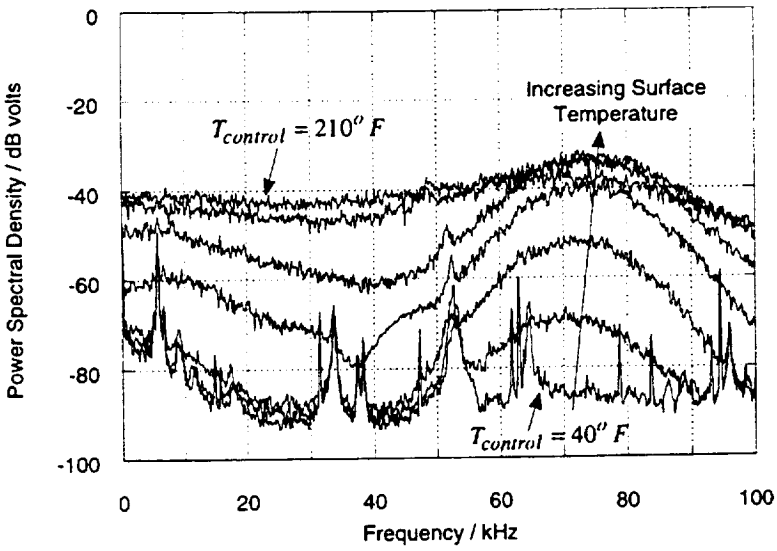

Figure 4-19. Power spectra of hot-wire response with increasing surface temperature. $40°F \leq T_{control} \leq 210°F$, $y/D = 4.4$, $\overline{R} \approx 800$.

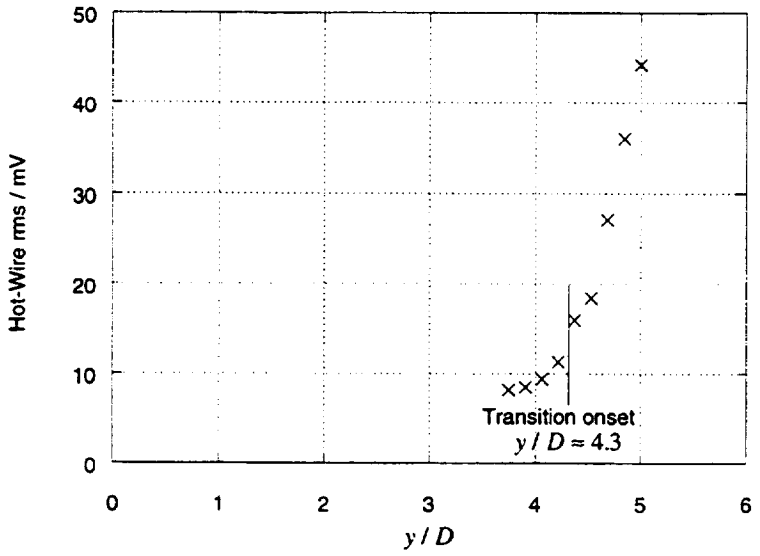

Figure 4-20. Transition onset at $y/D \approx 4.3$ as located by a hot wire, $Re_\infty = 3.56 \times 10^6$/ft and $T_{control}$ = 125°F ($\overline{R} \approx 800$).

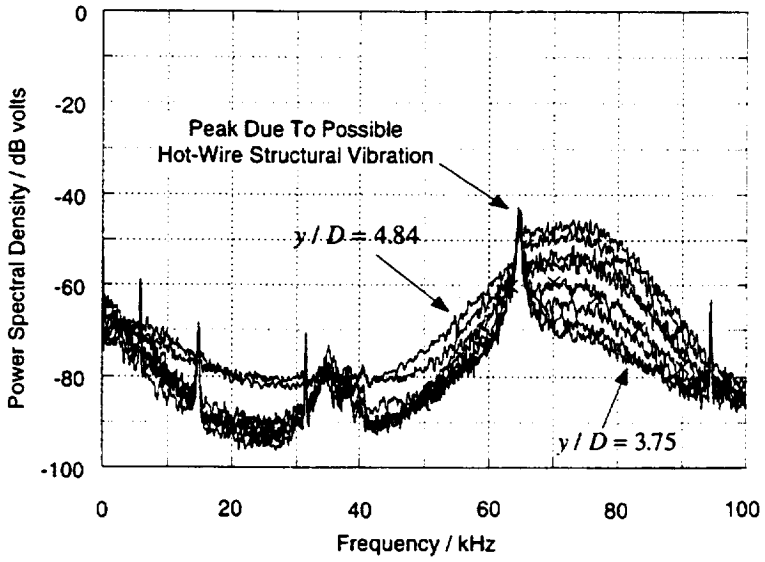

Figure 4-21. Power spectra of transition onset as located by a hot wire, $Re_\infty = 3.56 \times 10^6$/ft and $T_{control}$ = 125°F ($\overline{R} \approx 800$).

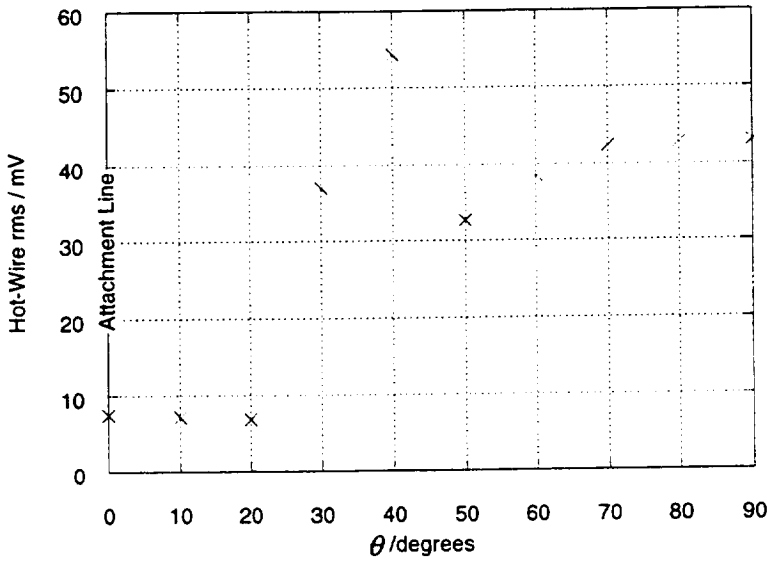

Figure 4-22. Rise in hot-wire rms signal with chordwise direction. y/D = 3.98, $\overline{R} \approx 680$, adiabatic wall condition.

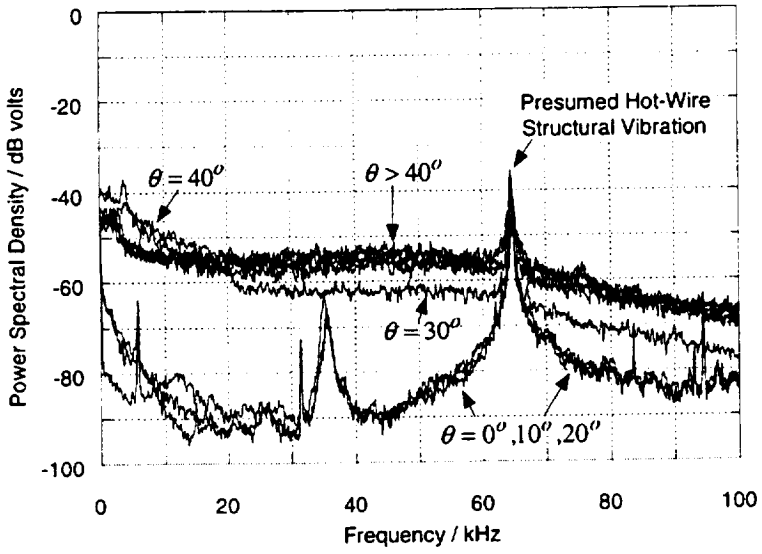

Figure 4-23. Power spectra of hot-wire signal with chordwise direction. y/D = 3.98, $\overline{R} \approx 680$, adiabatic wall condition.

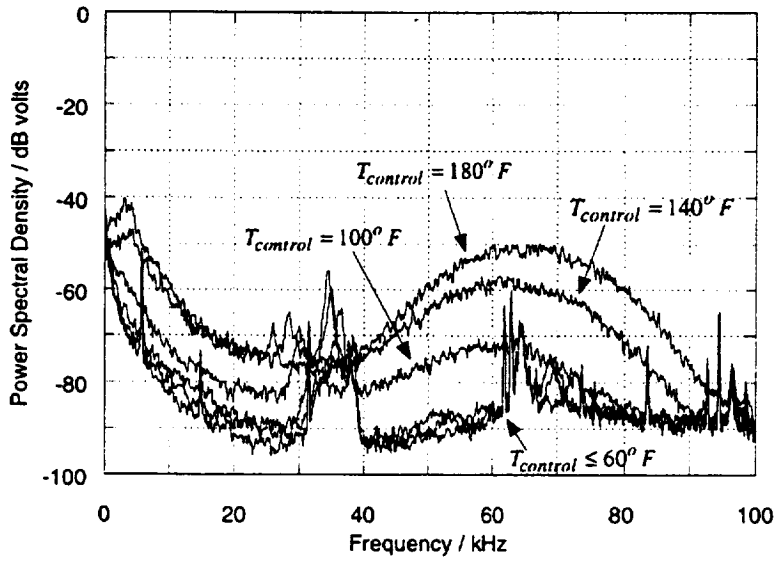

Figure 4-24. Power spectra of hot-wire signal at $\theta = 20°$ with increasing heating. $y/D = 3.59$, $\overline{R} \approx 680$.

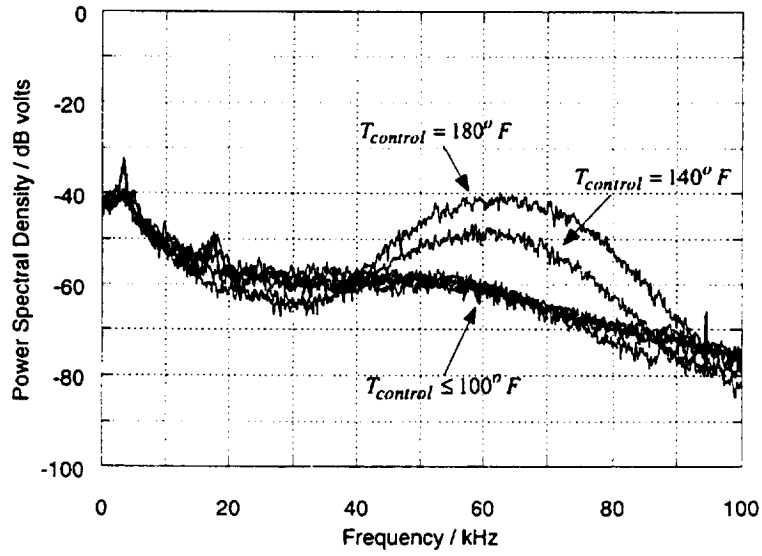

Figure 4-25. Power spectra of hot-wire signal at $\theta = 30°$ with increasing heating. $y/D = 3.59$, $\overline{R} \approx 680$.

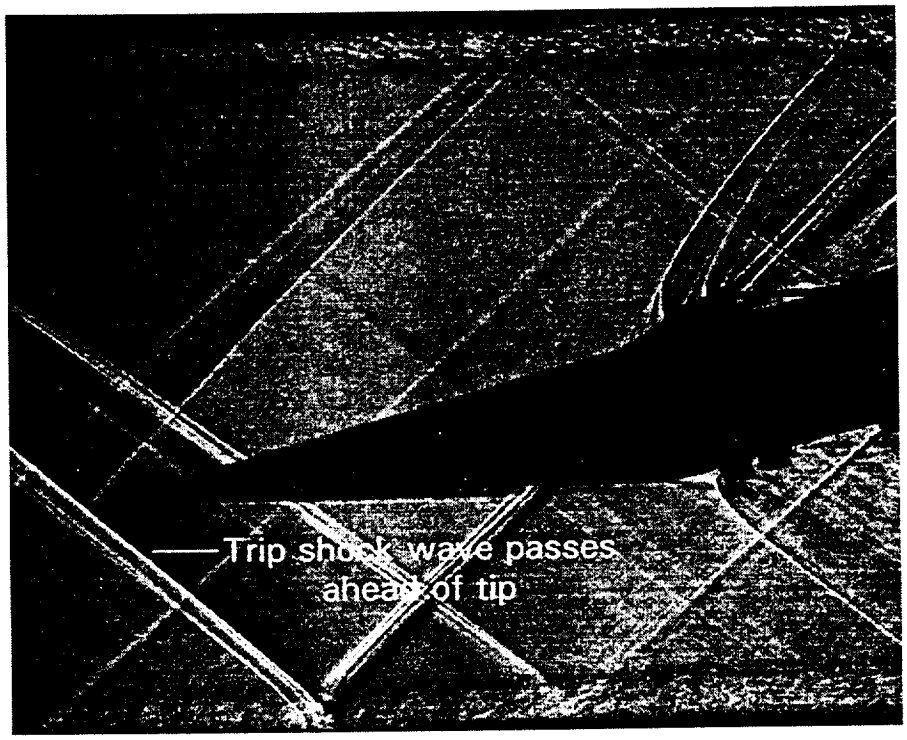

Figure 4-26. Shock wave from trip strip passes in front of cylinder tip.

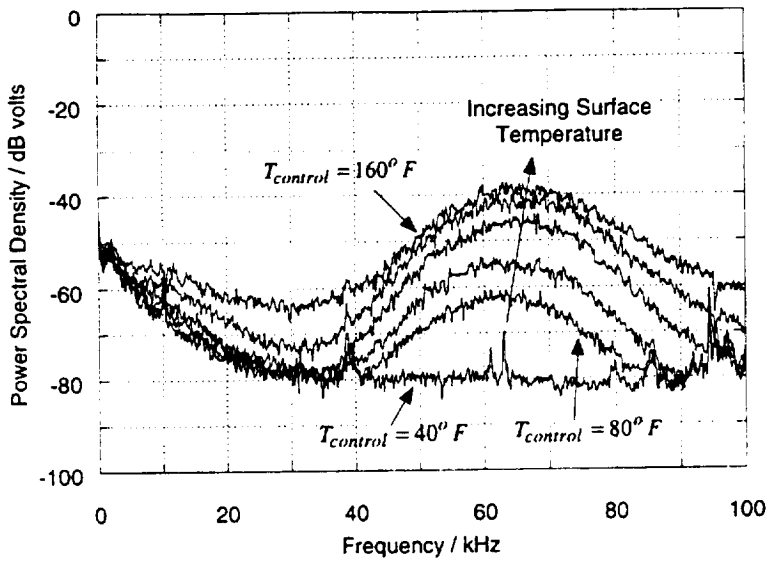

Figure 4-27. Power spectra of hot-wire response with increasing surface temperature under noisy conditions, $y/D = 4.02$, $\overline{R} \approx 780$.

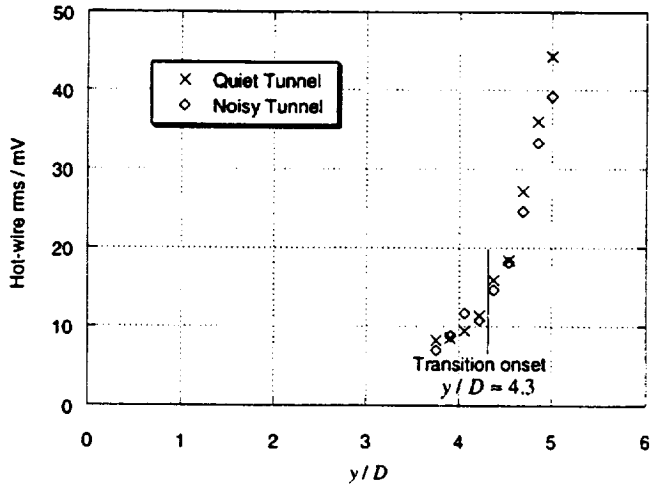

Figure 4-28. Experimental transition onset at $y/D \approx 4.3$ under noisy conditions as located by a hot wire, $Re_\infty = 3.36 \times 10^6$/ft and $T_{control} = 90°F$ ($\overline{R} \approx 780$). Effect of lower wall temperature counteracted by increased freestream disturbance level.

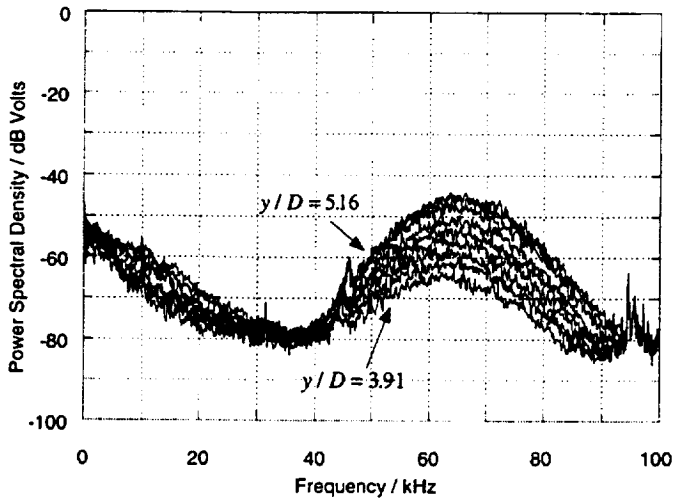

Figure 4-29. Power spectra of experimental transition onset under noisy conditions as located by a hot wire, $Re_\infty = 3.36 \times 10^6$/ft and $T_{control} = 90°F$ ($\overline{R} \approx 780$).

5. ATTACHMENT-LINE BOUNDARY LAYER STABILITY CALCULATIONS

An existing set of computational codes was modified in order to calculate the attachment-line boundary layer disturbances for this experiment. These codes were developed by R. -S. Lin (refs. 87 and 88) but the underlying theory and method are reproduced here for completeness with no claim of originality.

The overall procedure was to calculate an attachment-line boundary layer based on experimental conditions. A stability code which allowed for three-dimensional oblique waves (known as a two-dimensional eigenvalue approach) was then run for various wave angles and surface heating levels in order to quantify the frequencies of the most amplified disturbances.

5.1 Compressible Swept-Infinite Attachment-Line Boundary Layer Solver

A highly accurate spectral/finite-difference code was used for the solution of the compressible laminar attachment-line boundary layer over a swept-infinite leading edge. The numerical method consisted of a fifth-order, fully implicit marching scheme in the chordwise direction and a Chebyshev spectral collocation method in the wall-normal direction. Since a discrete set of local *Cp* distributions was available and the spanwise variation was known to be weak, this code was used to provide boundary layer velocity and temperature profiles for the investigation of compressible attachment-line boundary layer stability characteristics.

5.1.1 Boundary Layer Equations

For laminar flow on an attachment line, there exists a similarity solution for the compressible boundary layer equations (ref. 127). However, since information near, but off, the attachment line is also needed for the present two-dimensional stability theory, it is necessary to solve the nonsimilar boundary layer equations in order to provide mean flow information. The nonsimilar attachment-line equations for a swept-infinite cylinder are obtained from the general three-dimensional boundary layer equations by neglecting all spanwise derivatives. It is worth pointing out that for incompressible swept attachment-line boundary layer flow, the independence principle holds, namely, the solutions for the boundary layer in the plane normal to the attachment line are independent of the spanwise momentum equation. However, for compressible flow the independence principle does not apply, as the momentum equations are all coupled through the density variation. Thus the chordwise flow and the spanwise flow must be calculated simultaneously.

Consider a conventional boundary layer coordinate system x, y, z where x and y are within the plane of the surface and z is normal to it. For the attachment line problem, we take x in the chordwise (normal to leading edge) direction and y in the spanwise direction. The boundary layer equations for a steady compressible laminar flow over a swept-infinite cylinder are:

Continuity:

$$\frac{\partial(\rho u)}{\partial x}+\frac{\partial(\rho w)}{\partial z}=0 \tag{5-1}$$

Momentum:

$$\rho u\frac{\partial u}{\partial x}+\rho w\frac{\partial w}{\partial z}=-\frac{\partial p}{\partial x}+\frac{\partial}{\partial z}\left(\mu\frac{\partial u}{\partial z}\right) \tag{5-2}$$

$$\rho u\frac{\partial v}{\partial y}+\rho w\frac{\partial v}{\partial z}=\frac{\partial}{\partial z}\left(\mu\frac{\partial v}{\partial z}\right) \tag{5-3}$$

$$\frac{\partial p}{\partial z}=0 \tag{5-4}$$

Energy:

$$\rho c_p\left(u\frac{\partial T}{\partial x}+w\frac{\partial T}{\partial z}\right)=u\frac{\partial p}{\partial x}+\frac{\partial}{\partial z}\left(k\frac{\partial T}{\partial z}\right)+\mu\left[\left(\frac{\partial u}{\partial z}\right)^2+\left(\frac{\partial v}{\partial z}\right)^2\right] \tag{5-5}$$

where c_p is the specific heat at constant pressure, and k is the thermal conductivity. The viscosity and thermal conductivity are modeled by the Sutherland law for air.

State:

$$P=\rho RT$$

The boundary conditions for equations (5-1 to 5-5) are:

$$z=0,\ u=v=w=0,\text{ and } T=T_w \text{ or } v=v_w \text{ or } \frac{\partial T}{\partial z}=0$$

$$z\to\infty,\ u=u_e,\ v=v_e,\text{ and } T=T_e$$

The chordwise velocity outside the boundary layer satisfies the following form of Euler equation:

$$\rho_e u_e\frac{du_e}{dx}=-\frac{dp_e}{dx}$$

The boundary layer equations in their present form are singular at $x=0$. By an appropriate transformation the singularity is removed; specifically, the dependent variable U is replaced by dU/dx at $x=0$.

5.1.2 Numerical Method

The spectral code, named SCALBL, obtains the numerical solution of the compressible swept-infinite attachment-line boundary layer equations and provides high accuracy mean flows for the two-dimensional linear stability code described in Section 5.2. This boundary layer code uses a mixed Chebyshev-spectral and high order finite difference method, similar to the one employed by Pruett and Street (ref. 128), to solve the nonsimilar boundary layer equations (5-1 to 5-5). The numerical method incorporates a fifth-order, fully implicit, finite difference method in the marching (chordwise, or x) direction with a uniform step size. The scheme takes four initial steps of order one, two, three, and four before settling into fifth-order accuracy. In the wall-normal direction, a Chebyshev collocation technique is used. At each marching station, the discrete spectrally accurate governing equations (5.1 to 5.5) are fully coupled and are solved by a direct method, while in the work of Pruett and Street the system of discrete governing equations was solved by a preconditioned Richardson iteration.

5.1.3 SCALBL Code

SCALBL requires that the surface pressure (Cp) distribution be first given or prescribed (as a polynomial in x) for the case under consideration. In this case, the pressures were obtained from the pressure tapped swept cylinder model. Other parameters, such as freestream conditions, sweep angle, cylinder radius, domain size, and other numerical calculation quantities must also be stated. Wall heating and suction may also be specified. Various output files are created, including all the profiles at all chordwise stations, various Reynolds numbers, and local conditions at the attachment line. These profiles are then read by the stability code, 2DEIG.

5.2 Compressible Two-Dimensional Linear Stability Theory

5.2.1 Two-Dimensional Stability Theory

Assuming that there is an infinitesimal disturbance propagating within the attachment-line boundary layer, the instantaneous flow quantities (i.e., velocities, pressure, temperature, density, etc.) can then be expressed as:

$$q(x,y,z,t) = \overline{q}(x,z) + q'(x,y,z,t) \quad (5\text{-}6)$$

where $q = (u,v,w,p,T)$, and barred and primed quantities represent basic-state and disturbance-state quantities, respectively. According to the "locally" swept-infinite assumption (a good approximation for attachment-line flow), the basic state is assumed to be uniform in the spanwise direction. Substituting equation (5-6) into the compressible Navier-Stokes equations, subtracting the basic-state information, and linearizing with respect to small perturbations results in a full set of compressible linearized Navier-Stokes (stability) equations which best describes the stability characteristics of small perturbations.

In general, to solve the full set of linearized Navier-Stokes equations (a set of three-dimensional partial differential equations) is nontrivial. Therefore, in earlier studies, some ad hoc assumptions were

made to reduce the problem into something more manageable. For example, Malik and Beckwith (ref. 69) approximated the instantaneous values of velocities u, v, w as:

$$(u, v, w) = [0, V(z), 0] + [\hat{u}(y), \hat{v}(y), \hat{w}(y)]e^{i(\alpha x + \beta y - \omega t)}$$

where $(\hat{u}, \hat{v}, \hat{w})$ are the disturbance eigenfunctions. The pressure p, temperature T, and density ρ were represented similarly. Here α and β are the wavenumbers and ω is the disturbance frequency which, in general, are all complex. In temporal stability theory, α and β are assumed to be real and ω is complex. It is thus assumed that the wave-like oblique disturbances have x and y components of wave number α and β, respectively (fig. 5-1). Note that for an incompressible attachment-line boundary layer, the most unstable disturbance is a two-dimensional traveling wave ($\alpha = 0$), while in a compressible attachment-line boundary layer ($M_\infty < 4$) three-dimensional traveling waves have the largest growth rate (ref. 26).

Assuming the above form of the disturbances, Malik and Beckwith then applied a one-dimensional parallel stability theory. For incompressible attachment-line flow, previous work by Lin and Malik (ref. 54) has shown that this simplified theory has a tendency to underestimate the growth rate of unstable disturbances. For the compressible attachment line, a similar result has also been reported by Lin and Malik (ref. 87).

On the other hand, the two-dimensional stability theory proceeds from the full set of the linear Navier-Stokes equations without making any further simplifications, and recognizes that the problem consists of a set of coupled three-dimensional partial-differential equations with variable coefficients. These coefficients, which depend on the basic flow, change strongly in both the wall-normal (z) and the chordwise (x) directions, but for the present swept-infinite flow they are independent of spanwise (y) direction (see eq. 5-6). Consequently, the solutions are separable in the variables y and t, and the disturbance quantities of a general traveling mode can be expressed in the form:

$$q'(x, y, z, t) = \hat{q}(x, z)e^{i(\beta y - \omega t)} + c.c. \tag{5-7}$$

where c is the complex phase velocity whose real part represents the propagating speed of the disturbance in the spanwise direction and its imaginary part is proportional to the temporal growth rate ω_i ($\omega_i = \beta c_i$).

Note that the introduction of the method of separation of variables (eq. 5-7) reduces the three-dimensional linear partial-differential equations to two-dimensional ones in the x-z domain. Details of the set of two-dimensional linear stability equations are given in Lin (ref. 88).

For the attachment-line flow, two fundamentally different types of solution are conceivable. The spanwise disturbance-velocity component can have a symmetric solution, i.e. $\hat{v}(x, z) = \hat{v}(-x, z)$, and an antisymmetric solution, i.e., $\hat{v}(x, z) = -\hat{v}(-x, z)$. Both symmetric and antisymmetric perturbations can be amplified in the attachment-line boundary layer, but the symmetric modes are usually found to be the most unstable perturbation for both incompressible and compressible flows.

Appropriate boundary conditions in the z direction are:

$$\hat{u} = \hat{v} = \hat{w} = \hat{T} = 0, z = 0, \infty$$

which assign zero-disturbance amplitudes to the solid surface ($z = 0$) and at the far field ($z \to \infty$). In the x direction, the boundary conditions for symmetric modes are:

$$\hat{u} = \frac{\partial \hat{v}}{\partial x} = \frac{\partial \hat{w}}{\partial x} = \frac{\partial \hat{T}}{\partial x} = 0, x = 0$$

$$\hat{u}(x,z) = -\hat{u}(-x,z), \hat{q}(x,z) = \hat{q}(-x,z), \hat{q} = \left(\hat{v}, \hat{w}, \hat{T}\right), x = x_{\max}$$

Similarly, the appropriate boundary conditions in the x direction for an antisymmetric mode are:

$$\frac{\partial \hat{u}}{\partial x} = \hat{v} = \hat{w} = \hat{T} = 0, x = 0$$

$$\hat{u}(x,z) = \hat{u}(-x,z), \hat{q}(x,z) = -\hat{q}(-x,z), \hat{q} = \left(\hat{v}, \hat{w}, \hat{T}\right), x = x_{\max}$$

Due to the nonuniform nature of the attachment-line flow in the x direction, the method developed here is, strictly speaking, aimed at studying the stability of an oblique traveling wave in the following form:

$$q'_R = \hat{q}_R(x,z) e^{i\left[\int^x \alpha(\xi) d\xi + \beta y - \omega t\right]} + \text{c.c.} = \hat{Q}_R(x,z) e^{i[\beta y - \omega t]} + \text{c.c.}$$

where $\hat{Q}_R(x,z) \equiv \hat{q}_R(x,z) e^{i\int^x \alpha(\xi) d\xi}$. The above equation represents an oblique wave (i.e., a three-dimensional wave) propagating in both the positive x and y directions. (A two-dimensional mode, where nothing grows in the x direction, corresponds to $\alpha(x) = 0$.) However, due to the symmetric nature of the attachment-line flow with respect to $x = 0$, it is conceivable that an identical disturbance propagating toward negative x (still in the positive y) direction should also be possible. The linear combination (f') of these two (left and right) waves can be expressed as:

$$f' = \hat{Q}_R(x,z) e^{i[\beta y - \omega t]} + \hat{Q}_L(x,z) e^{i[\beta y - \omega t]} + \text{c.c.} = \hat{F}(x,z) e^{i[\beta y - \omega t]} + \text{c.c.}$$

where

$$\hat{Q}_R(x,z) = \hat{Q}_L(-x,z) \to \hat{F}(x,z) = \hat{F}(-x,z), \text{ for } v', w', p', T'$$

$$\hat{Q}_R(x,z) = -\hat{Q}_L(-x,z) \to \hat{F}(x,z) = -\hat{F}(-x,z), \text{ for } u'$$

Note that the linear combination does not alter the eigenvalue, which could be either β or ω. Thus, for oblique modes, the eigenfunctions obtained by the current method actually represent the sum of a pair of oblique traveling waves, however, propagating in different x directions. The effect of wavenumber $\alpha(x)$ is implicitly retained in the eigenfunction in this approach.

For the current supersonic attachment-line boundary layer, oblique traveling waves are expected to be the most relevant disturbances (ref. 26). In order to resolve this type of disturbance without excessive numerical effort, a trigonometric factorization is introduced:

$$q'(x,y,z,t) = \hat{q}(x,z)e^{i(\beta y-\omega t)} + \text{c.c.} = T_r(\alpha,x)\overline{q}(x,z)e^{i(\beta y-\omega t)} + \text{c.c.}$$

where $T_r(\alpha,x) = \sin(\alpha x)$ for $q' = u'$ and $T_r(\alpha,x) = \cos(\alpha x)$ for $q' = (v',w',p',T')$. Then the wave angle can be defined as $\psi = \tan^{-1}(\alpha/\beta)$ (fig. 5-1). As shown by Lin and Malik (ref. 87), the use of the trigonometric factorization allows the disturbance-amplitude functions to be resolved easier, numerically. As well, it provides a means for examining disturbances traveling in a specific direction.

5.2.2 Numerical Method

The disturbance variable $\hat{q}$ is represented in the double series:

$$\hat{q}(x,z) = \sum_{n=0}^{n_x-1}\sum_{k=0}^{n_z-1} c_{n,k}P_n(x)T_k(\xi) \tag{5-8}$$

where P_n are regular polynomials $\left\{P_n(x) = x^n, n = 0,1,2,...\right\}$ used for the x discretization, and T_k are Chebyshev polynomials of degree k used for the z discretization. In the x direction, both symmetric and antisymmetric solutions (with respect to the attachment line) are possible. For symmetric (even) solutions, all of the coefficients with n odd vanish identically, i.e., $c_{n,k} = 0$ for n odd. Conversely, the expansions with $c_{n,k} = 0$ for n even are antisymmetric (or odd). It is convenient to chose n_x even, so that $n_x = 2m$. Equation (5-8) can then be written as:

$$\hat{q}(x,z) = \sum_{n=0}^{m-1}\sum_{k=0}^{n_z-1} c_{2n,k}P_{2n}(x)T_k(\xi)$$

for even solutions, and

$$\hat{q}(x,z) = \sum_{n=0}^{m-1}\sum_{k=0}^{n_z-1} c_{2n+1,k}P_{2n+1}(x)T_k(\xi)$$

for odd solutions. By doing the above even and odd expansions, the symmetric and the antisymmetric boundary conditions in the x direction are satisfied automatically.

For temporal stability theory, the governing equations in the discrete sense can be represented as a generalized algebraic eigenvalue problem of the form:

$$[\mathbf{A}]\bar{q} = \omega[\mathbf{B}]\bar{q}$$

where $[\mathbf{A}]$ and $[\mathbf{B}]$ are complex non-Hermitian matrices. The above eigenvalue problem is solved by the QR algorithm which yields all the eigenvalues.

5.2.3 2DEIG Code

The two-dimensional stability theory is implemented in the program 2DEIG, with the basic flow information obtained from the code SCALBL. In the temporal eigenvalue problem, the spanwise wave number β is assumed to be real and must be prescribed, while the disturbance frequency ω is considered to be the complex eigenvalue to be solved for ($\omega = \omega_r + \omega_i$). In 2DEIG, there are two types of methods that can be used to locate the eigenvalues: global and local. For the global method, in which a generalized eigenvalue problem is set up, all of the eigenvalues are obtained by a direct method. Unfortunately, along with the accurately computed values of the true modes, there appear spurious unstable modes with large growth rates whose magnitude increases with an increase of the size of the algebraic system of equations. These spurious roots arise due to the approximation of the differential equations by a finite dimensional system of algebraic equations. Four filters are used to remove modes that are not relevant:

filter 1: removes roots whose moduli are larger than 2.0; i.e., $\|\omega\| > 2.0$. This filters out most of the spurious modes.

filter 2: removes modes propagating upstream; i.e., $c_r < 0$.

filter 3: removes highly stable modes; i.e., modes with $\omega_i < -0.5 \times 10^{-3}$.

filter 4: removes the supersonic modes (a disturbance which has a phase speed such that the difference between phase speed and freestream velocity is supersonic).

In addition, multiple calculations with different wave numbers (β) are possible. In the local method, an initial guess for the desired eigenvalue is required, and the root which lies closest to the guessed value is then computed by an iteration method.

Inputs to 2DEIG include wave angle, wave number range, symmetric or antisymmetric mode, and number of collocation points in wall-normal and chordwise directions. Output includes temporal growth rates and eigenfunction structure in a x-z domain. These complex data provide the amplitude and phase information about the velocity, pressure and temperature perturbations.

5.3 Boundary Layer Calculations Using SCALBL

A finite length swept cylinder will have a developing attachment-line boundary layer with increasing distance from the tip, asymptoting toward its swept infinite state. The local boundary layer conditions will therefore be changing with y. Thus, in order to apply SCALBL, a swept infinite code, one must first chose a crossflow plane in which to do the calculations. The effective local sweep angle is then found at that location, and SCALBL is used to produce the local boundary layer profiles.

5.3.1 Effective Local Sweep Assumption

The Cp distribution along swept cylinder model was obtained as described in Chapter 4. As seen in figure 5-2, the local value of the attachment line Cp varies in the spanwise direction. For each spanwise location, one can derive an effective local sweep angle based on the Cp at the attachment line (Cp_A) and freestream Mach number:

$$Cp_A \equiv \frac{p_A - p_\infty}{\frac{1}{2}\gamma M_\infty^2 p_\infty}$$

For $M_n < 1$, the isentropic relation applies:

$$\frac{p_A}{p_\infty} = \left[1 + \left(\frac{\gamma-1}{2}\right)M_n^2\right]^{\left(\frac{\gamma}{\gamma-1}\right)}$$

Combining gives:

$$Cp_A = \frac{2}{\gamma M_\infty^2}\left\{\left[1 + \left(\frac{\gamma-1}{2}\right)M_\infty^2 \cos^2\Lambda\right]^{\frac{\gamma}{\gamma-1}} - 1\right\}$$

Therefore, given the value of Cp_A from the experimental results, and knowing the freestream Mach number, the local effective sweep angle (Λ) can be deduced.

This assumption of endless swept flow at each crossflow plane is a fair approximation away from the tip of the model since properties are changing significantly faster in the chordwise direction than in the spanwise direction.

As seen in figure 5-2, the effective local sweep angle asymptotes toward its swept infinite value of 76° as distance from the tip increases.

5.3.2 Boundary Layer Profiles

The crossflow plane at $y/D = 3.6$ (local sweep angle of 72.8°) was considered to be a representative example of how the flow along the attachment line would behave with surface heating. $Cp(\theta)$ was obtained by fitting a polynomial of the form:

$$Cp = c_0 + c_1\theta^2 + c_2\theta^4 + c_3\theta^6$$

to the experimentally obtained surface pressure results. The boundary layer calculation extended from the attachment line to $\theta = \pm 5°$.

Figures 5-3 through 5-5 show the resultant velocity, temperature, and density profiles through the attachment-line boundary layer at $y/D = 3.6$ with surface heating. Figure 5-6 shows that points of inflection arise in the velocity profile with increasing surface heating. This effect is a consequence of the dependence of the viscosity μ of the fluid on the temperature T. The curvature of the profile $v(z)$ of the main flow at the wall is derived from equation (5-3) with $u = w = 0$:

$$\left(\frac{d^2v}{dz^2}\right)_w = -\frac{1}{\mu_w}\left(\frac{d\mu}{dz}\right)_w\left(\frac{dv}{dz}\right)_w$$

Now, if the wall is hotter than the fluid in the freestream, $T_w > T_\infty$; and the temperature gradient at the wall is negative $(dT/dz)_w < 0$, as shown in figure 5-4. Since for a gas the viscosity increases with temperature, $(d\mu/dz)_w < 0$. And since the velocity gradient is positive at the wall, it follows that:

$$T_w > T_\infty \text{ implies } \left(\frac{d^2v}{dz^2}\right)_w > 0$$

Thus for a heated wall the curvature of the velocity profile at the wall is positive, and it follows immediately that a point of inflection, $d^2v/dz^2 = 0$, must exist within the boundary layer because the curvature is vanishingly small but negative at $z = \infty$. This means that the transfer of heat from the wall to a gas flowing past it renders the boundary layer unstable (due to Raleigh's criterion) in a manner analogous to a pressure increase in the downstream direction. The net effect of surface heating can therefore be explained by the "opening up" of the neutral stability curve at high Reynolds numbers (typical of inviscid-type instabilities) as well as a general increase in the size of the neutral curve (to lower Reynolds numbers) with the subsequent decrease in the critical Reynolds number, as reported by Kazakov (ref. 129).

5.4 Stability Calculations Using 2DEIG

For every given Reynolds number ($\overline{R}$) and wave angle (ψ), calculations were carried out for a range of wavenumber (β). Keeping the Reynolds number fixed, the wave angle was then altered, and the calculations repeated. This process was repeated until the wave angle at which the absolute

maximum growth rate occurred had been obtained. Results shown are always for this wave angle, which produced the largest temporal growth rate.

Because of the introduction of a trigonometric factorization, a small number of grid points were required in the x (chordwise) direction to obtain a converged solution. An excessively large number of points in the z (wall-normal) direction resulted in a very stiff problem and caused the solution to be contaminated by round-off errors. Grid convergence tests conducted by Lin (ref. 88) had shown that 8 or 10 points in the x direction and 55 points in the z direction were typically required. For these calculations, 55 points were always used in the z direction, and 10 points were used in the x direction for wave angles between 30° and 45°. However, for a wave angle of 25°, it was found to be necessary to reduce the number of points to 4.

5.4.1 Adiabatic Wall Results

In order to see the effect of altering just the Reynolds number on the amplification of boundary layer disturbances, 2DEIG was run to obtain the temporal growth rates for the adiabatic wall condition at $y/D = 3.6$. Figure 5-7 shows the results at three Reynolds numbers:

$$\overline{R} = 685 \; (p_0 = 7.5 \text{ psia}, \; T_0 = 20°\text{F}, \; Re_\infty = 2.62 \times 10^6/\text{ft})$$

$$\overline{R} = 791 \; (p_0 = 10 \text{ psia}, \; T_0 = 20°\text{F}, \; Re_\infty = 3.49 \times 10^6/\text{ft})$$

$$\overline{R} = 840 \; (p_0 = 10 \text{ psia}, \; T_0 = -20°\text{F}, \; Re_\infty = 3.93 \times 10^6/\text{ft})$$

These numbers were chosen as they represent the full working range of the wind tunnel operating conditions. Notice that, as expected, increasing the Reynolds number increases the temporal growth rate of the disturbances. Note that the calculations were carried out in steps of $\psi = 5°$.

The total amplification factor, N, is defined as:

$$N = -\int_0^s \beta_i dy$$

where β_i is the spatial growth rate of the most unstable mode integrated along the attachment line to the point of consideration, s. The spatial growth rate may be obtained by converting the temporal growth rate using the group velocity, c_g:

$$\beta_i = -\frac{\omega_i}{c_g}, \text{ where } c_g = \frac{d\omega_r}{d\beta}$$

This operation is referred to as the Gaster transformation. For each condition, the group velocity was obtained from straight line plots of ω_r versus β. If it is then assumed that the local conditions at $y/D = 3.6$ can be applied to all points along the attachment line, a constant spatial amplification rate

can be integrated along the cylinder to obtain N factors. Figure 5-8 shows the N factors for the above operating conditions assuming a constant spatial amplification rate (uniform wall temperature and Reynolds number). Notice that the maximum N factor obtainable before the reflected shock wave ends the test at $y/D = 5.6$ is approximately 7 for the $\overline{R} = 791$ case (the most typical operating condition).

5.4.2 Surface Heating Results

Symmetric modes were always found to be the most amplified disturbances at adiabatic wall conditions. However, the effect of surface heating on the antisymmetric mode was unknown. Therefore, several calculations were made for both the symmetric and antisymmetric modes for the $T_{wall} = 138°F$ case. As can be seen in figure 5-9, the symmetric modes continue to be more amplified than the antisymmetric modes, and were therefore the only modes calculated.

The boundary layer disturbances at $y/D = 3.6$ were then studied as the surface temperature was increased from 0°F (near adiabatic wall condition) to 138°F. At each condition, the temporal amplification rate for each symmetric mode wave angle was determined over a range of frequencies, and the most amplified disturbances were determined. Figure 5-10 shows the evolution of the most amplified disturbances with increasing surface temperature for $\overline{R} = 791$ and local Mach number = 1.495. Note that the amplification rate, frequency, and wave angle all increase with increasing surface temperature. At a temperature of 0°F, the frequency of the most amplified disturbance was 63 kHz with a 30° wave angle, while at 138°F it had increased to 72 kHz at 40°. These results agree with those of Wie and Collier (ref. 70). They too calculated the most amplified disturbances for an adiabatic wall to be oblique waves at 30° to the attachment line at a local Mach number of 1.5 (fig. 5-11).

Again, if these local conditions are assumed to exist at all points along the attachment line (swept-infinite condition), one can calculate the N factors associated with these amplification rates (fig. 5-12). Surface heating is shown to have a marked effect on the achievable N factor along the attachment line, with the maximum obtainable N factor at $y/D = 5.6$ being in excess of 20.

Figure 5-13 shows the disturbance amplitude function for u', v', and T' at various chordwise locations for a $\beta = 0.14$, 40° oblique traveling wave at $\overline{R} = 791$. Notice that the predicted temperature disturbances are greater than the velocity disturbances along the attachment line. Also note that the temperature disturbances are a maximum at approximately $z/\delta = 0.38$. Figure 5-14 shows the phase relation between the disturbance amplitude functions at this condition. Note that the v' and T' disturbances are 180° out of phase at the height in the layer where their amplitudes are a maximum. Recall from Chapter 3 that a hot wire will respond in the same way to increases in total temperature and decreases in velocity. Since the temperature and velocity disturbances are out of phase at this height in the layer, their net effect on the hot wire would be an additive one, which is quite fortuitous.

To obtain the hot-wire response to the combined temperature and velocity fluctuations, the signals were vectorially represented:

$$\overline{T'} = T'\cos\theta_T\hat{i} + T'\sin\theta_T\hat{j} \quad \text{and} \quad \overline{W'} = W'\cos\theta_W\hat{i} + W'\sin\theta_W\hat{j}$$

If a is the coefficient which represents the hot-wire response to temperature fluctuations, and b the coefficient for velocity fluctuations (where $a + b = 1$), then the wire will respond to:

$$\bar{r} = \left(aT'\cos\theta_T - bW'\cos\theta_W\right)\hat{i} + \left(aT'\sin\theta_T - bW'\sin\theta_W\right)$$

where the out-of-phase relationship between the temperature and velocity fluctuations has been accounted for. Therefore, the magnitude of the hot-wire response is:

$$\bar{r} = \sqrt{\left\{\left(aT'\cos\theta_T - bW'\cos\theta_W\right)^2 + \left(aT'\sin\theta_T - bW'\sin\theta_W\right)^2\right\}}$$

As the overheat ratio is increased, the hot wire responds more to temperature fluctuations than to velocity fluctuations ($a > b$). Figure 5-15 shows $\bar{r}$ at three overheat settings. As can be seen, as the overheat ratio is increased, the overall hot-wire response decreases.

A visual representation of the oblique disturbances can be made by plotting the instantaneous contour of computed temperature fluctuation in the x-y plane at constant z (fig. 5-16). This "snapshot" was obtained by freezing time at $t = 0$ in equation (7), expanding the expression and taking the real part. The staggered pattern is the result of the combination of two traveling oblique waves. One is moving toward the positive x and the other toward the negative x direction; both are moving in the positive y direction. As can be seen, the interaction of the left and right propagating waves produces constructive and destructive interference in a pattern similar to that seen by Lin (refs. 87 and 88).

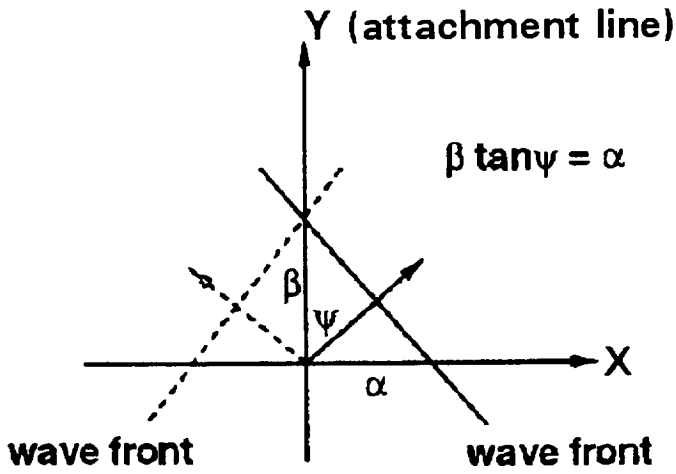

Figure 5-1. A pair of oblique waves; $\beta(\alpha)$ represents the wave number in the spanwise (chordwise) direction; ψ is the oblique angle of traveling waves.

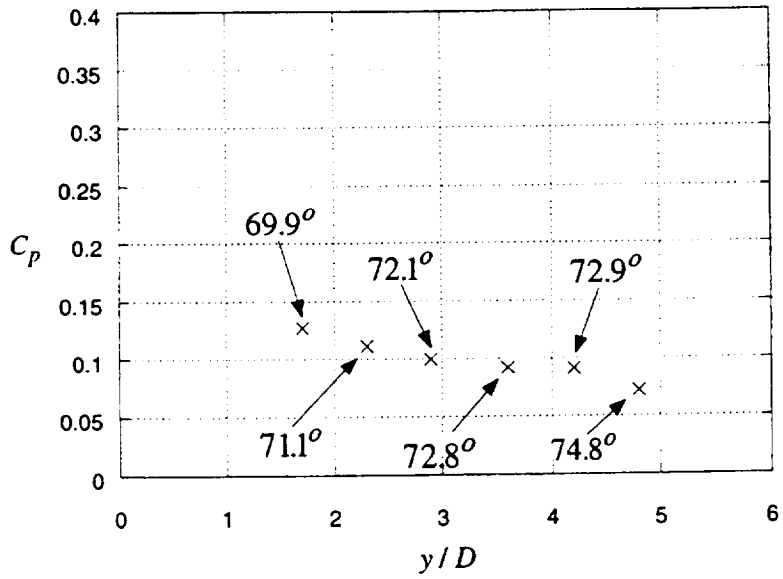

Figure 5-2. Effective local sweep conditions along the attachment line of the finite length model.

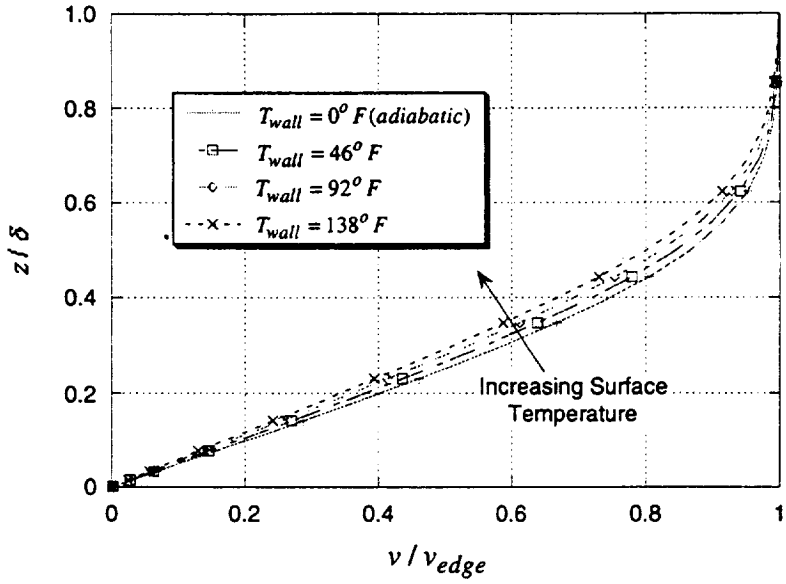

Figure 5-3. Velocity profiles for the attachment line at y/D = 3.6, $\overline{R}$ = 791, and local Mach number = 1.495.

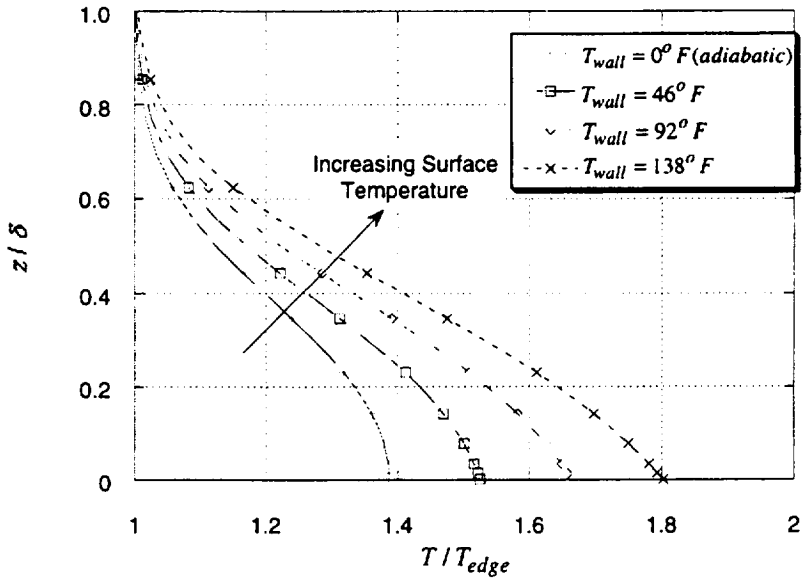

Figure 5-4. Temperature profiles for the attachment line at y/D = 3.6, $\overline{R}$ = 791, and local Mach number = 1.495.

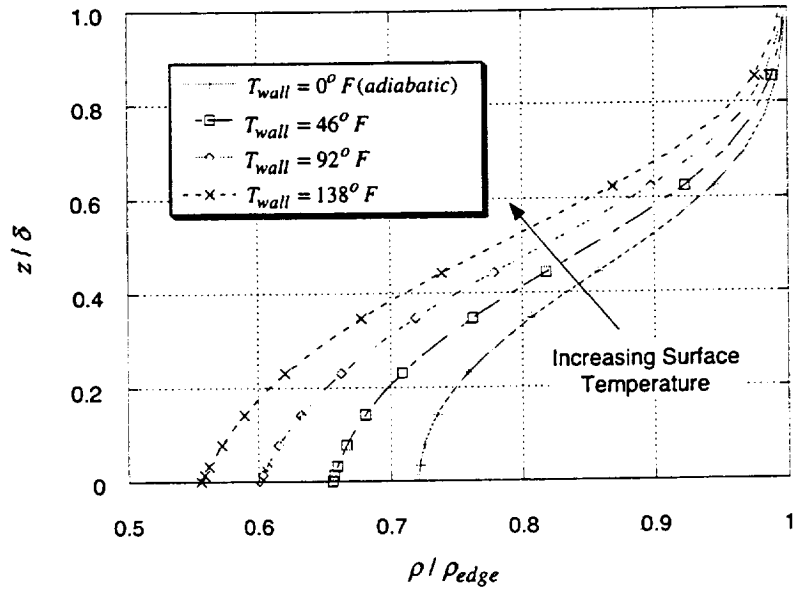

Figure 5-5. Density profiles for the attachment line at y/D = 3.6, $\overline{R}$ = 791, and local Mach number = 1.495.

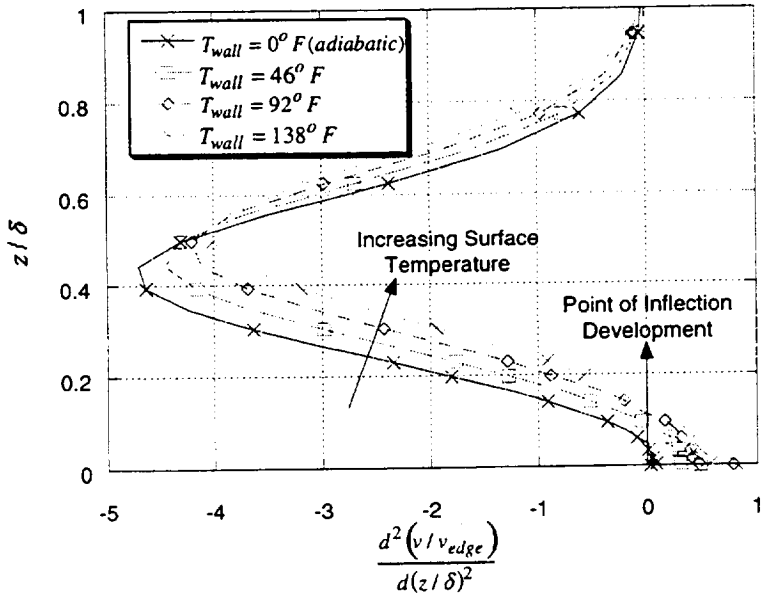

Figure 5-6. Points of inflection in the attachment-line velocity profile with surface temperature. y/D = 3.6, $\overline{R}$ = 791, and local Mach number = 1.495.

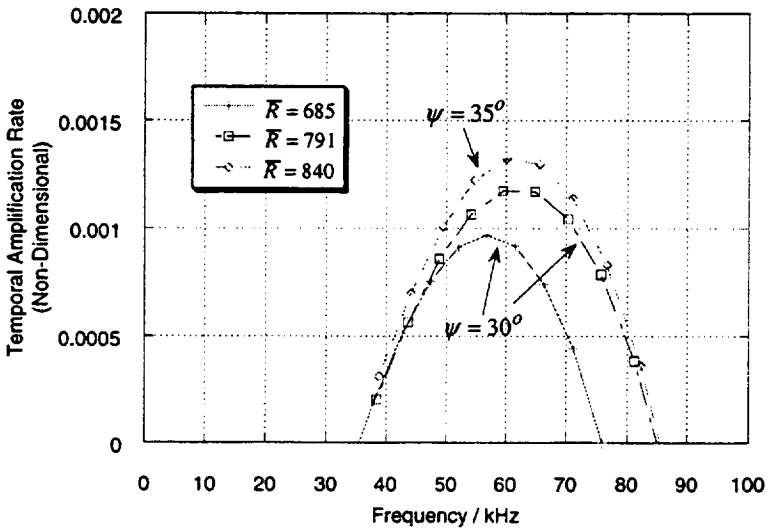

Figure 5-7. Comparison of the largest temporal growth rates with increasing Reynolds number for the adiabatic wall condition at y/D = 3.6.

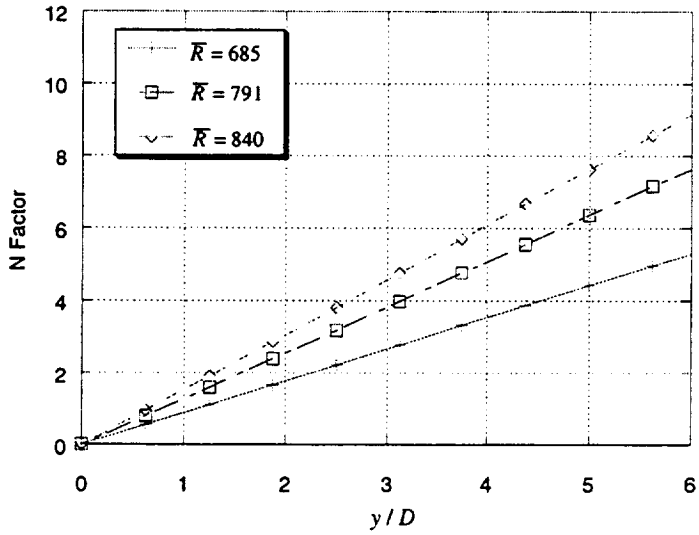

Figure 5-8. N factors for the adiabatic wall condition at y/D = 3.6 with increasing Reynolds number (assuming a constant spatial amplification rate along the attachment line).

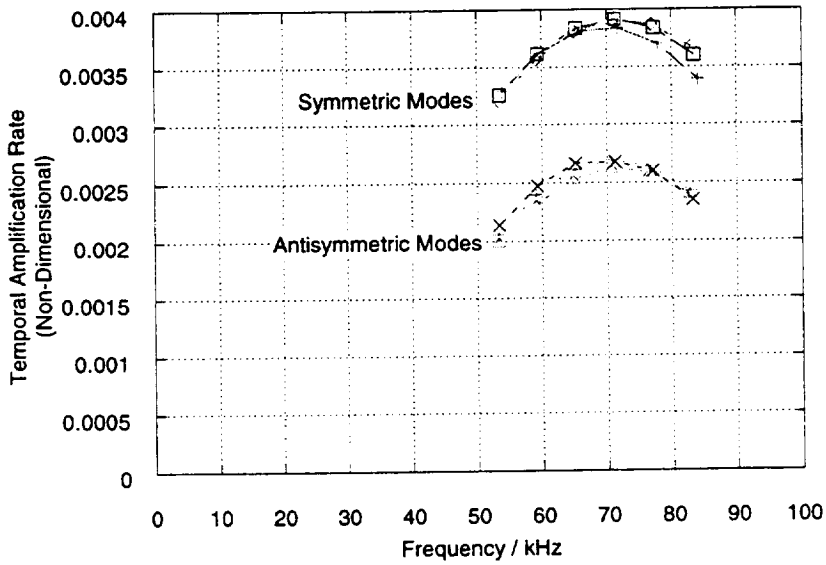

Figure 5-9. Symmetric and antisymmetric modes with surface heating. T_{wall} = 138°F, $\overline{R}$ = 791.

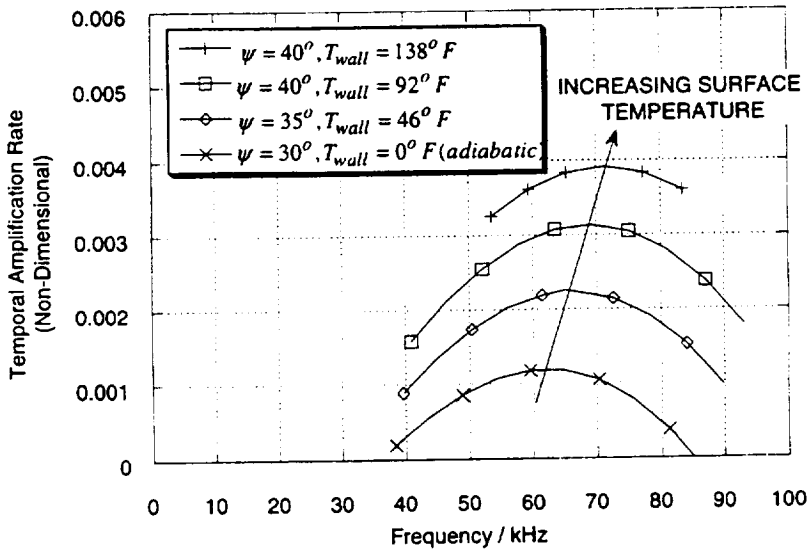

Figure 5-10. Stability code predictions for the heated attachment line at y/D = 3.6, $\overline{R}$ = 791, and local Mach number = 1.495.

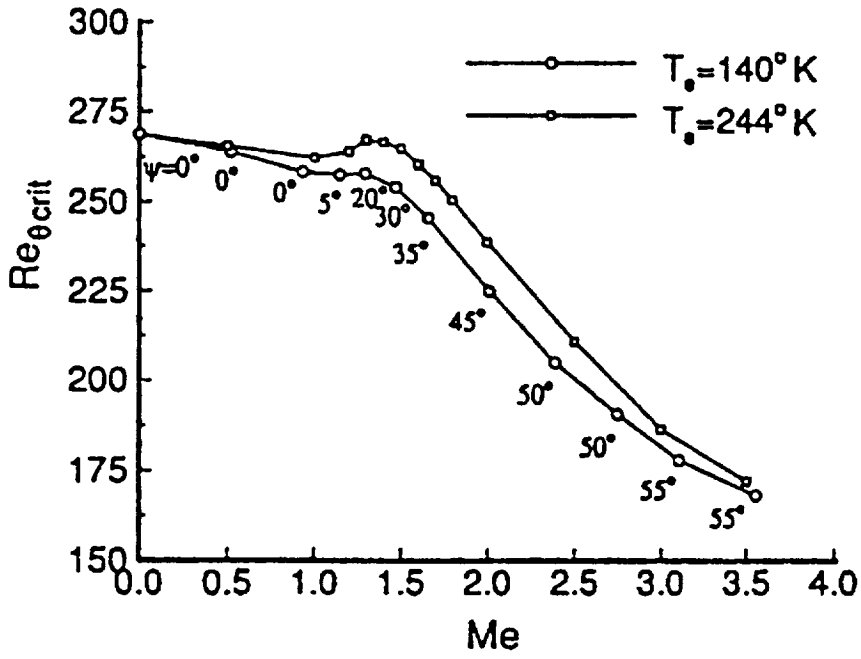

Figure 5-11. Variation of wave angle with edge Mach number calculated by Wie and Collier (ref. 70).

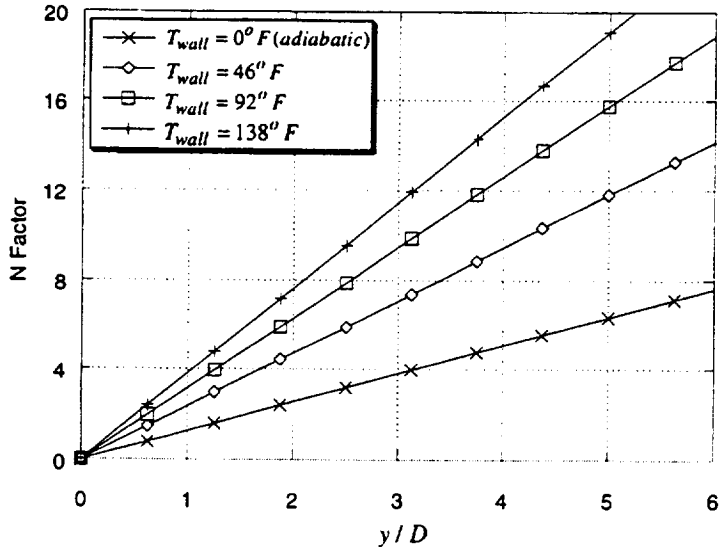

Figure 5-12. N factors for the swept-infinite heated attachment line at $\overline{R}$ = 791 and local Mach number = 1.495.

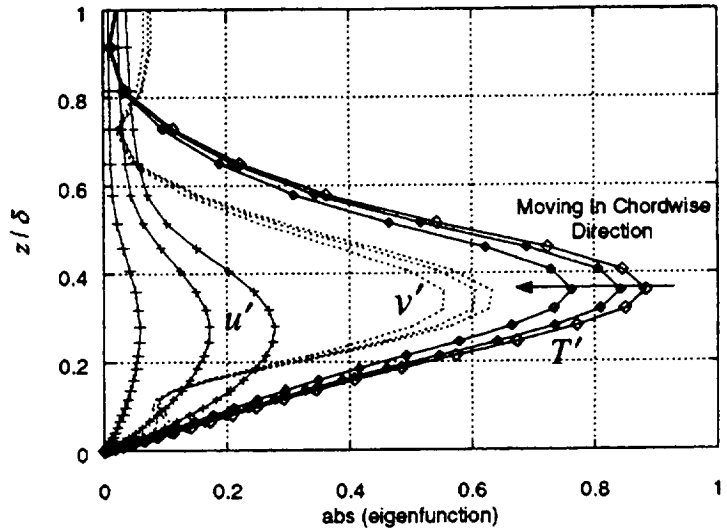

Figure 5-13. Disturbance amplitude functions through the heated attachment-line boundary layer. $\overline{R} = 791$, $T_{wall} = 138°\text{F}$, $\psi = 40°$, and $\beta = 0.14$.

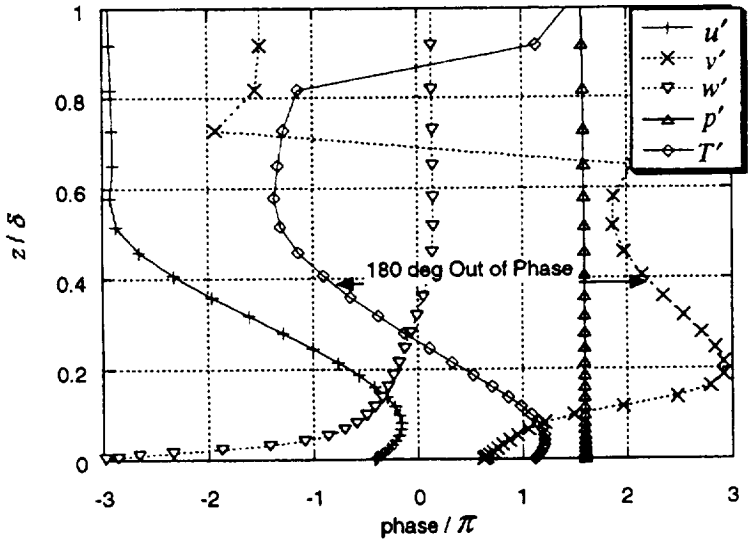

Figure 5-14. Phase relationships for the disturbance amplitude functions through the heated attachment-line boundary layer. $\overline{R} = 791$, $T_{wall} = 138°\text{F}$, $\psi = 40°$, and $\beta = 0.14$.

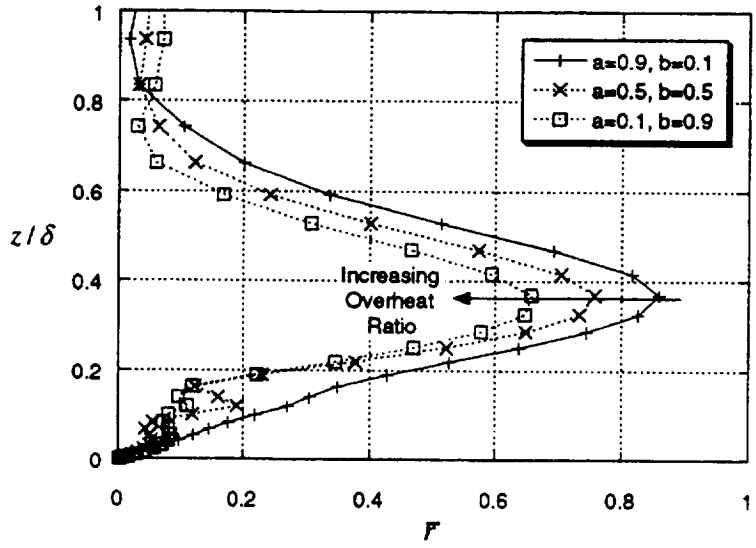

Figure 5-15. Predicted hot-wire response to combined velocity and temperature fluctuations for three different overheat ratios. $\overline{R} = 791$, $T_{wall} = 138°F$, $\psi = 40°$, and $\beta = 0.14$.

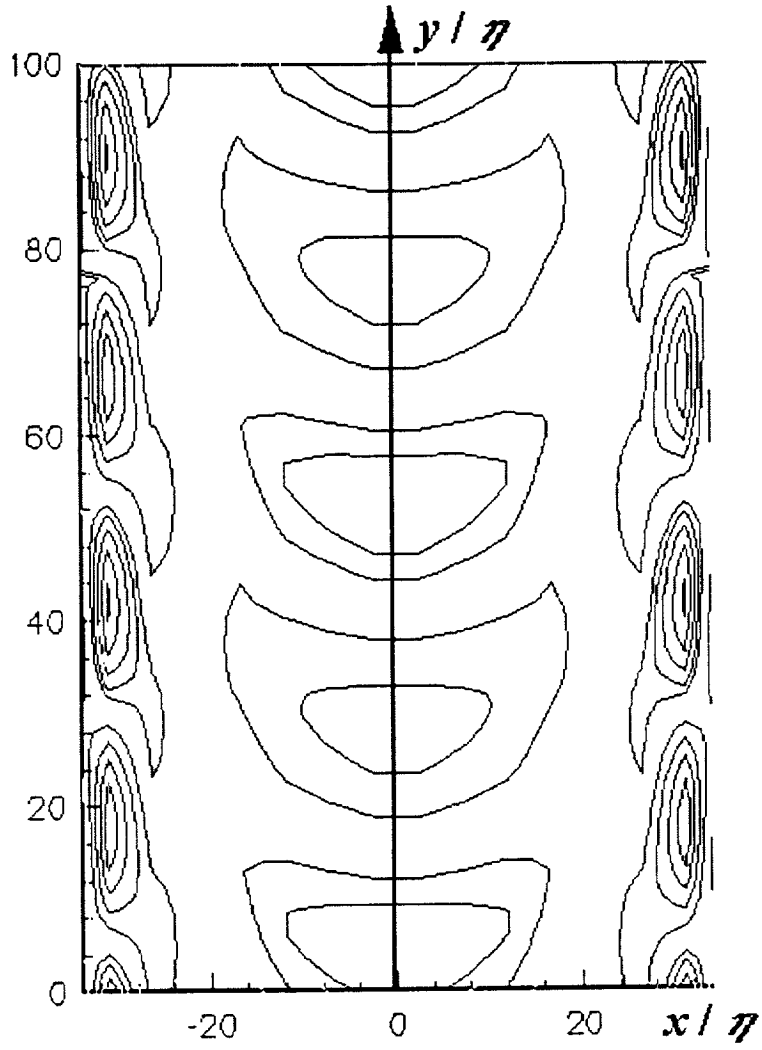

Figure 5-16. Predicted interaction of traveling oblique temperature eigenfunctions at $\overline{R}$ = 791 and local Mach number = 1.495.

6. DISCUSSION

6.1 General Experimental Configuration

The experimental configuration chosen for these tests was the best compromise for the given wind tunnel and test objectives. The use of a forward swept model eliminated the risk of attachment line contamination by the wind tunnel boundary layer, but raised the issue of the tests not being conducted in a truly parallel flow environment. However, the flow in this case has been shown to asymptote approximately to swept-infinite conditions within a few diameters' distance from the tip. What is truly important is that a well conducted experiment be accurately reported so that CFD and stability codes can be applied in the future.

The flow around the finite length swept cylinder was well modeled by the CFD code CFL3D. The predicted bow shock wave (fig. 2-10) was in good agreement with that seen with the Schlieren system (fig. 3-45). Measured equilibrium wall temperatures were also in close agreement with the BL3D predicted values (fig. 3-19).

Using the pressure tapped model to obtain the surface pressure distribution was essential for accurate determination of the length scale η and for values of $\overline{R}$. This was a major improvement over previous tests, which relied solely on CFD-generated values that had no experimental verification (e.g., refs. 65 and 85). Figure 4-11 shows that the attachment line *Cp* values obtained with CFL3D are in reasonable agreement with the experimentally obtained values. Experimentally obtained $\overline{R}$ values (fig. 4-13) are within 10% of the CFL3D solution (fig. 2-7).

Comparison of the chordwise velocity gradient term with other cylinders in supersonic flow revealed that there is an effect of the Mach number normal to the leading edge. As can be seen in figure 4-12, this effect is particularly important for cylinders with subsonic leading edges.

6.2 Trip Wire Data

It has been shown that attachment-line boundary layer transition under the influence of trip wires is a function of wind tunnel disturbance level. The apparent shift of the transition onset boundary to larger trip size, as shown in figures 4-6 and 4-7, could be attributed to a number of influences, most noticeably tunnel disturbance level. The presence of a slight, favorable pressure gradient along the attachment line may also be acting so as to damp out the disturbances and thus delay transition. If the low tunnel disturbance level is the main reason for this shift, then this would suggest that current design practice, based on previous results from conventional tunnels, may be conservative. This would imply that aircraft manufacturers could relax the leading edge machining tolerances for HSCT-type aircraft, thus saving production costs.

In order to more fully explore this new transition onset boundary, tests should be conducted at other values of $\overline{R}$. This would substantiate the current data set and extend the transition onset boundary to both higher and lower values of k/η, thus covering a wider range of $\overline{R}$.

One question that arises is whether the trip wire produced turbulence immediately at the wire or generate disturbances that grew as they convected downstream. If the wire produced turbulence immediately, then moving the trip closer to the hot wire would not alter the Reynolds number at which full turbulence occurs. If, however, the wire introduced disturbances that then amplified, then moving the trip closer to the wire would require a higher Reynolds number to create full turbulence. To answer this question thoroughly would require traverses along the attachment line downstream of a trip wire.

6.3 Observation of Instability Waves

Perhaps the most striking thing of all of the results obtained is the remarkably close agreement of the measured boundary layer disturbance frequencies (fig. 4-18) with those obtained with the stability code (fig. 5-10). Both show the same behavior of increasing amplitude and frequency with heating, and also have good agreement of the frequency of the most amplified disturbance (both around 70 kHz for $T_{wall} \approx 120°F$). This is the first time the frequencies of a supersonic attachment-line boundary layer had ever been experimentally quantified, and their agreement with the 2DEIG code is very encouraging. Further measurements, however, such as disturbance convection speed and disturbance wave angle, should be made before a complete verification of the stability code can be made.

6.4 N Factors

The calculation of N factors for the observed transition fronts (figs. 4-20 and 4-28) can be undertaken with various levels of sophistication. Ideally, one would perform stability analyses based on the local mean flow profiles and surface temperatures at various y/D stations and integrate these varying spatial amplification rates along the attachment line. In order to reduce the complexity of this calculation, approximations may be introduced.

The approximation of constant $\overline{R}$ along the attachment line is reasonable given the experimental evidence fig. 4-13). Therefore, the 2DEIG stability calculations at $y/D = 3.6$ ($\overline{R} = 791$) can be taken to apply to the entire length of the model. Consider again the transition onset in figure 4-20, which appears to occur around $y/D = 4.3$ ($y = 6.9$ inches). The control temperature for this case was 125°F, which is close to the 120°F case investigated with the temperature sensitive paint (fig. 3-65). As can be seen, the surface temperature under these conditions varies almost linearly from 50°F near the tip to 120°F at $y = 7$ inches. Since surface temperature is known to be a strong driver of the spatial amplification rate, this effect must be accounted for. Consider again the spatial amplification rates calculated for the $\overline{R} = 791$ case:

Wall temperature/°F	Spatial amplification rate/inch
0	0.79
46	1.48
92	1.97
138	2.39

Figure 3-65 may then be discretized according to the following:

y range/inch	Average wall temperature/°F	Average spatial amplification rate/inch	Δn_i
0–3.5	69.0	1.72	6.02
3.5–5.5	115.0	2.05	4.10
5.5–6.0	117.5	2.18	1.09
6.0–6.9	117.5	2.18	1.96

which gives a total N factor ($=\sum \Delta n_i$) of 13.17, which is substantially larger than those measured in conventional noisy tunnels.

In the case of the noisy tunnel, the transition onset was located at the same location along the attachment line as for the quiet tunnel, but at a lower control temperature of 90°F, as well as a slightly lower freestream Reynolds number (3.56×10^6/ft versus 3.36×10^6/ft). Referring to the temperature sensitive paint image in figure 3-63, we see that this control temperature corresponds to 30°F near the tip and 95°F at $y = 7$ inches:

y range/inch	Average wall temperature/°F	Average spatial amplification rate/inch	Δn_i
0–2.5	46.0	1.48	3.70
2.5–5.5	76.7	1.81	5.42
5.5–6.9	92.0	1.97	2.76

which gives a total N factor of 11.88.

The spatial amplification rate can be defined as:

$$\beta_i = -\frac{1}{A}\frac{dA}{dy} = -\frac{d}{dy}\ln A$$

(ref. 26), where A is the rms amplitude of any oscillating flow variable. Thus if a hot-wire anemometer follows the peak rms disturbance amplitude downstream, the logarithmic derivative of the signal amplitude can be interpreted as $-\beta$. Consider again the transition onset as located by a hot wire for the quiet tunnel case (fig. 4-20). If the log derivative of the rms signal is plotted versus y, and a straight line fitted to the results (fig. 6-1), a spatial amplification factor of 1.07/inch is obtained for the $T_{control}$ = 125°F case. This can be compared to the 2DEIG obtained rates of 1.97/inch for

T_{wall} = 92°F and 2.10/inch for T_{wall} = 138°F. Further work is obviously required before more conclusions can be drawn concerning the accuracy of the stability method.

6.5 Effect of Tunnel Noise on Attachment-Line Transition

Increasing the freestream disturbance level of the wind tunnel has been shown to hasten the attachment-line transition process, both in the case of the tripped boundary layer and with no trips. Consider again the definition of the N factor at transition onset:

$$e^N = \left(\frac{A_{tr}}{A_0} \right)$$

Therefore if the assumption is made that at transition the amplitude A_{tr} is the same for both quiet and noisy cases ($A_{tr_{noisy}} = A_{tr_{quiet}}$), then:

$$\frac{A_{0_{noisy}}}{A_{0_{quiet}}} = e^{\left(N_{quiet} - N_{noisy}\right)} = e^{13.17-11.88} = 3.6$$

The Kulite signal transducers gave $\left(p'_{noisy}/p'_{quiet}\right) \approx 8$. At first this suggests that the attachment line receptivity mechanism is not linear. However, attention must be brought to the fact that two (approximately determined) large (N factor) numbers are subtracted from each other, thus raising a high level of inaccuracy. More work is clearly necessary to address the mechanism of attachment-line receptivity before a statement concerning its functionality can be stated.

One fact remains clear—one should always have a measurement of the freestream disturbances to correlate with the data being obtained on the model.

6.6 Stability Code Comments

In order to criticize the computational stability results, one must review the approximations contained in both the 2DEIG stability code and the mean flow calculations.

The normal mode assumption (solution being separable in the time and spanwise directions) within 2DEIG was a fair one to make, since it is reasonable to assume that the spanwise wavelength of disturbances is much shorter than the typical length scale of boundary layer variation in the spanwise direction. For instance, the spanwise wavelength of disturbances for the adiabatic wall condition at $\overline{R}$ = 791 was approximately 13δ (≈ 0.13 inch), whereas the typical length scale of boundary layer variation in the spanwise direction was of the order of several cylinder diameters (where diameter = 1.6 inches). The code fully accounted for mean flow variations in both the chordwise and wall-normal directions and, in addition, it admitted general three-dimensional disturbances, which are known to be the most amplified type of disturbances at this Mach number. As a result, this code can be considered to be state of the art, and improvements in the overall technique must first be found in the mean flow calculations.

Two important considerations stand out as far as the mean flow calculations are concerned: (1) the resolution of the finite length flow field, especially near the cylinder tip region, and (2) the accurate definition of the attachment-line temperature distribution for input to the stability calculations.

The cylinder tip region has been shown to be an important consideration in initializing the attachment-line boundary layer. Great care must be exercised to ensure that a sufficiently dense and smooth computational (CFL3D) grid is placed around the tip to capture the rapidly changing flowfield in that area.

At the moment, the boundary layer mean flow input to the stability calculations are based on the locally swept infinite code SCALBL, which is sufficient for constant temperature regions far away from the tip. However, if there is a surface temperature gradient along the attachment line, then the temperature profile at a given distance along the cylinder will not be the same as if the whole cylinder were at the local wall temperature. This will lead to changes in density and viscosity profiles and, therefore, if the surface temperature gradient is large enough, to significant changes in stability characteristics. If possible, the attachment-line boundary layer should be calculated by a truly three-dimensional spanwise marching program or, otherwise, with (1) constant wall temperature or (2) the measured wall temperature. A stability calculation would then show whether these effects are large enough to worry about. However, no such code exists at this moment and such a calculation will probably never be done, since to facilitate marching, a set of initial conditions must be provided to the code. Unfortunately, for the current swept cylinder problem, there is no shortcut for finding that initial condition. This leaves the full Navier-Stokes solution, which, although not impossible, is a computationally expensive exercise.

As seen in the temperature sensitive paint images, a significant chordwise temperature gradient is established as surface heating is increased. The effect of this on the stability calculations has yet to be explored.

6.7 Crossflow

The hot-wire signals at $\theta = 30°$ repeatedly gave a turbulent signal (figs. 4-23 and 4-25), which suggests that crossflow instability is present and responsible for this amplification. Increasing the surface heating had no effect on the hot-wire signal for $T_{wall} \leq 100°F$, at which point the attachment-line-type bulge appeared, indicative of the large amplitude disturbances "spilling over" from the attachment line to the hot-wire position.

In order to predict the most amplified crossflow disturbances as a function of θ, a code such as COSAL (employing a swept-infinite assumption) could be used as a first approximation. This could also address the amplification of the traveling crossflow disturbances to check that stationary crossflow vortices are indeed the most amplified for this configuration.

6.8 Hot-Wire Instrumentation

Since the interpretation of the boundary layer physics relies on the instrumentation used to make measurements, attention must be paid to the primary diagnostic tool, namely the hot wire.

The first issue concerns the placement of the wire within the boundary layer. Since neither a boundary layer traverse mechanism nor a reliable optical verification were available, the exact position of the hot wire within the layer was always unknown. This raises the question of what part of the eigenfunction the wire was measuring. Since the boundary layer thickness will change slightly with surface temperature, then traversing the wire along the attachment-line temperature gradient at constant z will undoubtedly alter the z/δ location.

The calibration of the hot wire was also an issue, since it was desired to obtain quantified disturbance amplitudes and growth rates. However, as mentioned in Chapter 3, the hot-wire sensitivity to total temperature and the incorporation of Mach number into the $Nu = Nu(Re)$ relationship would first be required. Also, the dependence of the hot-wire sensitivity to overheat ratio would need to be more fully explored, as would the sensitivity of the calibration to increasing surface temperature (resulting in large temperature fluctuations).

6.9 Suggestions for Future Work

Future work in this area should address improvements to the current experiment as well as directions for increasing our understanding of the flow physics.

The current experiment can be improved primarily through better instrumentation. First and foremost, a boundary layer traverse is required not only to position the hot wire accurately in the z direction through the layer, but also to traverse along the span and in the chordwise directions of the model. This would produce the eigenfunction distribution through the layer, track disturbances generated downstream of trip wires, and detect the evolution of transition due to crossflow vortices. Time would also be saved since multiple points could be acquired during a single test. The positioning of the wire in the layer should also be initially verified by optical means, implying that a suitable vibration isolation scheme be found for the legs of the telescope tripod. To aid in the boundary layer mean flow determination, a small pitot pressure probe should be developed (less than 0.001 inch diameter). This could be attached to the boundary layer traverse mechanism. Pressures in the tunnel need to be accurately measured with respect to a reference condition, requiring a high accuracy absolute pressure transducer. The resolution of the data acquisition system would also be increased by replacing the 12 bit A/D card with a 16 bit A/D card. Oscillations in the tunnel stagnation pressure should be addressed by changing the appropriate proportional with integral and derivative (PID) parameters in the tunnel control system. If this is not possible, then the computer DMA buffer size should be increased so that longer periods of time-dependent data may be recorded. The hot-wire probe design should also be readdressed, with a smaller support block preferred (this is related to the boundary layer traverse). Hot-wire calibration would also be desirable, but would be a major research undertaking in its own right. Determination of the disturbance wave angle would be a major verification of the stability code, and might be achievable with two hot wires. Hot films laid on the surface of the cylinder could also be used in order to obtain the convection speed of the disturbances along the attachment line. Different internal heating arrangements could be tried in order to try to reduce the chordwise and spanwise temperature gradients. The naphthalene sublimation technique could be improved by trying a different sublimation chemical that has a vapor pressure/temperature characteristic which would allow sublimation at the adiabatic wall temperatures. And finally, observation of the transition onset might be achievable using the temperature sensitive paint technique if the model were thin-walled and made from a poor thermal conductor.

On the computational front, the current results could be improved by performing a finite-length stability analysis for the case of the captured transition front along the attachment line. Such an analysis would involve the generation of a flowfield by a Navier-Stokes code, providing sufficient resolution in the normal direction through the boundary layer to resolve the second derivatives necessary for stability analysis. This would provide a definitive solution for the generation of N factors that could be compared to the simplistic swept-infinite cylinder approximation.

Directions for future research should include the mapping out of the so-called Poll chart to both higher and lower values of $\overline{R}$. Three-dimensional disturbances could also be investigated, particularly placed in the chordwise direction to study the contamination of the attachment line. Many ideas arise concerning the input of controlled disturbances into the attachment-line flow, such as oblique disturbances and harmonic sources (to amplify a single frequency). Oblique disturbances could be input via suitably positioned electrodes in the surface of the model. Harmonic sources are usually input with subsurface speakers, or speakers in the settling chamber with a suitable receptivity mechanism.

Having established the physics of the attachment-line flow, the next phase of the investigation could revolve around control mechanisms, such as surface suction, and how suction should be applied (i.e., hole size, placement, suction coefficients). Only then could one definitively describe how to place a laminar flow control surface along the leading edge of a HSCT-type aircraft.

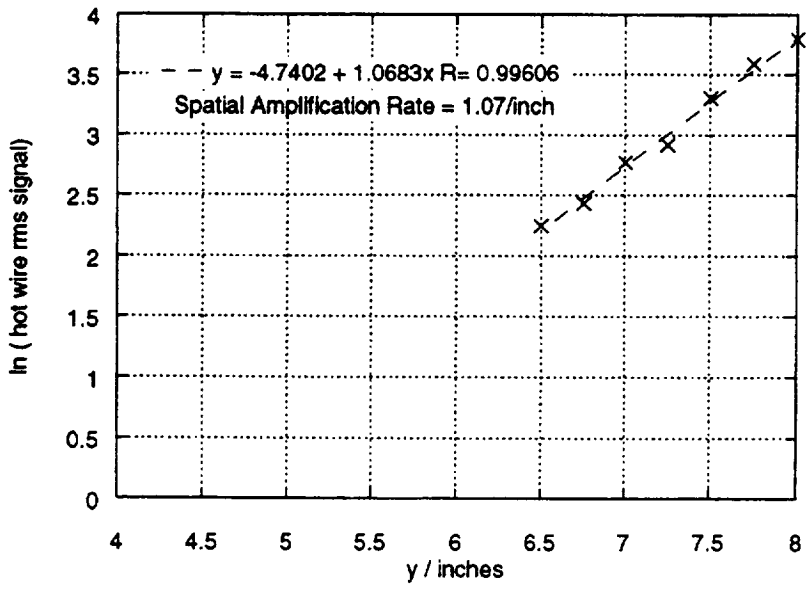

Figure 6-1. Measured spatial amplification rate for the quiet tunnel transition onset case. $Re_{\infty} = 3.56 \times 10^6$/ft and $T_{control}$ = 125°F ($\overline{R} \approx 800$).

7. CONCLUSIONS

- Experiments were conducted on a 76° swept cylinder to establish the behavior of the attachment-line transition process in a quiet, low supersonic Mach number flow. The use of a finite length cylinder has been shown to be a useful tool for modeling the flow along the leading edge of a highly swept supersonic wing and for studying the flow physics of the attachment-line transition process.

- The use of a pressure tapped model allowed for accurate values of $\overline{R}$ and η to be experimentally obtained, and these were in approximate agreement with those obtained with CFD.

- A hot-wire anemometer system, capable of achieving frequency responses in excess of 200 kHz, was developed for Mach 1.6 operation.

- For a near adiabatic wall condition, the attachment-line boundary layer remains laminar up to the largest obtainable $\overline{R}$ of 760 at an s/η of 3300.

- The attachment-line boundary layer transition under the influence of gross contamination (i.e., trip wires) is a function of wind tunnel disturbance level, and a transition onset boundary for this flow is established. This boundary suggests that current design practice, based on previous results from conventional tunnels, may be conservative.

- The use of internal heating to raise the surface temperature of the attachment line in order to induce boundary layer disturbances was demonstrated experimentally.

- The frequencies of the most amplified attachment-line boundary layer disturbances were quantified over a range of temperature settings.

- Experimental results were in very close agreement to those predicted by a linear stability code by R. -S. Lin of High Technology Corporation, Hampton, Virginia, and provided the first-ever experimental verification of these disturbances and the nature of their growth with surface heating.

- A controlled data set was obtained for transition onset along the heated attachment line at $\overline{R} \approx 800$ under quiet tunnel conditions. This transition location was found to correlate with an approximate N factor of 13.2.

- Increasing the tunnel disturbance level through the use of trips on the walls of the wind tunnel caused the transition onset to occur at lower wall temperatures. This transition location was found to correlate with an approximate N factor of 11.9, so suggesting that the attachment line is receptive to increases in the freestream disturbance level.

- Flow visualization techniques used included Schlieren photography, oil flow, temperature sensitive paint, and naphthalene sublimation. The latter revealed the presence of stationary crossflow vortices off the attachment line, and a hot wire traversed in the chordwise direction appeared to indicate that these vortices led to turbulent flow around an angle of 30°.

APPENDIX A—SWEPT CYLINDER LOAD ANALYSIS

The swept cylinder has spacer blocks which provide vertical height alteration. Maximum test section blockage is obtained with the cylinder in its lowest position. In this condition, the frontal area presented to the oncoming airflow is 5.5 inches long and 1.6 inches in width (8.8 in^2 area), resulting in 6.9% blockage.

Selected Materials

The following material properties were taken from CRC Handbook (ref. 130):

- Aluminum 6061 T6 (ultimate strength at 75°F = 45,000 psi) for cylinder model and window blank.
- Aluminum 2024 (ultimate strength at 75°F = 25,000 psi) for cylinder spacer (later changed to a fully cured polyurethane polymer), splitter plate, splitter plate spacer, and splitter plate support blocks.
- All screws were Grade 8 and met Mil Specifications.

Natural Frequencies of Model

The swept cylinder was modeled by a normally cantilevered circular beam of 16.534 inch length, 1.6 inch diameter, and 0.125 inch constant wall thickness. From reference 131, the frequencies (in hertz) of the first three fundamental modes of such a cantilevered beam are:

$$f_1 = \frac{1.758}{\pi L^2}\sqrt{\frac{EI}{\rho A}}$$

$$f_2 = \frac{11.015}{\pi L^2}\sqrt{\frac{EI}{\rho A}}$$

$$f_3 = \frac{30.850}{\pi L^2}\sqrt{\frac{EI}{\rho A}}$$

where $A = r^2\pi$ and $I = r^3 t\pi$.

Also from reference 130:

$$\rho\,(6061\ \text{AL}) = 0.098\ \text{lb/in}^3$$

$$E\,(6061\ \text{AL}) = 10.0 \times 10^6\ \text{psi}$$

Therefore:

$$f_1 = 10,\ f_2 = 64, \text{ and } f_3 = 180 \text{ Hz}$$

A potential for oscillatory, shedding vortices exists with frequencies in the range $431 < f < 582$ Hz (Section 3.5.8). Since the first three natural modes of vibration for the cylinder are not in this range, a state of vortex-induced cylinder resonance is not predicted.

Maximum worst case loading on the model is given by applying maximum tunnel pressure, i.e., applying p_0 over the area of the model. Maximum p_0 = 10 psia. If this loading were directed so as to be normal to the cylinder, then the projected area of the cylinder would be maximized at 26.2 in^2. This would produce a maximum total force of 264 lb. Resolving moments and forces about the root of the model produces a maximum root moment = 2178 in-lb, and a maximum vertical force at the root of 256 lb.

From Oberg et al. (ref. 132), the deflections at the tip of the model are given by:

$$\delta = \frac{WL^3}{8EI}$$

This yields a maximum deflection = 0.093 inch, which would correspond to an alteration of the sweep angle by 0.32°.

Bolt Failure Due to Shear

A bolt of diameter d and length L under tension and an applied normal force can be modeled by applied axial and normal forces of F_x and F_y, respectively, applied at the end of the bolt. According to reference 132, this gives rise to stresses at the built-in end of the bolt (at positions a and b) of:

$$\sigma_a = \frac{1.273}{d^2}\left(\frac{8LF_y}{d} - F_x\right) \quad \text{and} \quad \sigma_b = -\frac{1.273}{d^2}\left(\frac{8LF_y}{d} + F_x\right)$$

where the maximum normal stress is given by:

$$\tau_a = 0.5\sigma_a \quad \text{and} \quad \tau_b = 0.5\sigma_b$$

If all model loads are transmitted solely through the forward 0.5 inch support bolt, then F_x = 88 lb and F_y = 256 lb. With L = 4.5 inches, this produces a maximum stress at point b of σ_b = 1118 + F/4 or τ_b = 559 + F/4, where F is the tension due to bolt tightening. If we assume F = 100 lb, then τ_b = 584 lb/in^2 resulting in a shear force = 1174 lb.

Engineering Manual Series (ref. 133) gives the material strength for this support bolt as 17,535 lb. Therefore, the factor of safety for this design due to bolt shear failure is 15.

APPENDIX B—PRESSURE MODEL MACHINING NOTES

A 1.6 inch diameter cylindrical rod, made from AL 6060 T6 and gun-bored, and a 14° split box holder for the cylinder were supplied from the Ames Machine Shop. All machining mentioned here was undertaken in the Fluid Mechanics Laboratory by the author.

1. A milling machine was used to cut a 7 inch long, 120° wide opening in one side of the cylinder to create an access panel.

2. The smallest drill bit in the FML workshop was a size 70; hence the tap holes were chosen to be of 0.020 inch internal diameter. These holes were carefully drilled out perpendicular to the cylinder surface using the milling machine according to the pressure port hole pattern (see text).

3. Using a bull nose cutter, an access panel was cut from another 1.6 inch diameter AL 6061 T6 cylinder, also supplied by the Ames Machine Shop. This was fitted by hand into the opening of the original cylinder. The panel was then temporarily attached to the cylinder for finishing of the external diameter and initial polishing.

4. 8×2-56 (UNC) machine screws were drilled and tapped to hold the access panel onto the cylinder. These were countersunk with their heads contoured to fit the surface of the cylinder.

5. The cylinder was then placed in the 14° split box holder in order to cut the parallel ends of the model. Great care was exercised in making the final cuts to the apex. A special support structure was built around the apex to lessen the vibration level of the model. Final cuts were made at 0.001 inch to get a high surface finish.

6. The two holes for the attachment bolts were then drilled, followed by the hole for the pressure tubing. Since the latter hole was doglegged, great care was taken to align and assure correct depth of bores. The inside corner of this instrumentation hole was rounded so that the plastic pressure tubing did not become severed.

7. The access panel was then removed, and the pressure tap piping was constructed. External size 70 holes were widened to size 60 holes on the inside of the cylinder, into which small stainless steel pipes (size 17 AWG) were lightly hammered. An aluminum based bi-epoxy was then applied with a syringe to form the seal around the stainless steel piping and the interior cylinder surface.

8. 10 ft long pieces of clear Tygon tubing were fed through the instrumentation hole and connected to the stainless steel pipes (working rearward from cylinder tip) and numbered accordingly.

9. A vacuum test was then applied. Tape was used to seal off all the exterior faces of the pressure ports, and a vacuum pressure was sequentially applied to each. All ports held their applied pressure.

10. The tape was then removed and all but two ports returned to atmospheric pressure. A size 70 drill bit was used to remove superfluous filler, and both ports returned to atmospheric pressure.

11. The exterior faces of the ports and the ends of the Tygon tubing were then sealed.

12. Various designs were considered for sealing the apex area of the cylinder, but the most favorable was a solid insert that could slide into the open end of the model and be machined to shape. The insert was shaped so as to pass over the pressure port piping and yet have enough interior area to allow for fastening to the cylinder with machine screws.

13. Two 3/8 inch diameter breather holes were drilled into the model on the rearward facing side in the apex area. These were to allow for fast equalization of pressure at tunnel startup and also to aid in draining the model of water.

14. Final finishing was achieved by filling joins and screw heads with wax, then polishing.

15. With the complete assembly finished, the pressure tests were repeated with no failures.

Views of the finished pressure tap model can be seen in figure 3-20.

APPENDIX C—ESTIMATION OF POWER REQUIRED FOR HEATED CYLINDER

The first power estimation was taken from reference 115. For a cylinder in crossflow, a correlation of the form:

$$Nu_D = C\,Re_D{}^m Pr^n \left(Pr_\infty / Pr_w\right)^{1/4}$$

is proposed for the range $0.7 < Pr < 500$, $1 < Re_D < 10^6$. All properties are evaluated at T_∞, except Pr_w, which is evaluated at T_w. Common values of C and m were listed in tabular form for a range of operating conditions. Estimates were based on the following conditions:

$Re_\infty = 3.5 \times 10^6$

$Re_D = 0.46 \times 10^6$

$M_\infty = 1.6$

$T_w = 171°\text{F} = 350\text{K}$

$T_0 = 25°\text{F} = 269\text{K}$

From the provided tables:

$C = 0.076$

$m = 0.7$

$n = 0.37$

The Prandtl numbers were taken as:

$Pr_\infty = 0.746$

$Pr_w = 0.722$

$Pr = 0.7$

Therefore:

$$Nu_D = 639$$

Newton's law of convection cooling for a steady state process with uniform surface temperature and no radiative heat losses was assumed:

$$\frac{q_w}{A(T_w - T_\infty)} = Nu_D \frac{k}{D}$$

A 15% heat loss for conduction through the end of the model was also assumed. The surface area of the model was approximated by $A = \pi DL$. This resulted in a power requirement = 2 kW, which translated into a watt density = 33 W/m^2.

The second estimation was taken from reference 116:

$$Nu_D = 0.3 + \frac{0.62 Re_D^{1/2} Pr^{1/3}}{\left[1 + (0.4/Pr)^{2/3}\right]^{1/4}} \left[1 + \left(\frac{Re_D}{28200}\right)^{1/2}\right]$$

This was found to be a good correlation for flows in the range $0.746 \times 10^5 < Re_D < 4.046 \times 10^5$.

If the same approximations are made as before, this equation yields:

$$Nu_D = 746 \text{ (for } Pr = Pr_\infty)$$

and

$$Nu_D = 766 \text{ (for } Pr = Pr_w)$$

This results in power requirements of 2.3 and 2.4 kW, respectively, which are in approximate agreement with the previously obtained value of 2.0 kW.

REFERENCES

1. Boeing Commercial Airplanes: Current Market Outlook. Feb. 1988.
2. Boeing Commercial Airplanes New Airplanes Development: High Speed Civil Transport Study. NASA CR-4233, Sept. 1989.
3. McDonnell Douglas Corporation: 1989 High Speed Civil Transport Studies. NASA CR-187545, Sept. 1991.
4. Boeing Commercial Airplane Company: Application of Laminar Flow Control to Supersonic Transport Configurations. NASA CR-181917, July 1990.
5. Rayleigh, J. W. S., Lord: On the Stability of Certain Fluid Motions. Proceedings of the Mathematical Society of London, vol. 11, no. 57, 1880.
6. Gaster, M.: On the Flow Along Swept Leading Edges. The Aeronautical Quarterly, Vol. XVIII, May 1967, pp. 165–184.
7. Gregory, N.: Transition and the Spread of Turbulence on a 60° Sweptback Wing. Journal of the Royal Aeronautical Society, vol. 64, Sept. 1960, pp. 562–564.
8. Pfenninger, W.: Flow Phenomena at the Leading Edge of Swept Wings. Recent Developments in Boundary Layer Research, Part IV, AGARDograph 97, May 1965.
9. Topham, D. R.: A Correlation of Leading Edge Transition and Heat Transfer on Swept Cylinders in Supersonic Flow. Journal of the Royal Aeronautical Society, vol. 69, part 1, Jan. 1965, pp. 49–52.
10. Poll, D. I. A.: Some Aspects of the Flow Near a Swept Attachment Line with Particular Reference to Boundary Layer Transition. Cranfield Institute of Technology, College of Aeronautics Ph.D. Thesis, June 1978.
11. Poll, D. I. A.: Transition in the Infinite Swept Attachment Line Boundary Layer. The Aeronautical Quarterly, Vol. XXX, Part 4, Nov. 1979, pp. 607–629.
12. Poll, D. I. A.: A Simple Method for the Prediction of Skin Friction and Heat Transfer Rate at an Infinite Swept Attachment Line. Cranfield College of Aeronautics Report 8006, 1980.
13. Poll, D. I. A.: Skin Friction and Heat Transfer at an Infinite Swept Attachment Line. The Aeronautical Quarterly, Vol. XXXII, pp. 259-318, 1981.
14. White, F. M.: Viscous Fluid Flow. Second Edition, McGraw-Hill, New York, 1991.
15. Morkovin, M. V.: Critical Evaluation of Transition from Laminar to Turbulent Shear Layers with Emphasis on Hypersonically Traveling Bodies. Report AFFDL-TR-68-149, Mar. 1969.
16. Paté, S. R.: Effects of Wind Tunnel Disturbances on Boundary-Layer Transition with Emphasis on Radiated Noise. AIAA Paper 80-0431, 11th Aerodynamic Testing Conference, Mar. 18–20, 1980.

17. Dougherty, N. S.; and Fisher, D. F.: Boundary-Layer Transition on a 10-Degree Cone: Wind Tunnel/Flight Data Correlation. AIAA Paper 80-0154, AIAA 18th Aerospace Sciences Meeting, Jan. 1980.

18. Wilkinson, S. P.; Anders, S. G.; Chen, F. J.; and Beckwith, I. E.: Supersonic and Hypersonic Quiet Tunnel Technology at NASA Langley. AIAA Paper 92-3908, AIAA 17th Aerospace Ground Testing Conference, July 6–8, 1992.

19. Herbert, Th.: Boundary-Layer Transition-Analysis and Prediction Revisited. AIAA Paper 91-0737, AIAA 29th Aerospace Sciences Meeting, Jan. 7–10, 1991.

20. Bertolotti, F. P.: Linear and Nonlinear Stability of Boundary Layers with Streamwise Varying Properties. Ph.D. Thesis, Ohio State University, 1992.

21. Smith, A. M. O.: Transition, Pressure Gradient and Stability Theory. Proceedings of the International Congress of Applied Mechanics, Brussels, 1956, pp. 234–244.

22. Smith, A. M. O.; and Gamberoni, N.: Transition, Pressure Gradient and Stability Theory. Douglas Aircraft Report ES-26388, 1956.

23. Van Ingen, J. L.: A Suggested Semi-Empirical Method for the Calculation of the Boundary Layer Transition Region. University of Delft Report VTH-74, Delft, the Netherlands, 1956.

24. Gaster, M.: A Note on a Relation Between Temporally Increasing and Spatially Increasing Disturbances in Hydrodynamic Stability. Journal of Fluid Mechanics, vol. 14, 1962, pp. 222–224.

25. Mack, L. M.: The Stability of the Compressible Laminar Boundary Layer According to a Direct Numerical Solution. Proceedings of AGARD Specialists Meeting on "Recent Developments in Boundary Layer Research," Naples, Italy, May 10–14, 1965.

26. Mack, L. M.: Boundary Layer Stability Theory. Report 900-277 Rev. A., Jet Propulsion Laboratory, Pasadena, CA, Nov. 1969.

27. Mack, L. M.: Linear Stability Theory and the Problem of Supersonic Boundary-Layer Transition. AIAA Journal, vol. 3, 1975, pp. 278–289.

28. Mack, L. M.: Boundary-Layer Stability Theory. AGARD R-709, 1984.

29. Arnal, D.: Boundary Layer Transition: Prediction, Application to Drag Reduction. AGARD R-786, Mar. 1992.

30. Arnal, D.: Boundary Layer Transition: Predictions Based on Linear Theory. AGARD R-793, Apr. 1994.

31. Gray, W. E.: The Nature of the Boundary Layer Flow at the Nose of a Swept Wing. RAE TM 256, 1952.

32. Owen, P. R.; and Randall, D. G.: Boundary Layer Transition on a Sweptback Wing: a Further Investigation. R.A.E. TM Aero 330, Feb. 1953.

33. Gregory, N.; and Love, E. M.: Laminar Flow on a Swept Leading Edge—Final Progress Report. NPL Aero. Memo. 26, 1965.

34. Pfenninger, W.; and Bacon, J. W.: Amplified Laminar Boundary Layer Oscillations and Transition at the Front Attachment Line of a 45° Flat-Nosed Wing with and without Boundary Layer Suction. Viscous Drag Reduction, C. S. Wells, ed., Plenum Press, 1969.

35. Cumpsty, N. A.; and Head, M. R.: The Calculation of Three-Dimensional Turbulent Boundary Layers. Part II. Attachment Line Flow on an Infinite Swept Wing. The Aeronautical Quarterly, Vol. XVIII, May 1967, pp. 150–164.

36. Cumpsty, N. A.; and Head, M. R.: The Calculation of Three-Dimensional Turbulent Boundary Layers. Part III. Comparison of Attachment Line Calculations with Experiment. The Aeronautical Quarterly, Vol. XX, May 1969, pp. 99–113.

37. Poll, D. I. A.: Transition Description and Prediction in 3D Flows. AGARD Report 709, 1984, pp. 5.1–5.23.

38. Poll, D. I. A.; and Paisley, D. J.: On the Effect of Wing Taper and Sweep Direction on Leading Edge Transition. Aeronautical Journal, Mar. 1985, pp. 109–117.

39. Arnal, D.; and Juillen, J. C.: Etude de la Transition et de la Contamination de Bord d'Attaque sur Ailes en Fleche. AGARD CP 438, 1988.

40. Arnal, D.; and Juillen, J. C.: Leading Edge Contamination and Relaminarization on a Swept Wing at Incidence. 4th Symposium on Numerical and Physical Aspects of Aerodynamic Flows, Cebeci, T., ed., Springer-Verlag, 1989.

41. Hardy, D. C.: Experimental Investigation of Attachment Line Transition in Low Speed, High Lift Wind Tunnel Testing. AGARD CP 438, 1988.

42. Bippes, H.: Instability Features Appearing on Swept Wing Configurations. IUTAM Symposium "Laminar-Turbulent Transition," Toulouse, D. Arnal and R. Michel, eds., Springer-Verlag, 1990.

43. Fisher, D. F.; and Fischer, M. C.: Development Flight Tests of Jetstar LFC Leading-Edge Test Experiment. Research in Natural Laminar Flow and Laminar-Flow Control, NASA CP-2487, Part I, 1987, pp. 117–140.

44. Maddalon, D. V.; Collier, F. S.; Montoya, L. C.; and Land, C. K.: Transition Flight Experiments on a Swept Wing with Suction. AIAA Paper 89-1893, 1989.

45. Meyer, R. R.; Trujillo, B. M.; and Bartlett, D. W.: F-14 VSTFE and Results of the Clean Up Flight Test Program. Research in Natural Laminar Flow and Laminar-Flow Control, NASA CP-2487, 1989, pp. 819–844.

46. Joslin, R. D.: History of Laminar Flow Control. Submitted as a NASA RP, Mar. 1997.

47. Joslin, R. D.: Aircraft Laminar Flow Control. Annual Review of Fluid Mechanics, vol. 30, 1998.

48. Hall, P.; Malik, M. R.; and Poll, D. I. A.: On the Stability of an Infinite Swept Attachment Line Boundary Layer. Proceedings of the Royal Society London, A395, 1984, pp. 229–245.

49. Hall, P.; and Malik, M.: On the Instability of a Three-Dimensional Attachment-Line Boundary Layer: Weakly Nonlinear Theory and a Numerical Approach. Journal of Fluid Mechanics, vol. 163, 1986, pp. 257–282.

50. Spalart, P. R.: Direct Numerical Study of Leading Edge Contamination. AGARD CP 438, 1988.

51. Poll, D. I. A.; and Danks, M.: Relaminarization of the Swept Wing Attachment-Line by Surface Suction. IUTAM Symposium on Laminar-Turbulent Transition, Sendai, Japan, Sept. 5–9, 1994.

52. Juillen, J. C.; and Arnal, D.: Experimental Study of Boundary Layer Suction Effects on Leading Edge Contamination along the Attachment Line of a Swept Wing. IUTAM Symposium on Laminar-Turbulent Transition, Sendai, Japan, Sept. 5–9, 1994.

53. Joslin, R. D.: Direct Simulation of Evolution and Control of Nonlinear Instabilities in Attachment-Line Boundary Layers. AIAA Paper 94-0826, 32nd Aerospace Sciences Meeting and Exhibit, Jan. 1994.

54. Lin, R. -S.; and Malik, M. R.: The Stability of Incompressible Attachment-Line Boundary Layers—A 2D Eigenvalue Approach. AIAA Paper 94-2372, 1994.

55. Lin, R. -S.; and Malik, M. R.: A Generalized Method for the Stability of Incompressible Attachment-Line Flow. Transition, Turbulence and Combustion, Hussaini, et al., eds., Kluwer Academic Pub., 1994.

56. Lin, R. -S.; and Malik, M. R.: On the Stability of Attachment-Line Boundary Layers: Part 1. The Incompressible Swept Hiemenz Flow. Journal of Fluid Mechanics, vol. 311, 1996, pp. 239–255.

57. Dunning, R. W.; and Ulmann, E. F.: Effects of Sweep and Angle of Attack on Boundary Layer Transition on Wings at Mach Number 4.04. NACA TN-3473, Mar. 1955.

58. McTigue, J. G.; Overton, J. D.; and Petty, G. P.: Two Techniques for Detecting Boundary Layer Transition in Flight at Supersonic Speeds and at Altitudes above 20,000 Feet. NASA TND-18, Aug. 1959.

59. Beckwith, J. E.; and Gallagher, J. J.: Local Heat Transfer and Recovery Temperature on a Yawed Cylinder at a Mach Number of 4.15 and High Reynolds Numbers. NASA TR R-104, 1961.

60. Brun, E. A.; Diep, G. B.; and le Fur, B.: Transport de Chaleur et de Masse sur des Cylindres Circulaires en Fleche dans un Ecoulement Supersonique (Transport of Heat and Mass on Swept Circular Cylinders in a Supersonic Flow). AGARDograph 97, 1965.

61. Bushnell, D. M.: Interference Heating on a Swept Cylinder in Region of Intersection with a Wedge at Mach Number 8. NASA TN D-3094, July 1965.

62. Bushnell, D. M.; and Huffman, J. K.: Investigation of Heat Transfer to Leading Edge of a 76° Swept Fin with and without Chordwise Slots and Correlations of Swept-Leading Edge Transition Data for Mach 2 to 8. NASA TM X-1475, Dec. 1967.

63. Yeoh, K. B.: Transition Along the Attachment Line of a Swept Cylinder in Supersonic Flow. M. Sc. Thesis, Cranfield College of Aeronautics, Sept. 1980.

64. Collier, F. S.; Johnson, J. B.; Rose, O. J.; and Miller, D. S.: Supersonic Boundary-Layer Transition on the LaRC F-106 and the DFRF F-15 Aircraft, Part I: Transition Measurements and Stability Analysis; Part II: Aerodynamic Predictions. In Research in Natural Laminar Flow and Laminar-Flow Control, Symposium Proceedings, NASA CP-2487, Dec. 1987, pp. 997–1024.

65. Creel, T. R.; Beckwith, I. E.; and Chen, F. J.: Effects of Wind-Tunnel Noise on Swept Cylinder Transition at Mach 3.5. AIAA Paper 86-1085, AIAA/ASME 4th Fluid Mechanics, Plasma Dynamics and Lasers Conference, May 1986.

66. Creel, T. R.; Beckwith, I. E.; and Chen, F. J.: Transition on Swept Leading Edges at Mach 3.5. Journal of Aircraft, vol. 25, 1987, pp. 710–717.

67. Creel, T. R.; Malik, M. R.; and Beckwith, I. E.: Boundary-Layer Instability Mechanisms on a Swept-Leading Edge at Mach 3.5. SAE Paper 871858, SAE Aerospace Technology Conference and Exposition, Oct. 1987.

68. Malik, M. R.: COSAL—A Black-Box Compressible Stability Analysis for Transition Prediction in Three-Dimensional Boundary Layers. NASA CR-165915, 1982.

69. Malik, M. R.; and Beckwith, I. E.: Stability of a Supersonic Boundary Layer Along a Swept Leading Edge. AGARD CP-438, 1988.

70. Wie, Y. S.; and Collier, F. S.: Instability of a Swept Leading Edge Attachment Line Boundary Layer. FED-Vol. 151, Transitional and Turbulent Compressible Flows, ASME, 1993.

71. Wie, Y. S.: BLSTA—A Boundary Layer Code for Stability Analysis. NASA CR-4481, 1992.

72. Malik, M. R.: e^{Malik}: A New Spatial Stability Analysis Program for Transition Prediction Using the e^N Method. High Technology Corporation Report No. HTC-9203, 1992.

73. Creel, T. R.: Effects of Sweep Angle and Passive Relaminarization Devices on a Supersonic Swept-Cylinder Boundary Layer. AIAA Paper 91-0066, 29th Aerospace Sciences Meeting, Jan. 7–10, 1991.

74. Da Costa, J. L.; Alziary de la Chevalerie, D. A.; and de Roquefort, T. A.: Leading Edge Transition by Contamination in Hypersonic Flow. AGARD CP-438, 1988.

75. Da Costa, J. L.: Contribution a l'Etude de la Transition de Bord d'Attaque par Contamination en Ecoulement Hypersonique. Thesis, Poiters University, Mar. 1990.

76. Arnal, D.; Vignau, F.; and Juillen, J. C.: Boundary Layer Tripping in Supersonic Flow. IUTAM Symposium "Laminar-Turbulent Transition," Toulouse, D. Arnal and R. Michel, eds., Springer-Verlag, 1990.

77. Arnal, D.; Vignau, F.; and Laburthe, F.: Recent Supersonic Transition Studies with Emphasis on the Swept Cylinder Case. RAeS Boundary Layer Transition and Control Conference, Cambridge, Apr. 8–12, 1991.

78. Laburthe, F.; and Arnal, D.: Boundary Layer Transition. Final DERAT Report No. 55/5018.45, 1991.

79. Skuratov, A. S.; and Federov, A. V.: Supersonic Boundary Layer Transition Induced by Roughness on the Attachment Line of a Yawed Cylinder. Izvestiya Akademii Nauk SSSR, Mekhanika Zhidkosti i Gaza, vol. 6, Nov.–Dec. 1990, pp. 28–35.

80. Cattafesta, L. N.; Iyer, V.; Masad, J. A.; King, R. A.; and Dagenhart, J. R.: Three-Dimensional Boundary-Layer Transition on a Swept Wing at Mach 3.5. AIAA Paper 94-2375, 25th AIAA Fluid Dynamics Conference, June 1994.

81. Cattafesta, L. N.: Swept-Wing Suction Experiments in the Supersonic Low-Disturbance Tunnel. High Technology Corporation Report No. HTC-9605, 1996.

82. Lin, R. -S.; Masad, J. A.; and Iyer, V.: Computational Study on the Stability and Transition of Three-Dimensional Boundary Layers on a Swept Wing at Mach 3.5. High Technology Corporation Report No. HTC-9606, 1996.

83. Malik, M. R.: "$e^{Malik3D}$: An e^N Code for Three-Dimensional Flow Over Finite-Swept Wings. High Technology Corporation Report No. HTC-9502, 1995.

84. Holden, M.; and Kolly, J.: Attachment Line Transition Studies on Swept Leading Edges at Mach Numbers from 10 to 12. AIAA Paper 95-2279, AIAA 26th Fluid Dynamics Conference, June 19–22, 1995.

85. Murakami, A.; Stanewsky, E.; and Krogmann, P.: Boundary-Layer Transition on Swept Cylinders at Hypersonic Speeds. AIAA Journal, vol. 34, no. 4, 1996, pp. 649–654.

86. Bernard, E.; Gaillard, L.; and Alziary de Roquefort, T.: Influence of Roughness on Attachment Line Boundary Layer Transition in Hypersonic Flow. Experiments in Fluids, vol. 22, 1997, pp. 286–291.

87. Lin, R. -S.; and Malik, M. R.: Stability and Transition in Compressible Attachment-Line Boundary-Layer Flow. SAE Paper 952041, Aerotech '95, 1995.

88. Lin, R. -S.: Attachment-Line Stability and Transition Analysis for Supersonic Flow Along a Swept Leading-Edge. High Technology Report HTC-9602, June 1996.

89. Anderson, B. T.; and Bohn-Meyer, M.: Overview of the Supersonic Laminar Flow Control Research on the F-16XL Ships 1 and 2. SAE Paper 921994, Aerotech '92, 1992.

90. Fischer, M. C.; and Vemuru, C. S.: Application of Laminar Flow Control to the High Speed Civil Transport—the NASA Supersonic Laminar Flow Control Program. SAE Paper 912115, Aerospace Technology Conference and Exposition, Sept. 23–26, 1991.

91. Iyer, V.: Computation of Three-Dimensional Compressible Boundary Layers to Fourth-Order Accuracy on Wings and Fuselages. NASA CR-4269, 1990.

92. Woan, C. J.; Gingrich, P. B.; and George, M. W.: CFD Validation of a Supersonic Laminar Flow Control Concept. AIAA 91-0188, AIAA 29th Aerospace Sciences Meeting, Jan. 7–10, 1991.

93. Flores, J.; Tu, E.; Anderson, B.; and Landers, S.: A Parametric Study of the Leading Edge Attachment Line for the F-16XL. AIAA Paper 91-1621, AIAA 22nd Fluid Dynamics, Plasma Dynamics and Laser Conference, June 1991.

94. Smith, B. A.: Laminar Flow Data Evaluated. Aviation Week & Space Technology, Oct. 7, 1996, p. 30.

95. Thomas, J.; Krist, S.; and Anderson, W.: Navier-Stokes Computations of Vortical Flows. AIAA Journal, vol. 28, no. 2, 1990, pp. 205–212.

96. Iyer, V.: Three-Dimensional Boundary-Layer Program (BL3D) for Swept Subsonic or Supersonic Wings With Application to Laminar Flow Control. NASA CR-4531, 1993.

97. Walatka, P.; Buning, P.; Pierce, L.; and Elson, P.: PLOT3D User's Manual. NASA TM-101067, 1990.

98. Biedron, R.; and Thomas, J.: A Generalized Patched-Grid Algorithm with Application to the F-18 Forebody with Actuated Control Strake. Computing Systems in Engineering, vol. 1, nos. 2–4, 1990, pp. 563–576.

99. Krist, S.; Washburn, A.; and Visser, K.: A Computational and Experimental Investigation of a Delta Wing with Vertical Tails. AIAA Paper 93-3009, July 1993.

100. Rumsey, C.; and Vatsa, V.: A Comparison of the Predictive Capabilities of Several Turbulence Models Using Upwind and Central-Difference Computer Codes. AIAA Paper 93-0192, Jan. 1993.

101. Ghaffari, F.; Luckring, J.; Thomas, J.; Bates, B.; and Biedron, R.: Multiblock Navier-Stokes Solutions about the F/A-18 Wing-LEX-Fuselage Configuration. Journal of Aircraft, vol. 30, no. 3, 1993, pp. 293–303.

102. Robinson, B.; Verhoff, A.; and Bozzetta, W.: Preliminary Findings in Certification of CFL3D. AIAA Paper 94-2236, June 1994.

103. Steinbrenner, J.; Chawner, J.; and Fouts, C.: The GRIDGEN 3D Multiple Block Grid Generation System. Wright Research and Development Center TR 90-3022, July 1990.

104. Walatka, P.; Clucas, J.; McCabe, R.; Plessel, T.; and Potter, R.: FAST User Guide 1.1. NASA Ames Research Center NAS Report RND 93-010, July 1993.

105. Kovasznay, L. S. G.: The Hot-Wire Anemometer in Supersonic Flow. Journal of Aeronautical Sciences, vol. 17, 1950, pp. 565–573.

106. Izsak, M. S.: Wakes and Transition in a Rotating Gas Turbine Stage. M.Sc. Thesis, Oxford University, 1988, pp. 80–82.

107. Rose, W. C.; and McDaid, E. P.: Turbulence Measurements in Transonic Flow. AIAA Journal, vol. 15, no. 9, 1977, pp. 1368–1370.

108. Morkovin, M. V.: Fluctuations and Hot Wire Anemometry in Compressible Fluids. AGARDograph 24, Nov. 1956.

109. Smits, A. J.; Hayakawa, K.; and Muck, K. C.: Constant Temperature Hot Wire Practice in Supersonic Flows. Part 1: The Normal Wire. Experiments in Fluids, vol. 1, 1983, pp. 83–92.

110. Wolf, S. W. D.; Laub, J. A.; and King, L. S.: Flow Characteristics of the NASA Ames Laminar Flow Supersonic Wind Tunnel for Mach 1.6 Operation. AIAA Paper 94-2502, 18th AIAA Aerospace Ground testing Conference, June 20–23, 1994.

111. Wolf, S. W. D.; and Laub, J. A.: Low-Disturbance Flow Characteristics of the NASA-Ames Laminar Flow Supersonic Wind Tunnel. AIAA Paper 96-2189, 19th AIAA Advanced Measurements and Ground Based Testing Conference, June 18–20, 1996.

112. Laufer, J.: Factors Affecting Transition Reynolds Numbers on Models in Supersonic Wind Tunnels. Journal of Aeronautical Sciences, vol. 21, 1954, pp. 497–498.

113. Poll, D. I. A.: Boundary Layer Transition by Attachment-Line Contamination in a Compressible Flow with Heat Transfer. Department of Aeronautical Engineering Report 8911, University of Manchester, England, July 1989.

114. Poll, D. I. A.: 3-D Transition to Turbulence by Contamination. Part II—Accurate Determination of the Attachment-Line Chordwise Velocity Gradient. Department of Aeronautical Engineering Report 9311, University of Manchester, England, March 1993.

115. Incropera, F. P.; and DeWitt, D. P.: Fundamentals of Heat Transfer. John Wiley and Sons, New York, 1981, pp. 340–349.

116. Churchill, S. W.; and Bernstein, M.: A Correlating Equation for Forced Convection from Gases and Liquids to a Circular Cylinder in Crossflow. Journal of Heat Transfer, vol. 99, May 1977.

117. Murthy, V.; and Rose, W.: Form Drag, Skin Friction and Vortex Shedding Frequencies for Subsonic and Transonic Cross Flows on Circular Cylinder. AIAA Paper 77-687, June 1977.

118. Degani, D.; and Zilliac, G. G.: Experimental Study of Nonsteady Asymmetric Flow Around an Ogive-Cylinder at Incidence. AIAA Journal, vol. 28, no. 4, 1990, pp. 642–649.

119. Uberoi, M. S.; and Freymouth, P.: Spectra of Turbulence in Wakes Behind Circular Cylinders. Physics of Fluids, vol. 12, no. 7, July 1969, pp. 1359–1363.

120. Liu, T.; Campbell, B. T.; and Sullivan, J. P.: Thermal Paints for Shock/Boundary Layer Interaction in Inlet Flows. AIAA Paper 92-3626, AIAA/SAE/ASME/ASEE 28th Joint Propulsion Conference and Exhibit, July 6–8, 1992.

121. Coleman, C. P.; Poll, D. I. A.; and Lin, R. -S.: Experimental and Computational Investigation of Leading Edge Transition at Mach 1.6. AIAA Paper 97-1776, 28th AIAA Fluid Dynamics Conference, June 29–July 2, 1997.

122. Coleman, C. P.; Poll, D. I. A.; Laub, J. A.; and Wolf, S. W. D.: Leading Edge Transition on a 76 Degree Swept Cylinder at Mach 1.6. AIAA Paper 96-2082, 27th AIAA Fluid Dynamics Conference, June 17–20, 1996.

123. Gibbings, J. C.: On Boundary Layer Transition Wires. Aeronautical Research Council, CP-462, 1959.

124. Poll, D. I. A.: The Development of Intermittent Turbulence on a Swept Attachment Line Including the Effects of Compressibility. The Aeronautical Quarterly, Vol. XXXIV, Feb. 1983, pp. 1–23.

125. Poll, D. I. A.: Boundary Layer Transition on the Windward Face of Space Shuttle During Re-Entry. AIAA Paper 85-0899, June 1985.

126. Demetriades, A.: Comparison of Techniques for Defining the Transitional Region Extent. 5th NASP Transition Workshop, NASA Langley Research Center, Feb. 10–11, 1992.

127. Reshotko, E.; and Beckwith, I. E.: Compressible Laminar Boundary Layer Over a Yawed Infinite Cylinder with Heat Transfer and Arbitrary Prandtl Number. NACA TN-3986, 1957.

128. Pruett, C. D.; and Street, C. L.: A Spectral Collocation Method for Compressible, Non-Similar Boundary Layers. International Journal of Numerical Methods in Fluids, vol. 13, 1991, pp. 713–737.

129. Kazakov, A. V.: Influence of Surface Heating on the Stability of a Swept Attachment Line Boundary Layer. IUTAM Symposium on Nonlinear Instability and Transition in Three-Dimensional Boundary Layers, Manchester, England, July 17–20, 1995.

130. CRC Handbook of Materials Science. Volume II, Metals, Composites and Refractory Materials, CRC Press, pp. 183 and 198, 1975.

131. Megson, T.: Aircraft Structures for Engineering Students. 2nd Edition, Halsted Press, New York, 1991, pp. 545–546.

132. Oberg, E.; Jones, F. D.; and Horton, H. L.: Machinery's Handbook. 22nd Edition, Industrial Press Inc., New York, 1984, p. 252.

133. Engineering Manual Series, Aircraft and Missile Repair—Structural Hardware. (USAF) T.O. 1-1A-8 and (NAVY) NAVAIR 01-1A-8, Table 2-18, Sept. 1980, pp. 2–23.

REPORT DOCUMENTATION PAGE

Form Approved
OMB No. 0704-0188

1. AGENCY USE ONLY *(Leave blank)*	2. REPORT DATE	3. REPORT TYPE AND DATES COVERED
	March 1998	Technical Memorandum

4. TITLE AND SUBTITLE

Boundary Layer Transition in the Leading Edge Region of a Swept Cylinder in High Speed Flow

5. FUNDING NUMBERS

522-31-12

6. AUTHOR(S)

Colin P. Coleman

7. PERFORMING ORGANIZATION NAME(S) AND ADDRESS(ES)

Ames Research Center
Moffett Field, CA 94035-1000

8. PERFORMING ORGANIZATION REPORT NUMBER

A-98-09981

9. SPONSORING/MONITORING AGENCY NAME(S) AND ADDRESS(ES)

National Aeronautics and Space Administration
Washington, DC 20546-0001

10. SPONSORING/MONITORING AGENCY REPORT NUMBER

NASA/TM—1998-112224

11. SUPPLEMENTARY NOTES

Point of Contact: Colin P. Coleman, Ames Research Center, MS 260-1, Moffett Field, CA 94035-1000
(650) 604-0613

12a. DISTRIBUTION/AVAILABILITY STATEMENT

Unclassified — Unlimited
Subject Category 02

12b. DISTRIBUTION CODE

13. ABSTRACT *(Maximum 200 words)*

Experiments were conducted on a 76 degree swept cylinder to establish the behavior of the attachment line transition process in a low-disturbance level, Mach number 1.6 flow.

For a near adiabatic wall condition, the attachment-line boundary layer remained laminar up to the highest attainable Reynolds number. The attachment-line boundary layer transition under the influence of trip wires depended on wind tunnel disturbance level, and a transition onset condition for this flow is established.

Internal heating raised the surface temperature of the attachment line to induce boundary layer instabilities. This was demonstrated experimentally for the first time and the frequencies of the most amplified disturbances were determined over a range of temperature settings. Results were in excellent agreement to those predicted by a linear stability code, and provide the first experimental verification of theory.

Transition onset along the heated attachment line at an R-bar of 800 under quiet tunnel conditions was found to correlate with an N factor of 13.2. Increased tunnel disturbance levels caused the transition onset to occur at lower cylinder surface temperatures and was found to correlate with an approximate N factor of 11.9, so demonstrating that the attachment-line boundary layer is receptive to increases in the tunnel disturbance level.

14. SUBJECT TERMS

Boundary layer, Transition, Attachment line

15. NUMBER OF PAGES

205

16. PRICE CODE

A10

17. SECURITY CLASSIFICATION OF REPORT	18. SECURITY CLASSIFICATION OF THIS PAGE	19. SECURITY CLASSIFICATION OF ABSTRACT	20. LIMITATION OF ABSTRACT
Unclassified	Unclassified		